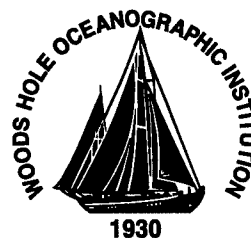


**Massachusetts Institute of Technology
Woods Hole Oceanographic Institution**



**Joint Program
in Oceanography/
Applied Ocean Science
and Engineering**



DOCTORAL DISSERTATION

*Oceanic Fluxes of Mass, Heat and Freshwater:
A Global Estimate and Perspective*

by

DISTRIBUTION STATEMENT A

Approved for public release
Distribution Unlimited

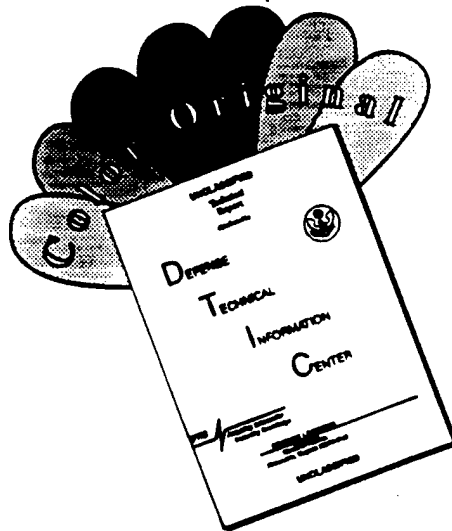
Alison Marguerite Macdonald

September 1995

DTIC QUALITY INSPECTED 3

19960910 124

DISCLAIMER NOTICE



THIS DOCUMENT IS BEST QUALITY AVAILABLE. THE COPY FURNISHED TO DTIC CONTAINED A SIGNIFICANT NUMBER OF COLOR PAGES WHICH DO NOT REPRODUCE LEGIBLY ON BLACK AND WHITE MICROFICHE.

MIT/WHOI

95-25

Oceanic Fluxes of Mass, Heat and Freshwater:
A Global Estimate and Perspective

by

Alison Marguerite Macdonald

Massachusetts Institute of Technology
Cambridge, Massachusetts 02139

and

Woods Hole Oceanographic Institution
Woods Hole, Massachusetts 02543

September 1995

DOCTORAL DISSERTATION

Funding was provided by the National Aeronautic and Space Administration through a Graduate Fellowship in Global Change Research and under Contract NAGW-1048 and by a National Science Foundation Grant No. OCE-9205942 through the Massachusetts Institute of Technology.

Reproduction in whole or in part is permitted for any purpose of the United States Government. This thesis should be cited as: Alison Marguerite Macdonald, 1995. Oceanic Fluxes of Mass, Heat and Freshwater: A Global Estimate and Perspective. Ph.D. Thesis. MIT/WHOI, 95-25.

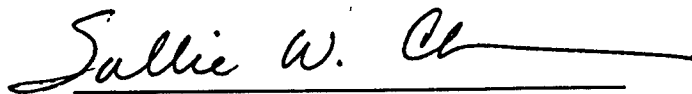
Approved for publication; distribution unlimited.

Approved for Distribution:

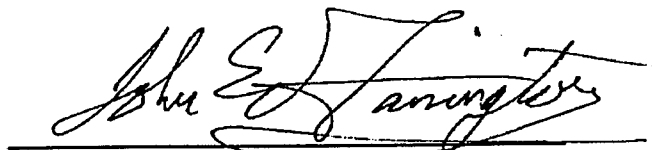


Philip L. Richardson, Chair
Department of Physical Oceanography

DTIC QUALITY INSPECTED 3



Sallie W. Chisholm
MIT Director of Joint Program



John W. Farrington
WHOI Dean of Graduate Studies

**OCEANIC FLUXES OF MASS, HEAT AND
FRESHWATER:
A GLOBAL ESTIMATE AND PERSPECTIVE**

by

Alison Marguerite Macdonald

B.A. Bryn Mawr College, Bryn Mawr Pa.

(1981)

S.M. Massachusetts Institute of Technology, Cambridge Mass.

(1991)

Submitted in partial fulfillment of the
requirements for the degree of

Doctor of Philosophy

at the

MASSACHUSETTS INSTITUTE OF TECHNOLOGY

and the

WOODS HOLE OCEANOGRAPHIC INSTITUTION

August 1995

© Alison M. Macdonald 1995

The author hereby grants to MIT and to WHOI permission to reproduce
and to distribute copies of this thesis document in whole or in part.

Signature of Author *Alison Macdonald*

Joint Program in Physical Oceanography
Massachusetts Institute of Technology
Woods Hole Oceanographic Institution
August 25, 1995

Certified by *Carl Wunsch*

Cecil and Ida Green Professor of Physical Oceanography
Thesis Supervisor

Accepted by *Carl Wunsch*

Chairman, Joint Committee for Physical Oceanography
Massachusetts Institute of Technology
Woods Hole Oceanographic Institution

OCEANIC FLUXES OF MASS, HEAT AND FRESHWATER: A GLOBAL ESTIMATE AND PERSPECTIVE

by

Alison Marguerite Macdonald

Submitted in partial fulfillment of the requirements for the degree of
Doctor of Philosophy at the Massachusetts Institute of Technology
and the Woods Hole Oceanographic Institution
August 28, 1995

Abstract

Data from fifteen globally distributed, modern, high resolution, hydrographic oceanic transects are combined in an inverse calculation using large scale box models. The models provide estimates of the global meridional heat and freshwater budgets and are used to examine the sensitivity of the global circulation, both inter and intra-basin exchange rates, to a variety of external constraints provided by estimates of Ekman, boundary current and throughflow transports.

A solution is found which is consistent with both the model physics and the global data set, despite a twenty five year time span and a lack of seasonal consistency among the data. The overall pattern of the global circulation suggested by the models is similar to that proposed in previously published local studies and regional reviews. However, significant qualitative and quantitative differences exist. These differences are due both to the model definition and to the global nature of the data set.

The picture of the global circulation which emerges from the models is a complex, turbulent flow. When integrated across ocean basins not one, but two major cells emerge. The first connects an Atlantic overturning cell (estimated at $18 \pm 4 \times 10^9 \text{ kg s}^{-1}$) to the Southern Ocean where the Antarctic Circumpolar Current carries lower deep waters to the Indian and Pacific basins where they are converted to upper deep and intermediate waters before returning to the Atlantic. The second cell connects the Pacific and Indian Basins to the north and south of Australia. In this cell deep waters pass into the Pacific and return within the Indian Basin as intermediate waters after passing through the Indonesian Passages. The two cells are found to be independent of one another, *i.e.* within the models, the Indonesian Passages do not represent a significant element in a net global circulation.

While there is ample evidence of westward flow around the southern tip of South Africa which would support a "warm" water path scenario, the variability of flow in this region, rich with eddies makes hydrography a poor estimator of the

relative strengths of the controversial "warm" and "cold" water paths. All existing estimates of Indonesian Passage throughflow, including the smallest ($0 \times 10^6 \text{ m}^3 \text{ s}^{-1}$) and the largest ($20 \times 10^6 \text{ m}^3 \text{ s}^{-1}$), are consistent with the model constraints. When the Pacific-Indian throughflow is not constrained, the model produces an estimate of $11 \pm 14 \times 10^9 \text{ kg s}^{-1}$.

The model heat flux estimates are both significantly different from zero and quite robust to changes in initial assumptions, with the exception of the choice of wind field. Although in this work it was not possible to compute freshwater fluxes which were significantly different from zero, future inclusion of salinity anomaly constraints along with terms describing vertical diffusion may yet make it possible to compute significant freshwater flux estimates from hydrography.

Thesis Supervisor: Carl Wunsch,
Cecil and Ida Green Professor of Physical Oceanography
Department of Earth, Atmospheric and Planetary Sciences
Massachusetts Institute of Technology

Acknowledgements

Although I am obliged to put my own name on the cover of this dissertation, I am by no means the only person to have put both time and effort into its creation. I would first like to thank my thesis advisor, Carl Wunsch whose support, patience and scientific guidance, have brought this thesis through its many iterations to a successful conclusion. I would also like to thank the other members of my thesis committee John Toole, Harry Bryden, Jochem Marotzke, Paola Malanotte-Rizzoli and my defense chairman Bill Schmitz for their suggestions, scientific critique and patience through not one, but two final drafts.

I am, once again, indebted to Bud Brown for his technical assistance in producing the figures. I also wish express my gratitude to Charmaine King and Linda Meinke, not only for their technical expertise, but also for the private use of their office. I would also like to acknowledge the help of Chelle Gentemann who spent a semester working on the initial data processing as a UROP student. Diana Spiegel, what can I say? A simple thank you hardly seems enough. But thank you all the same, for your help with everything from the copying, to the data processing, to the programming, and the running of the model and the analysis routines; and thank you for your friendship and kind words of comfort and encouragement given when I needed them most.

I also wish to express my appreciation to four very good friends, fellow students and colleagues: Molly Baringer, Cecilie Mauritzen, Jim Gunson and Einat Aharonov, for their willingness to be interrupted in their own work, their always thought provoking conversation and their advise, commiseration and comradeship.

Finally, I give my warmest thanks to my family: to my parents, sisters and brother for always being there; to my husband, Fran for all the love, support and dog walking that made going back to school possible and now it seems, successful; to Fiona, my sunshine, whose mind is quicker than my own and whose insight into the world at large never ceases to amaze me; and to little Pete for his smiles and laughter; your sister's timing was impeccable, but yours was even better. You have both brought me a new perspective and the best reason in the world for going home early. Fiona, you will be pleased know that my big work is now... done!

This research was partially funded by a NASA Global Change Fellowship and was also supported by NASA under contract NAGW-1048 and NSF under contract OCE-9205942.

Contents

Abstract	3
Acknowledgements	5
1 Introduction	9
1.1 Purpose/Motivation	9
1.2 The Global Ocean Circulation	10
1.3 Heat Flux Estimates	12
1.4 Freshwater Flux Estimates	14
1.5 Where We Go From Here	16
2 Data Set and Methodology	19
2.1 The Hydrographic Data	19
2.2 Formulation of the Model Equations	24
2.3 The RHS of the Equations	27
2.3.1 Freshwater and Salt Transport	27
2.3.2 Ekman Transport	30
2.3.3 Leakage Terms	33
2.4 Finding a Solution	34

2.4.1	Tapered Weighted Least Squares	34
2.4.2	Recursion of Tapered Weighted Least Squares	35
2.4.3	Estimating the Uncertainty in Transport	40
2.5	Choices Affecting the Model Equations	42
2.5.1	Choice of Isopycnal Layers	43
2.5.2	Choice of Initial Reference Levels	51
2.5.3	Choice of Equation Weights	52
3	The Standard Model	55
3.1	Introduction	55
3.2	Description of the Standard Model	55
3.2.1	Conservation Equations	56
3.2.2	Flux Constraints	58
3.2.3	Topographic Constraints	64
3.2.4	Wind	69
3.2.5	Weights	71
3.2.6	Initial Imbalances	72
3.3	The Standard Model Absolute Velocity Fields and Property Fluxes .	77
3.4	The Standard Model Results	134
	Standard Model Velocity and Mass Transport Results	
3.4.1	The Atlantic Ocean	136
3.4.2	The Southern Ocean	158
3.4.3	The Pacific Ocean	177
3.4.4	The Indian Ocean	192
3.4.5	Summary	204

3.4.6	The Standard Model Freshwater Fluxes	214
3.4.7	The Standard Model Heat Fluxes	223
4	Alternative Models	239
4.1	Introduction	239
4.2	Shallow versus Deep Reference Levels	240
4.3	Unconstrained and Constrained T_{PI}	243
4.4	Cross-Isopycnal Transfer	251
4.5	Model Summary	271
5	Summary and Conclusions	279
A	Station-Specific Reference Levels	293
B	Alternative Model Mass Transport Profiles	296
C	Comparison of the Standard Model and Model NBW	307
	References	316

Chapter 1

Introduction

1.1 Purpose/Motivation

A knowledge of how oceanic fluxes of heat and freshwater influence the equilibration of the global heat budget is fundamental to understanding climate and climate evolution. It is also a key to understanding the water mass transformations which occur within the thermohaline circulation. The character and strength of the global thermohaline circulation is immutably linked to the exchange of heat and freshwater within and among the ocean basins as these fluxes are defined by and actively influence the flow of deep, cold water traveling from pole to equator, the opposing path of warm thermocline water from equatorial climes to regions of water mass formation, and the passage around the globe of a myriad of water masses as they form, develop and interact with one another.

Previous studies, including the more recent ones which have drawn conclusions about the global circulation [*Gordon, 1986; Broecker, 1987; Rintoul, 1991; Gordon et al., 1992; Macdonald, 1993; Schmitz and McCartney, 1993; Schmitz, 1995*] have in general, either been qualitative in nature and/or have not been global in extent.

Those which have had a global scope have been created from a subjective synthesis of regional results. The purpose of the present research is twofold: first, to determine quantitative, globally consistent estimates of oceanic fluxes of mass, heat and freshwater from hydrographic data and second, to see what such a globally consistent circulation pattern can tell us about the exchanges of these properties both within and among the ocean the basins.

1.2 The Global Ocean Circulation

The recent popularity of pictorial schematics of global ocean circulation, such as the *conveyor belt* of Broecker [1987], within the climate change research community, highlights the need to get the picture right, both qualitatively and quantitatively. It should be a source of concern that these schematics give the impression that the global ocean circulation pattern is steady and laminar, which is unlikely, and also that its connections and pathways are simple and well understood, which they are not. Gordon [1986] presented a view of the global thermohaline circulation based on some quantitative observations which has provided a basis for comparison of other estimates and ideas.

The Atlantic Ocean is thought to be the source of most of the deep and bottom waters found throughout the world ocean. According to Gordon [1986], the feed water for the process of North Atlantic Deep Water (NADW) formation is derived from within the main thermocline, *i.e.* NADW upwells within the world ocean and is returned to the Atlantic in the upper layer. He proposed two possible return paths for the feed water. The “cold water path” allows the water to return through the Drake Passage into the South Atlantic at the relatively cold temperatures of Antarctic Intermediate Water and Subantarctic Mode Water. In the “warm water path”, the water would be returned from the Pacific to the Indian Oceans through the

Indonesian Archipelago, across the Indian Ocean in the South Equatorial Current, poleward through the Mozambique Current and eventually around the southern tip of Africa from the retroflection region of the Agulhas Current into the South Atlantic. This water, on entry to the South Atlantic, is warmer than that in Drake Passage, coming mainly from the Indian Ocean thermocline. Which route dominates this return of NADW feed water has been the source of some controversy.

Having assumed a heat flux across 30°S in the South Atlantic of $6.9 \times 10^{14} \text{ W}$ [Hastenrath, 1982], Gordon [1986] estimated that more than 75% of the feed water for NADW returned via the "warm water path". In Macdonald [1993] it was concluded that the data were consistent with a "warm water path" which included a significant transport ($>10 \times 10^9 \text{ kg s}^{-1}$) through the Indonesian Archipelago but which bypassed the Mozambique Channel. A major flow through the Indonesian Archipelago has been considered a necessary, though not sufficient condition for determining that the "warm water path" is the major return route for the feed water. It is not a sufficient condition because, once in the Indian Ocean, the water may still return to the Atlantic via the ACC, through Drake Passage, rather than around Cape Agulhas. The box model circulations of both Rintoul [1991] and Macdonald [1993] were unable to support the large, equatorward heat flux used by Gordon [1986] and were thus brought to the conclusion that the "cold water path" had to be the dominant source of the NADW feed water. In neither of these last two studies, could anything be said about the quantitative aspects of the exchange between the Indian and Atlantic Oceans.

More recently, Gordon *et al.* [1992] have estimated that 10 Sv out of a total of 16 Sv Benguela Current water warmer than 9°C is derived from the Indian Ocean Agulhas Retroflection region. They believe this water to be of South Atlantic origin which has entered the Indian Ocean, has been entrained in the Agulhas recirculation gyre and has then returned to the Atlantic via a process associated with the shedding

of eddies by the Agulhas Current. The upshot of the *Gordon et al.* result is that they expect that as much as two-thirds of the warm water traveling northward in the South Atlantic either originated in or is directly influenced by the Indian Ocean.

Such conclusions depend critically upon the ability to determine not only the mass, heat and freshwater fluxes which occur within the individual ocean basins, but also the exchanges which occur among them. No basin nor connection between basins can be ignored out of hand. For example, none of the above studies placed much, if any emphasis upon the northern connection between the Pacific and Atlantic Oceans through which, it has been suggested, a significant freshwater flux may be passing [*Wijffels et al.* 1992]. Similarly, the conveyor belt of *Broecker* [1991] completely disregards the Drake Passage, "cold water path" connection between the Pacific and Atlantic Basins. To gauge the importance of these various pathways in the maintenance of the global overturning cell it is necessary to determine the distribution of oceanic heat and freshwater fluxes over the *entire* world ocean. Although such a distribution is unlikely to be steady, it is a step forward to find a pattern which is at least consistent with observed data the world over.

1.3 Heat Flux Estimates

The oceans play a significant role in balancing the global heat budget. They have a large capacity for storing heat and the thermohaline circulation of the oceans is driven by the non-uniformity in the heating of the waters over the globe. In recent years, much effort has been expended in determining the magnitude of the meridional heat flux across the basins of the world ocean. A number of different techniques have been used and the result has been a broad range of values, illustrated in Figure 1.1.

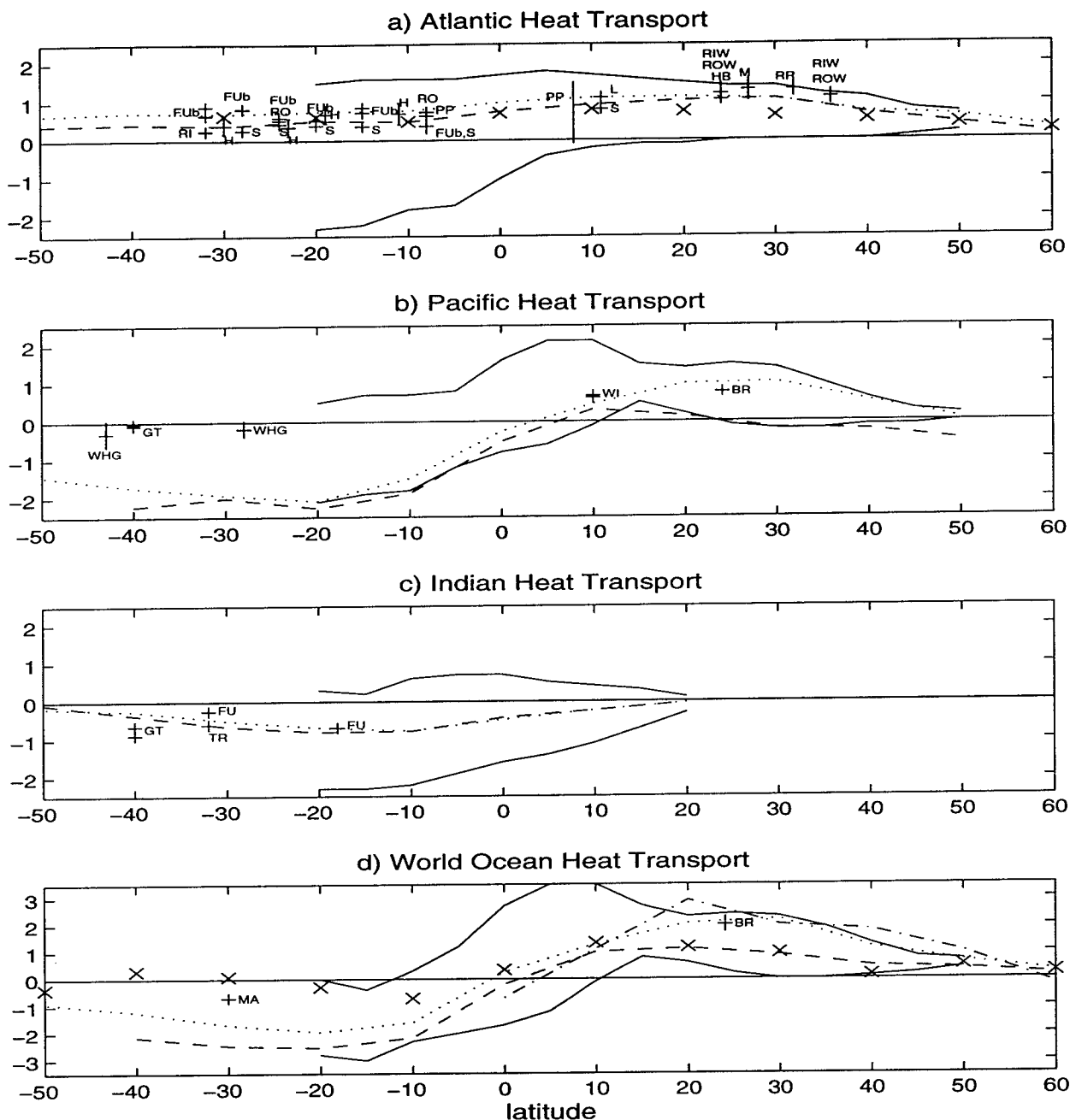


Figure 1.1: Estimates of northward meridional heat transport within the a) Atlantic Ocean, b) Pacific Ocean, c) Indian Ocean and d) World Ocean (units: PW). Solid curves: seasonal extrema reported by *Hsiung et al.* [1989], Dotted Curve: *Hastenrath* [1982], Dashed curve: *Talley* [1984], dash dot curve: *Oort and Van der Haar* [1976] and x's: *Semtner and Chervin* [1992].

The reference initials represent the following: BR: *Bryden et al.* [1991], FU: *Fu* [1986], FUb: *Fu* [1981], HB: *Hall and Bryden* [1982], GT: *Georgi and Toole* [1982], MA: *Macdonald* [1993], M: *Molinari et al.* [1985], H: *Holfort* [1994], PP: range reported by *Philander and Pacanowski* [1986], RI: *Rintoul* [1991], RIW: *Rintoul and Wunsch* [1991], RO: *Roemmich* [1983], ROW: *Roemmich and Wunsch* [1985], RR: *Rago and Rossby* [1987], S: *Sarmiento* [1986], TR: *Toole and Raymer* [1985], W: *Wijffels* [1993], HG: *Wunsch et al.* [1983].

Such a broad range of estimates attests to the great variation among the individual ocean basins and to the difficulty in consistently determining the magnitude of the oceanic heat flux across even a single latitude. Although there does appear to be some convergence in the more recent estimates (especially in the North Atlantic), at some latitudes not only the magnitude but also the sign of the heat flux is in question¹. Many of these results appear to conflict with both each other and current theory, however, the nearly ubiquitous lack of the uncertainties associated with heat flux estimates means that the significance of the variations is not clear. The intention of the present study is to compute estimates of zonally integrated meridional heat flux across all available latitudes based upon a globally consistent circulation pattern and to provide estimates of the uncertainty in these values.

1.4 Freshwater Flux Estimates

As difficult as it appears to be to determine the pattern of heat transport within the oceans, determining the pattern of oceanic freshwater flux represents a task which is, even more formidable. But a knowledge of the freshwater cycle within the oceans is important because it is this cycle which represents the second driving force in the thermohaline circulation. As changes in freshwater convergence and divergence result in changes in density, they affect the formation of water masses (*i.e.* how much deep and bottom water is formed and even whether or not they are formed) and the global thermohaline circulation.

Figure 1.2 presents several estimates from the literature of oceanic meridional freshwater transport. Without interpreting individual values, there are three obvious points to note about the estimates. First, there are discrepancies in both the mag-

¹Throughout this thesis positive values indicate motion northward and eastward, while negative values indicate motion southward and westward.

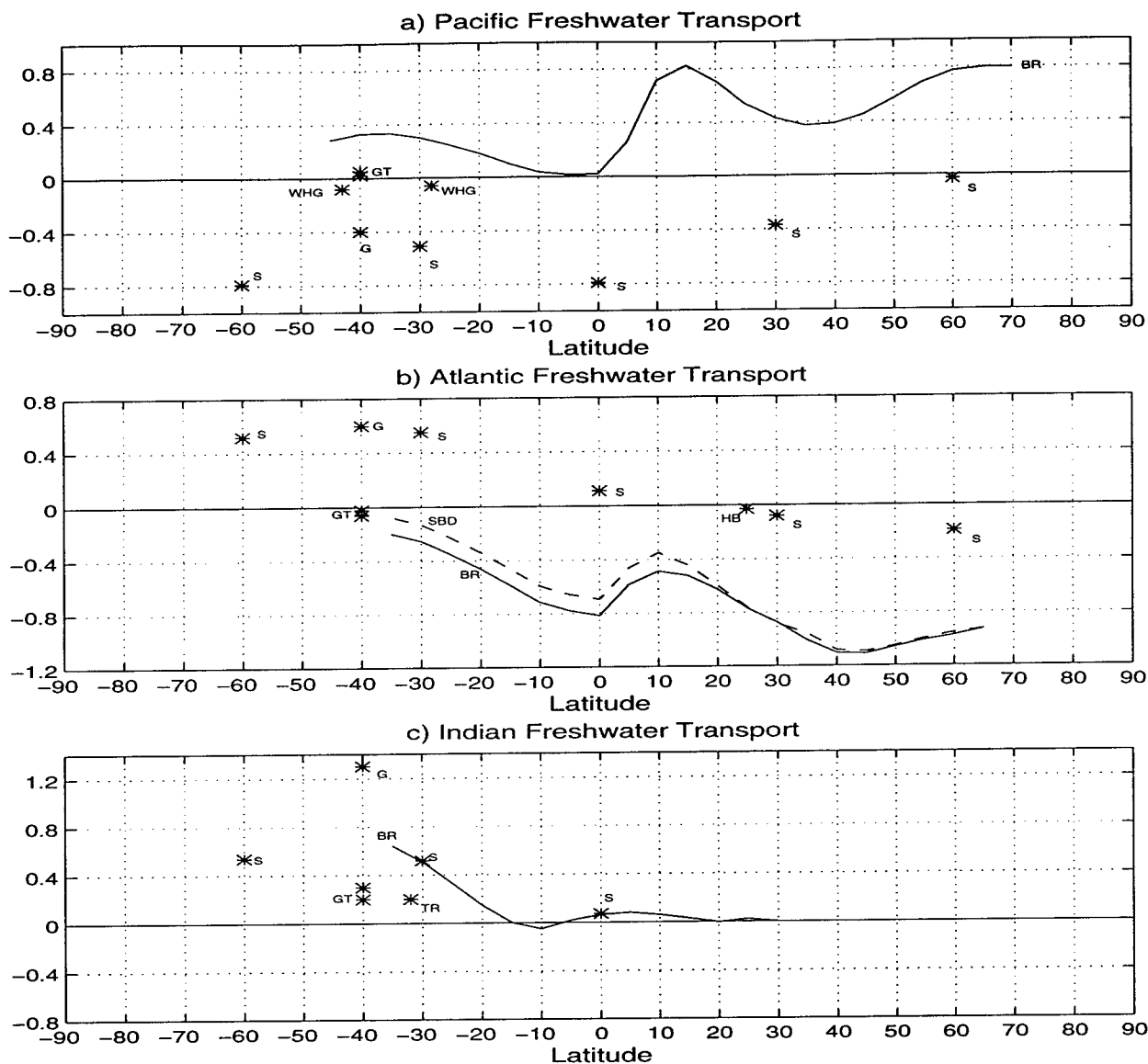


Figure 1.2: Estimates of northward meridional freshwater transport within the a) Pacific Ocean, b) Atlantic Ocean and c) Indian Ocean (units: $10^6 \text{ m}^3/\text{s}$).

The reference initials represent the following:

BR: Solid Curve *Baumgartner and Reichel* [1975] as integrated by *Wijffels et al.* [1992]
(Authors estimate a cumulative 30% uncertainty integrating from north to south)

G: *Guiffrida* [1985]

GT: *Georgi and Toole* [1982] (Authors estimate an uncertainty of about $1 \times 10^6 \text{ m}^3/\text{s}$.)

HB: *Hall and Bryden* [1982] (Authors consider this value to be negligible.)

S: *Baumgartner and Reichel* [1975] as integrated by *Stommel* [1980]

SBD: Dashed Curve *Schmitt et al.* [1989] as integrated by *Wijffels et al.* [1992]

TR: *Toole and Raymer* [1985]

WHG: *Wunsch et al.* [1983]

nitude and the sign of the freshwater fluxes. Secondly, few of the values come from direct oceanographic observations, and the values themselves are very tiny in comparison to most open ocean advective mass fluxes. Finally, in spite of the broad range in the values, there is, as with the heat flux estimates, a general lack of estimates of their uncertainty. What is not obvious from the figure is the historical confusion over the definition of freshwater transport which has made it difficult to even begin to compare individual estimates. This study will present an internally consistent picture of the global distribution of freshwater transport based upon hydrography with a starting reference for integration at the Bering Strait as suggested by *Wijffels et al.* [1992].

1.5 Where We Go From Here

To reiterate, the purpose of this research is to directly (*i.e.* from oceanographic observations) calculate using consistent physics, oceanic fluxes of heat and freshwater simultaneously, at all latitudes at which modern high resolution, basin wide hydrographic sections are available, in an effort to produce a consonant solution in which the effect of exchanges both within and among the ocean basins has been taken into account. The most basic question that can be asked about such an endeavor is whether it is actually possible to produce a globally *consistent* picture of the circulation within the World Ocean from hydrography, which is notoriously non-synoptic. For the standard model which will be described in Chapters 2 and 3, a consistent solution (*i.e. one which can meet the prescribed physical constraints*) can be found. The circulation patterns are however, not necessarily the same as one might expect from experience with local and regional analyses. Not surprisingly, it is found that the globally consistent solutions are affected the by same model choices which affect regional solutions, such as:

- the choice of particular topographic and flux constraints,

- the choice of annual vs. monthly mean winds to compute Ekman transport, as well as the choice of which compilation of wind stress values,
- the choice of geostrophic velocity reference levels.

The difference between the local and global solutions is that within the global model, the influence of these choices extends beyond the local region which was intended to be directly affected. The global model also makes it clear that the decision to include or not to include certain data sets can also affect the some of the results.

Yet globally consistent solutions can be found and given that this is so, the second task of this dissertation is to combine the resulting meridional heat and fresh-water fluxes with zonal estimates of the exchanges among the basins, to investigate the pathways and transformations of water masses which constitute the global thermohaline cell. Uncertainties will be estimated to assess the ability to determine the meridional, oceanic property fluxes from hydrographic CTD and bottle data. The end result is a quantitative schematic of the global ocean circulation and the "overturning cell" which provides not only estimates of mass, heat and freshwater transports, but also estimates of the uncertainty in the values.

The next chapter gives an overview of the data and methodology used in the research. Chapter 3 describes the setup and results of a "standard" global model, as well as, several test runs which attempt to bridge the gap between the standard solutions and the results of local analyses. A number of alternative models examining the effect on the solution of different velocity reference levels, different constraints on Pacific-Indian throughflow and different weights on the model unknowns are described in Chapter 4. The final chapter presents the conclusions from the analysis of the possible NADW return paths and the global overturning cell. It also discusses possibilities for the further investigation and improvement of the standard model.

Chapter 2

Data Set and Methodology

2.1 The Hydrographic Data

The data set used for this research is comprised of 15 basinwide zonal hydrographic/CTD sections (2 in the Indian Ocean, 5 in the Pacific Ocean and 8 in the Atlantic), as well as the hydrographic data from 4 cruises covering the region between Antarctica and the surrounding continents. With a short section across the Florida Straits and two sections in the Mozambique Channel there are a total of 1627 stations. Details specific to the individual cruises are provided in Tables 2.1 and 2.2. The cruise tracks are shown in Figure 2.1. These data were acquired over 25 years and were taken in all seasons. The data in the Atlantic are the most temporally condensed, as all were taken in the spring and summer months of the decade of the 1980s. Since these data are not synoptic, it is by no means clear that a globally consistent circulation can be derived from the observations.

To avoid confusion in the discussion of the data sets we have adopted a simple naming convention. Each zonal section shall be referred to by a name comprised of a pound sign, #, a letter identifying the basin (A for Atlantic, P for Pacific and I

Ocean Basin	Nominal Latitude	Ship & Reference	Abbreviation	Date & Season	# Stations Used
Pacific	47°N	R.V. T. Thompson, <i>Talley et al.</i> [1991]	#P47N	Summer 1985	115
	24°N	R.V. T. Thompson, <i>Roemmich et al.</i> [1991]	#P24N	Spring 1985	212
	10°N	RV Moana Wave, <i>Wijffels</i> [1993]	#P10N	Spring 1989	217
	28°S	Scorpio Eltanin 29, <i>Stommel et al.</i> [1973]	#P28S	Summer 1967	99
	43°S	Scorpio Eltanin 28, <i>Stommel et al.</i> [1973]	#P43S	Spring 1967	76
Indian	12°S	AODC*, <i>You & Tomczak</i> [1993]	#Mz.N	Spring 1965	6
	15°S	AODC <i>You & Tomczak</i> [1993]	#Mz.S	Spring 1965	4
	18°S	Atlantis II 93, <i>Warren</i> [1981b]	#I18S	Summer 1976	57
	32°S	RRS Darwin, <i>Toole & Warren</i> [1993]	#I32S	Winter 1987	106
Atlantic	48°N	Hudson 82, <i>Hendry</i> [1989]	#A48N	Spring 1982	78
	36°N	Atlantis II 109 leg 1, <i>Roemmich</i>	#A36N	Summer 1981	101
	24°N	Atlantis II 109 leg 3, & <i>Wunsch</i> [1985]	#A24N	Summer 1981	89
	11°N	Oceanus 338, <i>Friedrichs & Hall</i> [1993]	#A11N	Spring 1989	85
	11°S	Oceanus 133 leg 5, M. McCartney	#A11S	Spring 1983	82
	23°S	Oceanus 133 leg 3, M. McCartney	#A23S	Winter 1983	99
Atlantic	17°S	SAVE Knorr leg 3, <i>Scripps</i> [1992a]	#A27S	Winter 1988	33
Atlantic	40°S	SAVE Melville leg 4c, <i>Scripps</i> [1992b]	#A27S	Winter 1989	21
Atlantic	65°S	Meteor 11/5, <i>Roether et al.</i> [1990]	#A57S	Winter 1990	78
			#Drake		
			#0E2Afr		

Table 2.1: Details on the zonal hydrographic/CTD sections used in the models. Note that the SAVE legs 3 and 4 are combined. The section referred to as #A27S.W contains all the leg 3 stations and four leg 4 stations. The section #A27S.E contains only leg 4 stations. The stations from the the Meteor 11/5 cruise have been used in three different model sections.

* AODC: Australian Oceanography Data Centre

Between Antarctica &	Ship & Reference	Abbreviation	Start Date	End Date	# Stations Used
S. Africa	RV Knorr, <i>AJAX</i> [1985]	#0E	10/ 7/83	2/15/84	137
S. Africa	RV Conrad 17, <i>Jacobs & Georgi</i> [1977]	#30E	1/ 8/74	4/10/74	53
Australia	USNS Eltanin 41, <i>Nierenburg</i> [1970]	#132E	12/22/69	1/25/70	19

Table 2.2: Details on the meridional hydrographic sections covering the region between Antarctica and the continents.

Hydrographic Sections

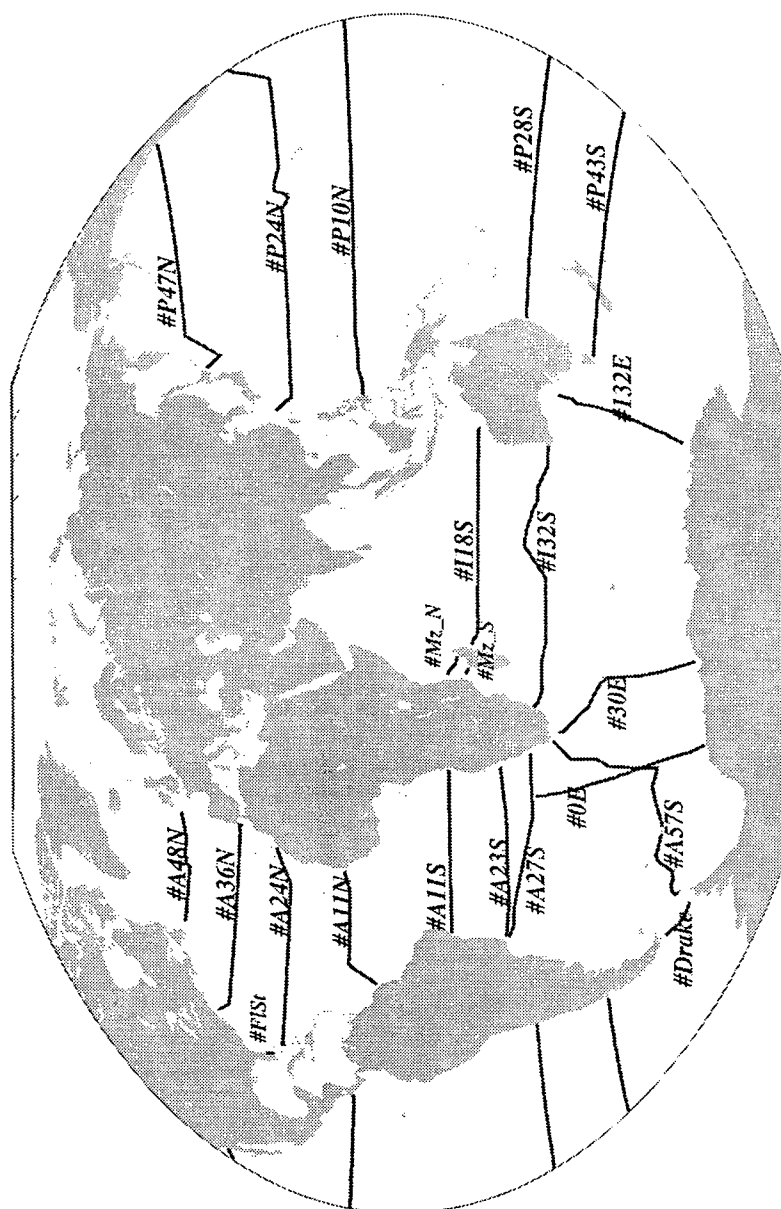


Figure 2.1: The station positions of the hydrographic/CTD sections used in this research. Further details are given in Tables 2.1 and 2.2.

for Indian), the mean latitude of the transect and a letter identifying the hemisphere (N for northern, S for southern). For example, the 1967 SCORPIO Eltanin cruise at 43°S in the South Pacific will be referred to as #P43S. When the need arises to refer to an eastern or western half of a section _E or _W will be appended to the name. The meridional sections will be referred to by their approximate line of longitude, *eg.* #30E is the Conrad 17 section running between South Africa and Antarctica. The letters _N or _S may be appended to indicate a reference to the northern or southern portions of a meridional section. The exceptions to this convention are the data in Drake passage which shall be referred to as #Drake, a section running from 0°E, 45°S to the coast of Africa at about 35°S, referred to as #0E2Afr, the section across the Florida Straits, #FlSt and the two sections in the Mozambique Channel; #Mz_N at 12°S and #Mz_S at 15°S. The pound sign, # which precedes the names is to remind the reader that these names have been created solely as labels for this dissertation. They are not intended to resemble labels produced from other naming conventions. In particular, they should not be confused with the WOCE (World Ocean Circulation Experiment) section labels.

Two of the bounding sections are composites of different data sets. #A27S_W includes data from legs 3 and 4 of the South Atlantic Ventilation Experiment (SAVE) transects. #A27S_E is the eastern end of SAVE leg 4. A57S is a combination of AJAX data (#A57S_W) just west of the South Sandwich Trench (-56°E to -28°E) and Meteor 11/5 data which continues to 2°E.

Along each of the cruise tracks, temperature, salinity, oxygen, phosphate and silica data were taken at a variety of depths, usually to within 5 to 10m of the bottom. A number of these data sets also provided measurements of nitrite, nitrate and chlorofluoromethane but these values were not used in this research. The units for each of the different types of variables are given in Table 2.3. All the data have been converted to these same units. The 1980 equation of state is used throughout

Pressure	db
Temperature	°C
Salinity	psu
Oxygen	ml/l
Phosphate	$\mu\text{moles/kg}$
Silicate	$\mu\text{moles/kg}$
PO38	$\mu\text{moles/kg}$

Table 2.3: Units of variables for all hydrographic/CTD sections used in this thesis.

the research, and salinities are quoted on the practical salinity scale in psu. However, measurement techniques and conductivity formulae have changed over the last 30 years so it is expected that earlier data will be affected by differences in the salinity scale. These differences are not expected to exceed 0.01 [Lewis and Perkins, 1981; Fofonoff, 1985] and since detailed comparisons between transects are not being made, it is not expected that these differences will affect the gross model results. The property values have been interpolated (extrapolated¹ where necessary) onto a set of 37 standard depths.² These depths were chosen to extend to the deepest station in the global data set and to resolve the upper portion of the water column somewhat better than the lower portion. Although some of the data sets contain 2 db CTD data, it was decided to place the CTD values on a coarser grid rather than interpolating bottle data to a finer grid.

The relative geostrophic velocities are computed using data on the standard depths, except in the case of the CTD data. For these data, the dynamic heights are computed at the observed intervals. Where the observed depth matches the standard

¹Stations which did not have temperature and/or salinity data within two standard depths of the bottom were removed, *i.e.* extrapolations were never done over more than a single standard depth.

²The standard depths are defined at 0, 50, 100, 150., 200, 250, 300, 400, 500, 600, 700, 800, 900, 1000, 1100, 1200, 1300, 1400, 1500, 1750, 2000, 2250, 2500, 2750, 3000, 3250, 3500, 3750, 4000, 4250, 4500, 4750, 5000, 5500, 6000, 7000, 8000 dbar.

depth, the observed value is used, otherwise the standard depth value is computed as a weighted average of the observed values above and below the standard depth. In most cases, the velocities are extrapolated below the deepest common depth of each station pair by retaining the isopycnal slope at the deepest common depth down to the bottom. However, in a few places where close station spacing over steep topography has caused an overshooting (an extended extrapolation of strong vertical gradients) in the velocity extrapolation, the velocity at the deepest common depth has been retained to the bottom.

2.2 Formulation of the Model Equations

An inverse box model technique is used to obtain the estimates of mass, heat and freshwater fluxes which will be used to investigate the global circulation pattern. The models are based upon the data described in the previous section, as well as the assumptions that the ocean is in a steady state, and in hydrostatic and geostrophic balance so that the thermal wind equations apply. In combining this set of hydrography we are also making the implicit assumption that each of the synoptic sections represents a time mean.

The models describe a set of boxes (also called areas) which are bounded in the horizontal by hydrographic sections and continents, and in the vertical by potential density interfaces. To resolve the broad range of water characteristics found throughout the global ocean, rather than partitioning the water column into a single large set of potential density layers, each ocean basin has been divided in the vertical, into an individualized set of potential density interfaces which best represent the water masses present in the particular region. Tables which describe the T/S characteristics

of these potential density layers are given in the next chapter where the model specifics are presented.

Given thermal wind, the models are defined through conservation constraints written for each of the areas as well as, flux statements for the individual transects. The equations describe conservation of mass, salt and other properties between potential density interfaces and allow for cross-isopycnal transfer. They are similar to those used by Wunsch *et al.* [1983], Rintoul [1991] and Macdonald [1993] and are of the form:

$$\begin{aligned} & \sum_{j=1}^S \rho_{ij} a_{ij}^S (\mathbf{v}_{ijR} + \mathbf{v}_U)^S C_{ij}^S - \sum_{j=1}^N \rho_{ij} a_{ij}^N (\mathbf{v}_{ijR} + \mathbf{v}_U)^N C_{ij}^N + \\ & \sum_{j=1}^W \rho_{ij} a_{ij}^W (\mathbf{v}_{ijR} + \mathbf{v}_U)^W C_{ij}^W - \sum_{j=1}^E \rho_{ij} a_{ij}^E (\mathbf{v}_{ijR} + \mathbf{v}_U)^E C_{ij}^E - \\ & a_i^{Htop} w_i^{*top} C_i^{Htop} + a_i^{Hbot} w_i^{*bot} C_i^{Hbot} \approx 0, \end{aligned} \quad (2.1)$$

where

- i, j layer and station pair indices;
- ρ density;
- S, N, E, W southern, northern, eastern, and western boundaries of the layer;
- \mathbf{v}_R relative velocity;
- \mathbf{v}_U unknown reference level velocity;
- w^* cross-isopycnal transfer (averaged horizontally over a layer interface);
- C property concentration;
- a interface area (vertical unless indicated otherwise);
- top, bot top and bottom of the layer, respectively;
- H horizontal layer interface.

Such an equation can be written for each conserved property in each layer, as well as for the top to bottom transport. Separate equations can be written to describe

the flux across individual sections. The right hand side can be written to include an estimated ageostrophic component. This set of equations is then manipulated into the form:

$$\sum_j \rho_j \mathbf{a}_j \mathbf{C}_j \mathbf{v}_U - \mathbf{a}^{Htop} \mathbf{C}^{Htop} \mathbf{w}^{*top} + \mathbf{a}^{Hbot} \mathbf{C}^{Hbot} \mathbf{w}^{*bot} \approx - \sum_j \rho_j \mathbf{a}_j \mathbf{v}_{jR} +$$

Ekman Component + Known Flux into or out of a Box etc ..., (2.2)

which can in turn be written,

$$\mathbf{A} \mathbf{b} + \mathbf{n} = -\mathbf{\Gamma}, \quad (2.3)$$

where, the elements of the \mathbf{A} matrix are $A_{ij} = \int_B^T \rho_{ij} \mathbf{a}_{ij} \mathbf{C}_{ij} dp$. The vector \mathbf{b} represents the unknown reference level velocities (\mathbf{v}_U) resulting from the dynamic method and the cross-isopycnal transfer terms (\mathbf{w}^*). $\mathbf{\Gamma}$ is the vector of known relative velocity transports and includes other optional right-hand side elements (*eg.* Ekman transport and leakage terms such as Bering Strait transport, Indonesian Passage throughflow and freshwater inflow/outflow). The \mathbf{A} matrix elements, associated with the individual \mathbf{b}_j 's are constructed from the integrated standard depth values which have been interpolated to the depth of the individual layers used in the integral.

Although cross-isopycnal transfer is allowed for, the models are in some sense two dimensional because all the resolution lies along the cruise transects which bound the boxes. There have been prior attempts to create 3-D inverse box models on the large scale. In particular, *Martel and Wunsch [1993]* produced a 3-D inverse box model of the North Atlantic by smoothing a combination of hydrography, current meter and float data from a five year period onto a 1° grid. They found a number of drawbacks in this method. First, the model was not capable of producing useful estimates of the flow away from the hydrographic lines. Further, because the data was not synoptic, contradictory features had to be removed by a space/time smoothing. This smoothing compromised the resolution of important features, producing for instance, a broad and weak Gulf Stream. Smoothing was also necessary to get the large scale

coverage required and this the authors felt would bias the flux estimates towards zero. Finally, the system was also quite large. Covering only the North Atlantic and using 11 layers, the model contained 260 million elements. To handle the global data set without the use of parallel machinery and to avoid the problems associated with smoothed data, we are using the unsmoothed hydrography.

Having described the basic construct of the models, *i.e.* the areas in which water properties are conserved, the latter sections of this chapter discuss the other basic elements of the models which are included in the right-hand side of Equation 2.3, the particular inverse technique which is used to solve the problem and specific choices which were made for the models used in this study, including: the choice of density layers, noise and solution covariances, and initial reference levels.

2.3 The RHS of the Equations

2.3.1 Freshwater and Salt Transport

Freshwater enters the oceans at the surface as precipitation from the atmosphere and as river runoff from surrounding land masses. It leaves the ocean system through the process of evaporation, again at the sea surface. Because evaporation and precipitation rates vary over the globe, it is expected that the ocean will exhibit non-zero convergences and divergences of freshwater. Salt, unable to move across the free surface must, in contrast be conserved.

Initial estimates of freshwater and salt transport enter the model equations as part of the right-hand side, that is, as a net flux into or out of an area, or across a section. The significance of these initial transport estimates for the model is that they allow for greater independence between the mass and salt conservation equations. All

the models described herein use initial estimates of freshwater exchange between the ocean and atmosphere/land taken from *Baumgartner and Reichel* [1975], except in the Atlantic where the initial estimates come from *Schmitt et al.* [1989]. The absolute velocity fields of the models will be used to produce new estimates of freshwater transport which are consistent with the input hydrographic observations and other model constraints.

For the purposes of this research, freshwater transport is defined as that portion of ocean transport (typically about 96.5%) which is *pure* water. Salt transport is defined similarly, as that portion of the ocean transport which is salt, *i.e.* not pure water (typically about 3.5%). The net gain of freshwater at the sea surface is $P - E + R$, where P is precipitation, E is evaporation and R is river runoff. The transport of salt is simply defined as $T_S = \int \rho v S dA$ and the transport of freshwater as $T_{FW} = \int \rho(v - vS) dA$.

At each latitude where transect data is available, the spatially varying velocities (v') and salinities (S') can be separated from the spatially averaged ones (\bar{v} , \bar{S}), such that,

$$\begin{aligned} v(x, z) &= \bar{v} + v'(x, z) \text{ and} \\ S(x, z) &= \bar{S} + S'(x, z) \end{aligned} \quad (2.4)$$

where the average is defined:

$$\overline{\text{value}} = \frac{\int \text{value}(x, z) dx dz}{\int dx dz}. \quad (2.5)$$

The salt and freshwater fluxes can then be written:

$$T_S = \rho(\bar{v}\bar{S} + \overline{v'S'}) \quad (2.6)$$

$$T_{FW} = \rho(\bar{v} - \bar{v}\bar{S} - \overline{v'S'}). \quad (2.7)$$

Wijffels et al. [1992] use the *Coachman and Aagaard* [1988] Bering Strait Arctic volume inflow estimate of $0.8 \pm 0.1 \times 10^6 \text{ m}^3 \text{ s}^{-1}$ along with the 32.5 salinity estimate

[*Aagaard and Carmack, 1989*] as the reference for integration of air-sea exchange and river runoff estimates to compute freshwater flux, $\rho(\bar{v} - \bar{v}\bar{S})$ and salt flux, $\rho(\bar{v}\bar{S})$. They draw several conclusions pertinent to our calculation.

- To obtain a consistent picture of the global oceanic hydrological cycle, freshwater and salt transports must be considered together.
- Although there is no net divergence of salt transport, the flux of salt across lines of latitude in the Atlantic and Pacific Basins is not zero but rather about $27 \times 10^6 \text{ kg/s}$ which is the flux through Bering Strait (see *Wijffels et al. [1992]* Figure 2).
- Across zonal lines in basins where there is only a small net mass flux, Equation 2.7 demands that the spatially varying component of the salt flux, $\rho\bar{v}'\bar{S}'$ provide the major portion of the transport.

Following the lead provided by these conclusions our model constraints and conclusions will be made under the following guidelines:

- For the sake of consistency, this study uses the estimate of annual mean Bering Strait transport ($0.8 \times 10^6 \text{ m}^3 \text{ s}^{-1}$) of *Coachman and Aagaard, [1988]* as the reference for the freshwater transport estimates. The $0.1 \times 10^9 \text{ kg s}^{-1}$ standard deviation which *Coachman and Aagaard* attached to this mean seems far too small to truly represent the uncertainty in the value. Therefore, the uncertainty which our models will use will be the range of the annual cycle ($0.6 \times 10^9 \text{ kg s}^{-1}$). The larger uncertainty should also allow for differences arising from the fact our model hydrography was obtained in all different seasons.
- Both salt and freshwater fluxes will be considered, and it is expected that the salt flux will not be equal to the negative of the freshwater flux as it is unlikely that \bar{v} will be zero across the basin wide sections.

- The salt fluxes will be considered non-divergent and the salt flux constraints will include the expected net $27 \pm 20 \times 10^6 \text{ kg/s}$ moving southward in the Atlantic and northward in the Pacific based on the Bering Strait transport at 32.5. The uncertainty associated with the salt flux is computed assuming that the uncertainty on the mass flux is the $0.6 \times 10^9 \text{ kg s}^{-1}$, as mentioned above, that the uncertainty on the salinity of the Bering Strait throughflow is the rather large though arbitrary value of 1.5 (using 10 only increases the salt flux uncertainty estimate by $2 \times 10^6 \text{ kg/s}$) and that there is no correlation between the uncertainty of the mass flux and the salinity.
- As in numerous inverse calculations (*i.e.* Wunsch *et al* [1983], Rintoul [1991] and Macdonald [1993]), both the spatially averaged and spatially varying component of the salt transport will be considered.

The term which is used by the model constraints $\sum_i \sum_j \rho_{ij} \mathbf{a}_{ij} \mathbf{v}_{ij} S_{ij}$ (see Equation 2.1) is $\rho \bar{v} \bar{S}$. Therefore, the salt flux computed by the model contains both the mean and spatially varying components and since $\rho \bar{v} \bar{S}$ can easily be computed, the spatially varying component may be extracted. It is expected that this meridional transport produced by correlations between high velocities and high salinities and likewise, low velocities and low salinities will vary in magnitude throughout the ocean, as will its relative importance to the global thermohaline circulation.

2.3.2 Ekman Transport

Estimates of Ekman transport across each of the sections are computed from the European Centre for Medium Range Weather Forecasts (ECMWF) wind stress values (Trenberth *et al.*, 1989). These wind stress values represent data from the years 1980 through 1986 and are based upon a twice daily 1000 mb ECMWF analysis

on a 2.5° grid. For each section, the Ekman transport is computed from the annual mean wind stress values (over the 7 year period), using the simplified formulas:

$$T_{Ek_y} = \sum_i^N \frac{-(\tau_i^x \Delta x_i)}{f} \quad \text{and} \quad T_{Ek_x} = \sum_i^N \frac{(\tau_i^y \Delta y_i)}{f_i} \quad (2.8)$$

where T_{Ek} is the Ekman transport normal to the wind direction, x and y represent the zonal and meridional directions, respectively, N is the number of 2.5° grid boxes associated with the section, Δx and Δy represent the distance associated with the grid box at the latitude of interest, τ is the wind stress from the Trenberth *et al.* (1989) data set and finally, f is defined as $2\Omega \sin\theta$.

Table 2.4 gives these annual mean Ekman transport estimates for each of the sections, as well as the mean for the months associated with each cruise for comparison. The uncertainty of Ekman transport ($\sigma_{T_{Ek}}$) is based upon the temporal and spatial variance of the mean wind stress across the section. As we are ignoring the fact that the hydrography has been taken in different seasons and we are assuming that it represents a mean circulation, it follows that an annually averaged Ekman transport should be used to balance it. In a few cases (in particular, #P24N, #P10N and #I18S) the annual mean estimate of Ekman transport is significantly different from the cruise mean. It might be argued that use of the annual mean in these cases would create an inconsistency between the hydrography and the wind field. However, a more apparent inconsistency occurs in the model results when using the cruise mean winds. Early models which attempted to use the cruise mean Ekman transport had trouble meeting mass conservation constraints and produced circulation patterns whose characteristics (especially in the Pacific and Indian Basins) were so completely different from conventional wisdom that it was decided to use annual winds instead.

Ekman transport is included in the right-hand side of the models in two ways. First, it is included as a net flux of mass and salt across individual sections. Secondly,

Section	Annual Mean	Standard Dev. in Annual Mean	Cruise Months	Cruise Mean	Standard Dev. in Cruise Mean
#A48N	-3.8	0.8	Apr.	-0.6	0.5
#A36N	-2.7	0.8	June	-1.9	0.4
#Flst	0.2	0.1	Sept.	0.13	0.04
#A24N	5.4	0.7	Aug.	5.9	0.3
#A11N	9.3	1.3	Feb.-March	13.0	1.0
#A11S	-11.2	0.7	March	-9.3	0.4
#A23S	-4.3	0.4	Feb.	-4.6	0.3
#A27S_W	0.2	0.5	Feb.	-1.0	0.2
#A27S_E	-0.2	0.3	Jan.	-0.3	0.2
#A57S_W	1.2	0.2	Feb.	0.9	0.3
#A57S_E	1.0	0.1	Feb	1.0	0.3
#0E2Afr	1.5	0.4	Feb.-March	1.9	0.4
#0E_N	1.2	0.3	Jan./Oct.	1.2	0.2
#0E_S	0.1	0.2	Jan.	0.2	0.3
#P47N	-5.4	1.0	Aug.-Sept.	-4.2	0.6
#P24N	8.8	1.3	Apr.-May	12.7	0.8
#P10N	24.3	2.7	Feb.-Apr.	41.8	1.9
#P28S	-5.5	1.0	June-July	0.2	1.0
#P43S	9.8	0.9	March-Apr.	7.9	0.8
#Mz_N	-0.6	0.5	May	-0.9	0.2
#Mz_S	-0.1	0.2	May	-0.2	0.1
#I18S	-15.9	1.5	July-Aug.	-24.6	1.2
#I32S	0.5	1.0	Nov.-Dec.	-0.5	0.6
#Drake	0.4	0.2	Jan.	0.3	0.1
#30E	2.9	0.7	Feb.-March	2.8	0.9
#132E	2.2	0.5	Dec.-Jan.	1.1	0.3

Table 2.4: Estimates of Ekman transport computed from the ECMWF wind stress values [Trenberth et al. 1989]. All units are $\times 10^6 \text{ m}^3 \text{ s}^{-1}$. Positive values are northward and eastward.

the convergence/divergence of Ekman fluxes within each area is included in the top to bottom mass and salt conservation equations. The mean salinity of the uppermost potential density layer in the section is used to compute the salt flux due to the Ekman transport across the individual sections. The Ekman salt flux across each of the bounding sections are added together to find the net convergence/divergence within an area.

The Ekman component is also indirectly included as one of the factors describing the uncertainty in the conservation equations for the surface layers of the models. This scaling factor for surface layers is computed as $T_{Ek} * A_{out} / A_{tot}$, where A_{out} is the area over which a particular layer outcrops and A_{tot} is the total surface area of the box. That is, conservation is required to a lesser degree in layers which outcrop and are therefore, likely to be directly affected by the wind. Thus, Ekman transport is not required to be balanced solely within the surface layer. The models are allowed to choose how (where in the vertical) to balance the Ekman flux. The weights make it somewhat easier for the compensation to occur in the upper layers which come in direct contact with the atmosphere.

2.3.3 Leakage Terms

Leakage terms on the right hand side of Equation 2.3 describe net fluxes of mass and other properties across sections. The Bering Strait transport of approximately $0.8 \times 10^9 \text{ kg s}^{-1}$ at 32.5 has already been described in Section 2.3.1 and is represented in all the mass and salt flux equations in the Pacific and Atlantic Basins. The transport through the Indonesian Archipelago represents a much larger unknown in the system. Even the most recent estimate of Indonesian Passage throughflow from the Pacific to the Indian range from indistinguishable from zero to as high as 20 Sv [Toole and Warren, 1993; Meyers *et al.*, 1995; Fieux *et al.*, 1994; Wijffels 1993]. The standard

model which will be described in Chapter 3 places a constraint of $10 \pm 10 \times 10^9 \text{ kg s}^{-1}$ on the flow through the Indonesian Passage. Subsequent models (described in Chapter 4) examine the effect of unconstrained and differently constrained throughflow.

Other right hand side terms which can be grouped with the leakage terms are those describing either net fluxes through sections or boundary currents which may not be adequately sampled by the data. Examples of such terms are the mass transport through Drake Passage, through the Florida Straits and in the North Brazil Current at 11°N . The specific values used will be described in the next chapter where the standard model is introduced.

2.4 Finding a Solution

2.4.1 Tapered Weighted Least Squares

As the set of simultaneous equations described above represents a noisy under-determined system, an inverse technique is used to solve it. The technique used in this research is a recursive, tapered weighted least squares. This section reviews the tapered weighted least squares (TWLS) method as applied to an ocean system where the unknowns are the geostrophic reference level velocities and the horizontally averaged cross-isopycnal transfer terms. It also discusses the advantages for this particular problem of using the TWLS method recursively.

The objective function, J to be minimized by the tapered, weighted least squares technique is:

$$J = (\mathbf{Ab} + \mathbf{\Gamma})^T \mathbf{N}^{-1} (\mathbf{Ab} + \mathbf{\Gamma}) + \mathbf{b}^T \mathbf{S}^{-1} \mathbf{b}, \quad (2.9)$$

The term "weighted" refers to the weighting of the equations by their expected noise covariances, \mathbf{N} . The term "tapered" refers here to scaling of the unknowns by their

expected order of magnitude, $S^{-\frac{1}{2}}$. N and S represent *a priori* estimates of the noise and solution covariance functions. The initial estimates of these estimated weighting factors are described in Section 2.5.3.

Minimizing the objective function ($\partial J / \partial \mathbf{b} = 0$):

$$2\mathbf{A}^T\mathbf{N}^{-1}(\mathbf{A}\mathbf{b} + \mathbf{\Gamma}) + 2\mathbf{S}^{-1}\mathbf{b} = 0$$

$$(\mathbf{S}^{-1} + \mathbf{A}^T\mathbf{N}^{-1}\mathbf{A})\mathbf{b} = \mathbf{A}^T\mathbf{N}^{-1}(-\mathbf{\Gamma})$$

$$\hat{\mathbf{b}} = (\mathbf{S}^{-1} + \mathbf{A}^T\mathbf{N}^{-1}\mathbf{A})^{-1}\mathbf{A}^T\mathbf{N}^{-1}(-\mathbf{\Gamma}) \quad (2.10)$$

$$\mathbf{P} = (\mathbf{S}^{-1} + \mathbf{A}^T\mathbf{N}^{-1}\mathbf{A})^{-1}$$

where \mathbf{P} is the covariance of the estimated solutions, $\hat{\mathbf{b}}$ about their unknown true values. Using the matrix inversion lemma (*e.g.* see *Brogan* [1982]), Equation 2.10 can be written,

$$\hat{\mathbf{b}} = \mathbf{K}(-\mathbf{\Gamma}) \quad \text{and} \quad \mathbf{P} = \mathbf{S} - \mathbf{K}\mathbf{A}\mathbf{S} \quad (2.11)$$

$$\text{where } \mathbf{K} = \mathbf{S}\mathbf{A}^T(\mathbf{N} + \mathbf{A}\mathbf{S}^{-1}\mathbf{A}^T)^{-1}$$

Equation 2.11 is the tapered weighted least squares solution. We now move on to a discussion of how this technique can be used recursively.

2.4.2 Recursion of Tapered Weighted Least Squares

In this research a large number of individual data sets (hydrographic sections) are combined. Each new data set provides new constraints on data already in the model but also carries a new set of associated unknowns (reference level velocities and

possibly vertical transfer terms). Imagine that we begin with a single box defined by two zonal hydrographic sections and land bounding the meridional walls. The unknowns are the reference level velocities at each station pair in each of the sections and possibly, vertical transfer terms. We solve the problem using the TWLS method (Equation 2.11).

$$\begin{aligned} J_1 &= (\mathbf{A}_1 \mathbf{b}_1 + \Gamma_1)^T \mathbf{N}_1^{-1} (\mathbf{A}_1 \mathbf{b}_1 + \Gamma_1) + \mathbf{b}_1^T \mathbf{S}_1^{-1} \mathbf{b}_1 \\ \hat{\mathbf{b}}_1 &= \mathbf{K}_1 (-\Gamma_1) \end{aligned} \tag{2.12}$$

$$\mathbf{P}_1 = \mathbf{S}_1 - \mathbf{K}_1 \mathbf{A}_1 \mathbf{S}_1$$

$$\mathbf{K}_1 = \mathbf{S}_1 \mathbf{A}_1^T (\mathbf{N}_1 + \mathbf{A}_1 \mathbf{S}_1 \mathbf{A}_1^T)^{-1}$$

The subscript ones ("1") indicate that this is the first step of the recursion and that this solution depends solely on the first set of observations. Beware, these subscripts are *NOT* indices to the matrices and vectors.

Now we introduce a new hydrographic section which when added to the previous observation creates a second box which is connected to the first by a common zonal boundary and a common set of unknowns. The new objective function becomes:

$$\begin{aligned} J_2 &= (\mathbf{A}_1 \mathbf{b}_1 + \Gamma_1)^T \mathbf{N}_1^{-1} (\mathbf{A}_1 \mathbf{b}_1 + \Gamma_1) + \\ &(\mathbf{A}_2 \mathbf{b}_2 + \Gamma_2)^T \mathbf{N}_2^{-1} (\mathbf{A}_2 \mathbf{b}_2 + \Gamma_2) + \mathbf{b}_2^T \mathbf{S}_2^{-1} \mathbf{b}_2, \end{aligned} \tag{2.13}$$

where \mathbf{b}_2 and \mathbf{S}_2 contain the information which has been gleaned from the first step in the recursion, as well as, the information associated with the unknowns for the

second step of the recursion, *i.e.*

$$\mathbf{b}_2 = \begin{bmatrix} \mathbf{b}_1 \\ \mathbf{b}_{\text{new unknowns}} \end{bmatrix} \quad \mathbf{S}_2 = \begin{bmatrix} \mathbf{S}_1 & 0 \\ 0 & \mathbf{S}_{\text{new unknowns}} \end{bmatrix}. \quad (2.14)$$

The second step of the recursion recognizes the existence of the unknowns associated with the first step *i.e.* \mathbf{A}_2 contains zeros in all columns associated with the unknowns in the first step of the recursion which are not used in the second step.

Minimizing \mathbf{J}_2 gives,

$$\hat{\mathbf{b}}_2 = \hat{\mathbf{b}}_1[1 \ 2] - \mathbf{K}_2(\mathbf{A}_2\hat{\mathbf{b}}_1[1 \ 2] + \mathbf{\Gamma}_2) \quad (2.15)$$

$$\mathbf{P}_2 = \mathbf{P}_1[1 \ 2] - \mathbf{K}_2\mathbf{A}_2\mathbf{P}_1[1 \ 2]$$

$$\mathbf{K}_2 = \mathbf{P}_1[1 \ 2]\mathbf{A}_2^T(\mathbf{N}_2 + \mathbf{A}_2\mathbf{P}_1[1 \ 2]\mathbf{A}_2^T)^{-1}$$

where the values in brackets indicate the sets of observation unknowns employed, *i.e.* $\hat{\mathbf{b}}_1[1 \ 2]$ is equivalent to $\hat{\mathbf{b}}_1$ with zeros at the positions of the new unknowns associated with the second step in the recursion.

Note that now if the subscript ones ("1") in Equations 2.12 are replaced with twos ("2"), let $\mathbf{S}_1 = \mathbf{P}_0$, and explicitly state that our initial estimate for all values of the unknowns $\hat{\mathbf{b}}_0$ is zero, then Equations 2.12 are exactly the same as Equations 2.15. In both cases, we have replaced the data, \mathbf{A} and $\mathbf{\Gamma}$ and an initial estimate of the unknowns and their uncertainty with new estimates of the unknowns and their uncertainty. The order in which this recursion is accomplished is immaterial. Mathematically the solutions found using a single step or two or more steps are exactly the same.

In this research we began with a model consisting of a few boxes in the South Atlantic (areas I-IV see Figure 2.2). As data processing allowed, new data sets were

Model Areas

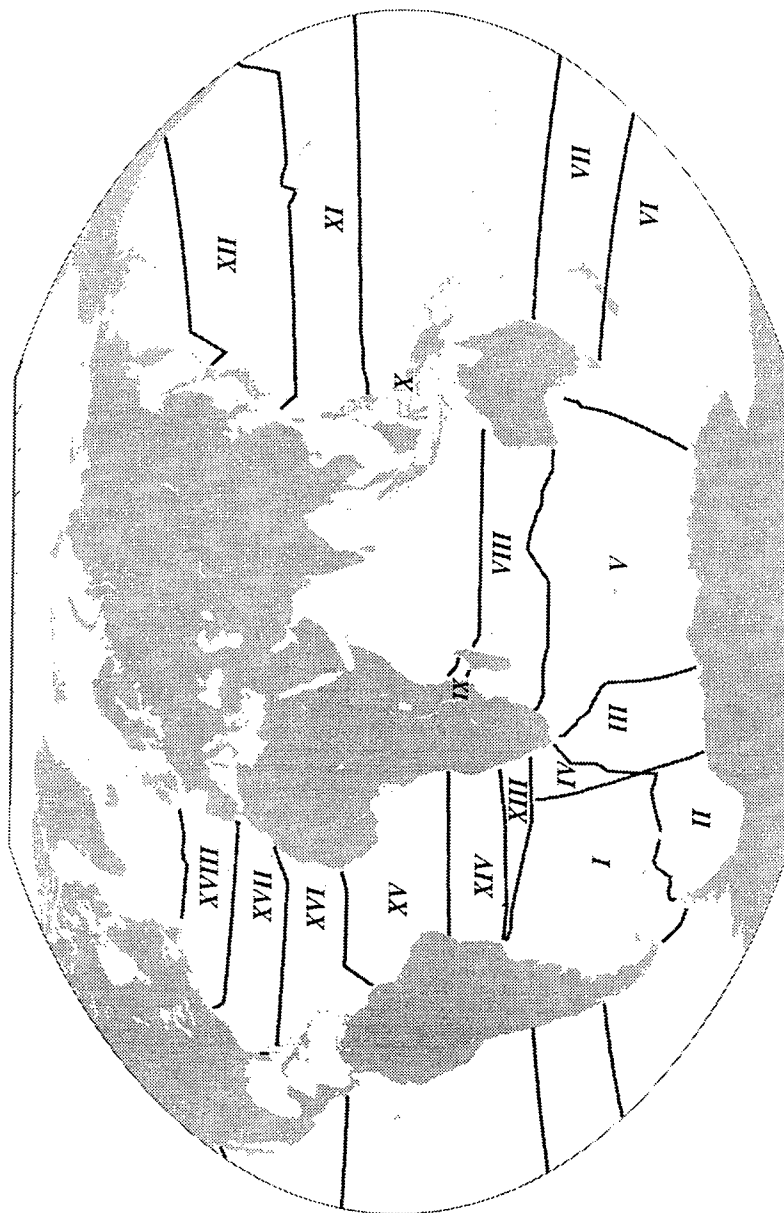


Figure 2.2: The model areas as defined by land and hydrography.

Recursion Regions

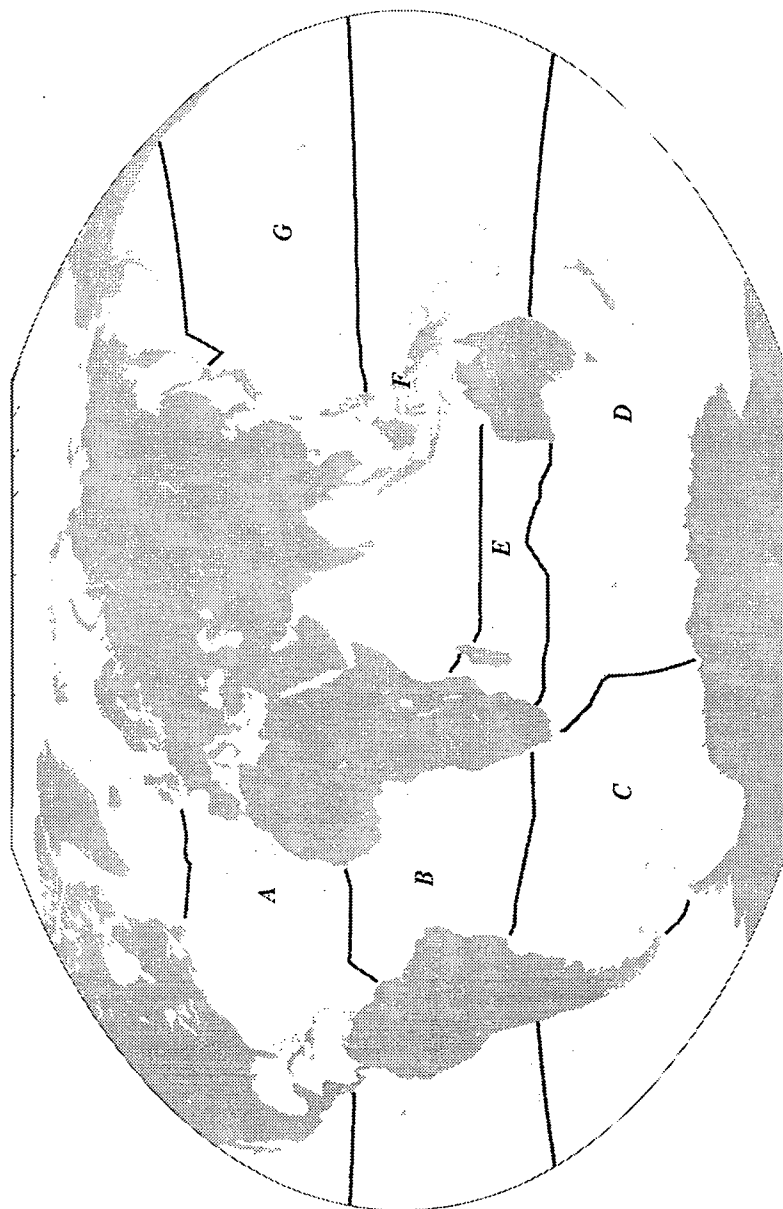


Figure 2.3: The regions or groups of areas which are used in the recursion. The individualized sets of isopycnal layers used within each region are described in Tables 2.5a through 2.5g.

included to create the standard global model discussed in Chapter 3. This was done by including the data recursively rather than by creating a single large A matrix containing all the constraint equations for all the areas. The groups of areas which made up the steps in the recursion are illustrated in Figure 2.3. The initial estimate of each variable b_{0j} was zero and each unknown had an associated initial estimate of its covariance P_{0j} . Once an estimate for the unknown b_{Xj} and its covariance P_{Xj} were found, the specific model (Model X as defined by its individual set of constraints) which produced the result was left behind. Thus, the inclusion into the model of some future data set (representing new constraints and/or new unknowns) can easily be accomplished and its affect upon the solution can be examined. Recursion is a valuable asset to researcher running the models. However, in the discussion of the model results, use of recursion as a solution technique should be transparent to the reader.

2.4.3 Estimating the Uncertainty in Transport

In the calculation discussed in the previous section, the initial estimate of the solution covariance, S (which begins in our problem as a diagonal matrix, *i.e.* an estimate of the solution variance) is reduced by an amount KAS to produce P . The P matrix describes the covariances of the estimated solutions \hat{b}_j about their unknown true values. The uncertainty of the reference level velocities and cross-isopycnal transfer terms, σ_b is taken to be the square root of the diagonal of the final (last step in the recursion) P matrix.

The reference level velocities only carry a portion of the total transport across a section. The total transport of any particular property C across a section can be written:

$$\begin{aligned}
 T_C &= T_R + T_b + T_N & (2.16) \\
 &= \text{Transport due to the relative velocities} + \\
 &\quad \text{Transport due to the reference level velocities} + \\
 &\quad \text{Transport due to the ageostrophic components of velocity.}
 \end{aligned}$$

Let $\hat{C}_j = \Delta x_j \int_{-D_j}^0 C_j \rho_j dz$, where J is the number of station pairs, j is the index to the individual stations, D_j is the depth a station pair, Δx_j is the spacing between the stations in the pair, then, Equation 2.16 becomes:

$$T_C = \hat{C} (v_R + v_b + v_N). \quad (2.17)$$

The uncertainty in transport estimates due to the uncertainty in the reference level velocities is taken to be,

$$\sigma_{T_b}^2 \equiv < (\sum_j \hat{C}_j \hat{b}_j)^2 > \quad (2.18)$$

$$\begin{aligned}
 &= < (\sum_i \hat{C}_i \hat{b}_i) (\sum_j \hat{C}_j \hat{b}_j) > & (2.19) \\
 &= \hat{C} P \hat{C}^T
 \end{aligned}$$

It is this uncertainty, σ_{T_b} which is quoted throughout the text as the uncertainty in the estimated transport. Estimates of σ_{T_b} for the property fluxes across the model sections are given in Table 3.5.

Since the model weights consist of an estimate of the overall uncertainty in the model equations, as well as, estimates of the uncertainty due to outcropping and the uncertainty in the Ekman transports, the estimate of $\sigma_{\hat{C}}$ also includes these elements. The estimate of σ_{T_b} only includes them as they relate to the uncertainty in the reference level velocities.

The main problem preventing the calculation of an estimate of the total uncertainty in transport, σ_{T_C} is our inability to compute σ_{T_R} , that portion which is due to the uncertainty in the relative velocity field, i.e the geostrophic calculation. It is here that the assumption that a set of hydrographic sections taken over a period of decades in all seasons is capable of representing a mean field, enters the estimate of the uncertainty in transport. As new data become available, it is beginning to be possible to perform temporal comparisons of hydrographic transects. Such comparisons are a starting point for determining an estimate of σ_{T_R} . *Roemmich and Cornuelle* [1990] have been investigating the temporal variations of the large scale circulation of the subtropical South Pacific through a time-series of XBT sections between New Zealand and Fiji in an effort to determine the statistics of the mean and time-varying components of hydrographic fields. With a four year record they find that the mean field dominates at wavelengths greater than 2000 km and the time varying component dominates at shorter wavelengths. Substantial interannual variability in the gyre-scale circulation exists and they conclude that longer (both spatially and temporally) transects are necessary for determining extent of these variations. We do not currently have the means for estimating σ_{T_R} on a global scale and since all three components of Equation 2.16 contribute to the uncertainty in any estimate of absolute transport *the transport uncertainties quoted within the text must be considered lower bounds for the true uncertainty!*

2.5 Choices Affecting the Model Equations

This section describes the many choices which can affect the model equations and therefore, solutions. Much of the information contained in this section can be found within the literature, (*e.g.* see *Wiggins* [1972], *Roemmich* [1980], *Wunsch et al.* [1983], *Rintoul* [1991] and *Macdonald* [1991]) and therefore, may not be of interest to all

readers. If skipping over this section please keep in mind that Tables 2.5a– 2.5g which describe the specific isopycnal layer definitions used in the models, are referred to in later chapters.

2.5.1 Choice of Isopycnal Layers

Each enclosed area in the inverse calculation is divided into a set of potential density layers in the vertical. Within these potential density layers, it is expected that mass and other properties will be approximately conserved. It can be argued that the neutral surface, defined as that in which the gradient normal to the surface is always parallel to the buoyancy force [McDougall, 1987] might be a more accurate choice. Here a compromise is made, in which rather than computing neutral surfaces, the pressure reference level is allowed to change as a bounding isopycnal surface expresses large vertical variations. The difference in pressure between the isopycnal surface and its reference pressure never exceeds 500 db. In this way, it approximates the neutral surface which by definition will be the same as the isopycnal surface at the reference pressure. The error introduced by this approximation is expected to be much less than the measurement error [Rintoul, 1988].

The layers used in this study are described in Tables 2.5a through 2.5g. The recursive inclusion of data is done several boxes or areas at a time. Within each region or group of areas (see Figure 2.3) individualized isopycnal layers are chosen. Sections which are used in more than one region are listed in the tables for every region in which they are used. The layers have been chosen to allow recognition of the variety of water masses found throughout the world's oceans. As the thickness of the layers can affect the size of the equation coefficients which can in turn affect the solution (see Section 2.5.3), there was also some attempt to use layers of similar thickness. However, this became extremely difficult near the poles and crossing the equator. As

	Upper Boundary	Lower Boundary	Temperature (°C) Salinity				
			#A48N	#A36N	#FLST	#A24N	#A11N
1	surface	$\sigma_\theta = 26.40$	–	19.51	23.378	22.062	21.50
			–	36.295	36.375	36.895	36.065
2	$\sigma_\theta = 26.40$	$\sigma_\theta = 26.80$	-0.42	16.51	16.22	16.713	13.237
			33.269	36.274	35.170	36.332	35.409
3	$\sigma_\theta = 26.80$	$\sigma_\theta = 27.10$	11.70	13.08	12.19	13.229	10.22
			35.553	35.762	35.545	35.796	35.079
4	$\sigma_\theta = 27.10$	$\sigma_\theta = 27.30$	10.31	10.78	8.98	10.548	7.49
			35.376	35.495	35.116	34.450	34.824
5	$\sigma_\theta = 27.30$	$\sigma_\theta = 27.50$	7.56	9.22	6.52	7.98	5.54
			35.097	35.427	34.902	35.182	34.743
6	$\sigma_\theta = 27.50$	$\sigma_\theta = 27.70$	5.64	7.76	5.38	6.08	4.81
			35.032	35.493	34.840	35.110	34.899
7	$\sigma_\theta = 27.70$	$\sigma_2 = 36.87$	4.22	4.90	–	4.84	4.20
			34.967	35.119	–	35.091	34.970
8	$\sigma_2 = 36.87$	$\sigma_2 = 36.94$	3.48	3.95	–	4.05	3.66
			34.933	35.029	–	35.050	34.972
9	$\sigma_2 = 36.94$	$\sigma_2 = 36.98$	3.19	3.44	–	3.54	3.26
			34.949	34.997	–	35.018	34.962
10	$\sigma_2 = 36.98$	$\sigma_2 = 37.02$	2.91	3.04	–	3.096	2.91
			34.951	34.973	–	34.984	34.948
11	$\sigma_2 = 37.02$	$\sigma_4 = 45.81$	2.65	2.68	–	2.70	2.59
			34.946	34.951	–	34.954	34.932
12	$\sigma_4 = 45.81$	$\sigma_4 = 45.85$	2.37	2.37	–	2.36	2.30
			34.931	34.930	–	34.928	34.914
13	$\sigma_4 = 45.85$	$\sigma_4 = 45.87$	2.18	2.13	–	2.13	2.08
			34.915	34.911	–	34.908	34.897
14	$\sigma_4 = 45.87$	$\sigma_4 = 45.90$	2.04	1.98	–	1.96	1.89
			34.915	34.903	–	34.894	34.880
15	$\sigma_4 = 45.90$	$\sigma_4 = 45.91$	1.91	1.85	–	1.81	1.74
			34.908	34.893	–	34.885	34.866
16	$\sigma_4 = 45.91$	$\sigma_4 = 45.92$	1.80	1.73	–	1.63	1.60
			34.903	34.879	–	34.862	34.854
17	$\sigma_4 = 45.92$	bottom	1.71	–	–	1.49	1.34
			34.897	–	–	34.844	34.823

Table 2.5a: Potential Density Layer Boundaries and Layer Average Potential Temperature and Salinity for zonal sections in the North Atlantic Ocean (Region A according to Figure 2.3). A dash indicates no water within the layer.

	Upper Boundary	Lower Boundary	Temperature (°C) Salinity				
			#A11N	#A11S	#A23S	#A27S.W	#A27S.E
1	surface	$\sigma_\theta = 26.20$	22.09 36.098	22.95 36.460	20.66 36.147	20.00 36.013	17.62 35.544
2	$\sigma_\theta = 26.20$	$\sigma_\theta = 26.80$	13.55 35.448	13.25 35.328	12.93 35.182	12.86 35.159	12.61 35.09
3	$\sigma_\theta = 26.80$	$\sigma_\theta = 27.20$	9.38 35.001	7.90 34.719	7.19 35.567	6.91 34.518	6.98 34.520
4	$\sigma_\theta = 27.20$	$\sigma_\theta = 27.40$	6.14 34.734	4.70 34.502	4.09 34.414	3.77 34.363	3.86 34.375
5	$\sigma_\theta = 27.40$	$\sigma_1 = 32.16$	5.12 34.798	3.94 34.612	3.40 34.534	3.11 34.491	3.15 34.496
6	$\sigma_1 = 32.16$	$\sigma_2 = 36.82$	4.59 34.940	3.86 34.806	3.25 34.700	2.97 34.653	2.92 34.641
7	$\sigma_2 = 36.82$	$\sigma_2 = 36.89$	4.00 34.974	3.66 34.907	3.18 34.817	2.93 34.771	2.86 34.755
8	$\sigma_2 = 36.89$	$\sigma_2 = 36.94$	3.60 34.972	3.41 34.935	3.08 34.873	2.86 34.831	2.77 34.814
9	$\sigma_2 = 36.94$	$\sigma_2 = 36.98$	3.26 34.962	3.12 34.937	2.93 34.902	2.76 34.872	2.61 34.43
10	$\sigma_2 = 36.98$	$\sigma_2 = 37.03$	2.85 34.946	2.73 34.924	2.63 34.906	2.56 34.894	2.34 34.854
11	$\sigma_2 = 37.03$	$\sigma_4 = 45.82$	2.51 34.927	2.43 34.911	2.39 34.902	2.38 34.901	2.17 34.857
12	$\sigma_4 = 45.82$	$\sigma_4 = 45.85$	2.27 34.911	2.24 34.902	2.18 34.889	2.15 34.882	2.05 34.856
13	$\sigma_4 = 45.85$	$\sigma_4 = 45.87$	2.08 34.897	2.05 34.891	2.03 34.887	2.03 34.881	1.87 34.845
14	$\sigma_4 = 45.87$	$\sigma_2 = 37.09$	1.97 34.888	1.95 34.883	1.94 34.881	1.88 34.873	1.59 34.817
15	$\sigma_2 = 37.09$	$\sigma_4 = 45.895$	1.86 34.877	1.80 34.869	1.76 34.858	1.79 34.867	1.46 34.804
16	$\sigma_4 = 45.895$	$\sigma_4 = 45.925$	1.73 34.865	1.62 34.850	1.57 34.840	1.58 34.840	1.40 34.798
17	$\sigma_4 = 45.925$	$\sigma_4 = 46.00$	1.34 34.823	1.09 34.795	1.09 34.793	1.02 34.783	0.87 34.746
18	$\sigma_4 = 46.00$	bottom	– –	0.38 34.723	0.38 34.726	0.46 34.726	– –

Table 2.5b: Potential Density Layer Boundaries and Layer Average Potential Temperature and Salinity for zonal sections in the South Atlantic Ocean (Region B according to Figure 2.3). A dash indicates no water within the layer.

	Upper Boundary	Lower Boundary	Temperature (°C) Salinity						
			P43S	P28S	I32S	A27S_W	A27S_E	A57S_W	A57S_E
1	surface	$\sigma_\theta = 26.20$	13.14 34.381	17.85 35.352	17.62 35.583	20.00 36.013	17.62 35.544	– –	– –
2	$\sigma_\theta = 26.20$	$\sigma_\theta = 26.80$	9.93 34.585	11.64 34.868	12.67 35.169	12.86 35.159	12.61 35.094	– –	– –
3	$\sigma_\theta = 26.80$	$\sigma_\theta = 27.20$	6.484 34.393	6.49 34.415	7.80 34.590	6.91 35.518	6.98 34.520	2.37 33.938	1.38 33.835
4	$\sigma_\theta = 27.20$	$\sigma_1 = 32.00$	3.97 34.366	4.21 34.406	4.31 34.420	3.82 34.357	3.91 34.370	1.45 34.070	0.60 33.979
5	$\sigma_1 = 32.00$	$\sigma_1 = 32.16$	3.06 34.470	3.25 34.502	3.33 34.505	3.13 34.482	3.18 34.488	1.02 34.186	0.17 34.097
6	$\sigma_1 = 32.16$	$\sigma_1 = 32.36$	2.34 34.607	2.31 34.606	2.66 34.636	2.97 34.681	2.89 34.690	1.21 34.437	0.20 34.311
7	$\sigma_1 = 32.36$	$\sigma_2 = 37.00$	1.74 34.686	1.66 34.670	2.07 34.733	2.78 34.586	2.63 34.834	1.41 34.571	0.57 34.438
8	$\sigma_2 = 37.00$	$\sigma_2 = 37.04$	1.42 34.709	1.36 34.691	1.67 34.745	2.50 34.899	2.25 34.855	1.39 34.609	0.71 34.480
9	$\sigma_2 = 37.04$	$\sigma_2 = 37.09$	1.09 34.718	1.10 34.709	1.26 34.734	2.12 34.883	1.87 34.842	1.20 34.666	1.02 34.575
10	$\sigma_2 = 37.09$	$\sigma_3 = 41.60$	0.78 34.716	0.76 34.716	0.82 34.717	1.39 34.821	0.96 34.755	1.02 34.684	1.243 34.644
11	$\sigma_3 = 41.60$	$\sigma_3 = 41.63$	0.59 34.714	0.61 34.713	0.51 34.705	0.74 34.755	0.72 34.732	0.83 34.685	0.681 34.685
12	$\sigma_3 = 41.63$	$\sigma_3 = 41.65$	0.55 34.739	– –	0.25 34.694	0.40 34.721	– –	0.40 34.679	0.16 34.678
13	$\sigma_3 = 41.65$	$\sigma_3 = 41.66$	– –	– –	0.11 34.685	0.16 34.695	– –	-0.02 34.666	0.03 34.673
14	$\sigma_3 = 41.66$	$\sigma_4 = 46.08$	– –	– –	0.04 34.681	-0.01 34.679	– –	-0.13 34.663	-0.10 34.669
15	$\sigma_4 = 46.08$	$\sigma_4 = 46.14$	– –	– –	– –	-0.18 34.664	– –	-0.38 34.657	-0.41 34.658
16	$\sigma_4 = 46.14$	bottom	– –	– –	– –	– –	– –	-0.653 34.650	-0.67 34.650

Table 2.5c: Potential Density Layer Boundaries and Layer Average Potential Temperature and Salinity for zonal sections in the Southern Ocean (Regions C and D according to Figure 2.3). A dash indicates no water within the layer.

	Upper Boundary	Lower Boundary	Temperature (°C) Salinity					
			#Drake	#0E.N	#0E.S	#0E2Afr	#30E	#132E
1	surface	$\sigma_\theta = 26.20$	9.08 33.761	16.36 35.575	– –	17.07 35.252	17.02 35.166	14.98 35.226
2	$\sigma_\theta = 26.20$	$\sigma_\theta = 26.80$	7.52 34.037	11.43 34.861	– –	10.66 34.711	9.98 34.576	10.75 34.775
3	$\sigma_\theta = 26.80$	$\sigma_\theta = 27.20$	4.35 34.156	5.80 34.330	0.80 33.899	5.79 34.355	5.44 34.285	7.02 34.465
4	$\sigma_\theta = 27.20$	$\sigma_1 = 32.00$	2.42 34.176	3.13 34.250	0.58 33.979	3.47 34.275	3.22 34.279	3.46 34.308
5	$\sigma_1 = 32.00$	$\sigma_1 = 32.16$	2.19 34.359	2.60 34.406	0.05 34.072	2.83 34.346	2.47 34.405	2.70 34.425
6	$\sigma_1 = 32.16$	$\sigma_1 = 32.36$	2.12 34.583	2.47 34.619	-0.58 34.316	2.50 34.586	2.06 34.585	2.32 34.608
7	$\sigma_1 = 32.36$	$\sigma_2 = 37.00$	1.80 34.701	2.28 34.769	0.41 34.563	2.31 34.767	2.04 34.744	1.95 34.723
8	$\sigma_2 = 37.00$	$\sigma_2 = 37.04$	1.47 34.724	2.01 34.808	0.64 34.635	2.03 34.808	1.88 34.790	1.58 34.742
9	$\sigma_2 = 37.04$	$\sigma_2 = 37.09$	1.11 34.723	1.66 34.802	0.74 34.679	1.50 34.783	1.44 34.767	1.15 34.731
10	$\sigma_2 = 37.09$	$\sigma_3 = 41.60$	0.75 34.715	0.95 34.741	0.58 34.684	0.90 34.738	0.87 34.726	0.75 34.715
11	$\sigma_3 = 41.60$	$\sigma_3 = 41.63$	0.52 34.709	0.55 34.709	0.40 34.684	0.58 34.714	0.50 34.704	0.49 34.705
12	$\sigma_3 = 41.63$	$\sigma_3 = 41.65$	0.29 34.703	0.23 34.683	0.19 34.679	0.22 34.684	0.26 34.690	0.23 34.690
13	$\sigma_3 = 41.65$	$\sigma_3 = 41.66$	0.18 34.696	0.02 34.671	0.06 34.674	0.03 34.673	0.10 34.680	0.10 34.685
14	$\sigma_3 = 41.66$	$\sigma_4 = 46.08$	– –	-0.11 34.668	-0.09 34.668	-0.14 34.663	-0.07 34.673	-0.01 34.682
15	$\sigma_4 = 46.08$	$\sigma_4 = 46.14$	– –	-0.17 34.668	-0.40 34.659	-0.24 34.654	-0.39 34.660	-0.29 34.677
16	$\sigma_4 = 46.14$	bottom	– –	– –	-0.73 34.652	– –	-0.65 34.652	-0.52 34.679

Table 2.5d: Potential Density Layer Boundaries and Layer Average Potential Temperature and Salinity for meridional sections in the Southern Ocean (Regions C and D according to Figure 2.3). A dash indicates no water within the layer.

	Upper Boundary	Lower Boundary	Temperature (°C) Salinity			
			#I32S	#I18S	#Mz_N	#Mz_S
1	surface	$\sigma_\theta = 25.00$	20.20 34.711	22.87 34.910	24.46 34.877	24.13 34.897
2	$\sigma_\theta = 25.00$	$\sigma_\theta = 26.20$	17.51 35.620	17.77 35.449	17.29 35.318	16.89 35.243
3	$\sigma_\theta = 26.20$	$\sigma_\theta = 26.60$	14.10 35.370	14.13 35.352	13.57 35.212	13.69 35.230
4	$\sigma_\theta = 26.60$	$\sigma_\theta = 27.00$	10.14 34.830	10.08 34.873	10.33 34.925	10.45 34.998
5	$\sigma_\theta = 27.00$	$\sigma_\theta = 27.40$	5.28 34.447	5.98 34.604	7.02 34.755	7.07 34.758
6	$\sigma_\theta = 27.40$	$\sigma_1 = 32.16$	3.37 34.500	4.33 34.668	5.09 34.783	5.39 34.780
7	$\sigma_1 = 32.16$	$\sigma_1 = 32.36$	2.66 34.636	3.04 34.706	3.43 34.769	– –
8	$\sigma_1 = 32.36$	$\sigma_2 = 36.95$	2.20 34.721	2.22 34.729	2.48 34.767	– –
9	$\sigma_2 = 36.95$	$\sigma_2 = 37.00$	1.92 34.742	1.86 34.732	2.08 34.768	– –
10	$\sigma_2 = 37.00$	$\sigma_4 = 45.85$	1.60 34.745	1.56 34.732	1.69 34.752	– –
11	$\sigma_4 = 45.85$	$\sigma_4 = 45.95$	1.13 34.730	1.10 34.723	1.40 34.743	– –
12	$\sigma_4 = 45.95$	$\sigma_4 = 45.99$	0.69 34.712	0.74 34.716	– –	– –
13	$\sigma_4 = 45.99$	bottom	0.34 34.697	0.66 34.726	– –	– –

Table 2.5e: Potential Density Layer Boundaries and Layer Average Potential Temperature and Salinity for zonal sections in the Indian Ocean (Region E according to Figure 2.3). A dash indicates no water within the layer.

	Upper Boundary	Lower Boundary	Temperature (°C) Salinity			
			#I18S	#Mz_N	#P28S	#P10N
1	surface	$\sigma_\theta = 24.30$	23.60 34.811	25.58 34.778	— —	25.81 34.496
2	$\sigma_\theta = 24.30$	$\sigma_\theta = 26.00$	19.07 35.360	18.72 35.284	18.46 35.391	16.70 34.667
3	$\sigma_\theta = 26.00$	$\sigma_\theta = 26.80$	13.16 35.233	12.83 35.141	12.26 34.924	10.77 34.670
4	$\sigma_\theta = 26.80$	$\sigma_\theta = 27.20$	8.18 34.680	8.70 34.804	6.49 34.415	7.43 34.574
5	$\sigma_\theta = 27.20$	$\sigma_1 = 32.16$	4.81 34.645	5.66 34.772	3.74 34.453	4.36 34.563
6	$\sigma_1 = 32.16$	$\sigma_2 = 36.80$	3.39 34.696	3.80 34.772	2.63 34.453	2.84 34.604
7	$\sigma_2 = 36.80$	$\sigma_2 = 36.90$	2.67 34.717	2.94 34.766	2.14 34.625	2.19 34.633
8	$\sigma_2 = 36.90$	$\sigma_2 = 36.96$	2.18 34.730	2.41 34.768	1.75 34.661	1.74 34.658
9	$\sigma_2 = 36.96$	$\sigma_2 = 37.00$	1.83 34.733	2.04 34.768	1.55 34.679	1.48 34.671
10	$\sigma_2 = 37.00$	$\sigma_4 = 45.85$	1.56 34.732	1.68 34.752	1.36 34.690	1.28 34.679
11	$\sigma_4 = 45.85$	$\sigma_4 = 45.87$	1.38 34.728	1.45 34.743	1.23 34.699	1.19 34.685
12	$\sigma_4 = 45.87$	$\sigma_4 = 45.90$	1.22 34.725	1.35 34.744	1.15 34.708	1.07 34.691
13	$\sigma_4 = 45.90$	$\sigma_4 = 45.95$	0.99 34.720	— —	0.96 34.716	0.93 34.699
14	$\sigma_4 = 45.95$	bottom	0.74 34.716	— —	0.683 34.714	— —

Table 2.5f: Potential Density Layer Boundaries and Layer Average Potential Temperature and Salinity for zonal sections which surround the Indonesian Archipelago (Region F according to Figure 2.3). A dash indicates no water within the layer.

Upper Boundary	Lower Boundary	Temperature (°C) Salinity		
		#P10N	#P24N	#P47N
1 surface	$\sigma_\theta = 24.30$	25.81 34.496	23.63 35.08	15.26 32.61
2 $\sigma_\theta = 24.30$	$\sigma_\theta = 26.00$	16.70 34.667	16.97 35.721	8.85 32.813
3 $\sigma_\theta = 26.00$	$\sigma_\theta = 26.80$	10.77 34.670	9.14 35.170	4.47 33.524
4 $\sigma_\theta = 26.80$	$\sigma_\theta = 27.30$	6.90 34.566	4.98 34.243	3.55 34.077
5 $\sigma_\theta = 27.30$	$\sigma_1 = 32.16$	4.06 34.568	3.40 34.477	2.72 34.390
6 $\sigma_1 = 32.16$	$\sigma_2 = 36.80$	2.84 34.604	2.55 34.558	2.20 34.504
7 $\sigma_2 = 36.80$	$\sigma_2 = 36.90$	2.19 34.633	2.01 34.603	1.85 34.574
8 $\sigma_2 = 36.90$	$\sigma_2 = 36.96$	1.74 34.658	1.63 34.638	1.56 34.624
9 $\sigma_2 = 36.96$	$\sigma_2 = 37.00$	1.48 34.671	1.39 34.660	1.35 34.654
10 $\sigma_2 = 37.00$	$\sigma_4 = 45.85$	1.28 34.679	1.25 34.672	1.23 34.699
11 $\sigma_4 = 45.85$	$\sigma_4 = 45.87$	1.19 34.685	1.17 34.680	1.16 34.679
12 $\sigma_4 = 45.87$	$\sigma_4 = 45.885$	1.11 34.689	1.10 34.685	1.10 34.685
13 $\sigma_4 = 45.885$	$\sigma_4 = 45.90$	1.04 34.693	1.03 34.690	1.06 34.688
14 $\sigma_4 = 45.90$	bottom	0.93 34.699	0.97 34.694	– –

Table 2.5g: Potential Density Layer Boundaries and Layer Average Potential Temperature and Salinity for zonal sections in the North Pacific Ocean (Region G according to Figure 2.3). A dash indicates no water within the layer.

a result, some of the layers are very thin and even completely empty in some of the sections.

To facilitate comparisons with previous results, specific potential density interfaces for certain basins were based upon those used by other authors. Some changes to the values suggested by the literature were necessary to describe the changes in water mass characteristics in areas extending across the equator and towards the polar regions. Changes were also necessary to deal with isopycnal reference levels. That is, potential density interfaces which were used as velocity reference levels had to be included in all areas containing the section which referenced them. The most obvious example is the $\sigma_2 = 37.09$ isopycnal which had to be included in both region B (Table 2.5b) and region C (Table 2.5c) as it was used as a reference level for the #A27S sections.

2.5.2 Choice of Initial Reference Levels

The tapered weighted least squares technique attempts to not only minimize the residuals, $(A\hat{\mathbf{b}} + \Gamma)^T N^{-1}(A\hat{\mathbf{b}} + \Gamma)$ but also the solution size, $\hat{\mathbf{b}}^T S^{-1} \hat{\mathbf{b}}$. It is, therefore, desirable to choose an initial reference level where it is expected that the *true* velocities are zero, or more reasonably, as small as possible. The method of choosing a reference level has grown into an art in itself, with a variety of possibilities having been put forth by equally as many oceanographers. Good discussions of these various methods can be found in *Pond and Pickard* [1983], *Rintoul* [1988], *Schott and Stommel* [1978] and *Wunsch* [1978]. The best decision which can be made, applies all the *a priori* knowledge or beliefs about the ocean circulation to the problem so that at the very least, the clearly irrational choices are avoided.

In choosing the initial reference levels for this research we have attempted to apply what is supposedly known about each particular section to the choice and

then consider what happens if that choice is varied. There were two initial runs of the model, one using deep reference levels and one using shallow reference levels. In three cases (#I32S, #A11N and #P10N) station specific reference levels, provided by previous studies were also compared. The choice of reference level for the standard model was based upon the magnitude of the resulting reference level velocities (we tended to choose the reference level which gave the smaller solution size), as well as how reasonable the circulation looked in light of what is thought to be known about the particular regions. The choice of reference levels is discussed in more detail in Chapter 4.

2.5.3 Choice of Equation Weights

The problem as described above, has been reduced to the familiar and simple form $\mathbf{A}\mathbf{b} + \mathbf{n} = -\mathbf{\Gamma}$, which is to be solved via an objective function Equation 2.9. The use of \mathbf{N} and \mathbf{S} in the objective function is equivalent to a row and column weighting of the system. It is desirable to perform such weighting on the equations as the least squares technique has the tendency to produce solutions

- in which equations (\mathbf{A} matrix rows) containing the larger coefficients have been used to a greater extent than those containing the smaller coefficients,
- which are proportional in magnitude to the corresponding elements (columns) of the matrix \mathbf{A} .

The first of these biases is removed through the weighting of the constraint equations, that is, the rows of the \mathbf{A} matrix. The row weighting performs two functions. To remove artificially large or small coefficients which are due to the arbitrary units in which the various concentrations are measured, each row is divided by the rms value of the associated concentration. This prevents, for instance, the salinity coefficients from being 35 times the size of the mass coefficients. The rms value has

been used instead of the mean to allow for the possible inclusion of salinity anomaly constraints. Test runs indicated that the differences resulting from the use of an rms value as opposed to a mean were insignificant. The second use of the row scaling is to allow weighting by the expected error in the various equations. A simple example of this is: given two equations with coefficients of equal magnitude, but in which one of the equations has an expected uncertainty of 1 and the second an expected uncertainty of 100, we would wish to downweight the second equation in order that it does not have as much effect on the solution as the first.

The row weights are defined by the matrix $N^{-1/2}$, where $N = \sigma^2 \bar{C}^2$, \bar{C} is the diagonal matrix of mean concentrations, σ^2 is the problem variance. N is essentially the covariance matrix for the noise in the observations. The fact that the N is diagonal implies the assumption that the noise in each of the equations is uncorrelated. There are most likely correlations between the neighboring layers and a more complicated form could certainly be used if more detailed knowledge of the covariance functions were available. The use of the covariance matrix indicates that an *a priori* estimate of the noise in the observations has been made.

For the problem to be consistent, the resulting estimate of problem residuals, $A\hat{b} + \Gamma$ ought to be of similar magnitude to those initially estimated (Wiggins 1972). If the residuals are much smaller than expected from the estimated variance in the observations, then it is possible to conclude that the observation error was overestimated or that the model is wrong. If the residuals are very large compared to the estimated observation variance then the observation error may have been underestimated or the model itself is not adequate to explain the data. Residuals which retain recognizable structure can be a good indication of the latter, though trends in observation error may also lead to trends in the residuals. Rintoul (1988) gives a good discussion of the possible sources of observational error in this problem. These include errors in navigation, measurement, interpolation and extrapolation. Following

his example, the layer equations in all the models studied here are expected to approximate conservation to within $1 \times 10^9 \text{ kg s}^{-1}$. There may be other uncertainties in particular layers or sets of layers, due for instance, to outcropping (see Section 2.3.2), making it necessary to further downweight particular equations.

The second bias listed above, that which causes the solutions b_j to be proportional to the corresponding elements of the matrix A is used to allow the scaling of the columns of A to produce solutions of an expected order of magnitude. It is expected that certain elements of b will be larger than others, so for instance, in general we assume that the reference level velocities are of the order of 1 cm s^{-1} , while the anticipated magnitude of the vertical transfer terms is about $10^{-4} \text{ cm s}^{-1}$.

The tapered weighted least squares as described in Section 2.4.1 assumes that initial estimates of both the noise and solution covariance exist. The row weights represent the noise covariance, the column weights an estimate of the solution covariance. Given these two *a priori* estimates there is no further choice to be made in determining a solution

Having given a brief introduction to the data and methodology employed in this research, the following chapters present a view of the global thermohaline circulation as seen through the combination of a number of modern hydrographic transects. The solutions are sought, in expectation that although the hydrography is not synoptic, it can still provide us with a meaningfully consistent picture of the general circulation.

Chapter 3

The Standard Model

3.1 Introduction

This chapter describes the constraints used to define what shall be called the *standard* global ocean model. It examines the resulting velocity fields and zonally averaged fluxes of mass, heat and freshwater within all the basins in light of previous estimates. Extending this examination to the exchanges which occur between the ocean basins, the consistency between our current understanding of the global thermohaline overturning cell and these results is investigated.

3.2 Description of the Standard Model

The hydrographic sections described in Chapter 2 divide the world's oceans into the 18 areas illustrated in Figure 2.1. Each area of the model is divided in the vertical by an individualized set of potential density layers. These layer interfaces have been chosen to resolve the water masses found within each region and to facilitate

comparison with previous studies. The nominal layer boundaries and their associated temperature and salinity characteristics were described in Tables 2.5c through 2.5g. These tables illustrate the great variety of water masses which exist and also give some indication of their geographical extent. The water mass characteristics of individual regions will be discussed in more detail later in the chapter.

3.2.1 Conservation Equations

The specific set of constraints used in the standard model has been developed through a great deal of experimentation. Even so, the standard model does not represent an end point, as it has been found that learning about the data and the model and how the two interact to produce solutions is a continuing process which warrants constant revision of what defines a best estimate model. This section describes the constraints which define the standard model. A few of these constraints have since been determined to be either inconsistent or unnecessary and as such are discussed later in the chapter. Some of the different constraints which might go into a future revision of the standard model are discussed in Chapter 4.

The standard model is defined by the set of conservation equations and external constraints summarized in Table 3.1. Within each region, these constraints include conservation of total mass and salt, conservation of mass and salt within potential density layers, conservation of silica below the euphotic zone and above the bottom and conservation of the phosphate and oxygen combination PO38¹ below the euphotic zone.

The tapered weighted least squares technique used here does not provide the information contained in the resolution matrices of an singular value decomposition,

¹PO38 represents the combination of oxygen and phosphate in the ratio of 1 mole of oxygen to 138 moles of phosphate [Redfield, 1963; Minster and Boulhadid, 1987].

	Constraint
Mass and Salt	Conservation in all layers. Ekman convergence/divergence within each area = net top to bottom geostrophic outflow/inflow. Geostrophic + Ekman flux across each section = net inflow/outflow.
Silica	Consrv. of Silica below euphotic zone & above bottom
Phosphate	Consrv. of Phosphate & Oxygen (1:138) below euphotic zone
Net Flux Estimates	Freshwater Fluxes: from <i>Baumgartner and Reichel</i> [1975] and <i>Schmitt et al.</i> [1989] with an integration reference point at Bering Strait Salt Fluxes: based on Bering St. transport: $0.8 \pm 0.6 \times 10^9 \text{ kg s}^{-1}$, $S=32.5$ Antarctic Circumpolar Current: $142 \pm 5 \times 10^9 \text{ kg s}^{-1}$ North Brazil Current: $26.5 \pm 5 \times 10^9 \text{ kg s}^{-1}$ Florida Straits: $30.8 \pm 0.5 \times 10^9 \text{ kg s}^{-1}$ Kuroshio: $26.6 \pm 3.3 \times 10^9 \text{ kg s}^{-1}$ Indonesian Passage: $10 \pm 10 \times 10^9 \text{ kg s}^{-1}$ Indian Ocean bottom water transport: see page 62 Atlantic bottom water transport: see page 62 Net transport across the eastern portion of #A48°N: see page 64 Weddell Scotia (area II): net inflow of $0.1 \pm 0.05 \text{ PW}$ Ekman Fluxes: ECMWF winds [†] , see Table 2.4
Topographic Constraints	Conservation of mass in the eastern basin of the North Atlantic Zero net flux below the sill depth: across the Walvis Ridge (#A27S_E) across the Agulhas Plateau (#30E) within Mozambique Basin (#I32S) across Southwest Indian Ridge (#I32S) in the Tasman Sea (#P43S) in the Philippine Basin (#P24N)
Weights	All equations are weighted by their rms property value. Expected uncertainty of individual layers: $1 \times 10^9 \text{ kg s}^{-1}$. Expected uncertainty of top to bottom equations: $2 \times 10^9 \text{ kg s}^{-1}$ and the uncertainty in the Ekman component. The surface layers are further weighted by the magnitude of the Ekman component based on area of outcropping.

Table 3.1: Constraints for the standard model.

[†] Note that the Ekman transport for the #P10N section was taken from *Wijffels* [1993]. See the discussion on page 187.

therefore, it is not possible to quantify the effect of the individual constraints on the final solution. It is expected, however, that the relative information content of the various constraints used in the standard model will be similar to what has been found in previous studies [Macdonald 1991, Rintoul and Wunsch 1991, Wunsch *et al.* 1983], that is, the solution is mainly driven by the mass and salt constraints, with some independent information being derived from the silica constraints and very little coming from the PO38 constraints.

The expected extent of conservation is defined by the winds (Table 2.4), the freshwater ($P-E+R$) flux and the topography of each region. Across each section, the total (geostrophic + Ekman) fluxes of mass and salt are expected to be balanced by the net leakage (Bering Strait, Indonesian Archipelago, $P-E+R$) through the boundaries. The reference levels used to calculate the relative geostrophic velocities and transports and to define the depth of the initially unknown reference level velocities are given in Table 3.2.

3.2.2 Flux Constraints

Freshwater and Salt Fluxes

The initial estimates of freshwater transport across each of the sections are computed from the Schmitt *et al.* [1989] air-sea exchange values in the Atlantic and from the Baumgartner and Reichel [1975] values in the other ocean basins. The integration reference is set at the Bering Strait using, as mentioned in Chapter 2, the annual mean Bering Strait transport. A 30% uncertainty has been placed on these integrated values. The initial salt fluxes estimates are also based on the Bering Strait throughflow using a salinity of 32.5.

<u>Model</u> →	<u>Standard</u>	<u>Model A (shallow)</u>		<u>Model B (deep)</u>	
Section	Potential Density	Potential Density	Comment	Potential Density	Comment
#A48N	$\sigma_2=36.87$	$\sigma_\theta=27.30$	850 db	$\sigma_4=45.85$	above AABW
#A36N	$\sigma_4=45.81$	$\sigma_\theta=27.70$	1300 db	$\sigma_4=45.81$	3000 db
#Flst	$\sigma_\theta=27.20$	$\sigma_\theta=27.20$	bottom	$\sigma_\theta=27.20$	bottom
#A24N	$\sigma_4=45.81$	$\sigma_\theta=27.70$		$\sigma_4=45.81$	3000 db
#A11N	PS1	PS1		$\sigma_4=45.895$	$\Theta < 1.8$
#A11S	$\sigma_1=32.16$	$\sigma_1=32.16$	Si max,Ox min	$\sigma_2=37.09$	$\Theta < 1.8$
#A23S	$\sigma_1=32.16$	$\sigma_1=32.16$	Si max,Ox min	$\sigma_2=37.09$	$\Theta < 1.8$
#A27S_W	$\sigma_2=37.09$	$\sigma_1=32.16$	Si max,Ox min	$\sigma_2=37.09$	$\Theta < 1.8$
#A27S_E	$\sigma_2=37.09$	$\sigma_1=32.16$		$\sigma_2=37.09$	
#A57S_W	$\sigma_3=41.65$	$\sigma_3=41.65$	1000-2500 db	$\sigma_4=46.14$	
#A57S_E	$\sigma_3=41.65$	$\sigma_3=41.65$	1000-2500 db	$\sigma_4=46.14$	bottom
#0E2Afr	$\sigma_3=41.60$	$\sigma_1=32.36$	500-1800 db	$\sigma_3=41.60$	1500-3800
#0E_N	$\sigma_3=41.60$	$\sigma_1=32.36$	500-1800 db	$\sigma_3=41.60$	1800-4400
#0E_S	$\sigma_3=41.63$	$\sigma_3=32.36$	800-1800 db	$\sigma_4=46.08$	bottom
#P47N	$\sigma_4=45.87$	$\sigma_3=36.90$	2000 db	$\sigma_4=45.87$	4000 db
#P24N	$\sigma_2=36.90$	$\sigma_3=36.90$	2000 db	$\sigma_4=45.85$	4000 db
#P10N	PS2	$\sigma_3=36.90$	2000 db	$\sigma_4=45.85$	4000 db
#P28S	$\sigma_2=37.00$	$\sigma_\theta=27.20$	2000 db	$\sigma_2=37.00$	3500 db
#P43S	$\sigma_2=37.04$	$\sigma_\theta=27.20$	2000 db	$\sigma_2=37.00$	3500 db
#Mz_N	$\sigma_1=32.16$	$\sigma_2=32.16$	1300 db	$\sigma_4=45.85$	near bottom
#Mz_S	$\sigma_0=27.40$	$\sigma_1=27.40$	1300 db	$\sigma_4=45.85$	bottom
#I18S	$\sigma_4=45.85$	$\sigma_2=32.16$	1300 db	$\sigma_4=45.85$	3000 db, $\Theta < 1.8$
#I32S	PS3	$\sigma_2=32.16$		PS3	2000 db-bottom
#Drake	$\sigma_3=41.66$	$\sigma_2=3700$	700 db	$\sigma_3=41.66$	near bottom
#30E	$\sigma_4=46.14$	$\sigma_3=32.36$	500-1500 db	$\sigma_4=46.14$	near bottom
#132E	$\sigma_4=46.14$	$\sigma_2=32.36$	300-1800 db	$\sigma_4=46.144$	near bottom

Table 3.2: Potential Density of the initial levels of no motion used to calculate the relative velocities and transports for the standard model (described in this chapter) and the two test models A and B (described in the next chapter).

PS1 : Station specific levels, from *Friedrichs and Hall* [1993]

PS2 : Station specific levels, from *J. Toole* (pers comm.)

PS3 : Station specific levels, from *S. Wijffels* (pers. comm.)

The station specific reference levels are given in Appendix A.

ACC Transport

Nearly all estimates of ACC transport have been made in Drake Passage as it is the most constricting (800 km wide) of the choke points between Antarctica and the continents. There is however, a broad range in these estimates even within the confines of Drake Passage (see the tables of estimates given by *Peterson and Stramma* [1991]). However, the more recent estimates of mean transport lie in the range of 120 to $150 \times 10^9 \text{ kg s}^{-1}$ [*Georgi & Toole*, 1982; *Whitworth et al.*, 1982; *Whitworth*, 1983; *Whitworth and Peterson*, 1985]. The data used in this study at Drake Passage produce a relative (the standard model's reference level is $\sigma_3 = 41.66$) transport of $150 \times 10^9 \text{ kg s}^{-1}$. Experiment has shown however, that to meet the constraints provided by the rest of the data in the South Atlantic, the models tend to reduce the absolute ACC transport within Drake Passage to about third of this value. What exactly causes this reduction is not yet understood but in order maintain a transport which is close to the average expected, in the standard model, the net mass and salt fluxes within the ACC are specified at Drake Passage. The initial mass flux estimate of $142 \pm 5 \times 10^9 \text{ kg s}^{-1}$ is a weighted mean of the estimates and uncertainties provided by *Whitworth et al.* [1982]. The salt flux is the $142 \times 10^9 \text{ kg s}^{-1}$ multiplied by the mean salinity of the flow through Drake Passage (34.598, computed as an areal mean using the Meteor 11/5 hydrography).

North Brazil Current Transport

At 11°N . the hydrographic section does not resolve the full width of the shallow North Brazil Current. The flow in the interior is therefore expected to balance that portion of the North Brazil Current transport which is not contained within the section. For the standard model, the annual mean North Brazil Current transport is taken as $26.5 \pm 5 \times 10^9 \text{ kg s}^{-1}$ [*W. Johns* pers. comm.] and as done by *Friedrichs and Hall* [1993] it is assumed that $7 \times 10^9 \text{ kg s}^{-1}$ of this transport is within the #A11N stations. Therefore, the resulting absolute velocity field is constrained to balance

a $19.5 \times 10^9 \text{ kg s}^{-1}$ northward flow. The effect of varying the North Brazil Current transport estimate in the model flux constraint is discussed in section 3.4.7.

Florida Straits and Kuroshio Transport

The initial estimate of the geostrophic transport through the Florida Straits is taken to be $31 \pm 0.5 \times 10^9 \text{ kg s}^{-1}$. The $31 \times 10^9 \text{ kg s}^{-1}$ is taken from *Schmitz and Richardson* [1991]. The uncertainty which they attached to this annual average value was $2 \times 10^9 \text{ kg s}^{-1}$. As will be discussed later in the chapter, this uncertainty has been reduced in order to force the model to produce a Florida Strait transport estimate with the $\pm 2 \times 10^9 \text{ kg s}^{-1}$ suggested by *Schmitz and Richardson*. The transport within the Kuroshio at 24°N in the Pacific is initially estimated at $26.6 \pm 3.3 \times 10^9 \text{ kg s}^{-1}$ [*Bingham and Talley*, 1991].

Indonesian Passage Throughflow

In early models, the lack of a constraint on the flow from the Pacific to the Indian Basins through the Indonesian Archipelago produced some surprisingly large P-I transport estimates. These models had P-I transport of the order of $30 \times 10^9 \text{ kg s}^{-1}$, well beyond previous estimates which range between 0 and $20 \times 10^9 \text{ kg s}^{-1}$. Furthermore, the predicted magnitude of the P-I throughflow was found to be extremely sensitive to the choice of velocity reference levels. This sensitivity is likely due to a dearth of constraints. The region which surrounds the Indonesian Archipelago (area X), made up of #P28S, #P10N, #I18S and #Mz_N (see Figures 2.3 and 2.1) is the least well constrained of the entire system, containing 383 unknowns and only 41 equations. Since there was little reason to place much confidence in the value of throughflow transport obtained from the unconstrained model, a constraint on the P-I transport of $10 \pm 10 \times 10^9 \text{ kg s}^{-1}$ was included in the standard model. As it turns out, and will be discussed later on, left to its own devices the standard model would actually produce a value of about $10 \times 10^9 \text{ kg s}^{-1}$ for the P-I throughflow.

Indian and Atlantic Bottom Water Constraints

Due to the global nature of the constraints placed upon the system, the earlier models produced net southward transports in the lowest layer of Indian Ocean sections. As it is thought that bottom water is not created within the Indian Basin, a constraint is placed upon the flow in this lowest layer in the standard model, requiring it to flow northward. This constraint is discussed in greater detail later in the chapter (see page 199).

The bottom water flowing northward in the South Atlantic to the west of the Mid-Atlantic Ridge is confined to the Argentine Basin by the Rio Grande Rise. According to *Hogg et al.* [1982] the only viable conduit into the Brazil Basin is the Vema Channel located at 30°S, 39°E. The current meter observations of Hogg[227z *et al.* suggest a northward transport of AABW through this passage of 4.0 ± 1.2 Sv. The more recent estimates of *Speer and Zenk* [1993] are consistent, as they find 3.9 Sv flowing through the Vema Channel, but their estimate of total northward transport of bottom water across the Rio Grande Rise increases to 6.7 ± 0.4 Sv when flows within the western boundary (between the Lower Santos Plateau and the continental slope) and through the Hunter Channel are included. To the north of these channels, *Speer and Zenk* find an estimated 5.0 ± 1.1 Sv relative to $\sigma_4 = 45.85$ (approximately 2.1°C). This reference level lies between our interfaces 9 (averaging 2.4°C) and 10 (averaging 1.8°C). The standard model constraint of 5 ± 1.1 Sv is placed upon the flow of water below layer 10 ($\sigma_2 < 37.09$) across the 27°S section to the west of the Mid-Atlantic Ridge. Thus placed, this constraint may slightly overestimate the net northward transport of bottom water at this latitude, however, in comparison to other estimates (6.4 Sv [*Wright*, 1970]; 6.7 Sv [*McCartney and Curry*, 1993]) it appears reasonable.

In an effort to constrain the standard model as much as possible, constraints on the net northward transport of AABW (Θ less than about 1.8°C) have been placed throughout the Atlantic in the standard model. These are outlined in Table 3.3. Later

Section	Reference	Below	Starting Longitude	Ending Longitude	Transport Constraint
#A36N	S&M	$\sigma_4 = 45.895$	73.5°W	38.4°W	2 ± 1.0
#A24N	S&M	$\sigma_4 = 45.895$	75.5°W	47.6°W	2 ± 1.0
#A11N	S&M	$\sigma_4 = 45.895$	51.3°W	17.6°W	4 ± 1.0
#A11S	SP&Z	$\sigma_4 = 45.85$	36.9°W	13.7°W	3 ± 1.4
#A23S	SP&Z	$\sigma_4 = 45.85$	41.9°W	13.8°W	5 ± 1.1
#A27S	SP&Z	$\sigma_2 = 37.09$	41.4°W	13.7°W	5 ± 1.1

Table 3.3: Constraints placed on the transport of Atlantic bottom water in the standard model. SP&Z refers to *Speer and Zenk* [1993]. S&M refers to *Schmitz and McCartney* [1993]. The uncertainties associated with the South Atlantic values come from SP&Z. Those in the North Atlantic were chosen arbitrarily as no uncertainties were given by S&M.

on, it will be shown that the bottom water constraints placed at 24°N and 36°N are inconsistent with the standard model.

Constraints on the Flow Across the Eastern Portion of #A48N

The study of *Schmitz and McCartney* [1993] suggests that the net transport east of (32°W) in the North Atlantic at 48°N latitude is minimal ($1 \times 10^6 \text{ m}^3 \text{ s}^{-1}$ of water warmer than 7°C and $2 \times 10^6 \text{ m}^3 \text{ s}^{-1}$ in the temperature range 1.8°C to 4°C). Left to its own devices the standard model tends to produce a strong circulation east of 32°W at this latitude, characterized by a northward flow in the upper layers and southward flow in the deeper waters. In an attempt to verify the consistency of the previous study, constraints based on the results of S&M were placed on the flow in the eastern basin across #A48N. As discussed later, the model was unable to meet these constraints.

Weddell Scotia Heat Transport

The final net flux constraint placed upon the standard model is one which requires a net input of heat into the Weddell Sea region, area II. Earlier models found

an insignificant loss of heat to the atmosphere in this region where the expected formation of deep and bottom water through convective processes would require it.

3.2.3 Topographic Constraints

In creating models such as those to be presented here, it is necessary to take a careful look at the topography of the region. However, it is not our intention to write a dissertation on the bathymetry of the world's oceans. Therefore, the focus of the following discussion is upon that bathymetry which is not represented in our data set and which is capable of blocking flow.

North Atlantic Topographic Constraints

The recent study of *Dickson and Brown* [1994] suggests that the $13 \times 10^6 \text{ m}^3 \text{ s}^{-1}$ of "almost-developed" NADW which flows past Cape Farewell at 60°N and flows southward into the western basin of the North Atlantic is the source of the deep flow ($17 \times 10^6 \text{ m}^3 \text{ s}^{-1}$ *Rintoul* [1991]) which passes through the South Atlantic. This pathway suggests that a well developed southward transport of deep waters within the western basin at 48°N should exist. However, without constraints supplying the information, the standard model does not recognize the east-west obstruction created by the Mid-Atlantic Ridge (Figure 3.1) and tends to produce a strong southward transport of deep waters in the eastern basin at 48°N which moves into the western basin by 36°N . The standard model therefore includes constraints which require conservation of mass within the eastern basin of the North Atlantic in areas XVII and XVIII, below the sill depth of the Mid-Atlantic Ridge.

South Atlantic Topographic Constraints

In the South Atlantic Ocean the bathymetry suggests a number of topographic constraints (Figure 3.2). The Walvis Ridge which runs on a diagonal from the west coast of South Africa at 20°S to the Mid-Atlantic Ridge at about 40°S blocks the

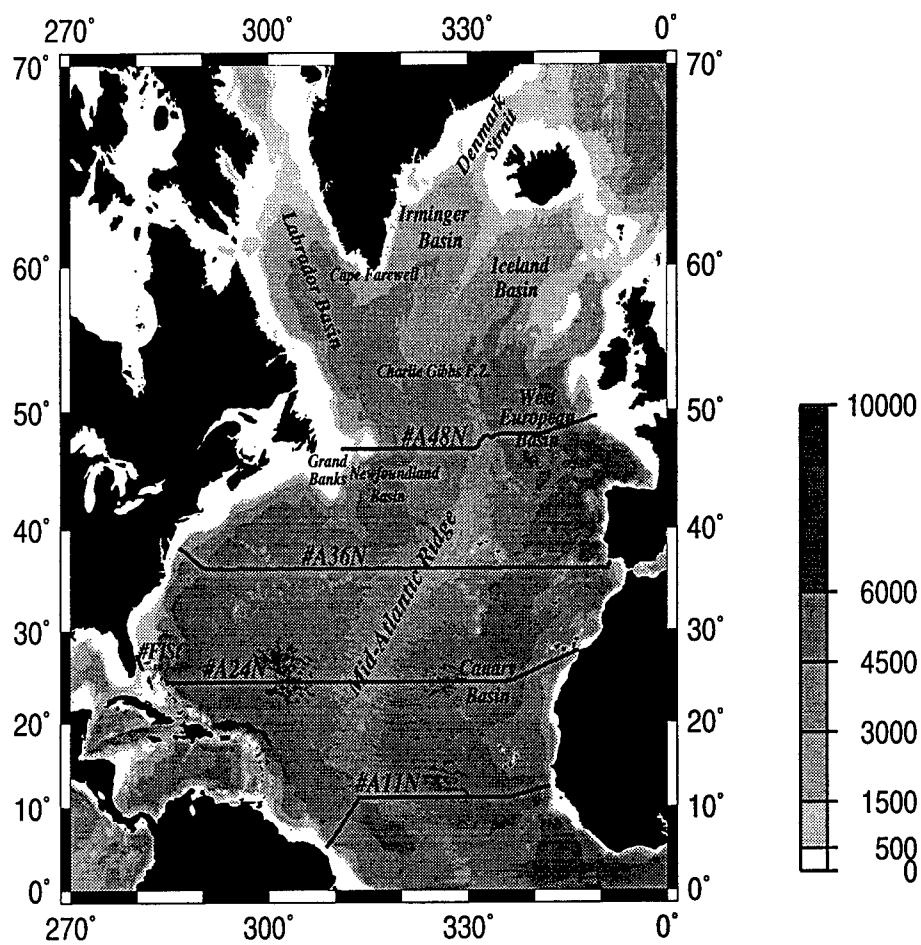


Figure 3.1: North Atlantic bathymetry and standard model hydrographic sections.

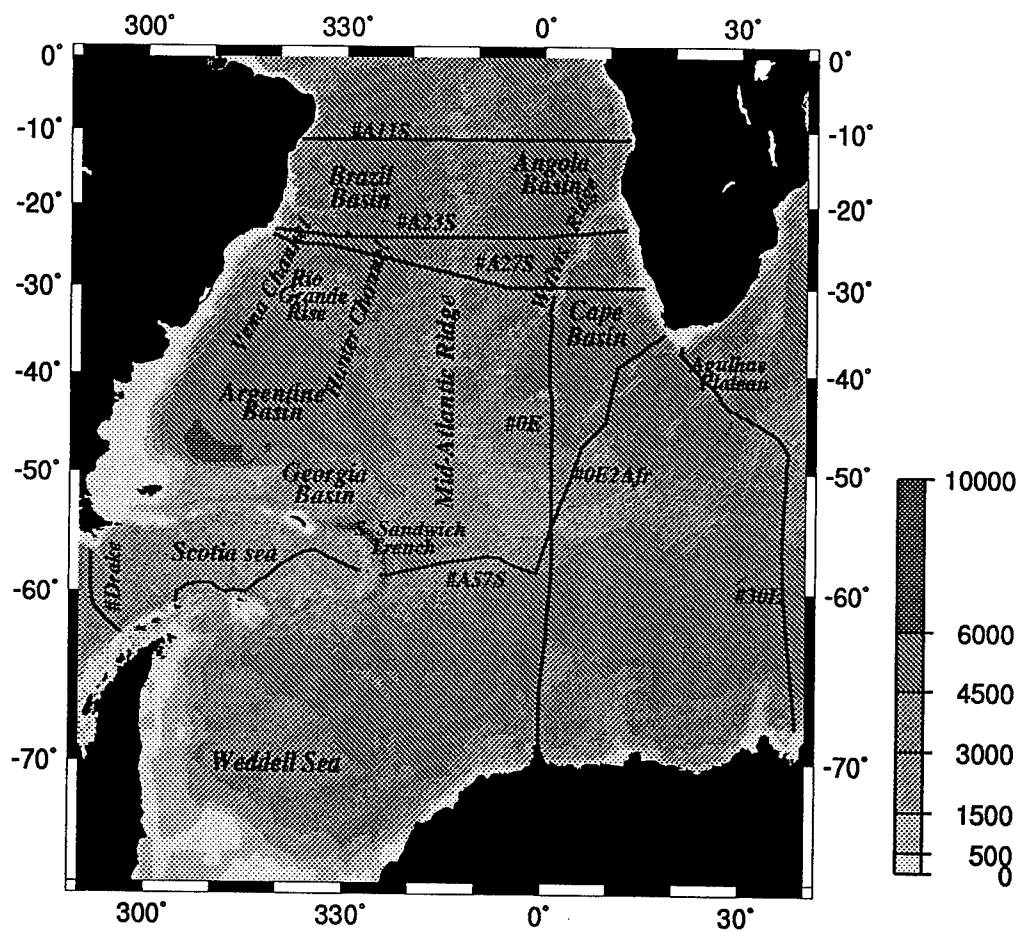


Figure 3.2: South Atlantic bathymetry and standard model hydrographic sections.

deep flow through the Cape Basin in the south from entering the Angola Basin in the north. To take this into account, there is constraint upon the 27°S section east of the Mid-Atlantic Ridge allowing no net flow below the sill depth of 3500 m. A small amount of bottom water is thought to follow a northward route out of the Cape Basin through the Walvis Channel. We are assuming, however, that this transport is less the $\pm 2 \times 10^9 \text{ kg s}^{-1}$ which is the uncertainty ascribed to the zero flux constraint. A similar zero flux constraint on the northern portion of 30°E section is used to represent the obstruction to deep (> 4000 m) flow created by the Agulhas Plateau.

Indian Basin Topographic Constraints

The Indian Ocean is completely closed off to the north and west by the continents of Africa and Asia, but to the east, it is connected to the Pacific, between Australia and the island chain of Timor, Java and Sumatra. The topography within the Indian Ocean Basin is extremely complex (Figure 3.3). The Southwest Indian Ridge system forms an inverted V with the Southeast Indian Ridge systems from about 55°S, 30°E to an apex at 25°S, 70°E and back down to 50°S, 110°E. Within the Indian sector the Kerguelen Plateau creates a meridional block below about 2500 m. Another meridional blockage is formed by the Macquarie Ridge Complex which extends northward as the islands of New Zealand. In the southern region the ocean is divided into several separate basins, by the ridges running in the north-south direction. At 18°S, running from the west to the east coast, there is the Mozambique Basin, Mascarene Basin, Central Indian Basin and the Northwest Australian or Wharton Basin. The two eastern basins are completely separated by the island of Madagascar. At 32°S, the eastern ocean divides into the Mozambique and Madagascar basins. The Central Indian and Wharton basins are continuous between the two latitudes except for an east-west ridge between $\sim 30^\circ$ - 35° S, off the coast of Australia.

The large number of basins provides an equally large number of western boundaries along which deep water entering the Indian Ocean can flow. In spite of the com-

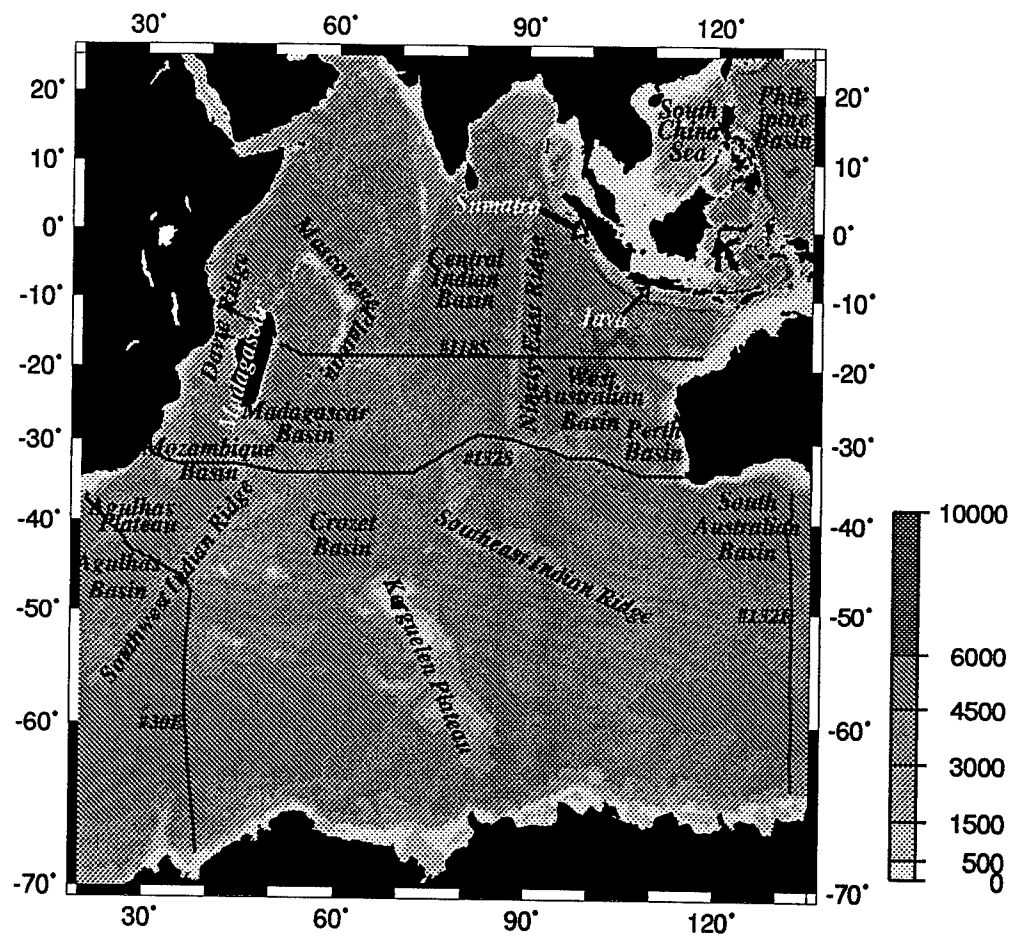


Figure 3.3: Indian bathymetry and standard model hydrographic sections.

plex topography or rather, due to the numerous deep fractures, there are few known complete blocks to the major flows. To the north of the #I32S section, one of these obstructions is created by the Davie and Madagascar Ridges which confine the flow below about 2500 m [Toole and Warren, 1993] to the Mozambique Basin. A second block is formed by the Southwest Indian Ridge which hinders the northward flow out of the Crozet Basin and into the Madagascar Basin. It is littered with fractures zones but contains no passages deeper than 4000 m. Both these topographic obstructions to the flow are included in the constraints listed in Table 3.1.

Pacific Basin Topographic Constraints

The bathymetry of the Pacific sector of the Southern Ocean is far less severe than that found in either the Indian or Atlantic sectors. The only notable feature poleward of 30° south latitude is the separation of the basin meridionally by the East Pacific Rise and its more southerly component, the Pacific-Antarctic Ridge. The only two bathymetric constraints placed upon the sections in the Pacific are no net flow constraints 1) across the #P43S line below the sill depth of the topography to the north which blocks off the deep Tasman Sea and 2) below the sill depth of the Philippine Basin at #P24N (Figure 3.4).

3.2.4 Wind

As discussed in Chapter 1 most of the input estimates of the Ekman transport have been computed from the ECMWF wind data [Trenberth *et al.*, 1989]. All the models presented here use the Ekman transport computed from the annual mean wind stress estimates. These values were shown Table 2.4, along with their associated uncertainty. The #P10N section is an exception. The ECMWF wind stress estimates used here are considered to be too low in the tropics [Trenberth *et al.* 1990]. This systematic under-estimate of the tropical wind stress is particularly evident in

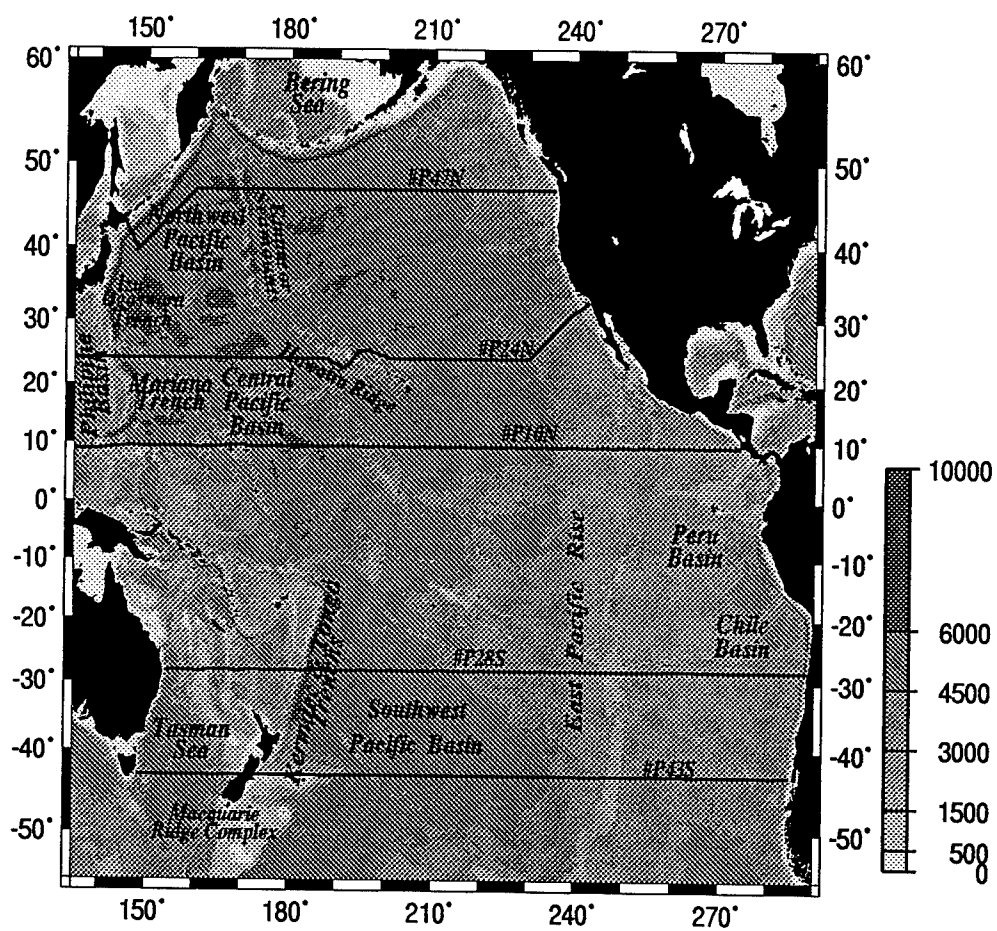


Figure 3.4: Pacific bathymetry and standard model hydrographic sections.

the estimated Ekman transport across the #P10N section where the ECMWF Ekman transport estimate is only $24.3 \pm 2.7 \times 10^6 \text{ m}^3 \text{ s}^{-1}$ compared other estimates which range between 32 and $42 \times 10^6 \text{ m}^3 \text{ s}^{-1}$ [*Harrison*, 1989; *Goldenburg and O'Brien*, 1981; *Hellerman and Rosenstein*, 1983 and *Wijffels* 1993]. As the ECMWF winds may severely under-estimate the strength of the Ekman transport across this section, the standard model takes its input estimate of Ekman transport from *Wijffels* [1993], $38.6 \times 10^9 \text{ kg s}^{-1}$. The effect of this choice will be discussed later in the chapter. The models include the initial Ekman estimates as described in Chapter 2 as a net flux of mass and salt across individual sections, as a net convergence/divergence within each area and indirectly as a scaling factor to downweight the conservation equations of the upper layers of the models.

3.2.5 Weights

The justification for row and column scalings used to weight the matrix of equations was described in the previous chapter. Specifically, the rows have been scaled by the rms property values and the uncertainty ascribed to the individual equations. The columns have been scaled by the expected order of magnitude of the solution which represents an estimate of the variance of the solution about an initial estimate of $\hat{\mathbf{b}} = 0$.

An expected order of magnitude of 1 cm/sec as been used for the reference level velocities across most sections. The exceptions are for those sections which are likely to display strong velocities throughout the water column. These sections are the ones affected by the ACC and the short section which crosses the Florida Straits. The reference level velocities have been given an expected order of magnitude weighting of 10 cm/s for the effected pairs in these sections. The expected order of magnitude for the cross-isopycnal transfer terms is $1 \times 10^{-4} \text{ cm s}^{-1}$ for all areas, except area XVIII

Section	Initial Imbalance	Initial Uncertainty	Section	Initial Imbalance	Initial Uncertainty
#A48N	13.0	2.3	#A36N	18.2	2.3
#A24N & #Flst	17.2	2.3	#Flst	-7.7	0.5
#A11N	-5.6	5.8	#A11S	6.9	2.3
#A23S	5.0	2.2	#A27S	27.3	2.2
#0E_S	2.4	1.0	#Drake	9.3	4.9
#P47N	17.8	2.4	#P24N	1.8	2.5
Kuroshio	1.8	3.5	#P10N	-16.4	3.6
#I18S & #Mz_N	4.3	10.3	#I32S	-10.4	10.3

Area	Initial Imbalance	Initial Uncertainty	Area	Initial Imbalance	Initial Uncertainty
I	41.0	2.2	II	-17.6	2.1
III	-27.3	2.3	IV	-12.3	2.2
V	-64.0	2.5	VI	37.3	2.4
VII	-48.8	2.5	VIII	12.9	2.9
IX	-6.6	2.1	X	66.4	4.0
XI	-18.3	3.7	XII	-16.1	2.7
XIII	22.3	2.3	XIV	-2.0	2.4
XV	12.5	5.8	XVI	-22.7	5.7
XVII	-1.0	2.5	XVIII	3.2	2.5

Table 3.4: Initial imbalances in the standard model mass flux constraints and top to bottom conservation constraints. Imbalance = $\Gamma = A v_R - \text{RHS}$ (see Equations 2.2 and 2.3). A constraint is met if the initial imbalance is zero to within the uncertainty listed. North and east are positive for the section flux imbalances. Convergence is positive for the area conservation imbalances.

which required a larger initial estimate ($5 \times 10^{-4} \text{ cm s}^{-1}$ was used) in order to balance mass in the region.

3.2.6 Initial Imbalances

Many of the constraints described above are not met to within the estimated uncertainty by the initial (relative) velocity fields. Figure 3.5 illustrates the initial layer mass imbalances in each of the areas defined in Figure 2.2. Table 3.4 lists the initial top to bottom mass imbalance in each area, as well as, the initial mass imbalances in the flux equations describing net transport across sections.

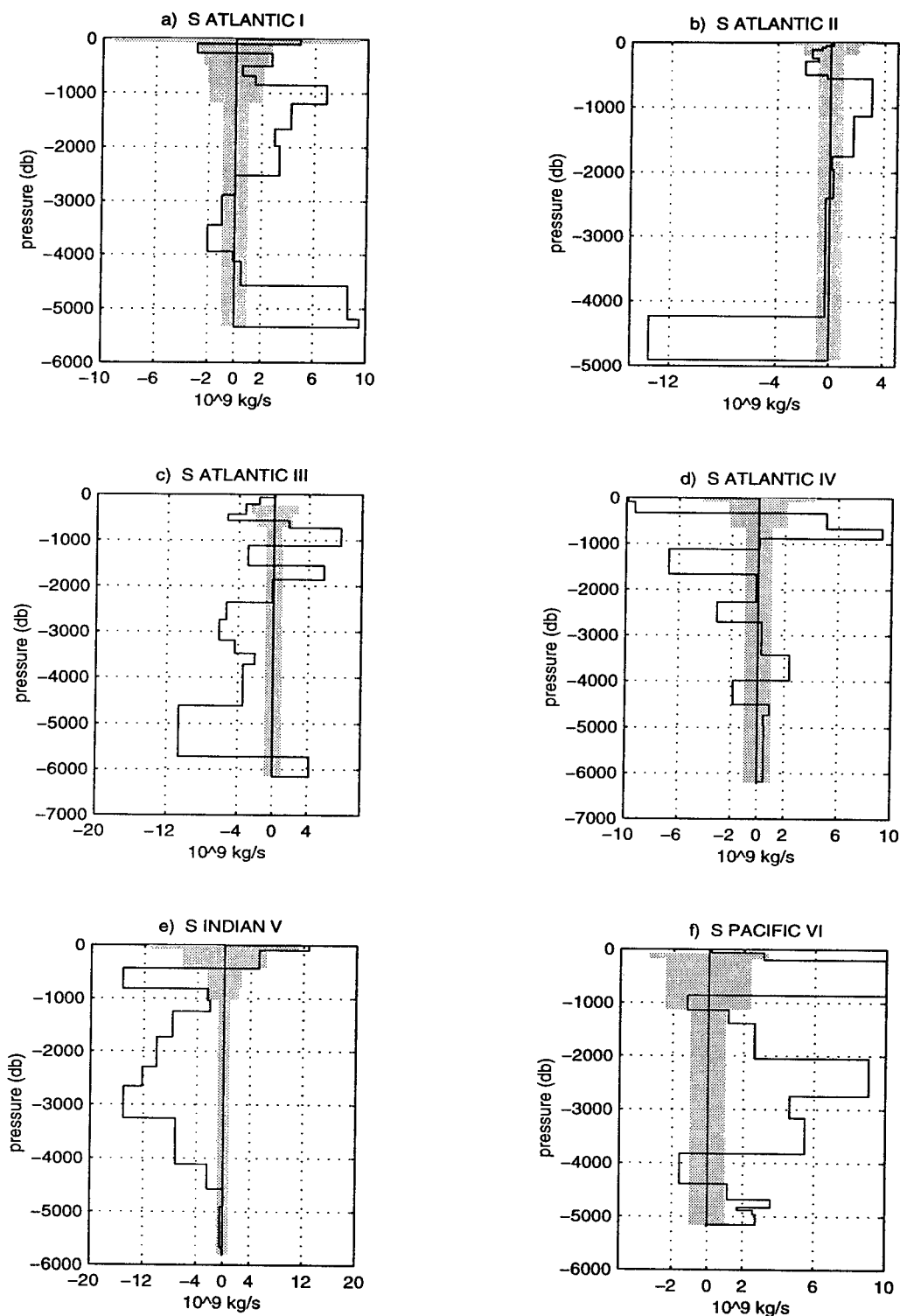


Figure 3.5: Illustration of the initial layer mass imbalances in model areas I through VI as defined in Figure 2.2. Positive values indicate a convergence of mass in the layer. Negative values indicate a divergence. The shaded region indicates the uncertainty to within which an imbalance should be considered zero. Layers in which a shaded region does not exist are associated with an uncertainty which is larger than the scale of the plot (*i.e.* conservation is essentially not required in such a layer).

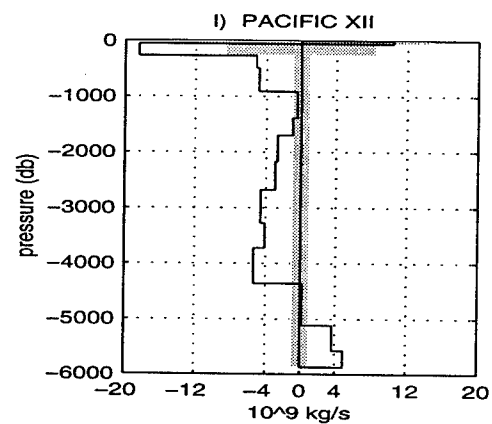
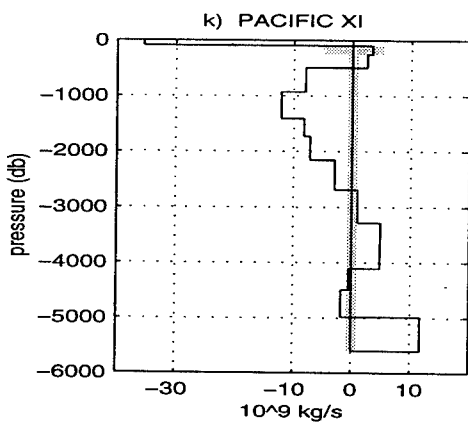
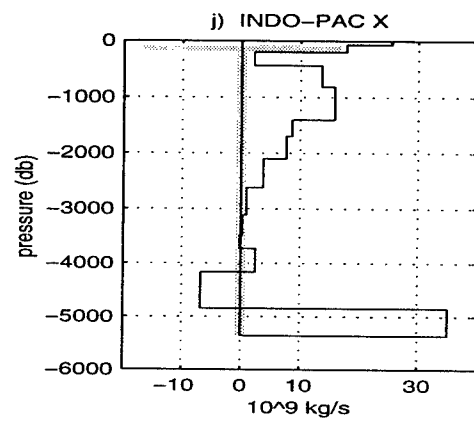
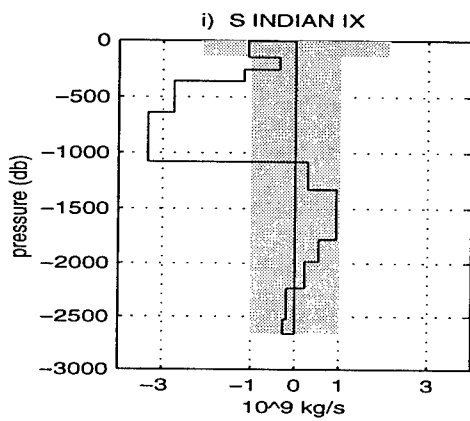
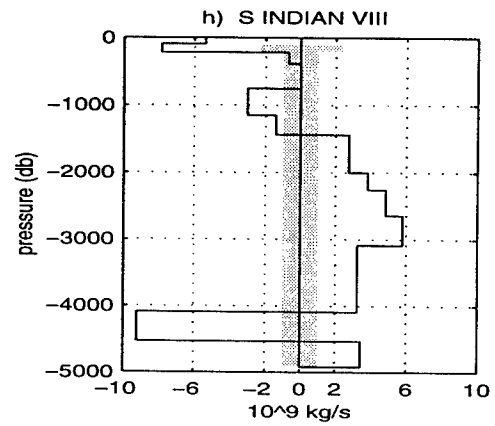
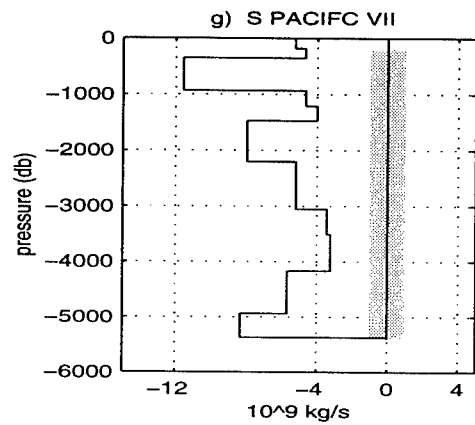


Figure 3.5 continued: Illustration of the initial layer mass imbalances in model areas VII through XII as defined in Figure 2.2.

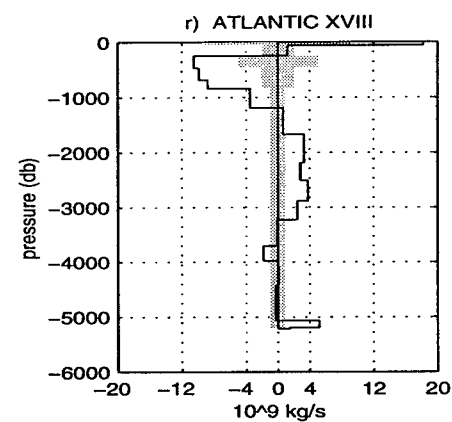
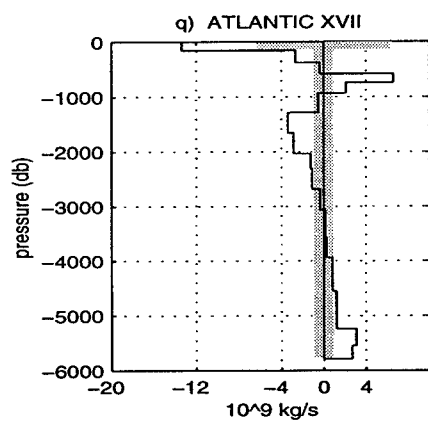
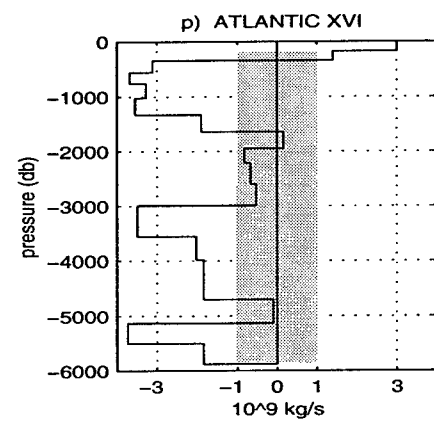
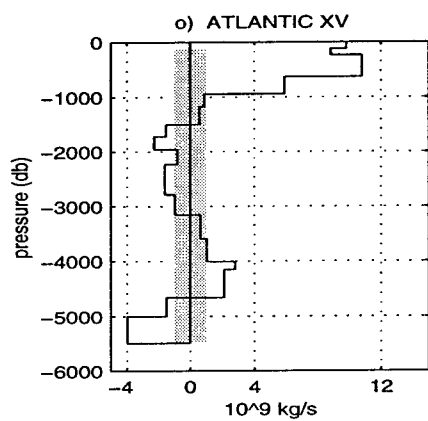
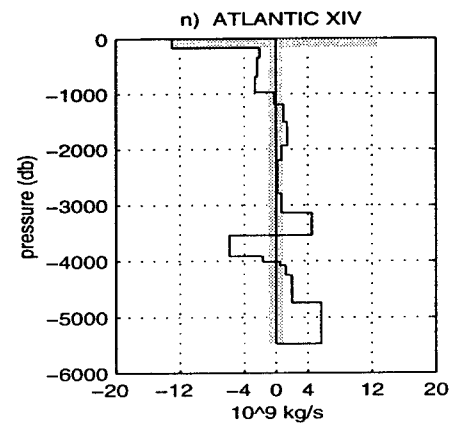
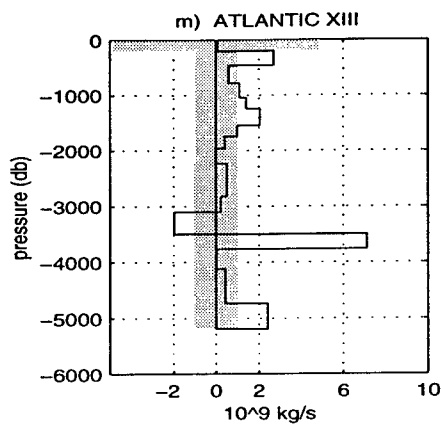


Figure 3.5 continued: Illustration of the initial layer mass imbalances in model areas XIII through XVIII as defined in Figure 2.2.

Within the South Atlantic sector of the Southern Ocean (areas I, II and III) the largest imbalances occur in the bottom layers. The exception is the small area (IV) to the southwest of Africa, in which the largest imbalances occur above about 1700 db. In the rest of the Southern Ocean (areas V, VI) the mass imbalances are spread throughout the water column. The same is true in the South Pacific area VII, between #P43S and #P28S. In the southern Indian Ocean (area VIII) there are significant imbalances in deep and bottom waters. The Mozambique Channel area (IX) initially meets most of its mass conservation constraints. The same can not be said for the Indo-Pacific region which shows large imbalances at mid-depths and most especially in the bottom layers. Within the North Pacific there are imbalances throughout the water column. The Atlantic areas are comparatively well balanced initially. In area XV which covers the Atlantic equatorial region, the largest imbalances occur above 1000 db and may be due to the presence of North Brazil Current. In the northernmost Atlantic area (XVIII), between #A36N and #A48N there are significant imbalances above 1200 db. The greatest overall imbalance occurs in the Indo-Pacific equatorial region (area X) but significant imbalances are seen throughout the areas and sections. It is the job of the inversion to reduce these initial imbalances to acceptable values (*i.e.* to within the range of estimated uncertainties) through the addition of velocities at the reference level and transfer across isopycnals.

As shall be seen, the standard model produces the broad qualitative aspects of the overturning cell within the Atlantic which we might expect from the discussion in Chapter 1. It enhances the picture with quantitative estimates of transport and allows questions to be raised concerning the details of these results. In the spirit of providing the quantitative details of the circulation the next section contains the absolute velocity fields resulting from the standard model run, as well as, the mass, heat and property fluxes associated with these fields. The sections which follow discuss the standard model solution, its velocity and transport fields, as well as associated

heat and freshwater fluxes. The standard model cross-isopycnal transfer terms are mentioned in passing in this chapter and discussed in more detail in Chapter 4.

3.3 The Standard Model Absolute Velocity Fields and Property Fluxes

The first part of the section which follows contains profiles of the integrated property fields (potential temperature, salinity, oxygen, phosphate, silica and PO38) in the potential density layers used in the standard model and described in Table 2.5. These profiles are followed by plots of the absolute velocity field for each of the hydrographic transects as computed from the standard model. The velocity at the reference level is traced in the upper portion of each figure. Section 3.4 discusses these results. Finally, tables are presented which summarize the fluxes of mass, salt, oxygen phosphate, silica and PO38 across the sections which result from these velocity fields.

NOTE: The depths of the isopycnal interfaces used in the section average profiles are computed by summing the section average vertical heights of each of the isopycnal layers. This method allows for an accurate representation of the section thickness of the isopycnal layers. However, in those sections which display large variations in the depth of the defined layers, this method sometimes results in a total depth which is greater than the actual ocean depth in the region.

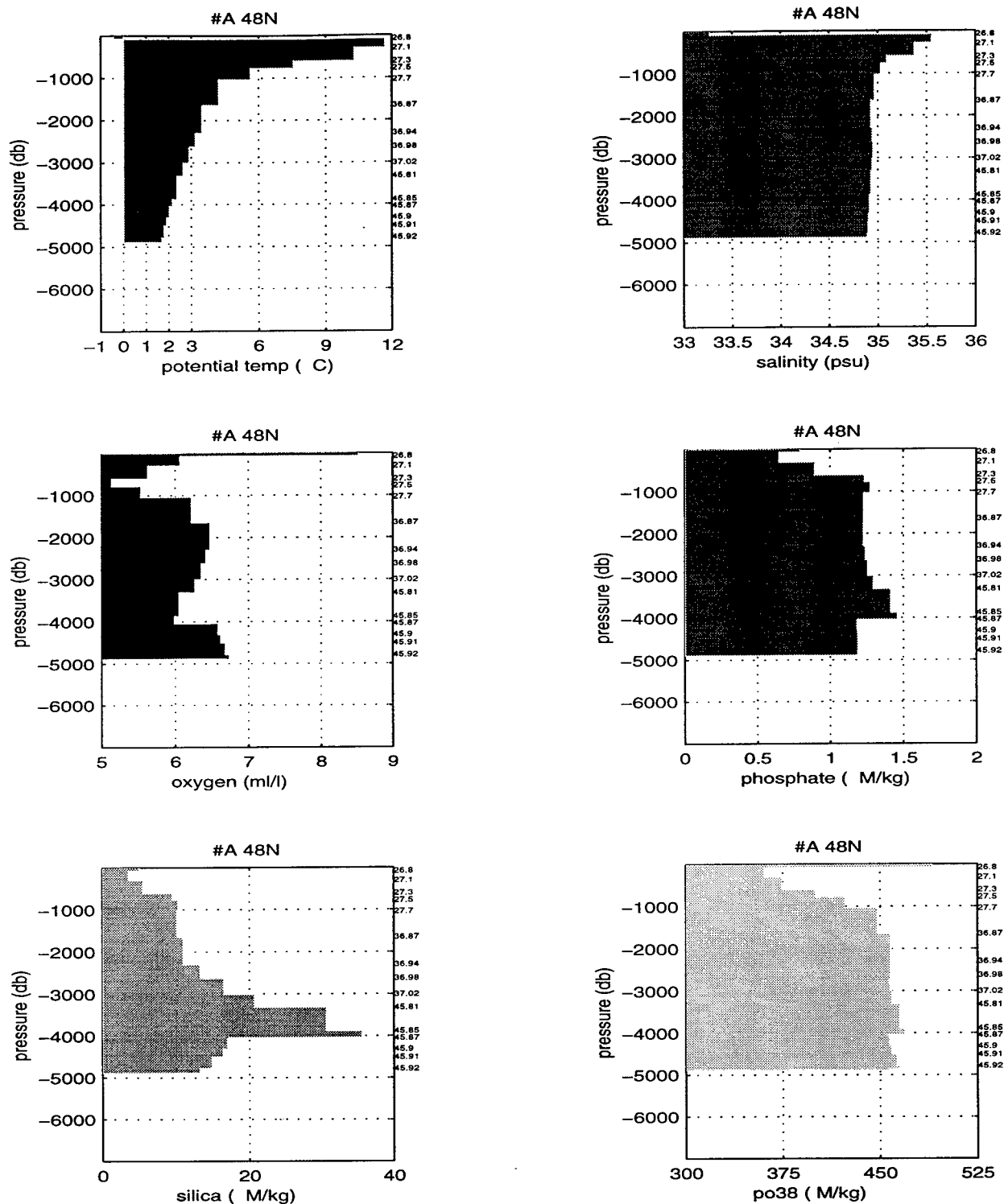


Figure 3.6a: The zonally integrated property values in potential density layers from the Hudson section across 48°N in the Atlantic.

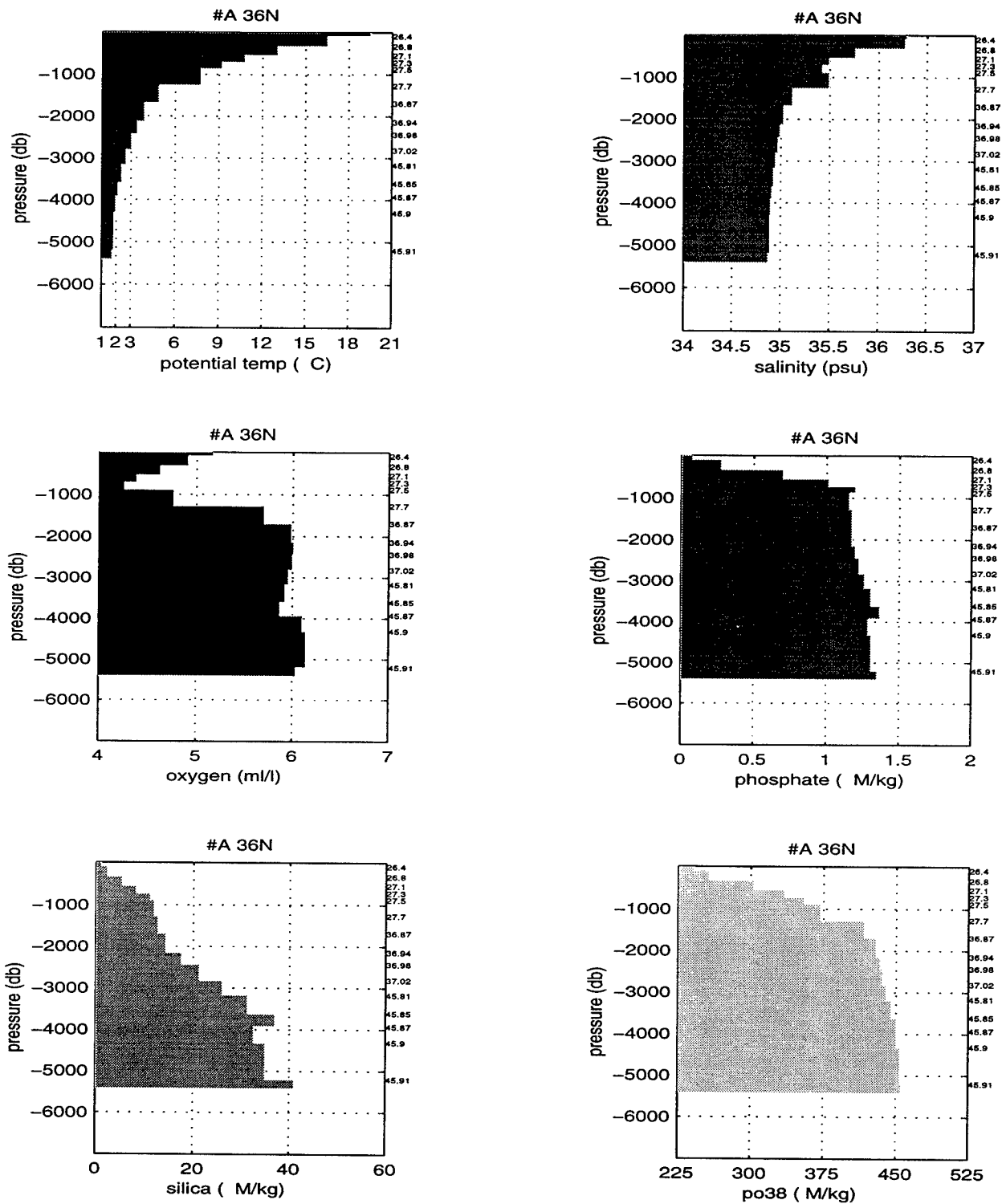


Figure 3.6b: The zonally integrated property values in potential density layers from the Atlantis 109 section across 36°N in the Atlantic.

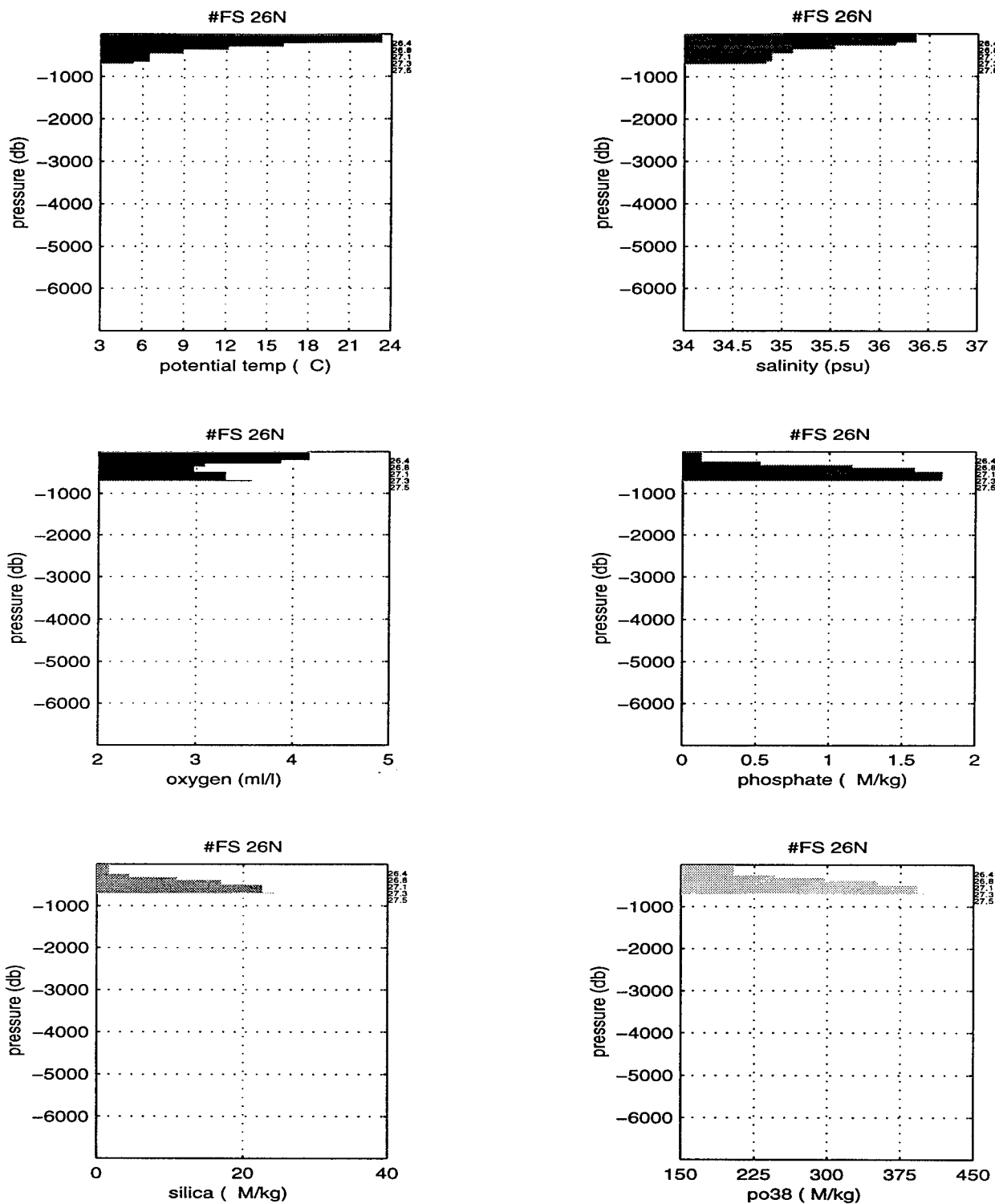


Figure 3.6c: The zonally integrated property values in potential density layers from the Atlantis 109 section across the Florida Straits.

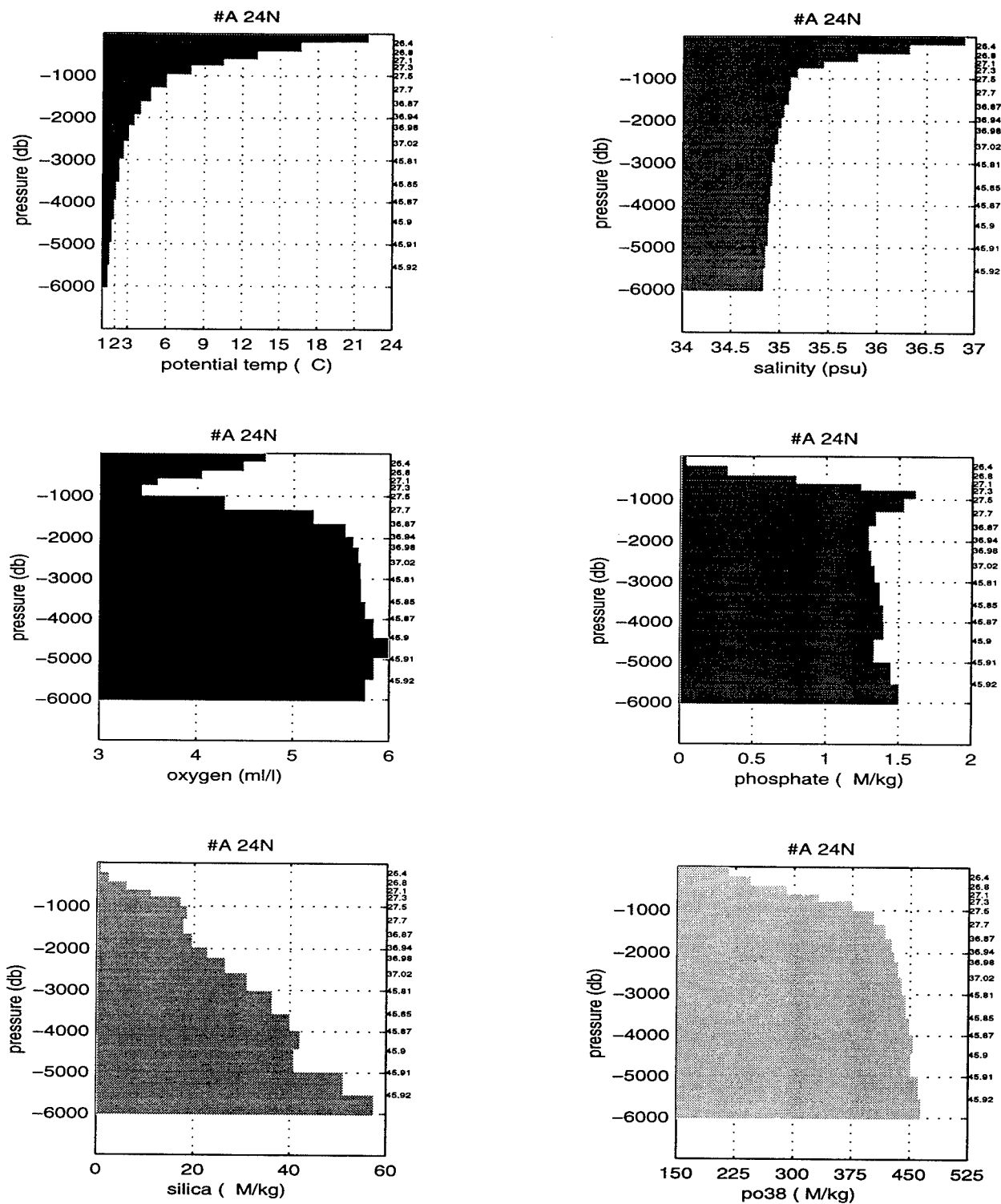


Figure 3.6d: The zonally integrated property values in potential density layers from the Atlantis 109 section across 24°N in the Atlantic.

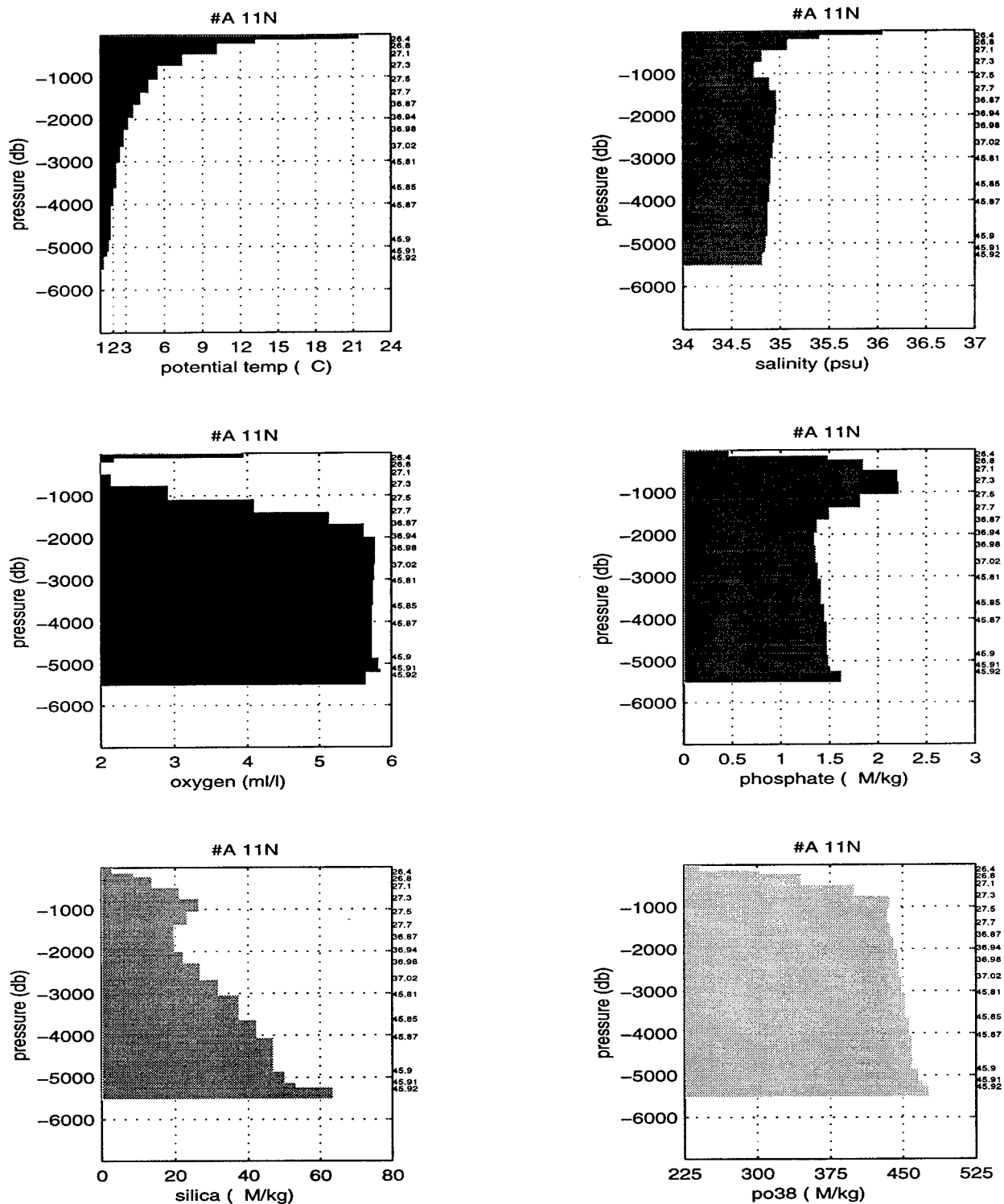


Figure 3.6e: The zonally integrated property values in potential density layers from the Oceanus 338 section across 11°N in the Atlantic.

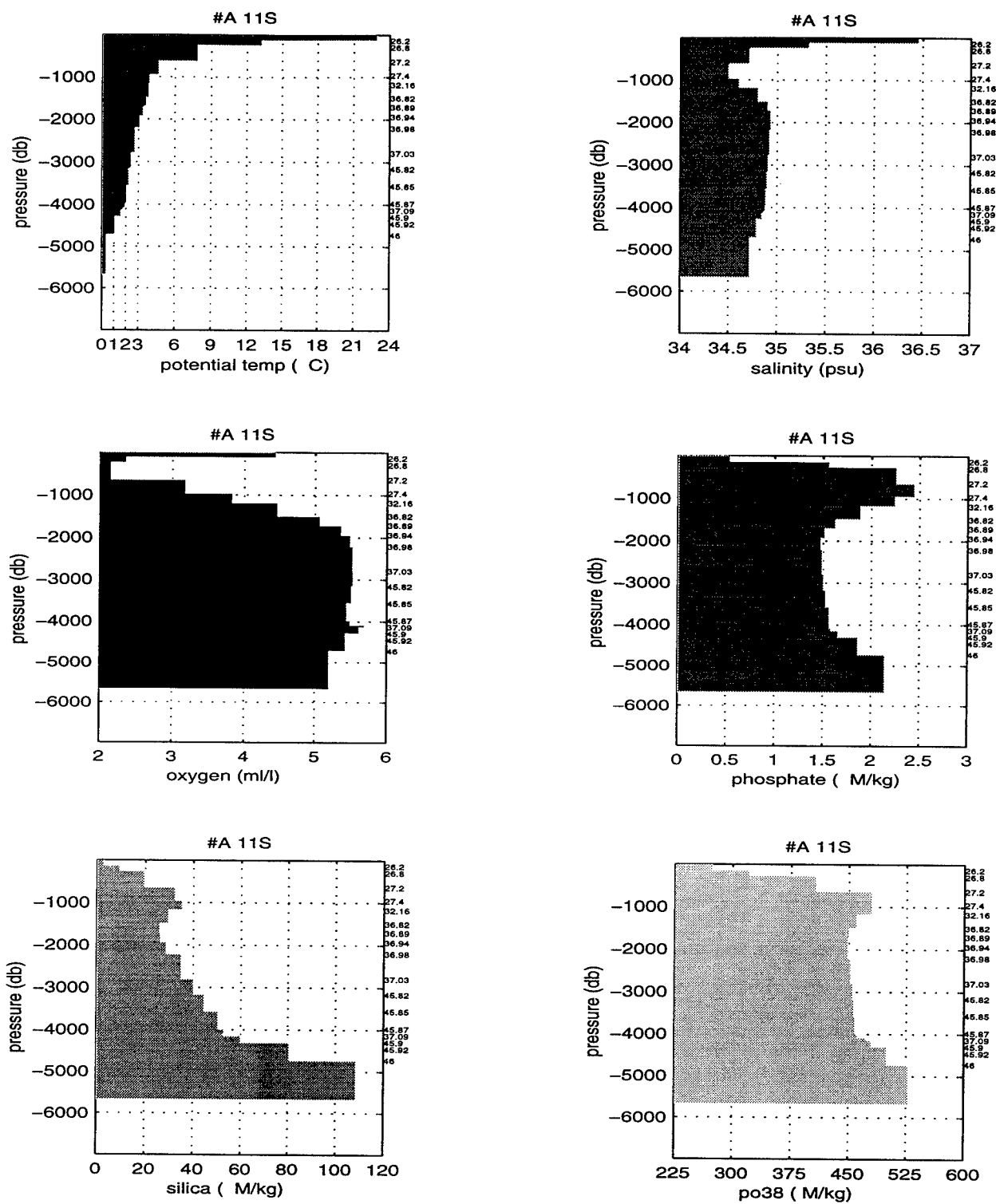


Figure 3.6f: The zonally integrated property values in potential density layers from the Oceanus 133 section across 11°S in the Atlantic.

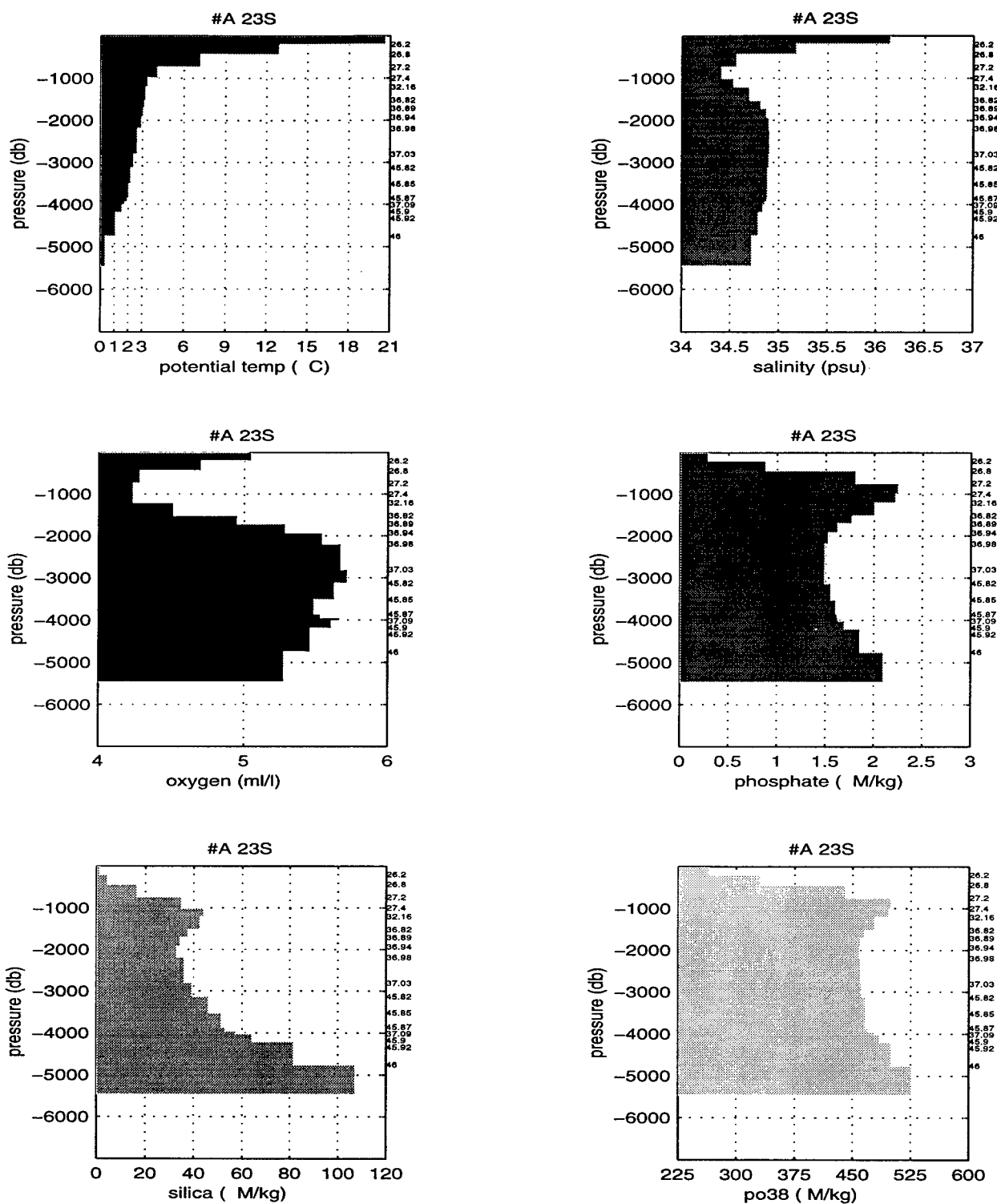


Figure 3.6g: The zonally integrated property values in potential density layers from the Oceanus 133 section across 23°S in the Atlantic.

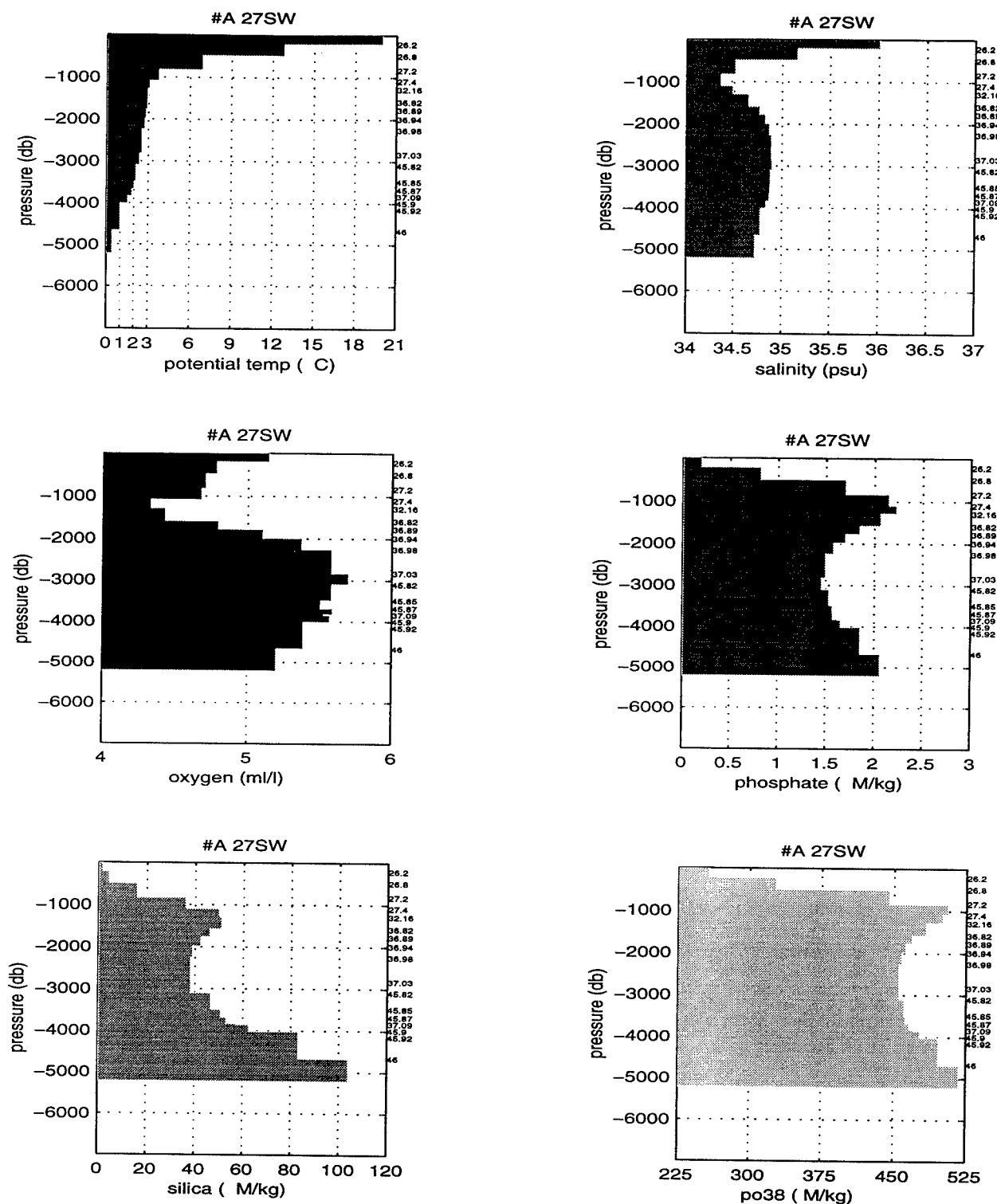


Figure 3.6h: The zonally integrated property values in potential density layers from the SAVE legs 3 and 4 from the west coast of the South Atlantic to 0°E at about 27°S.

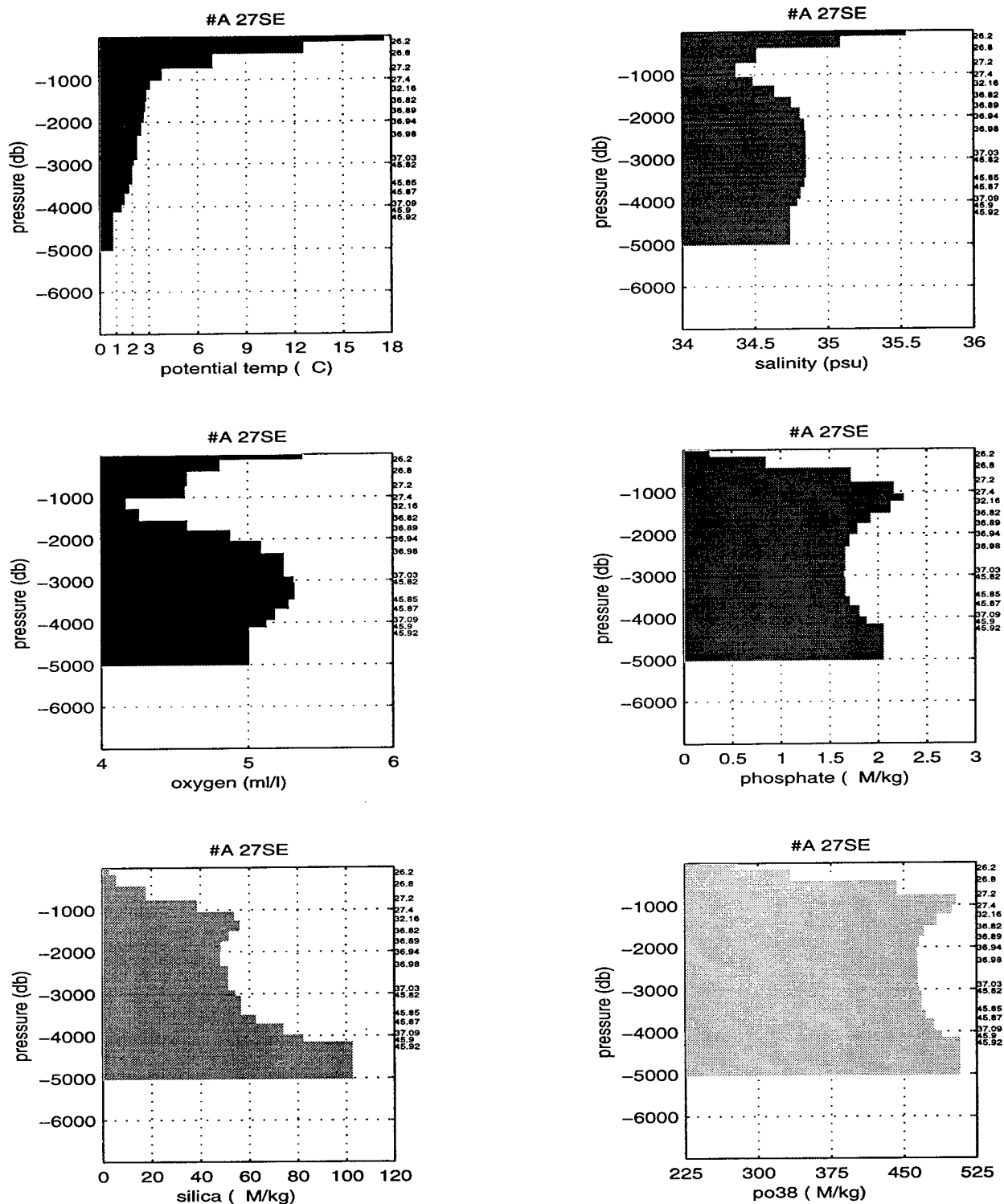


Figure 3.6i: The zonally integrated property values in potential density layers from the SAVE leg 4 from the 0°E to the east coast of the South Atlantic at 30°S.

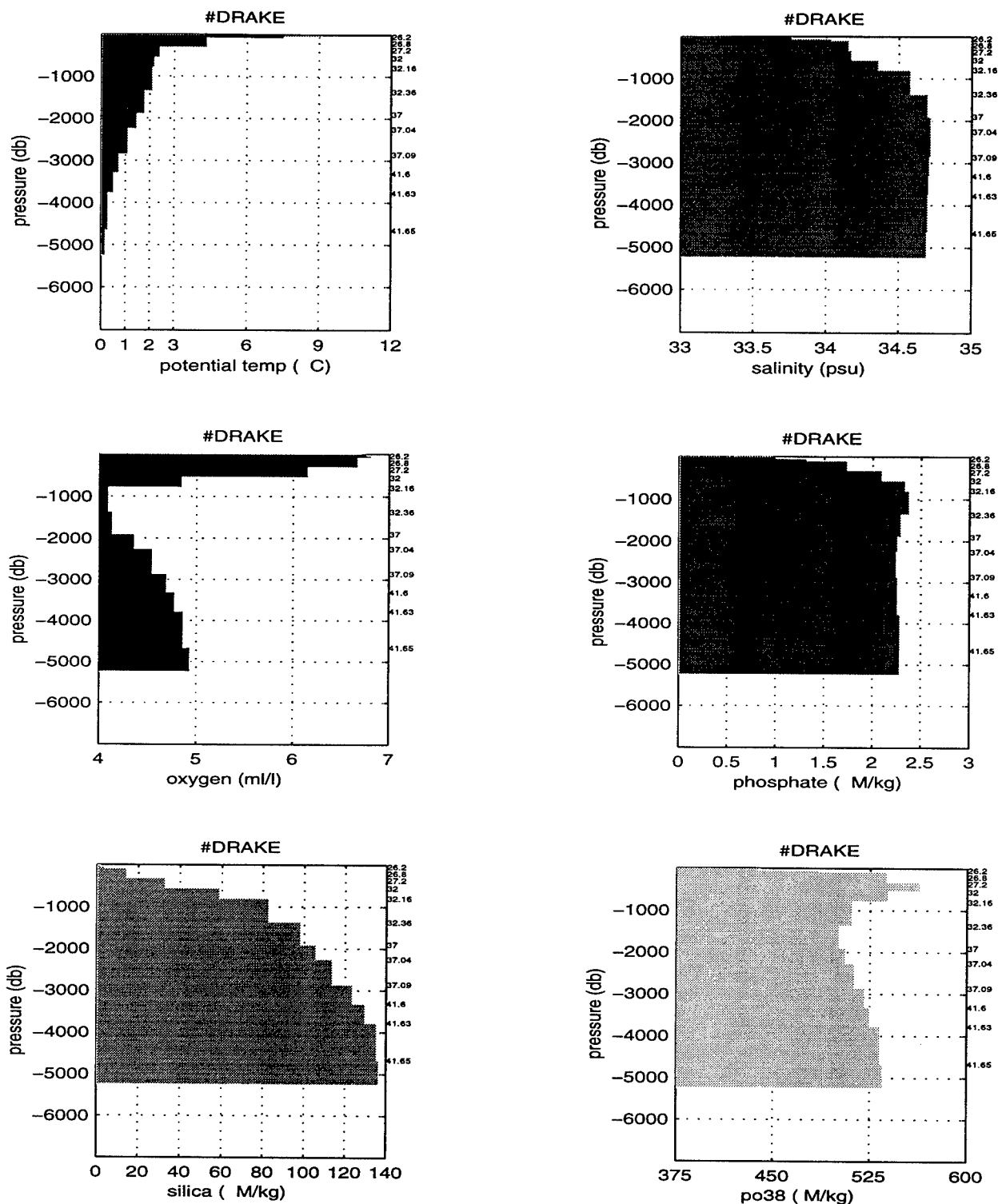


Figure 3.7a: The meridionally integrated property values in potential density layers from the Meteor 11/5 section across Drake Passage.

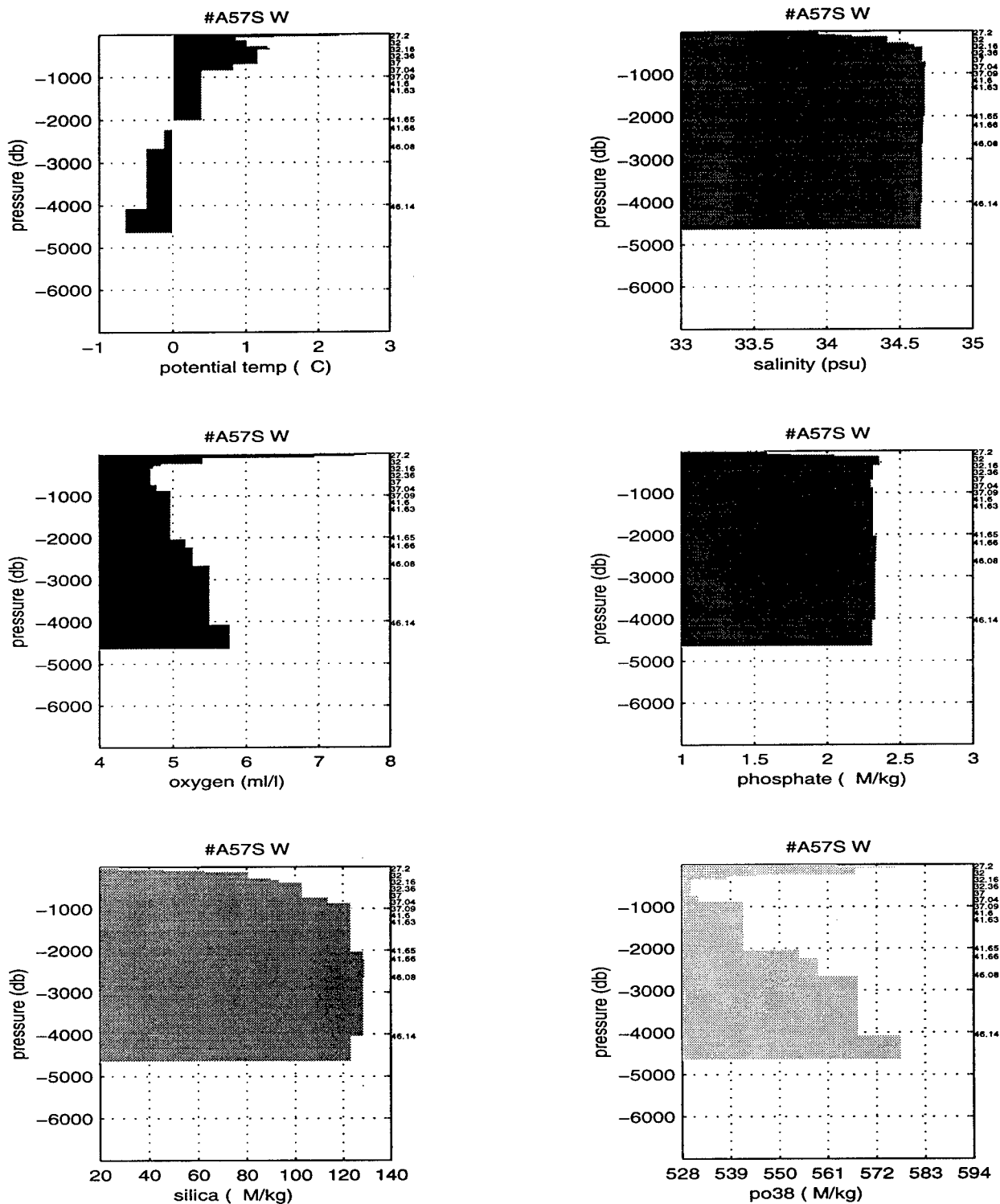


Figure 3.7b: The zonally integrated property values in potential density layers from the AJAX section along 57°S in the western South Atlantic bordering the Weddell Sea.

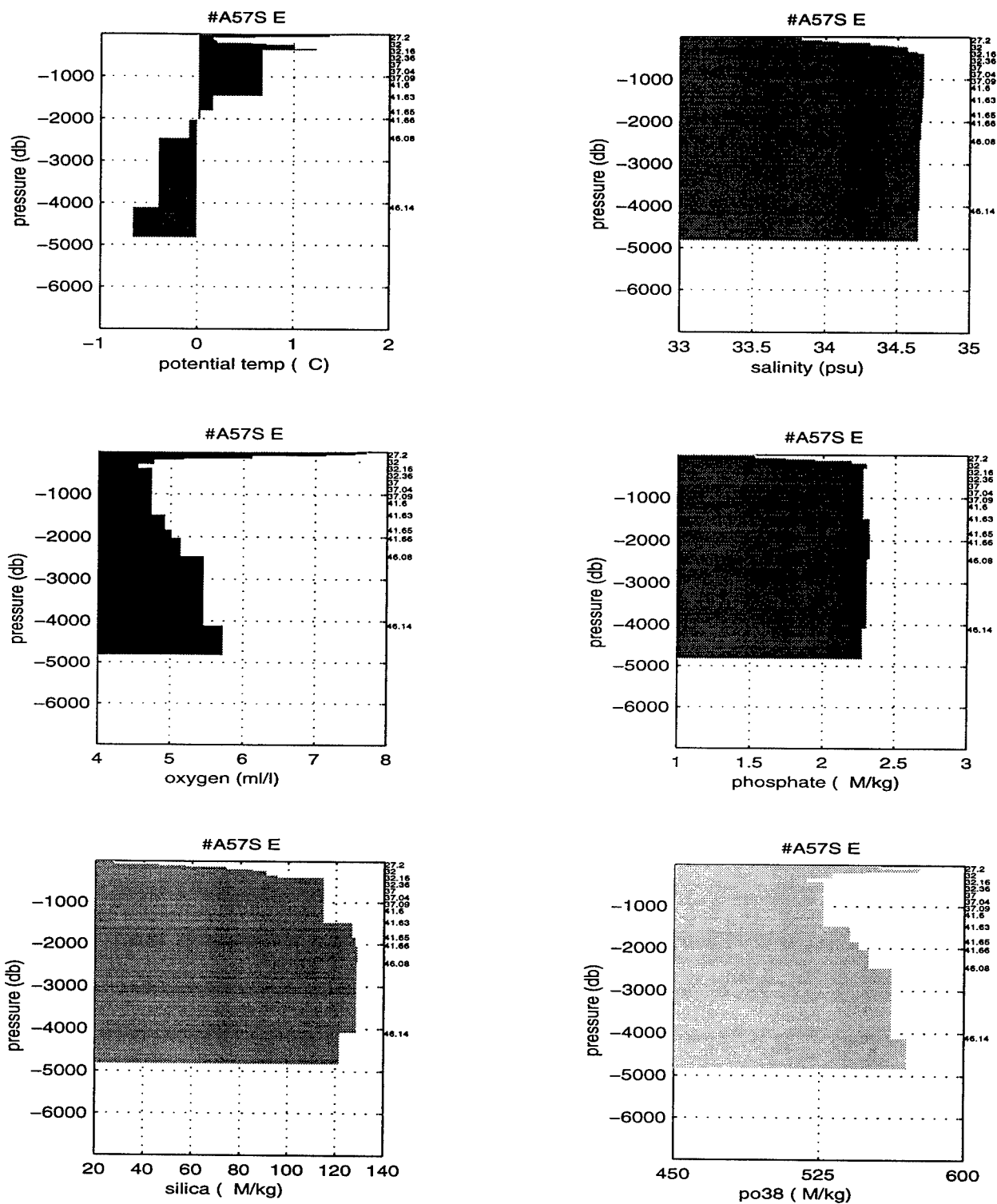


Figure 3.7c: The zonally integrated property values in potential density layers from the Meteor 11/5 section along 57°S bordering the eastern portion of the Weddell Sea and running to 0°E.

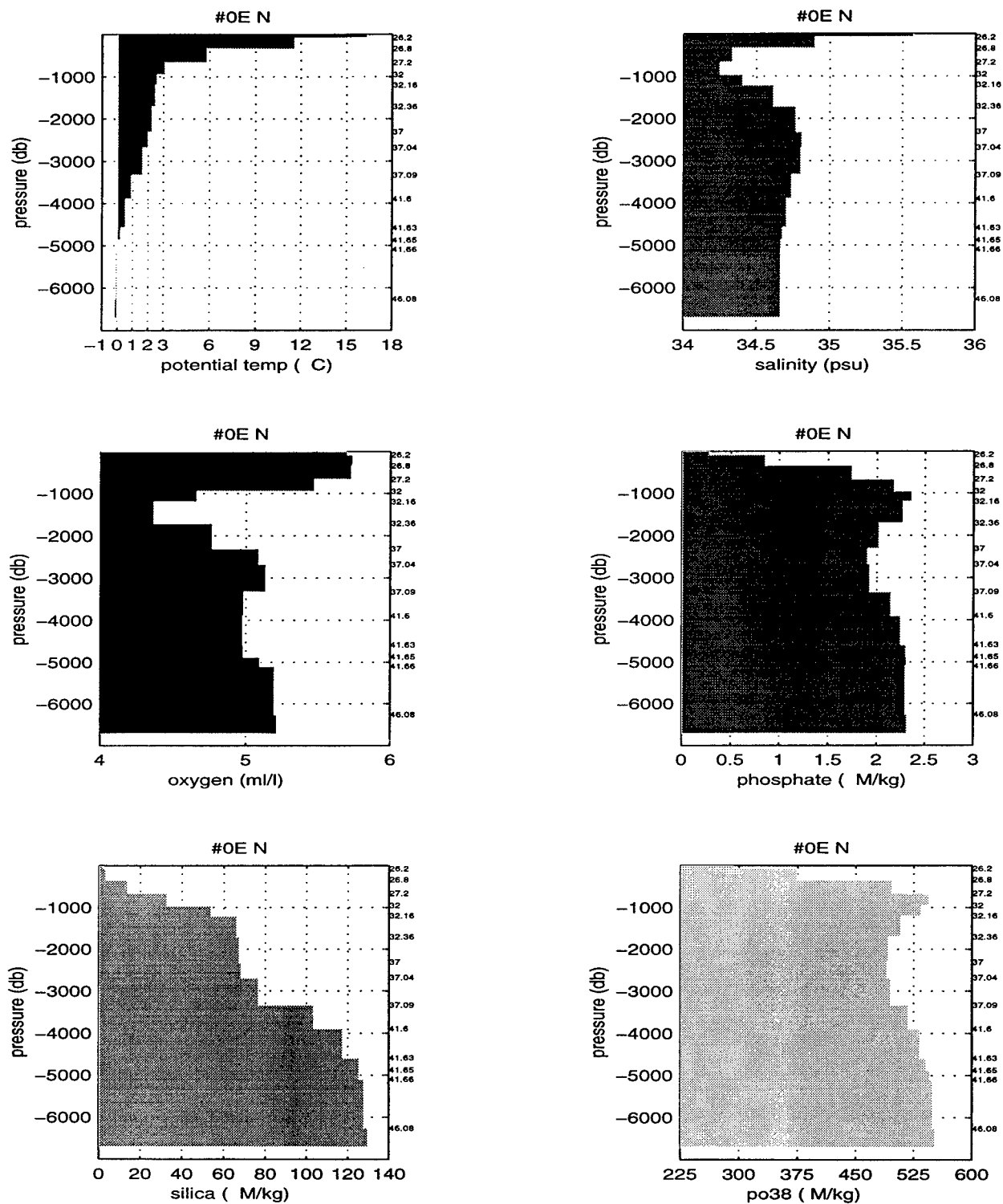


Figure 3.7d: The meridionally integrated property values in potential density layers from the AJAX section along 0°E in the South Atlantic north of 55°S.

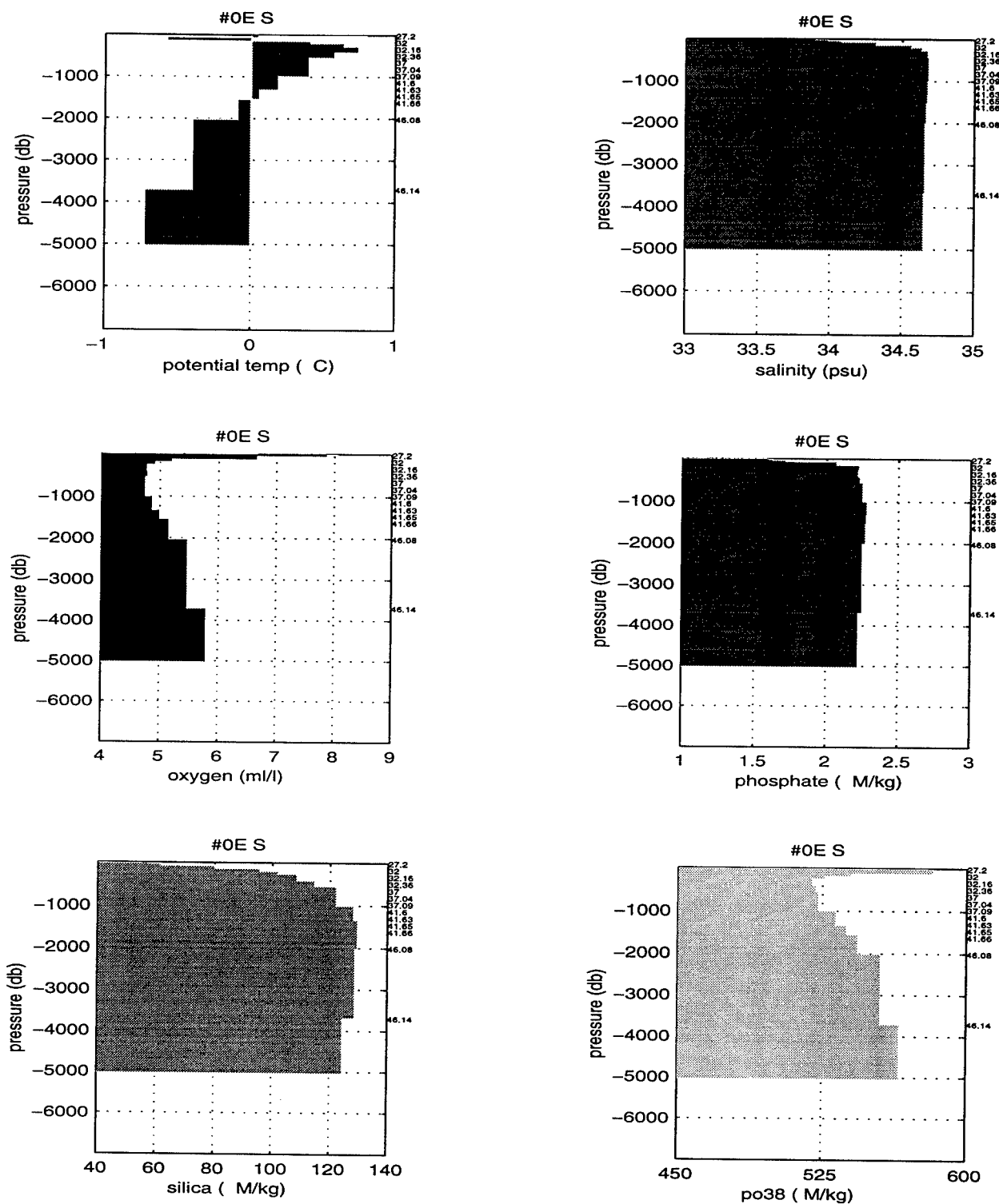


Figure 3.7e: The meridionally integrated property values in potential density layers from the AJAX section along 0°E in the South Atlantic south of 55°S.

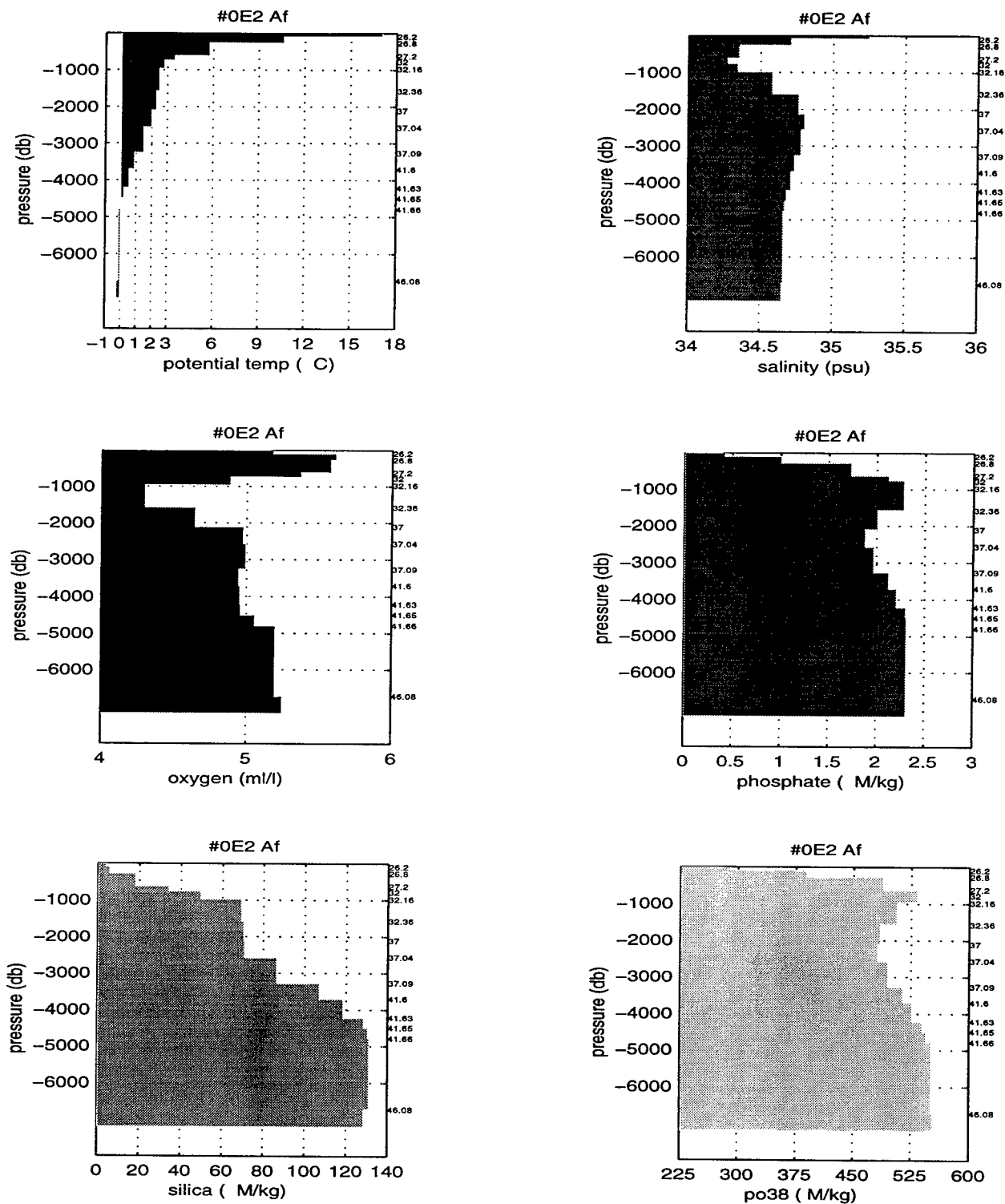


Figure 3.7f: The integrated property values in potential density layers from the Meteor 11/5 section running from 0°E, 55°S to the southern tip of South Africa.

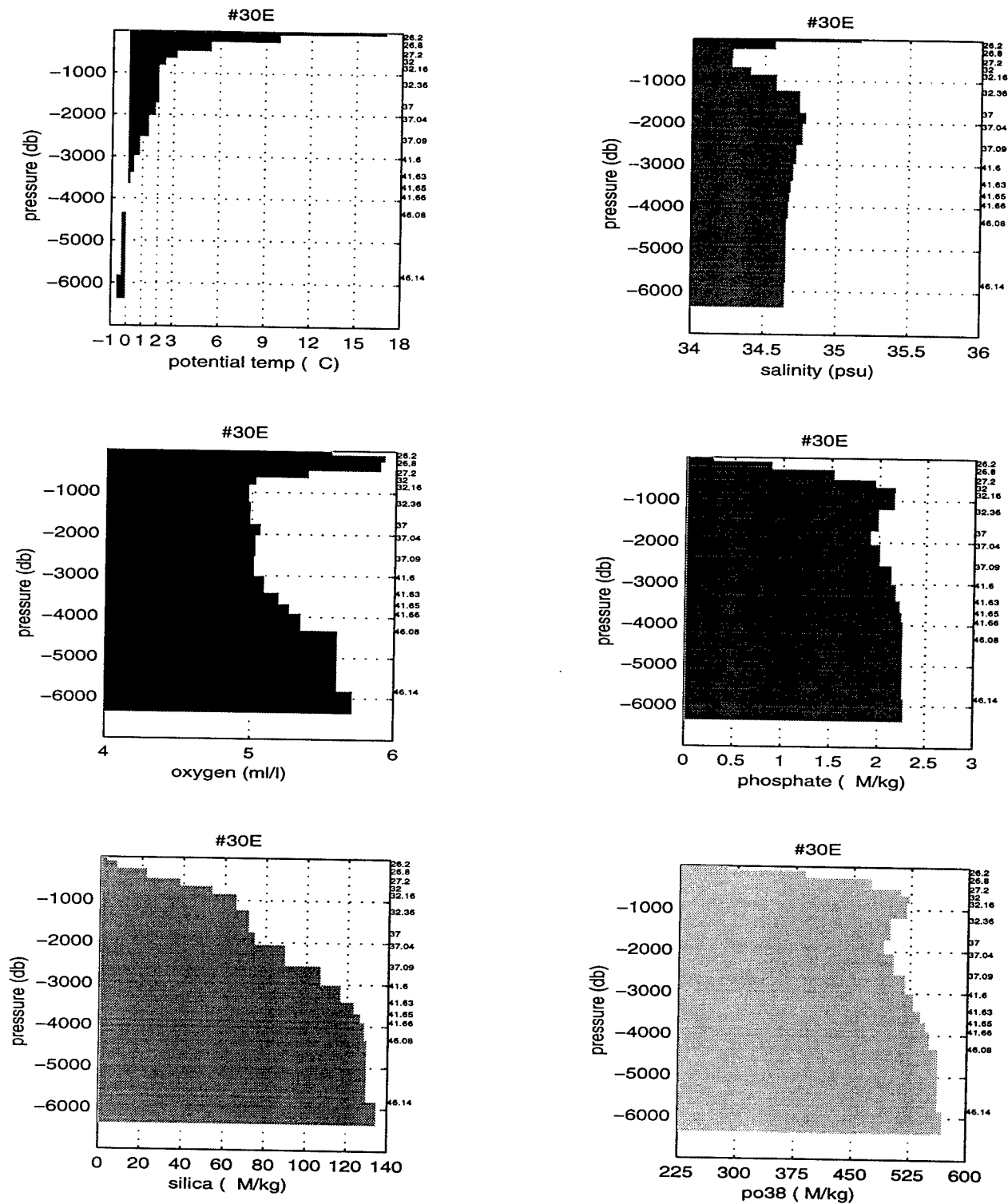


Figure 3.7g: The meridionally integrated property values in potential density layers from the Conrad 17 section along 30°E between South Africa and Antarctica.

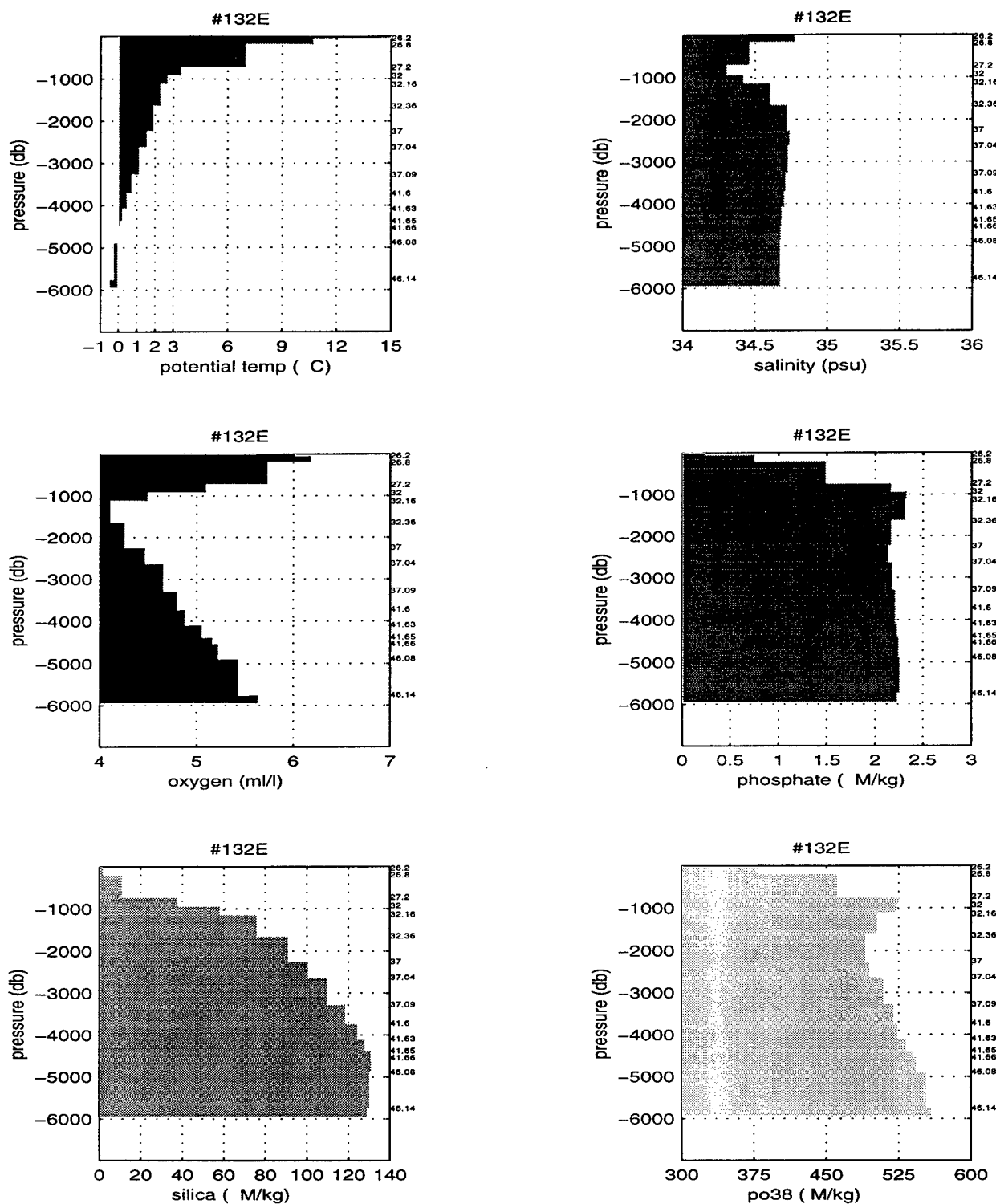


Figure 3.7h: The meridionally integrated property values in potential density layers from the Eltanin 41 section along 132°E between Australia and Antarctica.

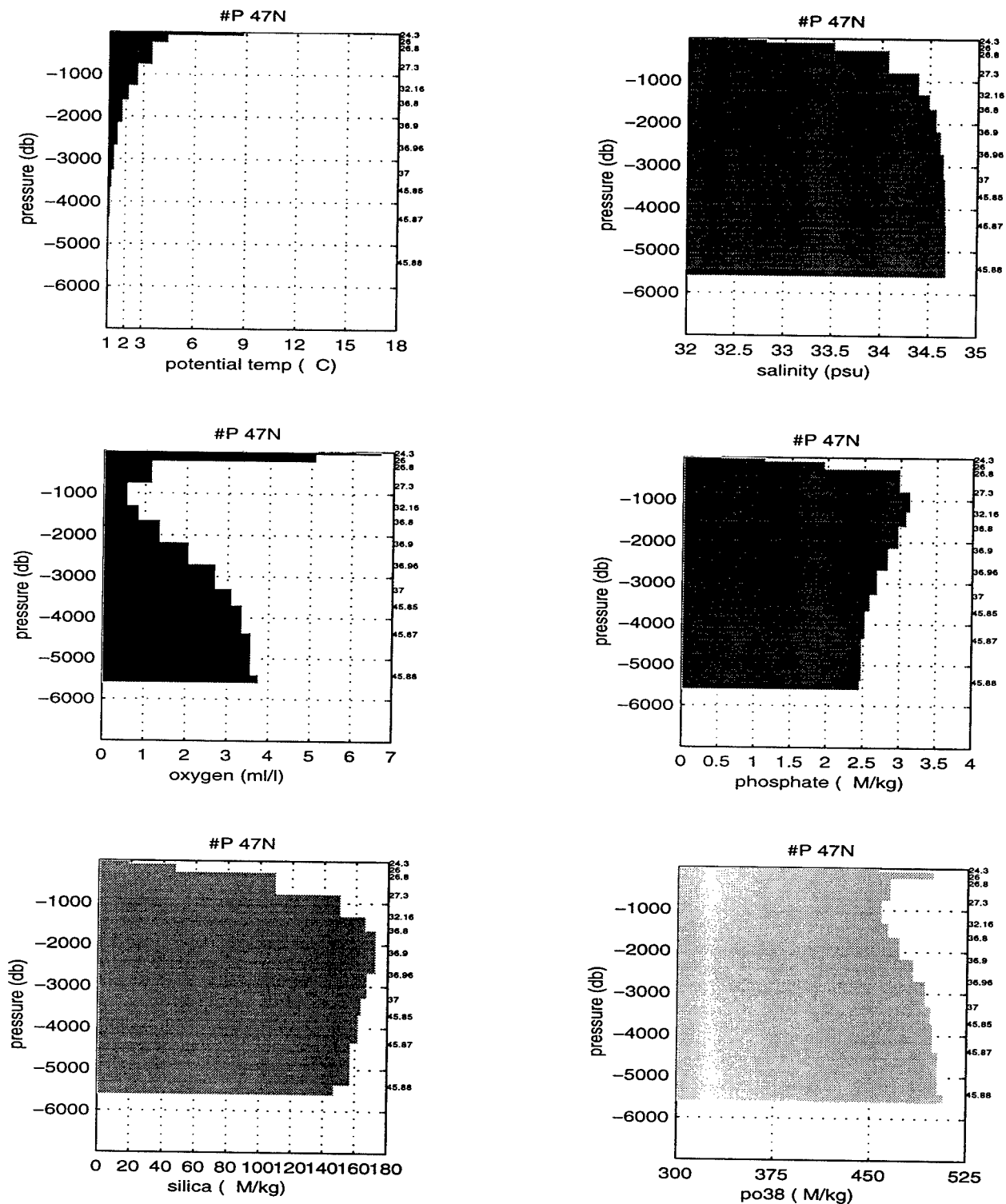


Figure 3.8a: The zonally integrated property values in potential density layers from the Thomas Thompson section across 47°N in the Pacific.

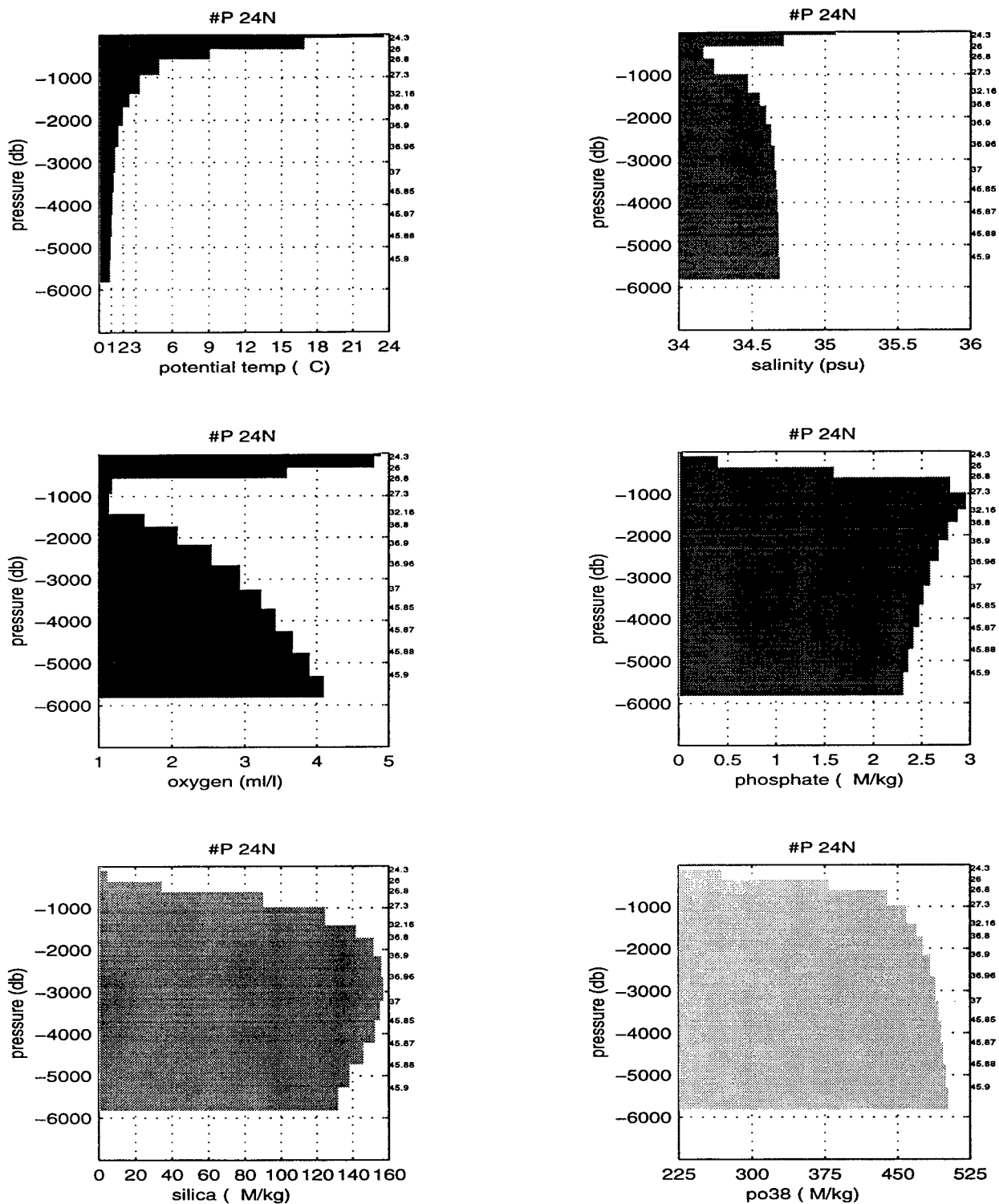


Figure 3.8b: The zonally integrated property values in potential density layers from the Thomas Thompson section across 25°N in the Pacific.

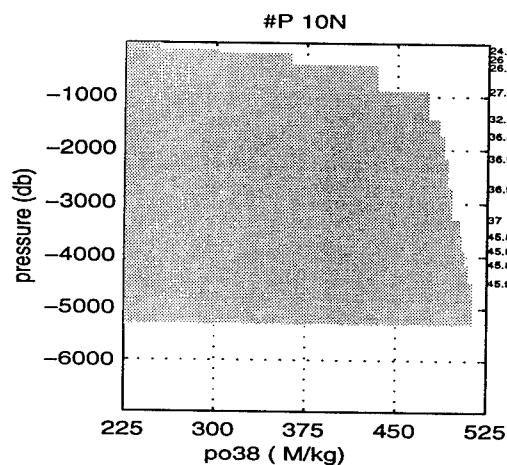
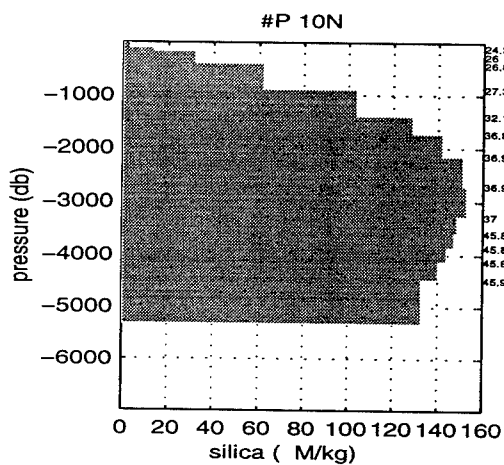
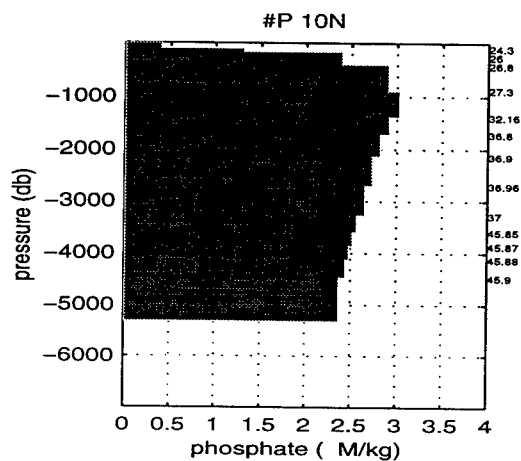
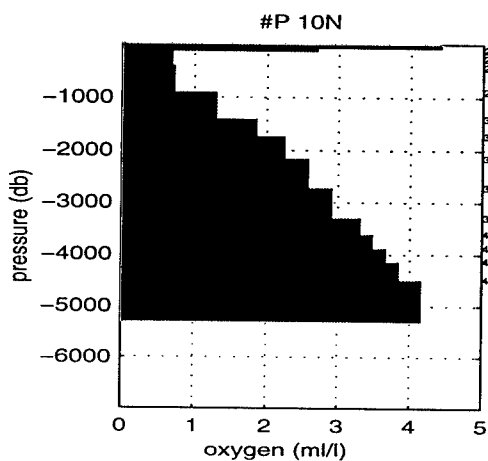
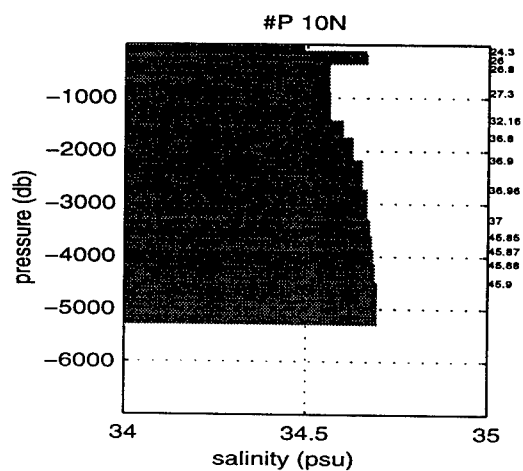
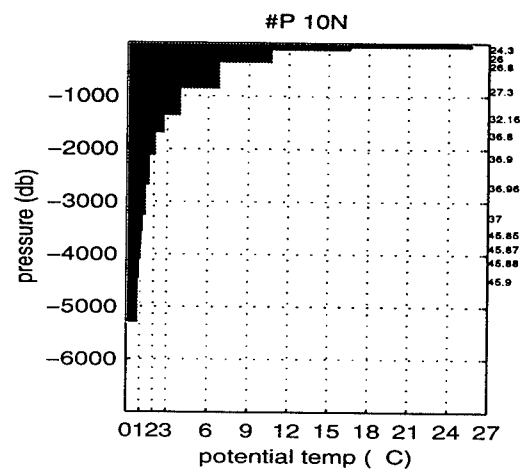


Figure 3.8c: The zonally integrated property values in potential density layers from the Moana Wavw section across 10°N in the Pacific.

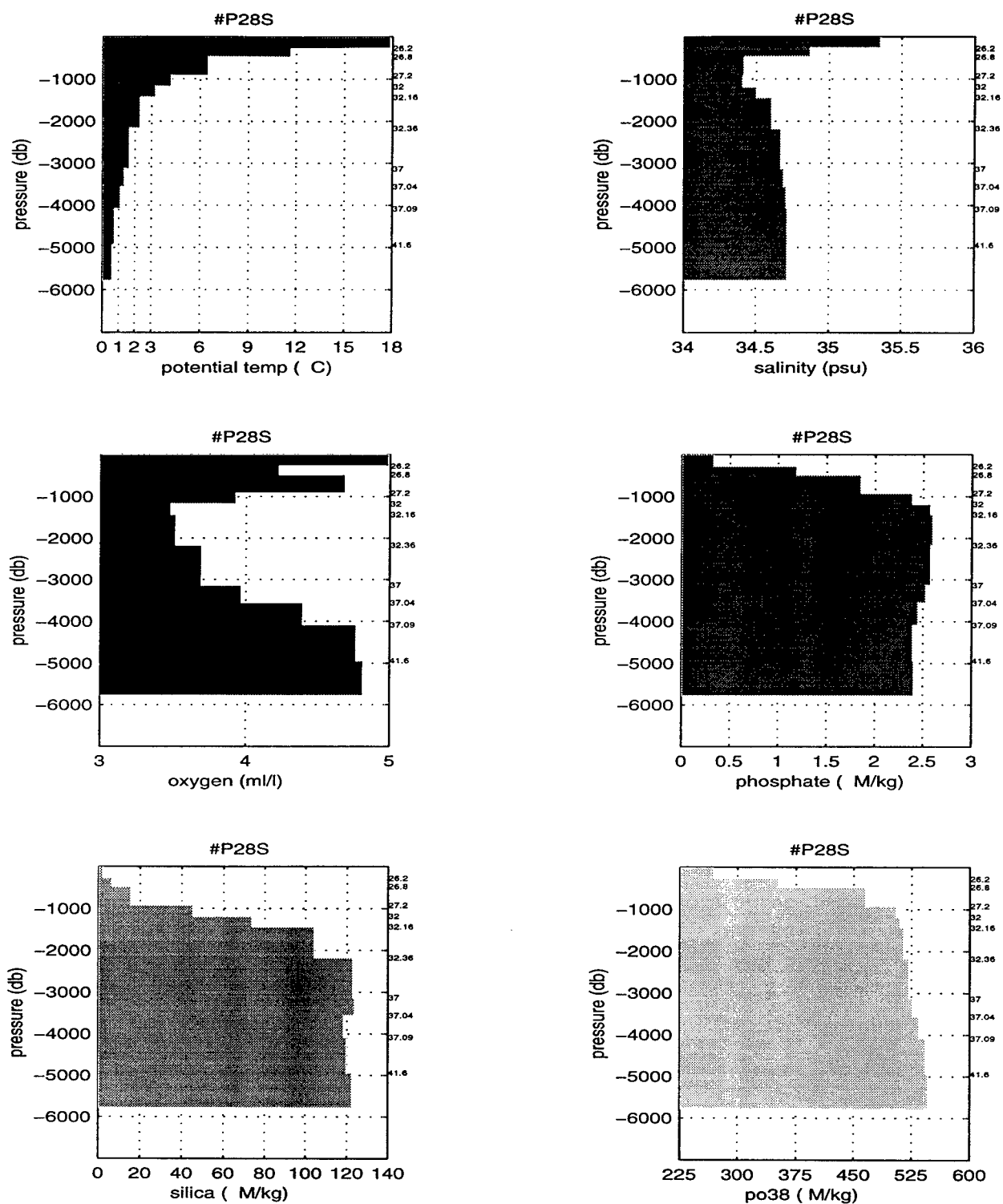


Figure 3.8d: The zonally integrated property values in potential density layers from the Eltanin transect across the Pacific Basin at 28°S.

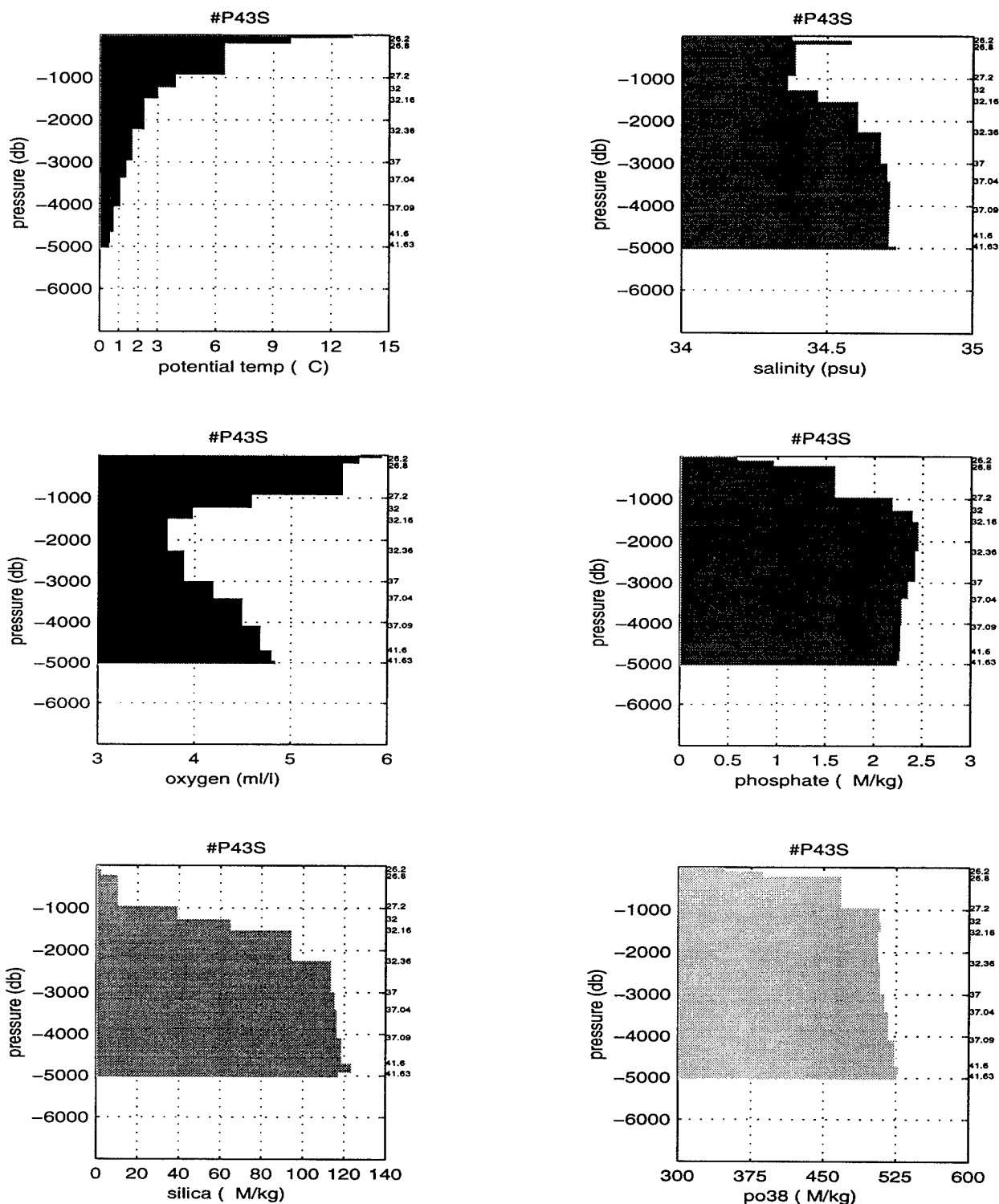


Figure 3.8d: The zonally integrated property values in potential density layers from the Eltanin transect across the Pacific Basin at 43°S, including the data from Australia to New Zealand across the Tasman Sea and from New Zealand to Chile.

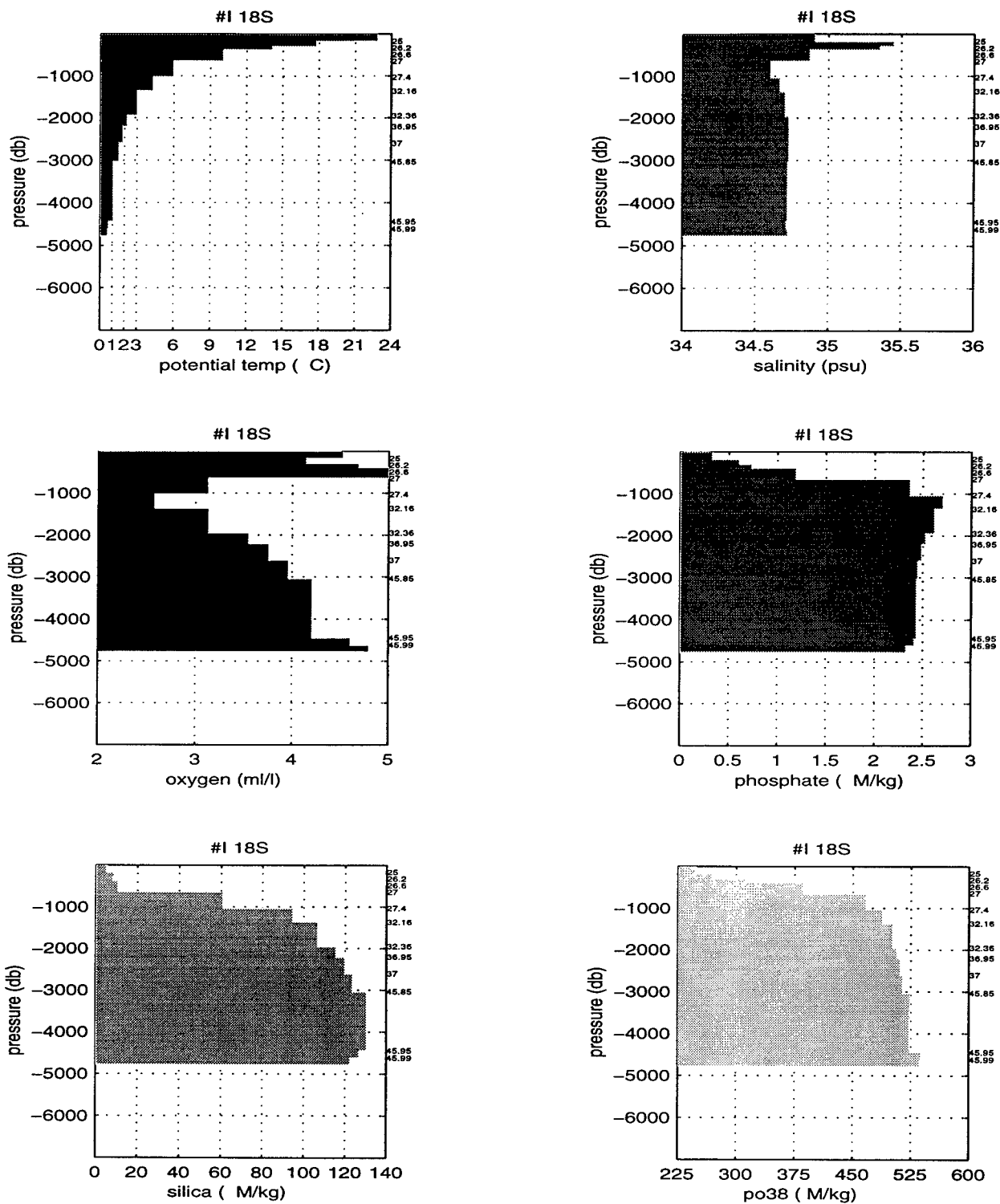


Figure 3.9a: The zonally integrated property values in potential density layers from the Atlantis 93 section across 18°S in the Indian Ocean.

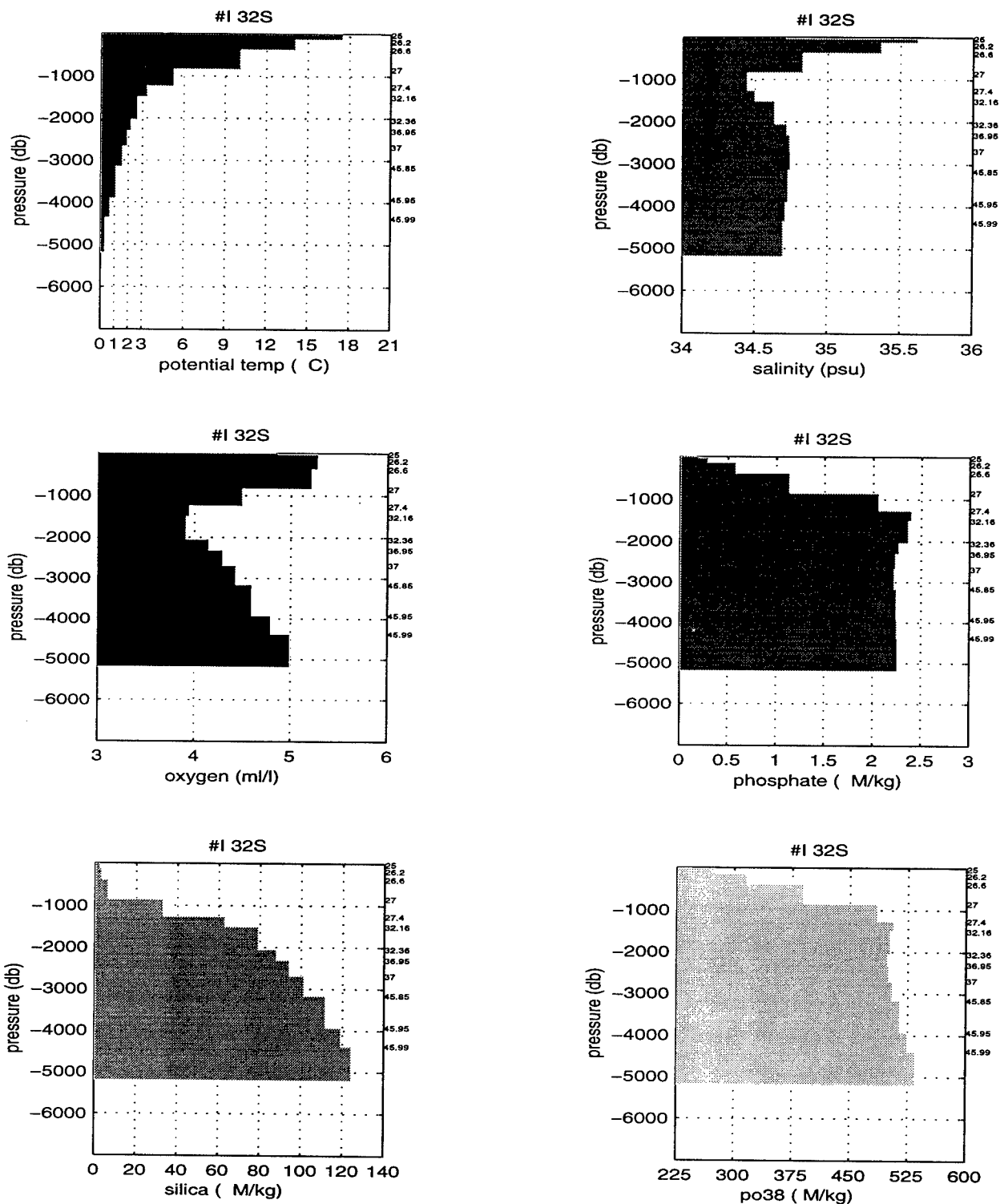


Figure 3.9b: The zonally integrated property values in potential density layers from the Charles Darwin 29 section across 32°S in the Indian Ocean.

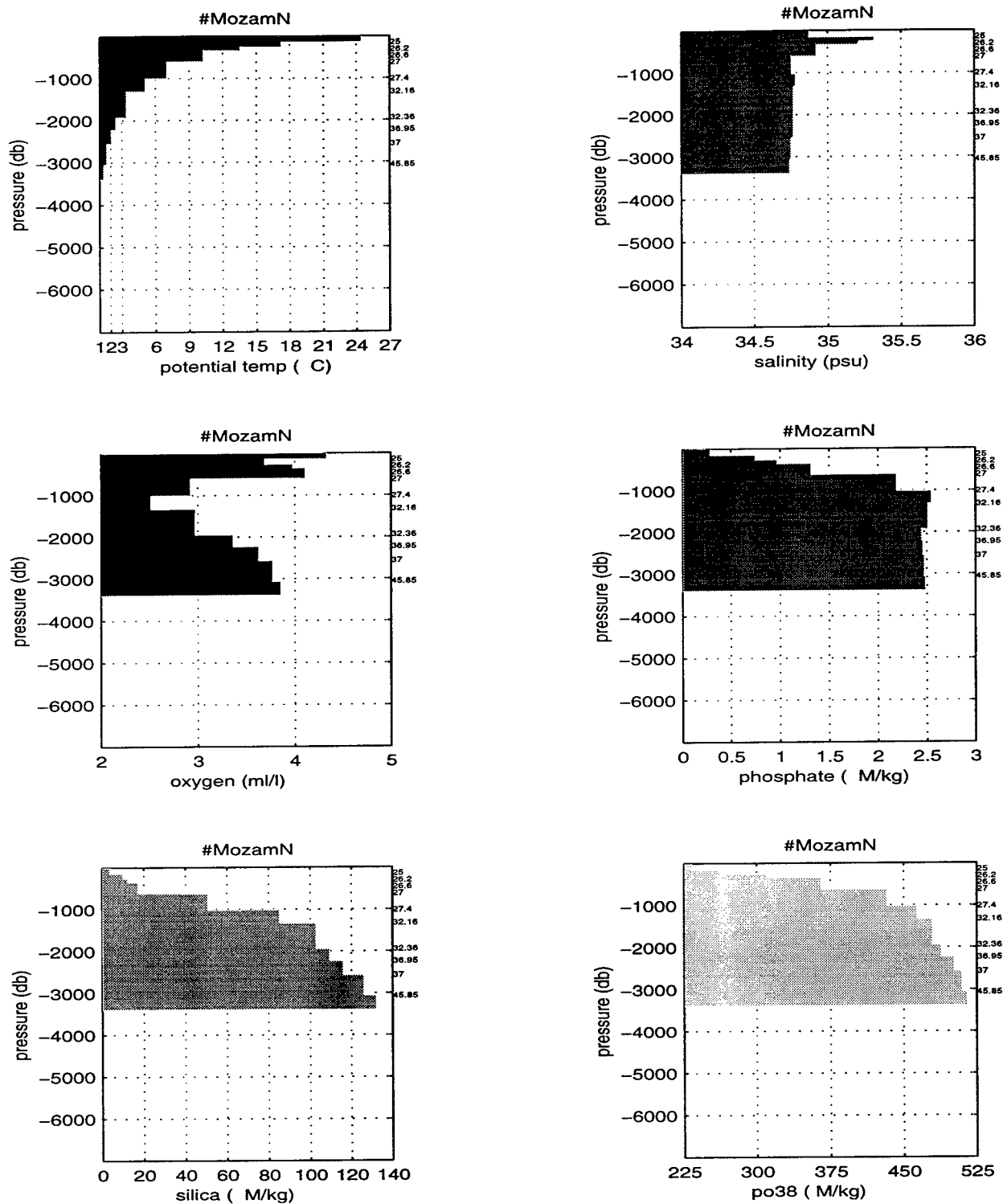


Figure 3.9c: The zonally integrated property values in potential density layers from the Australian NODC sections across the Mozambique Channel at 12°S.

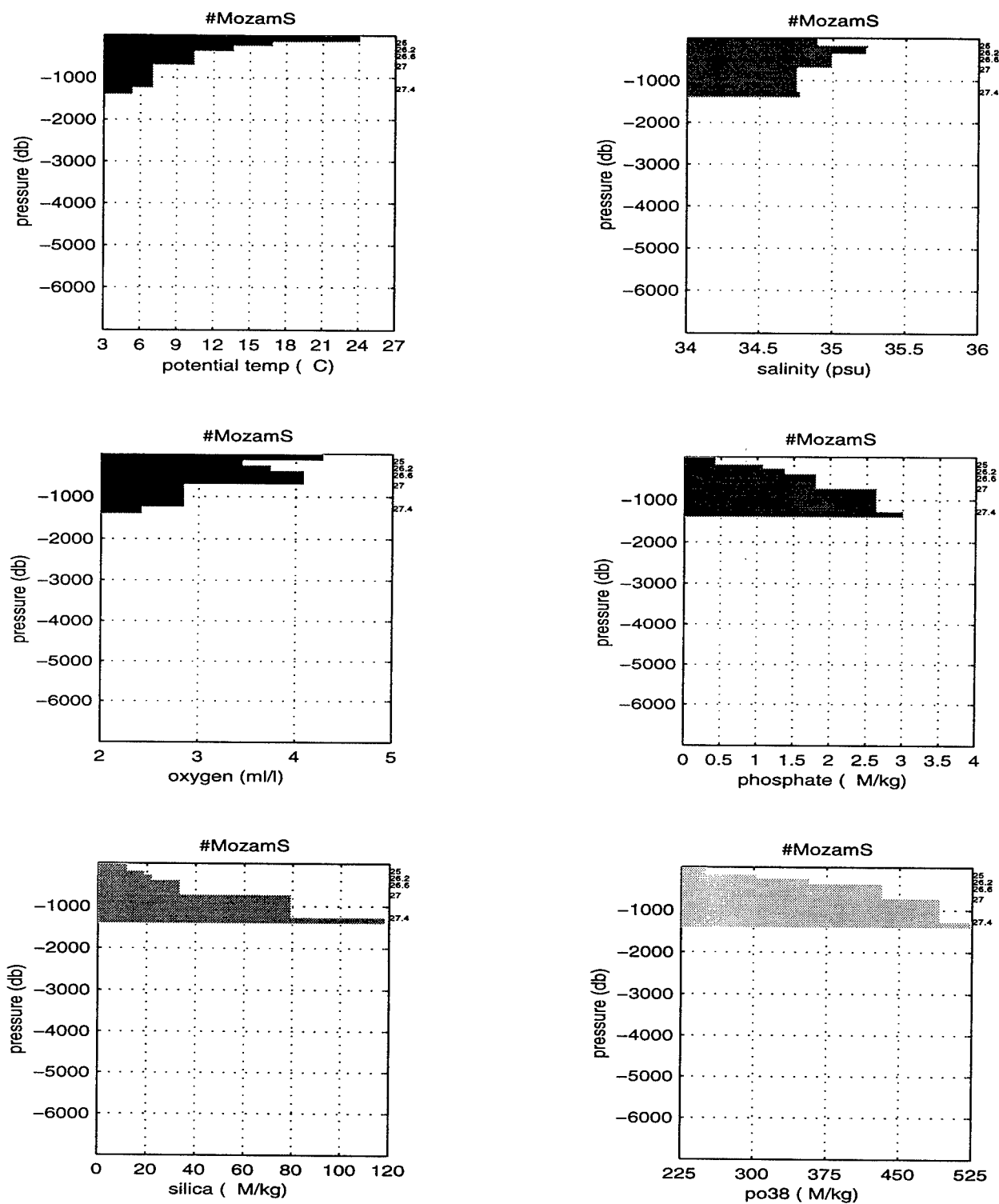


Figure 3.9d: The zonally integrated property values in potential density layers from the Australian NODC section across the Mozambique Channel at 15°S.

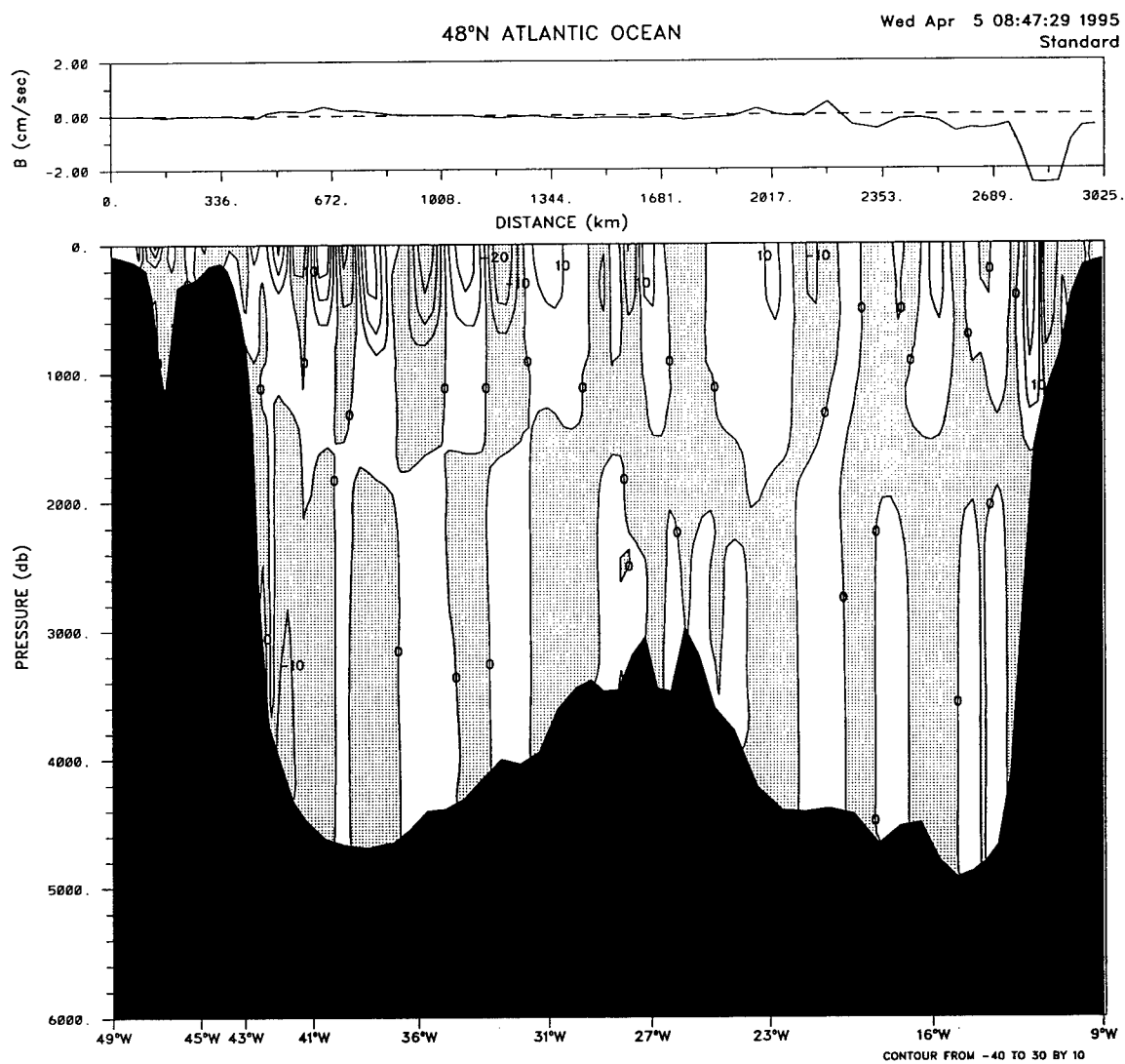


Figure 3.10a: The absolute velocity field across 48°N in the Atlantic, from the standard model. The hydrography comes from the Hudson 1982 data set. The reference level velocities at $\sigma_2 = 36.87$ are displayed at the top of the figure.

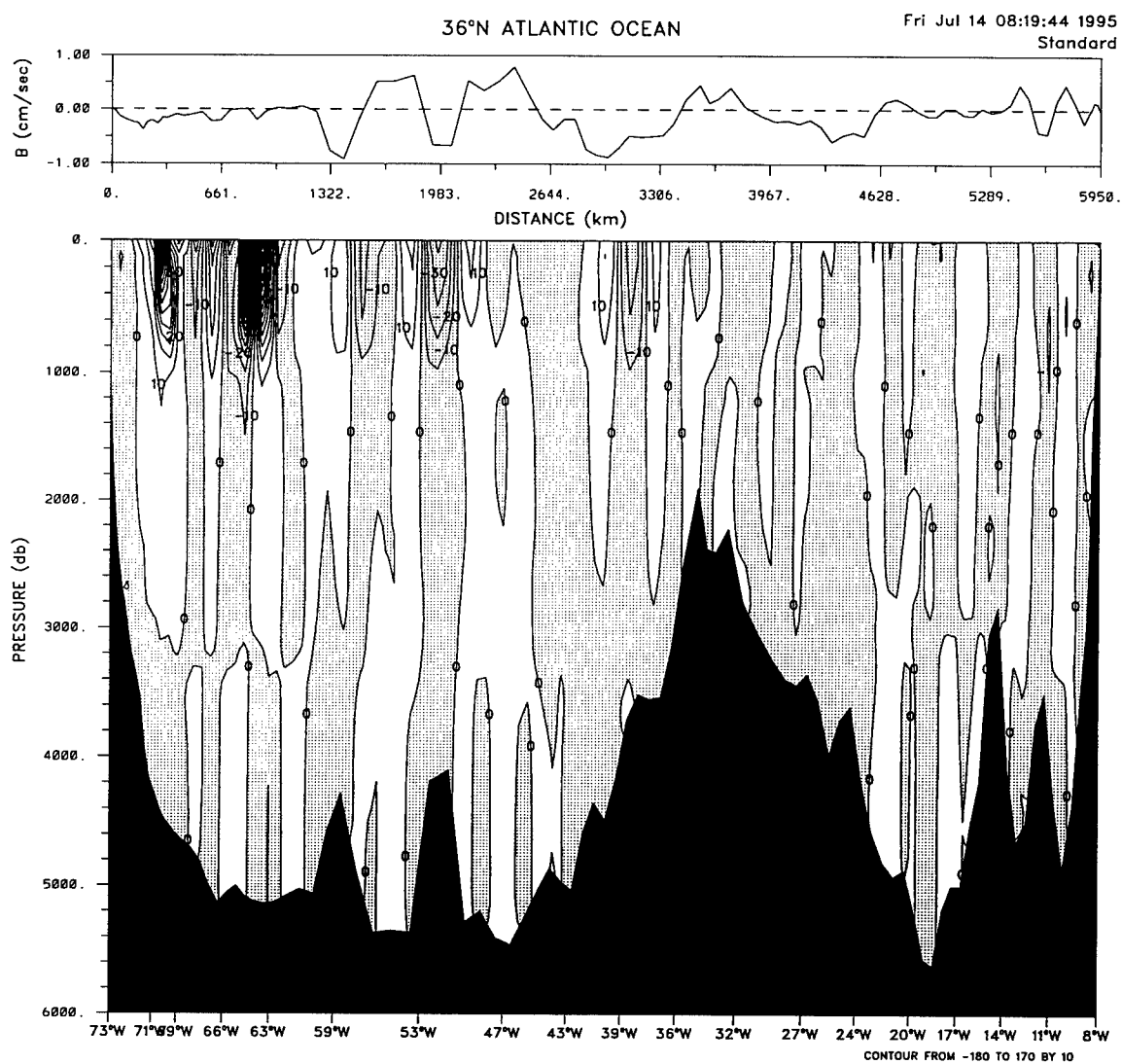


Figure 3.10b: The absolute velocity field across 36°N in the Atlantic, from the standard model. The hydrography comes from the Atlantis 109, 1981 data set. The reference level velocities at $\sigma_4 = 45.81$ are displayed at the top of the figure.

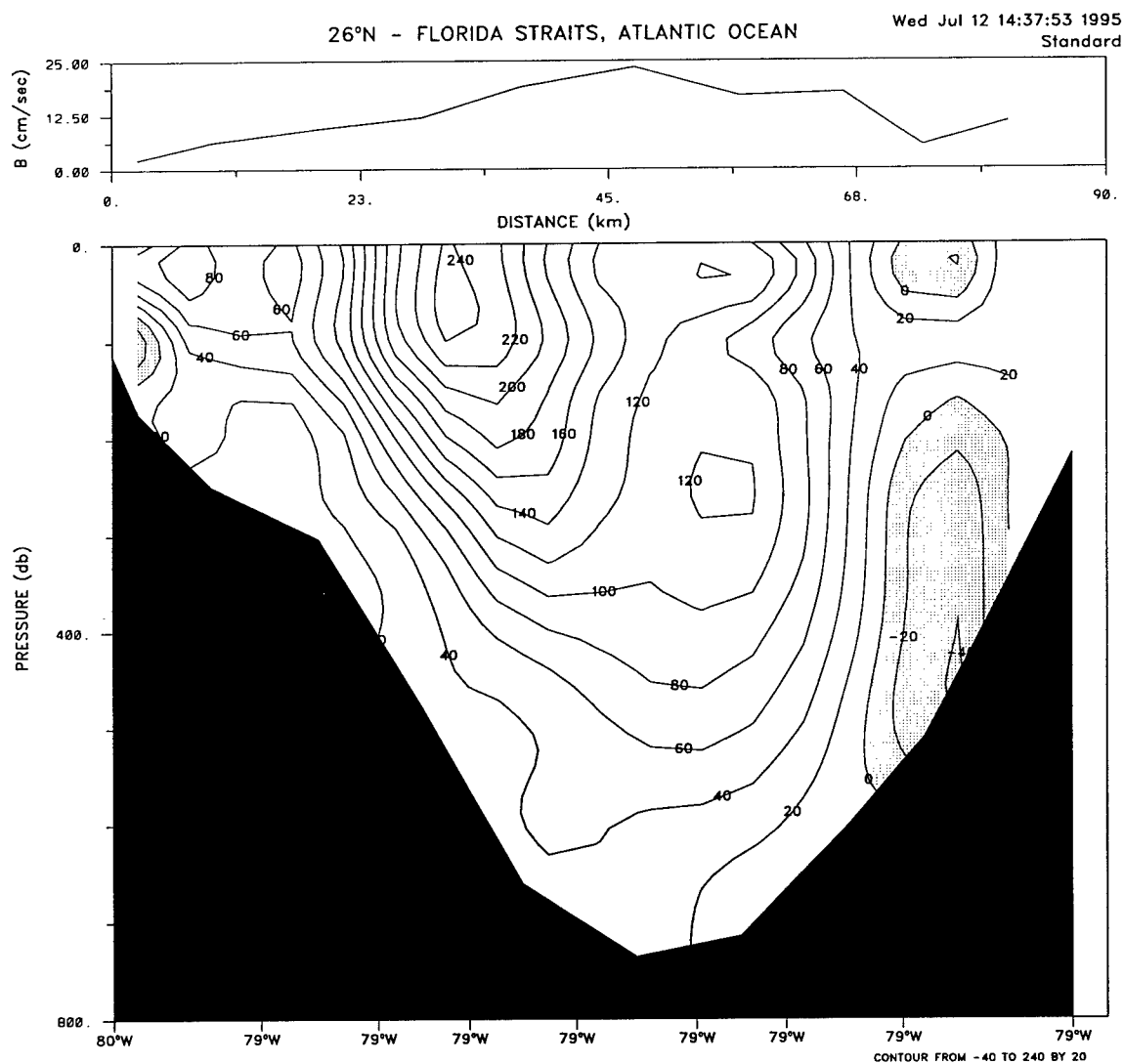


Figure 3.10c: The absolute velocity field across the Florida Straits section at 27°N in the Atlantic, from the standard model. The hydrography comes from the Atlantis 109, 1981 data set. The reference level velocities at $\sigma_0 = 27.50$ are displayed at the top of the figure.

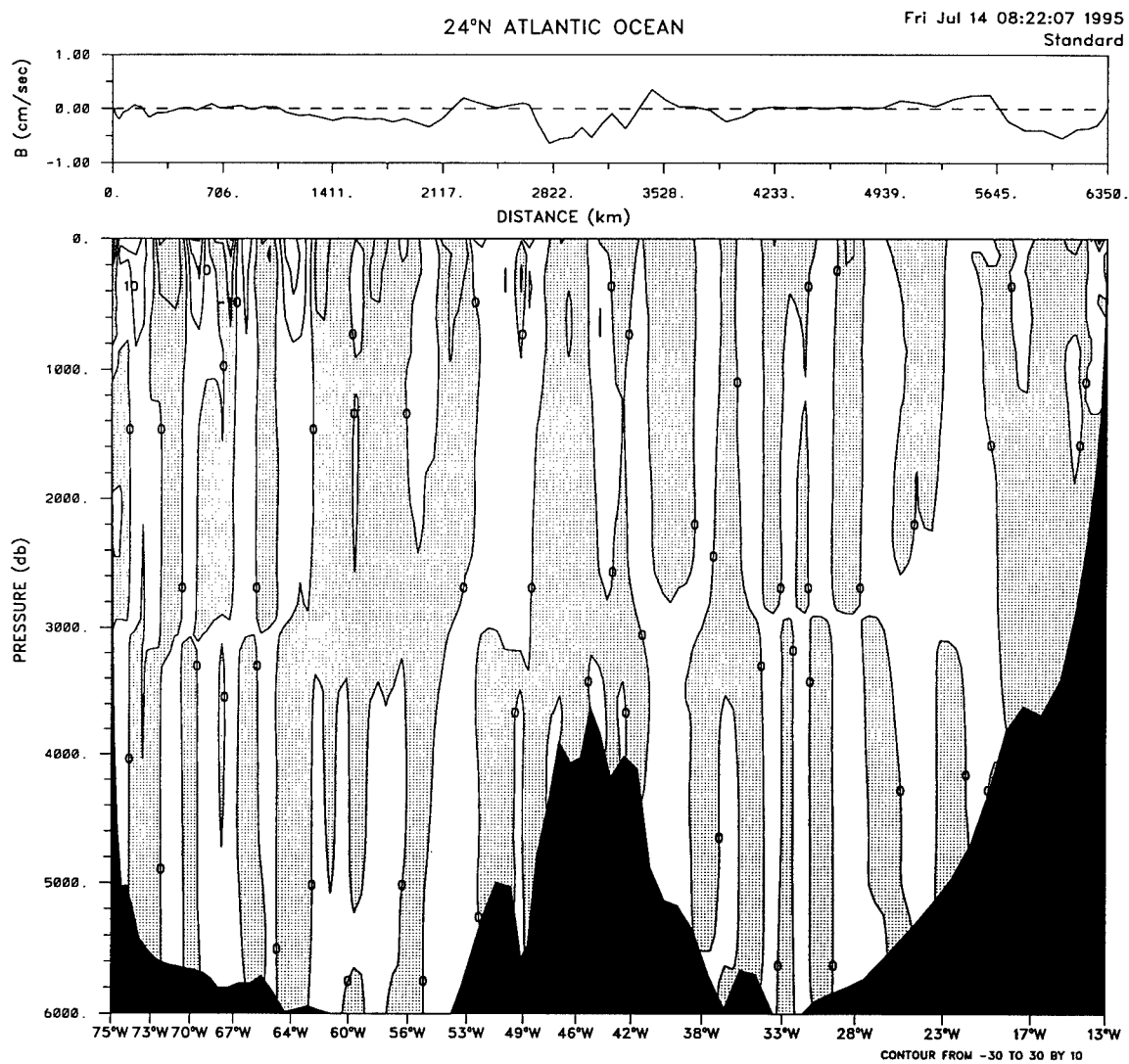


Figure 3.10d: The absolute velocity field across 24°N in the Atlantic, from the standard model. The hydrography comes from the Atlantis 109, 1981 data set. The reference level velocities at $\sigma_4 = 45.81$ are displayed at the top of the figure.

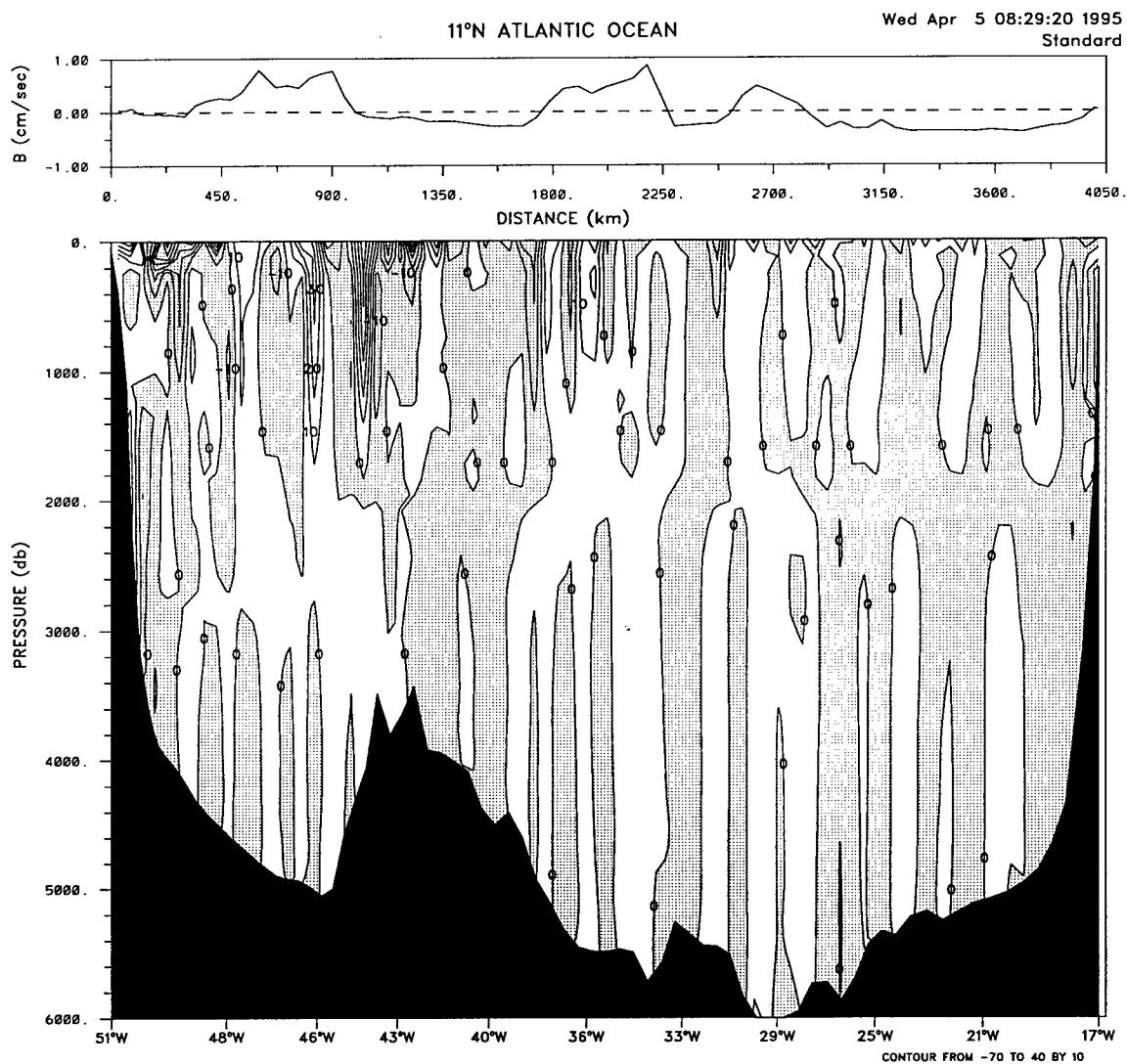


Figure 3.10e: The absolute velocity field across 11°N in the Atlantic, from the standard model. The hydrography comes from the Oceanus 338, 1989 data set. The reference level velocities at the reference depths suggested by *Friedrichs and Hall* [1993] are displayed at the top of the figure.

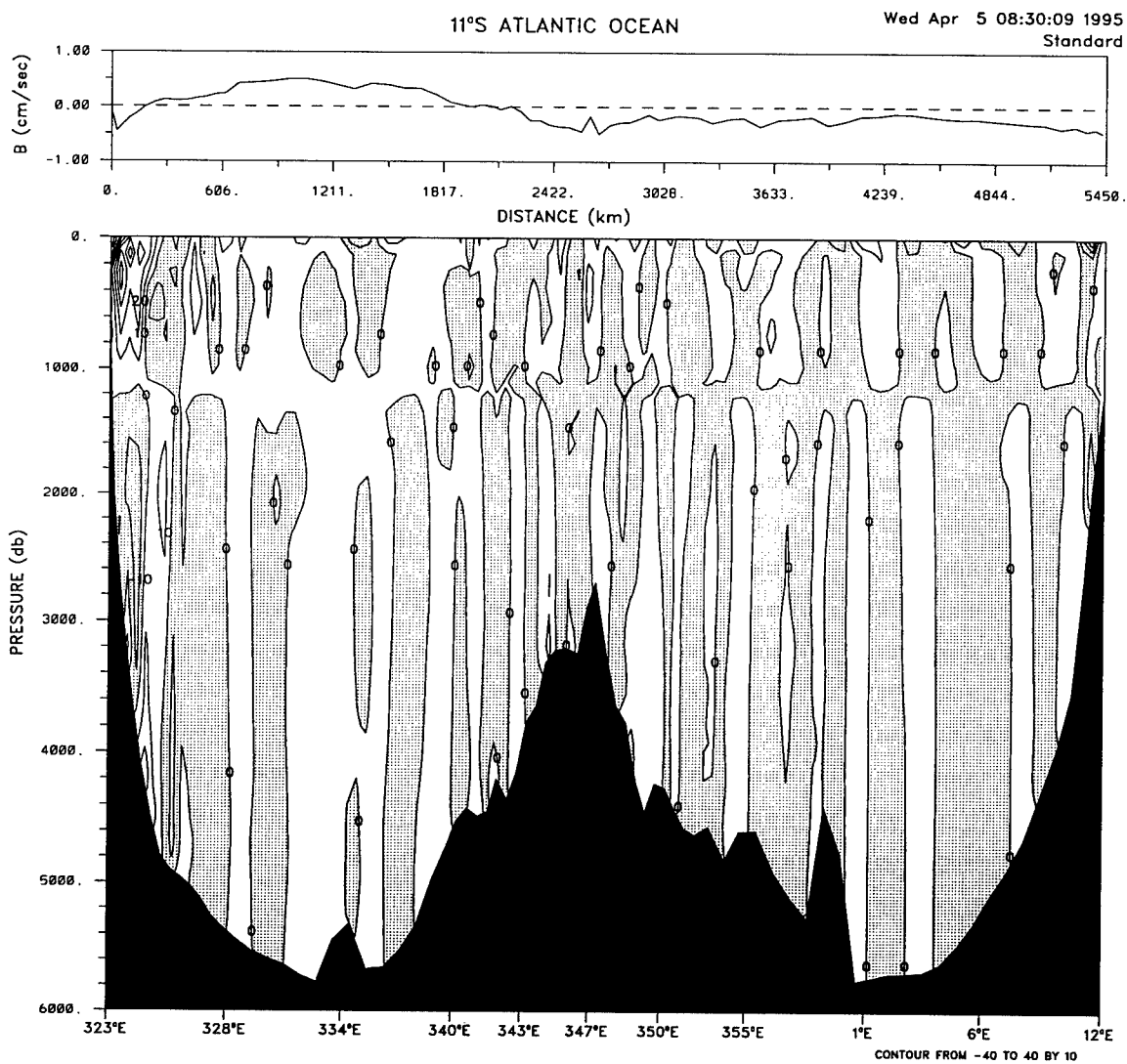


Figure 3.10f: The absolute velocity field across 11°S in the Atlantic, from the standard model. The hydrography comes from the Oceanus 133, leg 5, 1983 data set. The reference level velocities at $\sigma_1 = 32.16$ are displayed at the top of the figure.

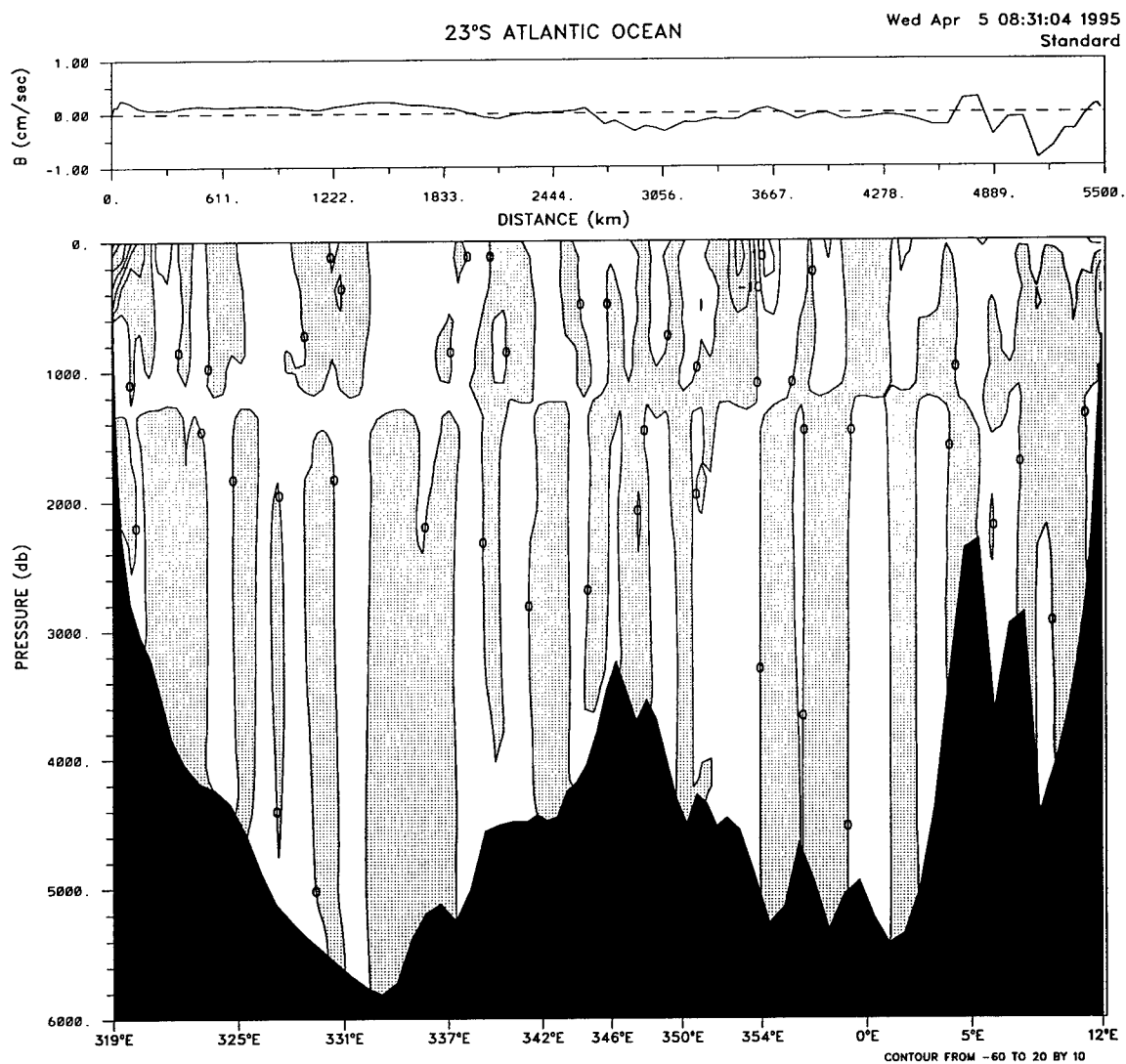


Figure 3.10g: The absolute velocity field across 23°S in the Atlantic, from the standard model. The hydrography comes from the Oceanus 133, leg 3, 1983 data set. The reference level velocities at $\sigma_1 = 32.16$ are displayed at the top of the figure.

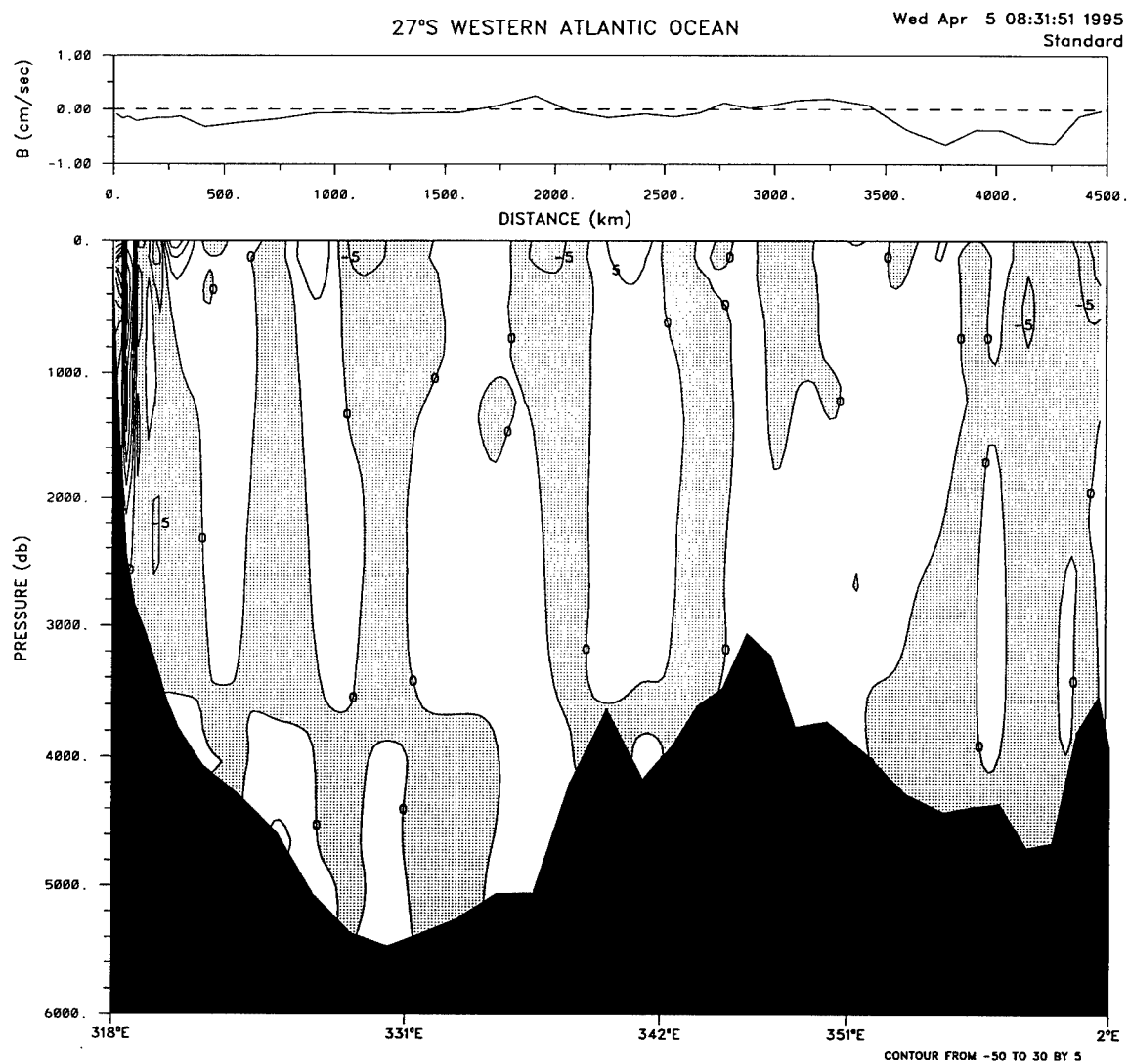


Figure 3.10h: The absolute velocity field across 27°S in the South Atlantic west of the Greenwich Meridian, from the standard model. The hydrography comes from the SAVE expedition legs 3 (1988) and 4 (1989). The reference level velocities at $\sigma_2 = 37.09$ are displayed at the top of the figure.

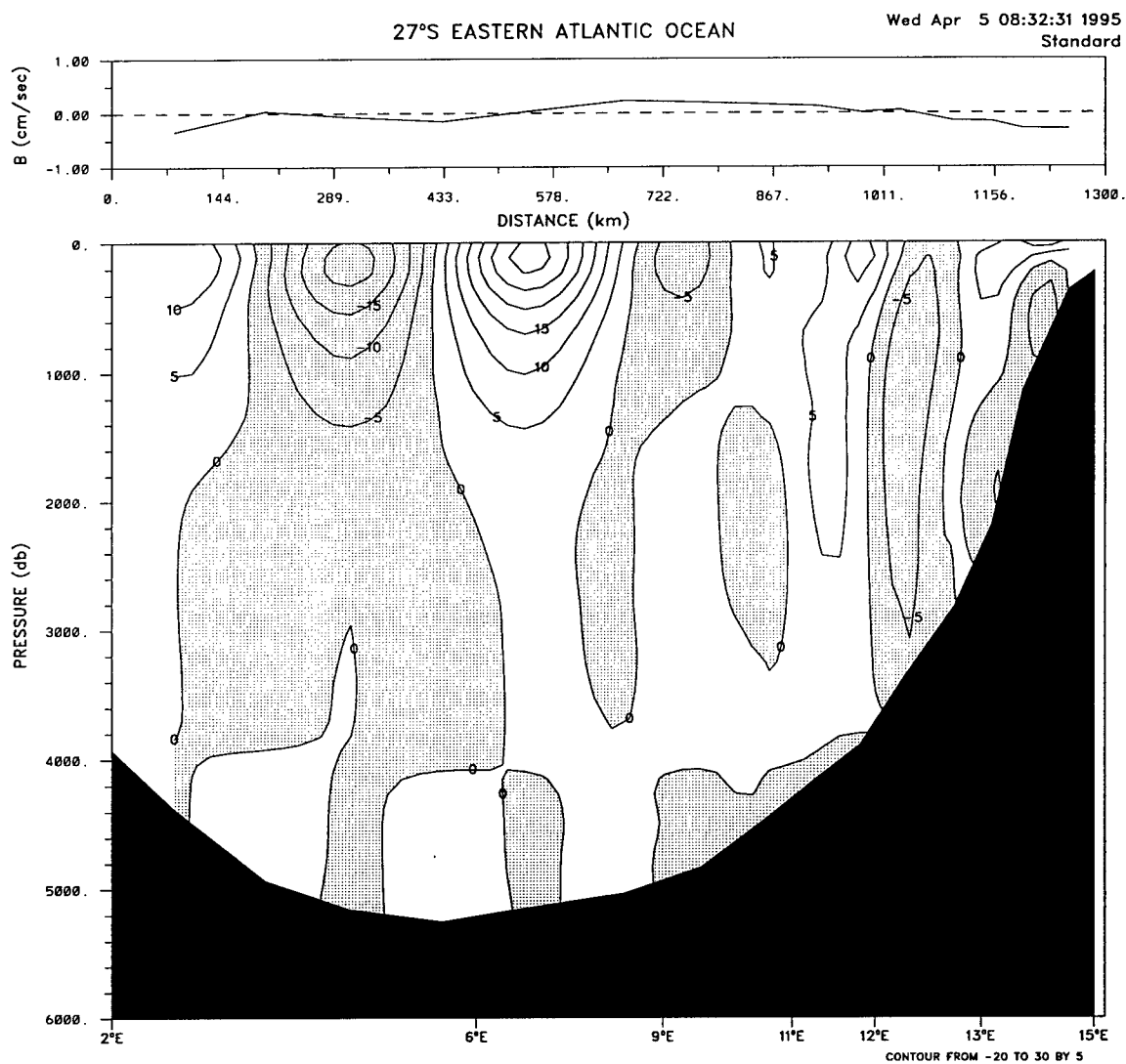


Figure 3.10i: The absolute velocity field across 27°S in the Atlantic east of the Greenwich Meridian from the standard model. The hydrography comes from the SAVE expedition legs 3 (1988) and 4 (1989). The reference level velocities at $\sigma_2 = 37.09$ are displayed at the top of the figure.

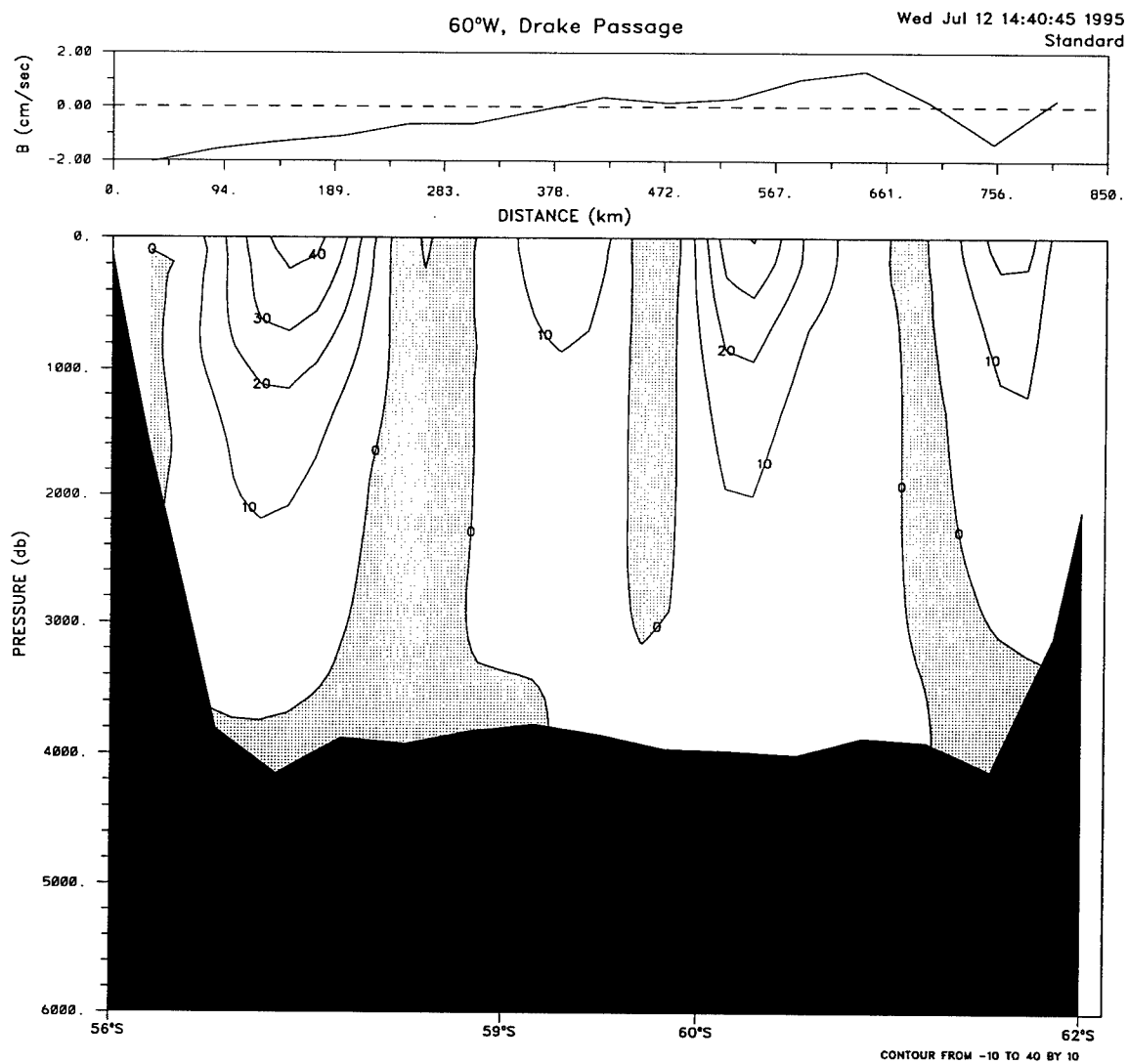


Figure 3.11a: The absolute velocity field across Drake Passage from the standard model. The hydrography comes from the Meteor 11/5 1990 data set. The reference level velocities at $\sigma_3 = 41.66$ are displayed at the top of the figure.

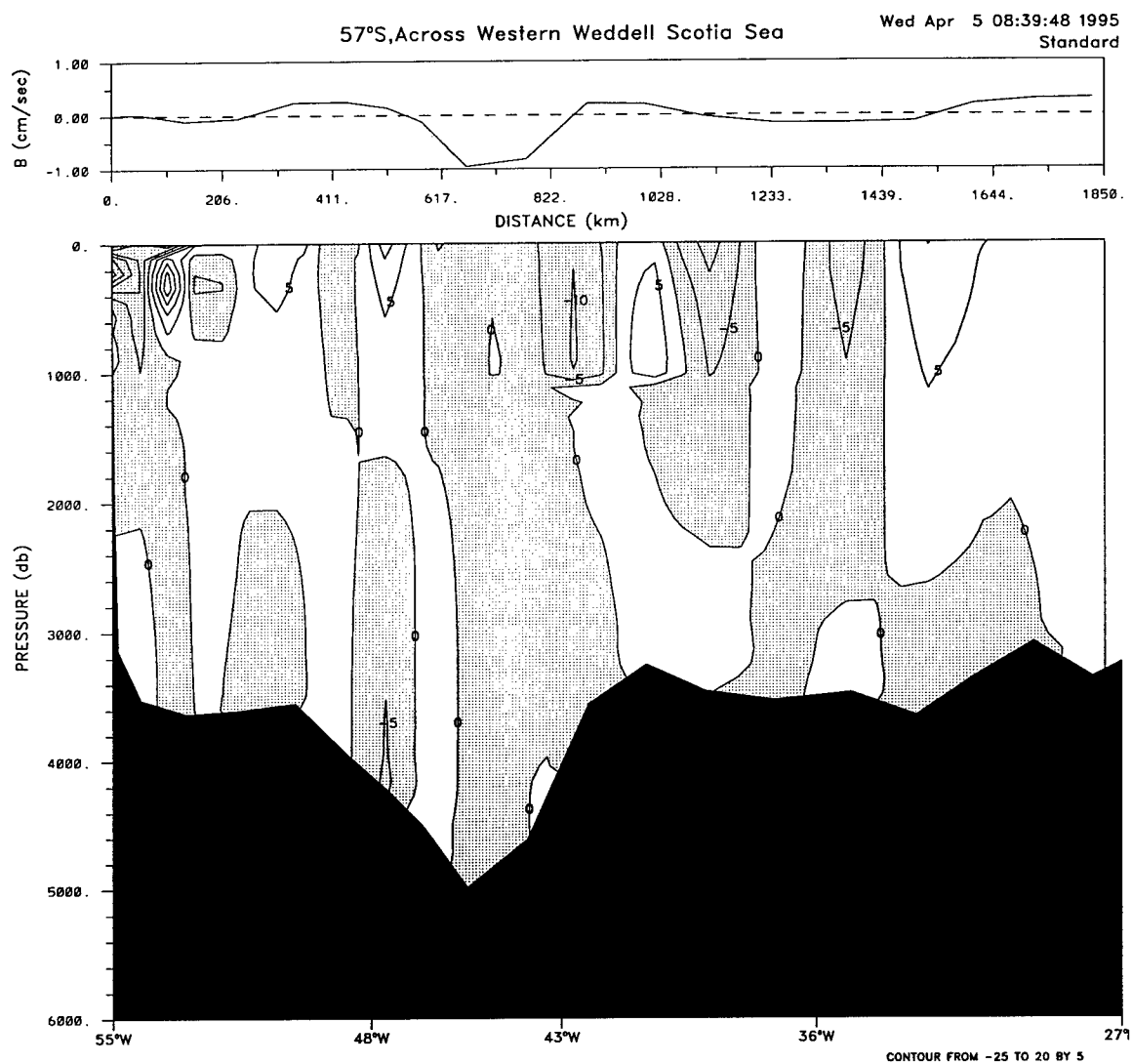


Figure 3.11b: The absolute velocity field across about 57°S in the Atlantic, bordering the western portion of the Weddell Sea, from the standard model. The hydrography comes from the AJAX 1983-84 cruise. The reference level velocities at $\sigma_3 = 41.65$ are displayed at the top of the figure.

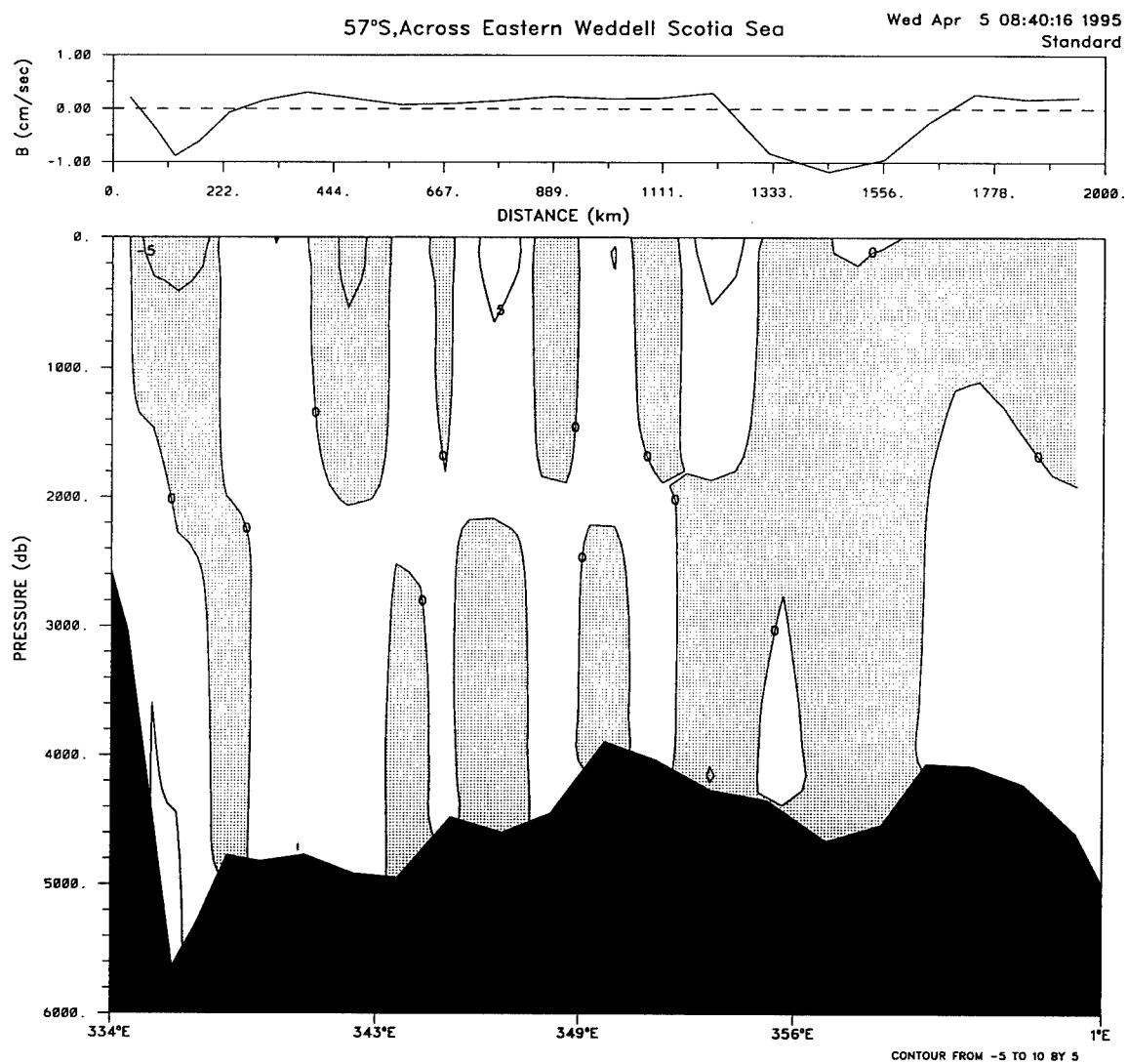


Figure 3.11c: The absolute velocity field across about 57°S in the Atlantic, bordering the eastern portion of the Weddell Sea, from the standard model. The hydrography comes from the Meteor 11/5 1990 cruise. The reference level velocities at $\sigma_3 = 41.65$ are displayed at the top of the figure.

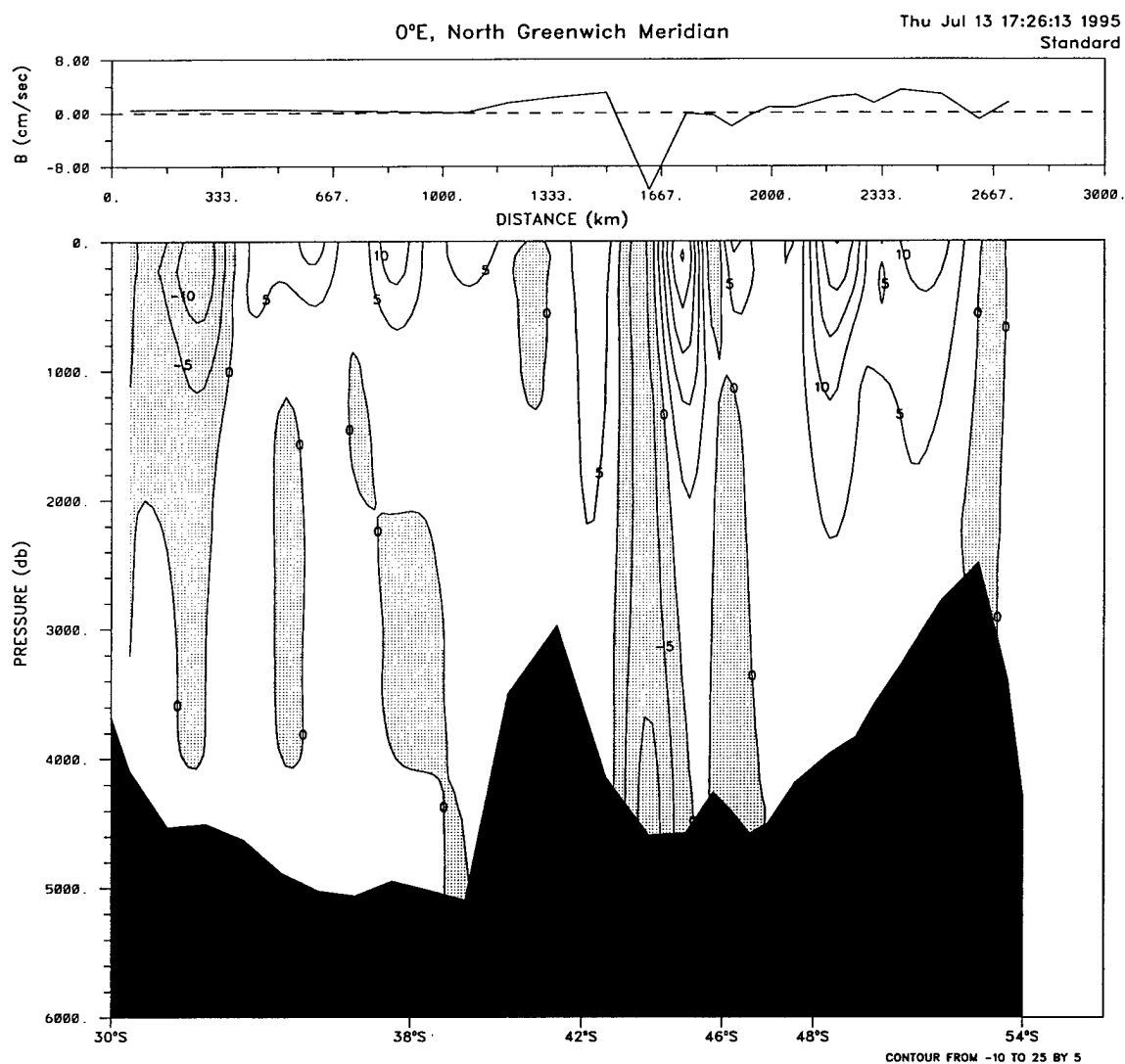


Figure 3.11d: The absolute velocity field across 0°E from 30°S to 55°S, from the standard model. The hydrography comes from the AJAX 1983–1984 data set. The reference level velocities at $\sigma_3 = 41.60$ are displayed at the top of the figure.

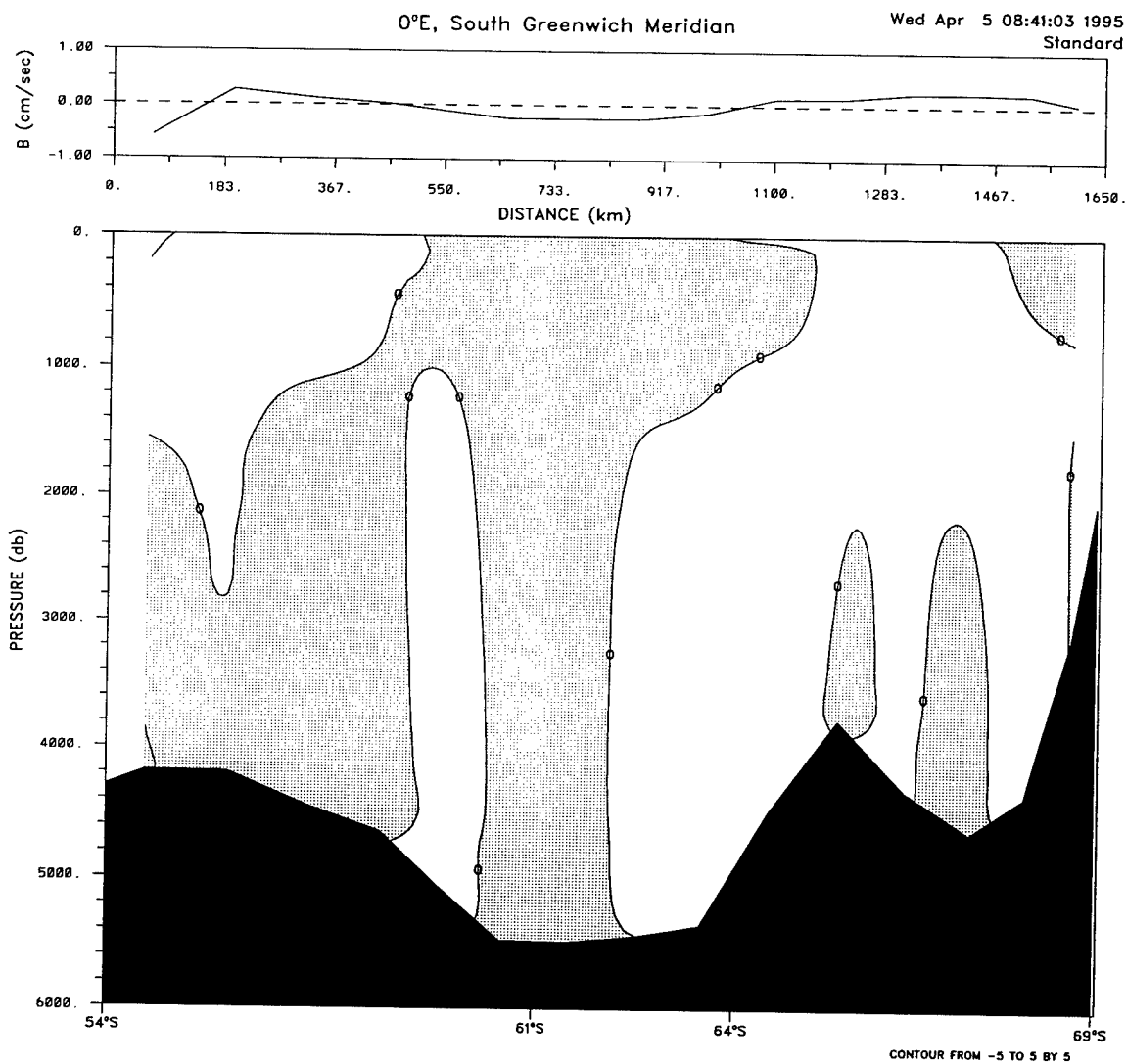


Figure 3.11: The absolute velocity field across 0°E 55°S to 70°S, from the standard model. The hydrography comes from the AJAX 1983–1984 data set. The reference level velocities at $\sigma_3 = 41.63$ are displayed at the top of the figure.

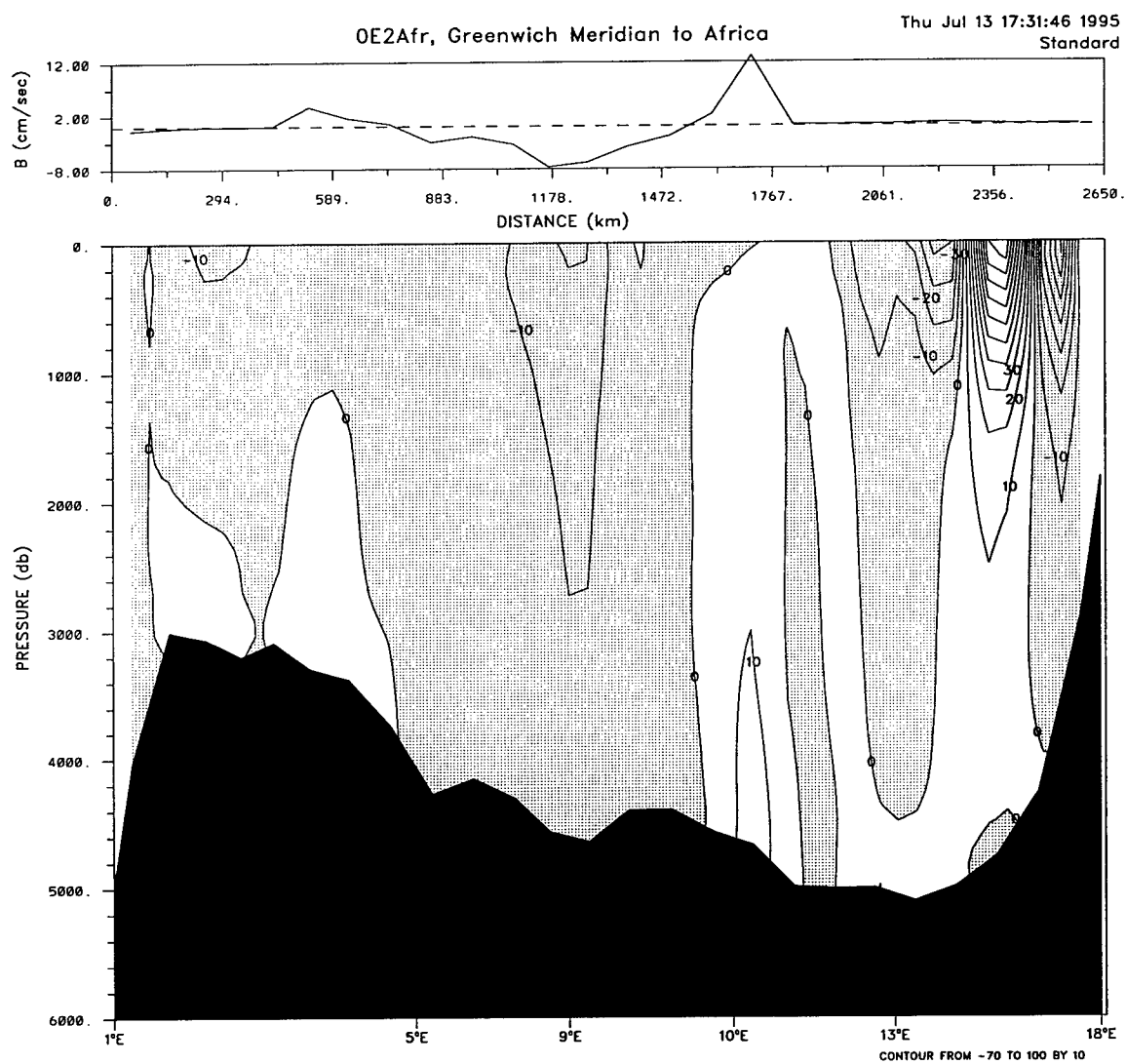


Figure 3.11f: The absolute velocity field along the Atlantic section running from the Greenwich Meridian at about 55°S to the South Africa. Note that in this section negative (shaded) values indicate motion towards the southeast. The results come from the standard model. The hydrography comes from the Meteor 11/5 1990 data set. The reference level velocities at $\sigma_3 = 41.60$ are displayed at the top of the figure.

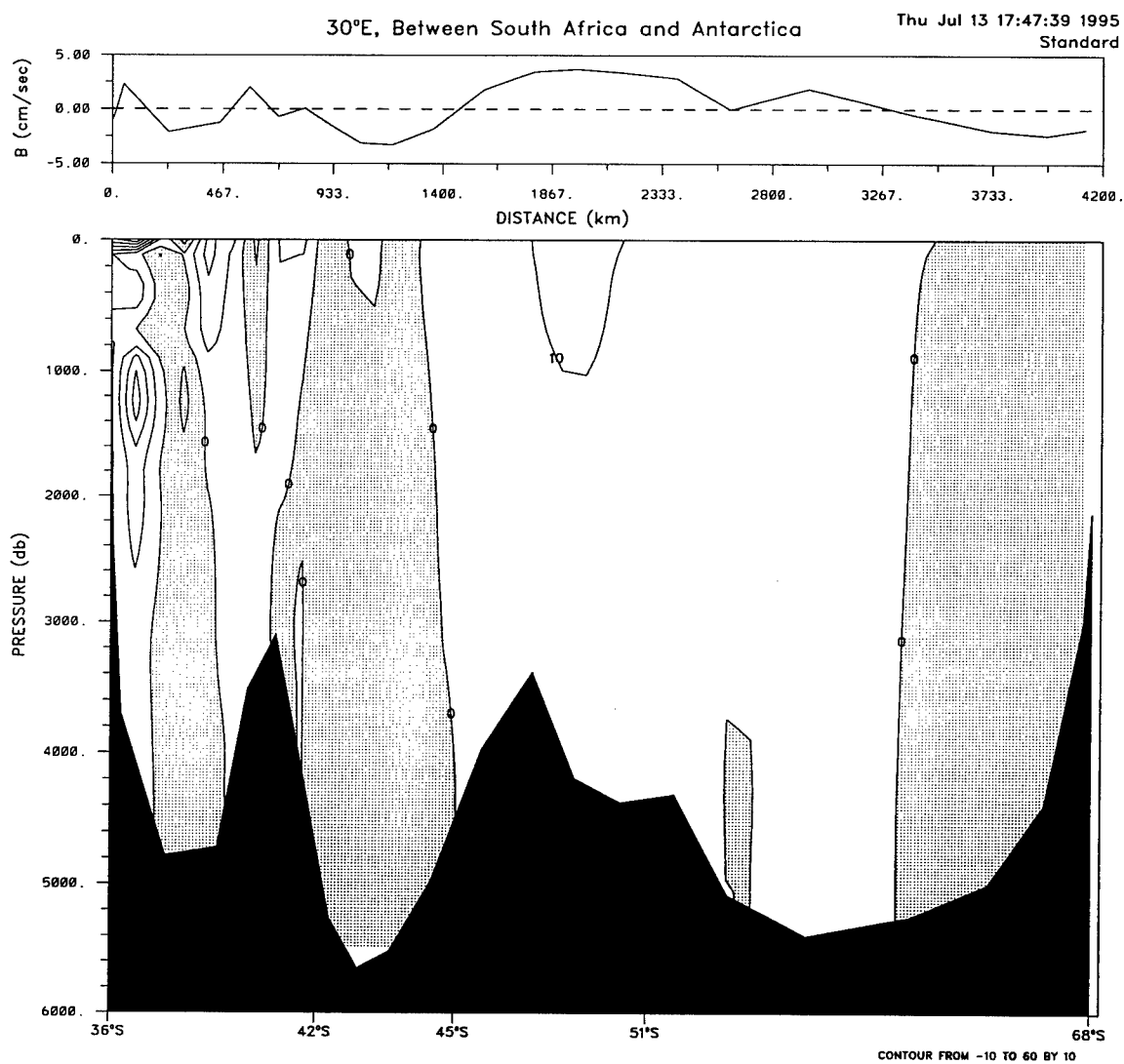


Figure 3.11g: The absolute velocity field across 30°E (south of South Africa) from the standard model. Southern Ocean Model, SOC.A. The hydrography comes from the Conrad 17, 1974 data set. The reference level velocities at $\sigma_4 = 46.14$ are displayed at the top of the figure.

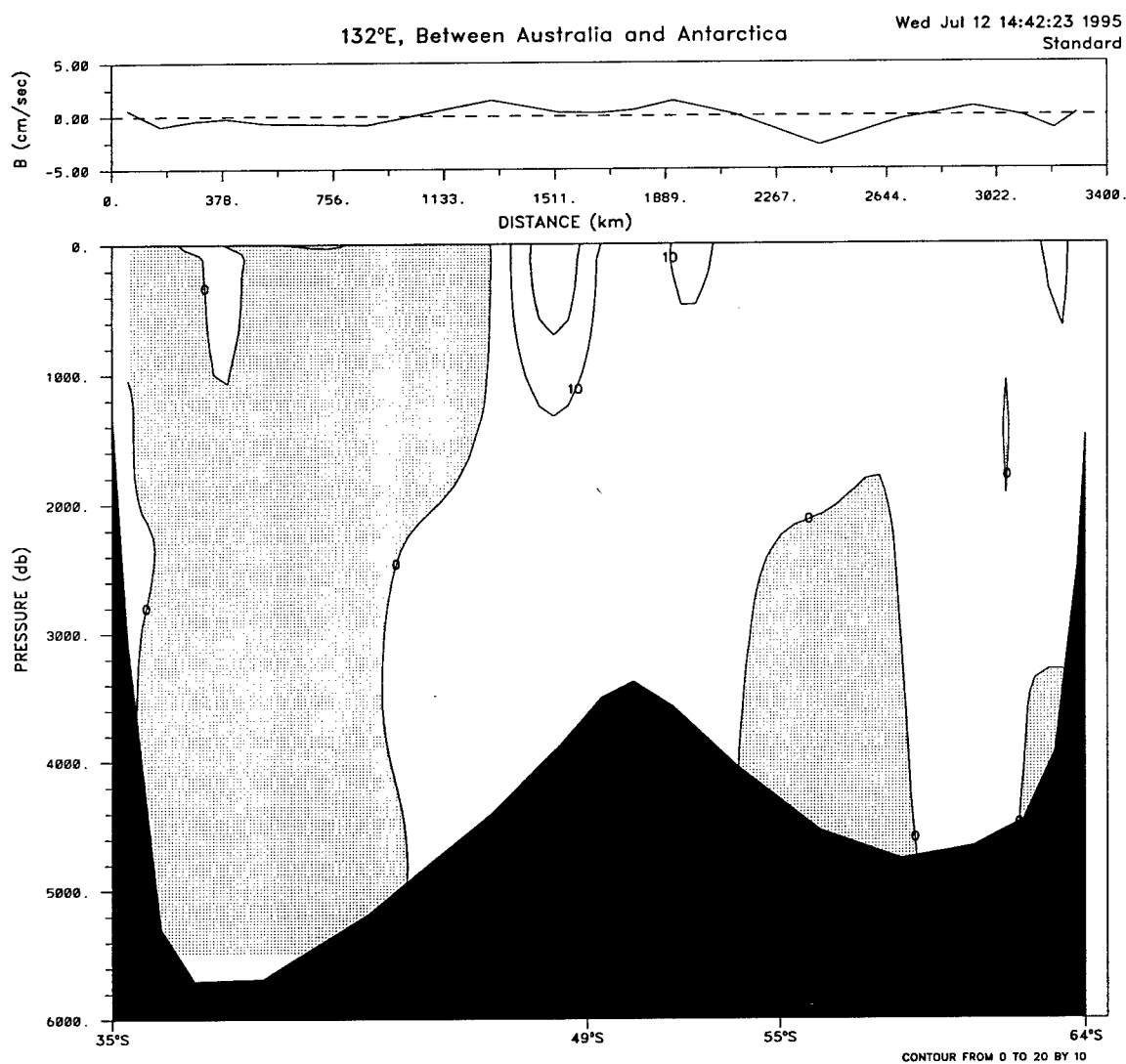


Figure 3.11h: The absolute velocity field across 132°E (south of Australia) from the standard model. The hydrography comes from the Eltanin 41, 1969 data set. The reference level velocities at $\sigma_4 = 46.14$ are displayed at the top of the figure.

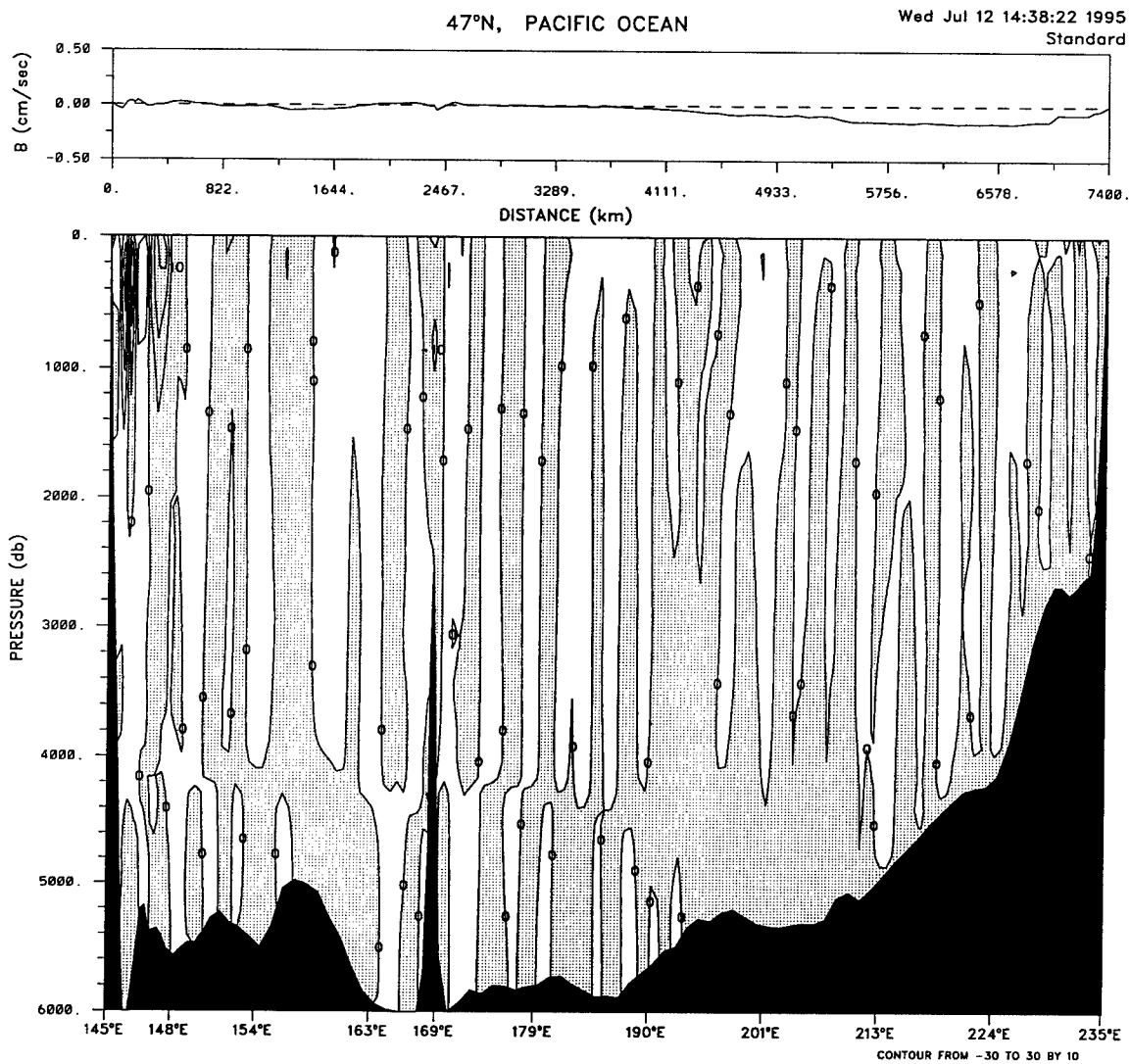


Figure 3.12a: The absolute velocity field across 47°N in the Pacific, from the standard model. The hydrography comes from the R.V. Thomas Thompson 1985 data set. The reference level velocities at $\sigma_4 = 45.87$ are displayed at the top of the figure.

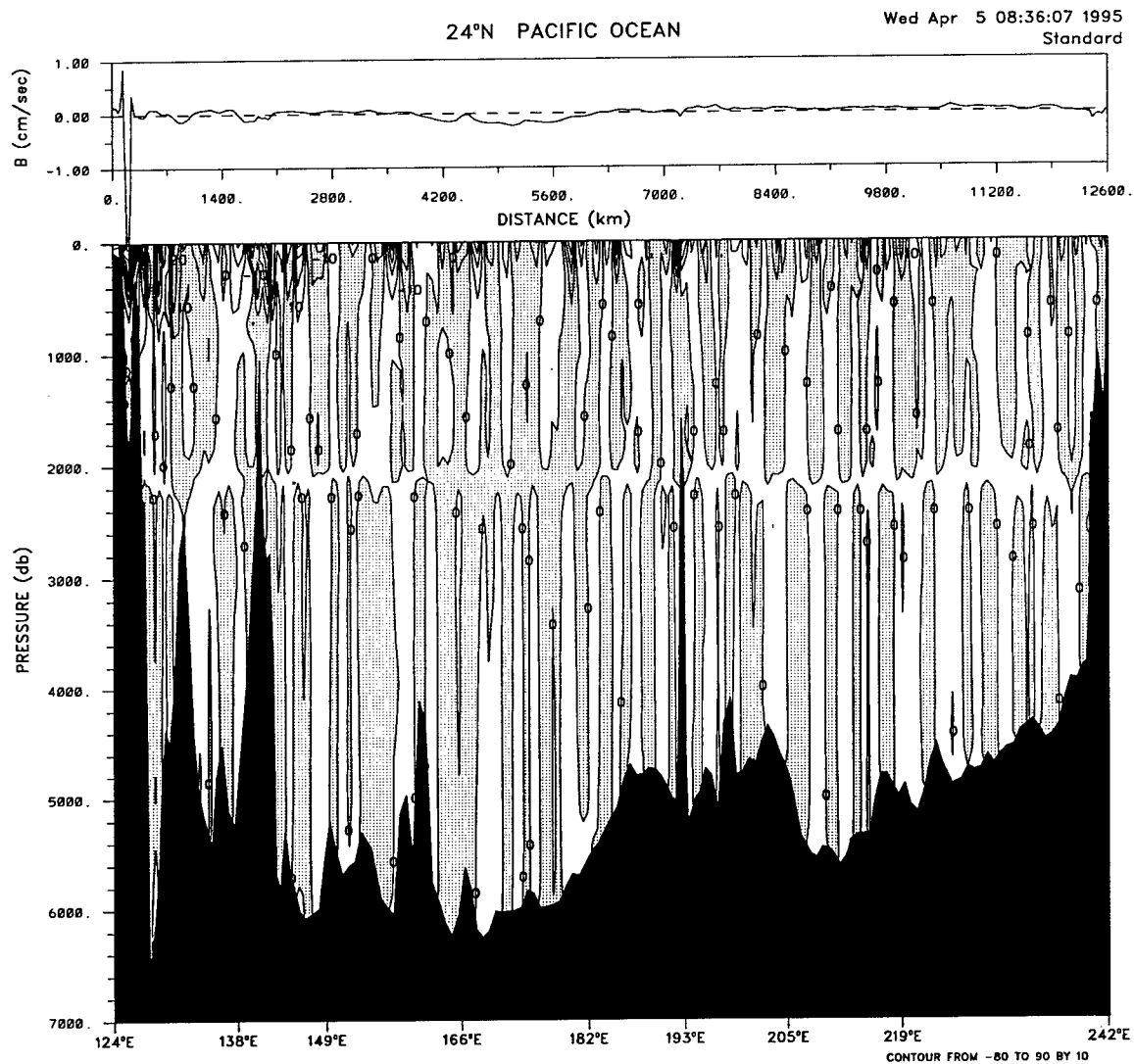


Figure 3.12b: The absolute velocity field across 24°N in the Pacific, from the standard model. The hydrography comes from the R.V Thomas Thompson 1985 data set. The reference level velocities at $\sigma_2 = 36.90$ are displayed at the top of the figure.

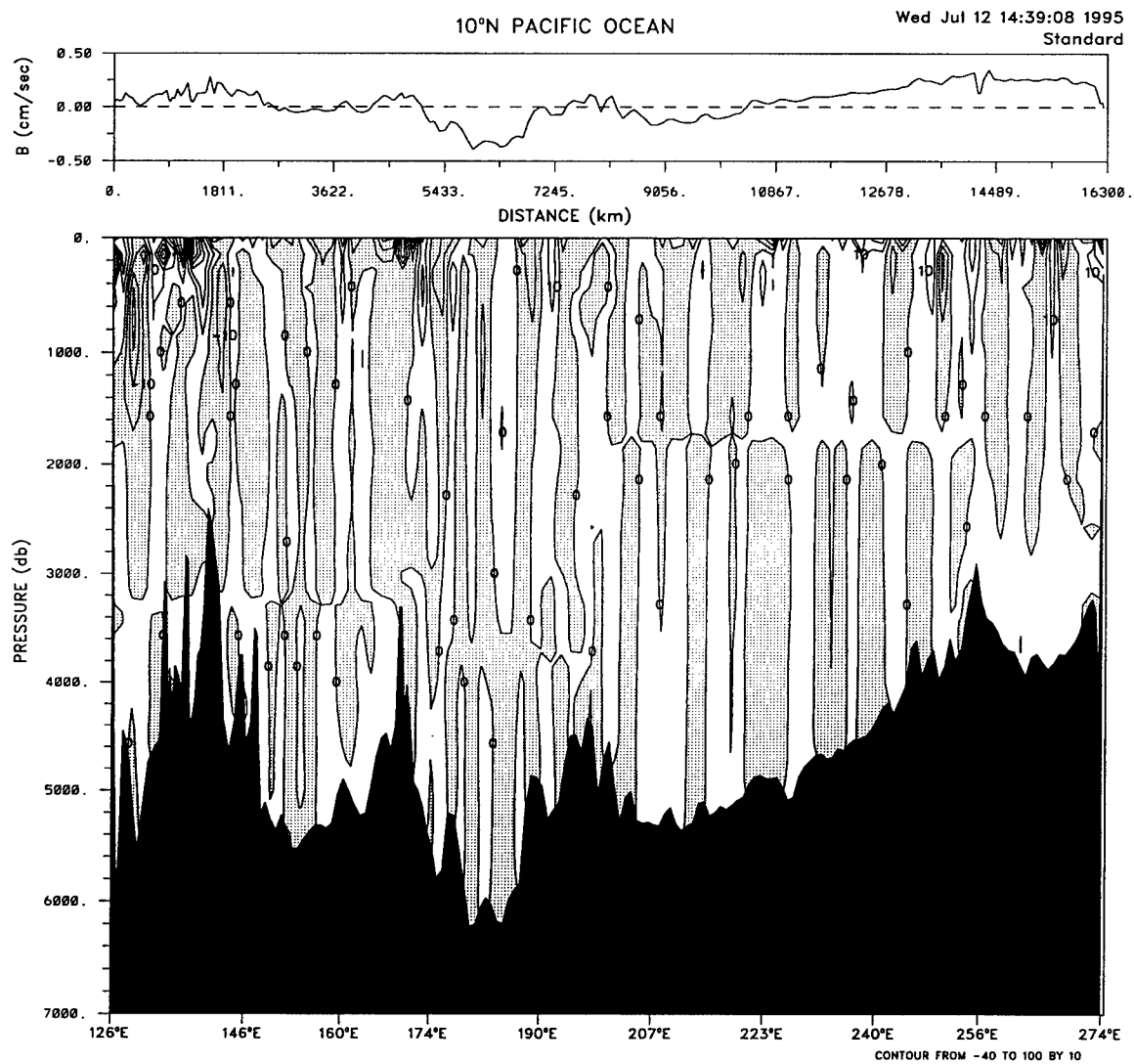


Figure 3.12c: The absolute velocity field across 10°N in the Pacific, from the standard model. The hydrography comes from the Moana Wave 1989 data set. The reference level velocities at the reference levels supplied by S. Wijffels (pers. comm.) are displayed at the top of the figure.

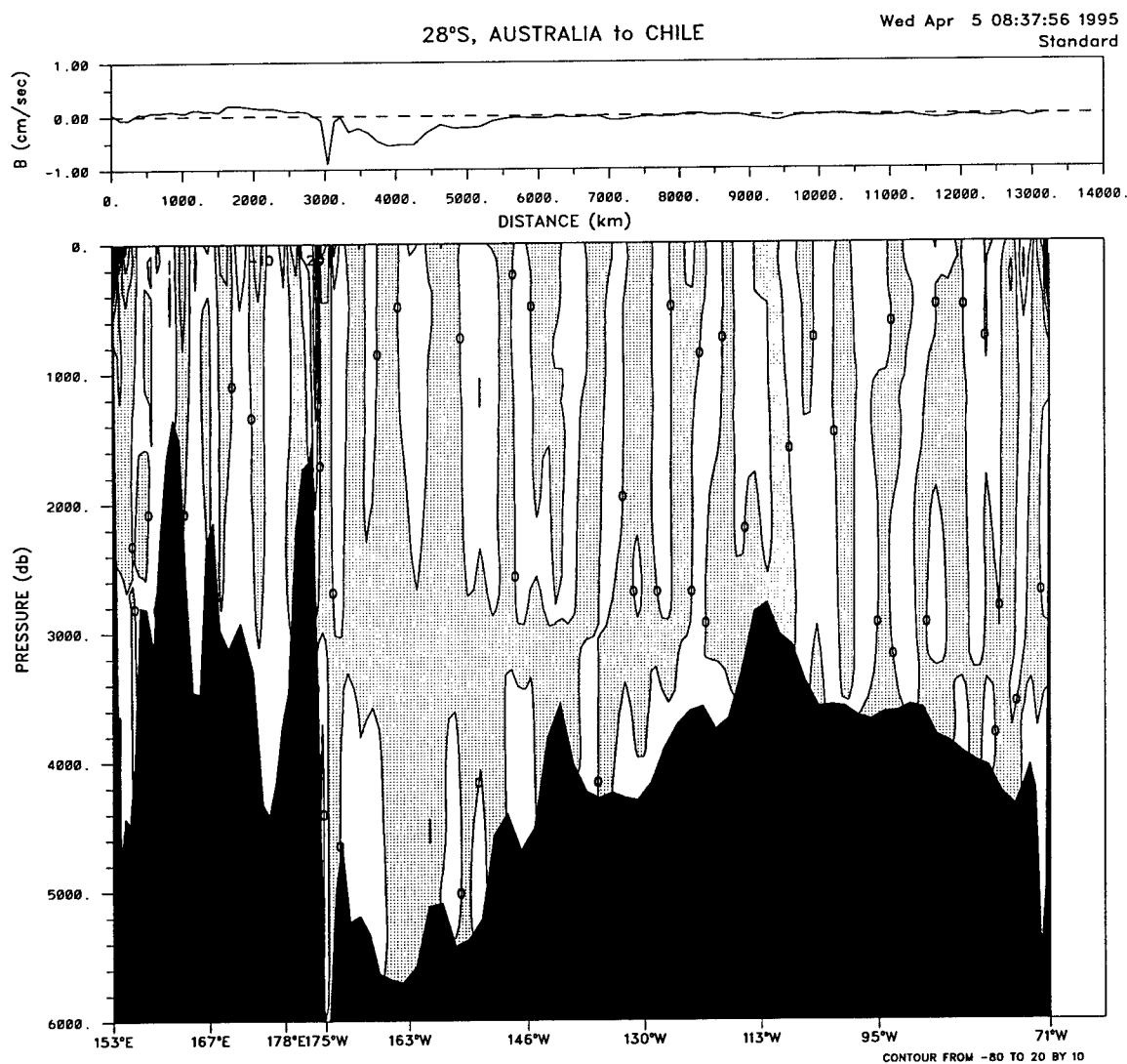


Figure 3.12d: The absolute velocity field across 28°S in the Pacific from the standard model. The hydrography comes from the Eltanin 29, SCORPIO 1967 data set. The reference level velocities at $\sigma_2 = 37.00$ are displayed at the top of the figure.

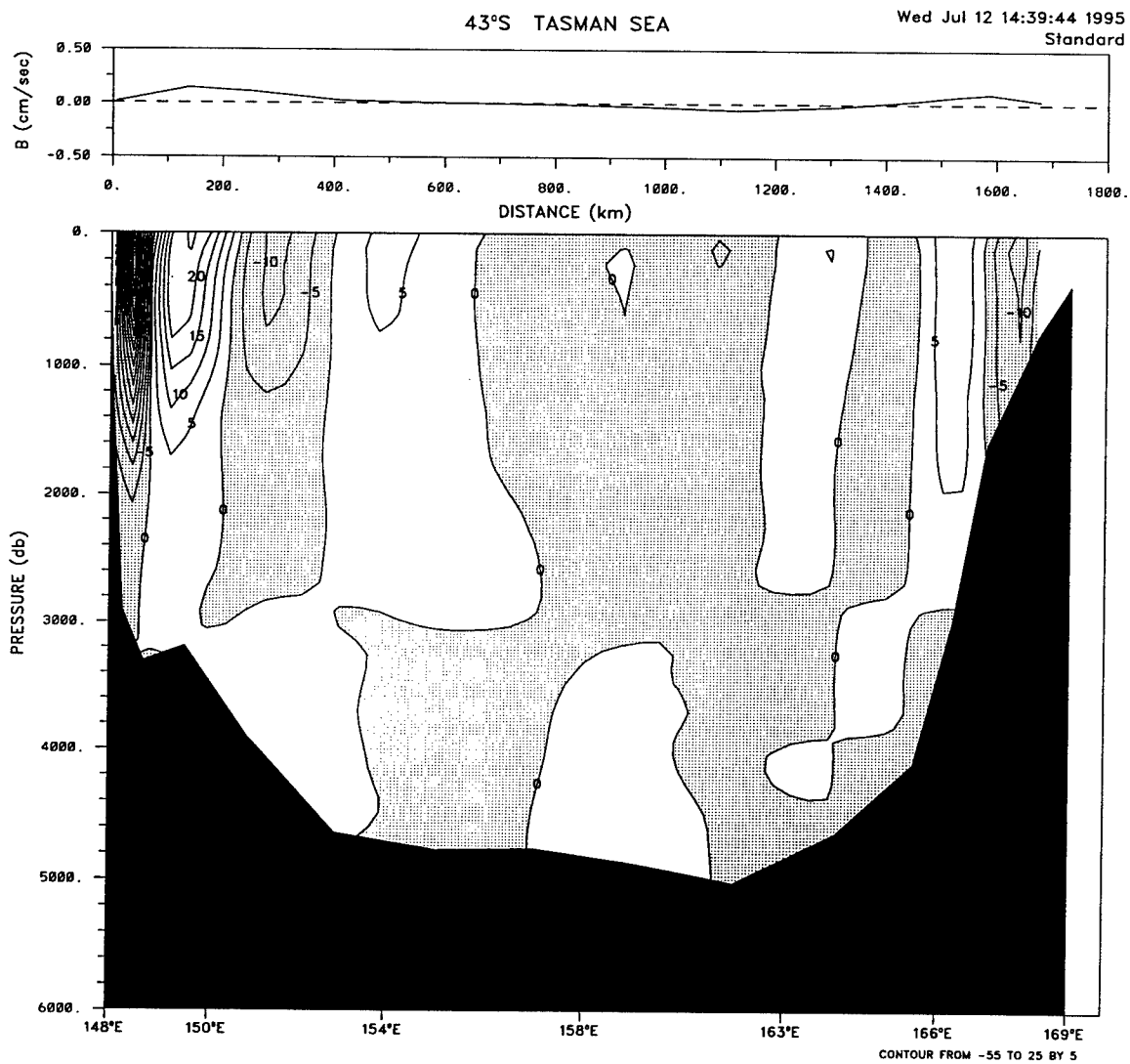


Figure 3.12d: The absolute velocity field across 43°S in the Pacific from Australia to New Zealand across the Tasman Sea, from the standard model. The hydrography comes from the first leg of the Eltanin 28 SCORPIO transect performed in 1967. The reference level velocities at $\sigma_2 = 37.09$ are displayed at the top of the figure.

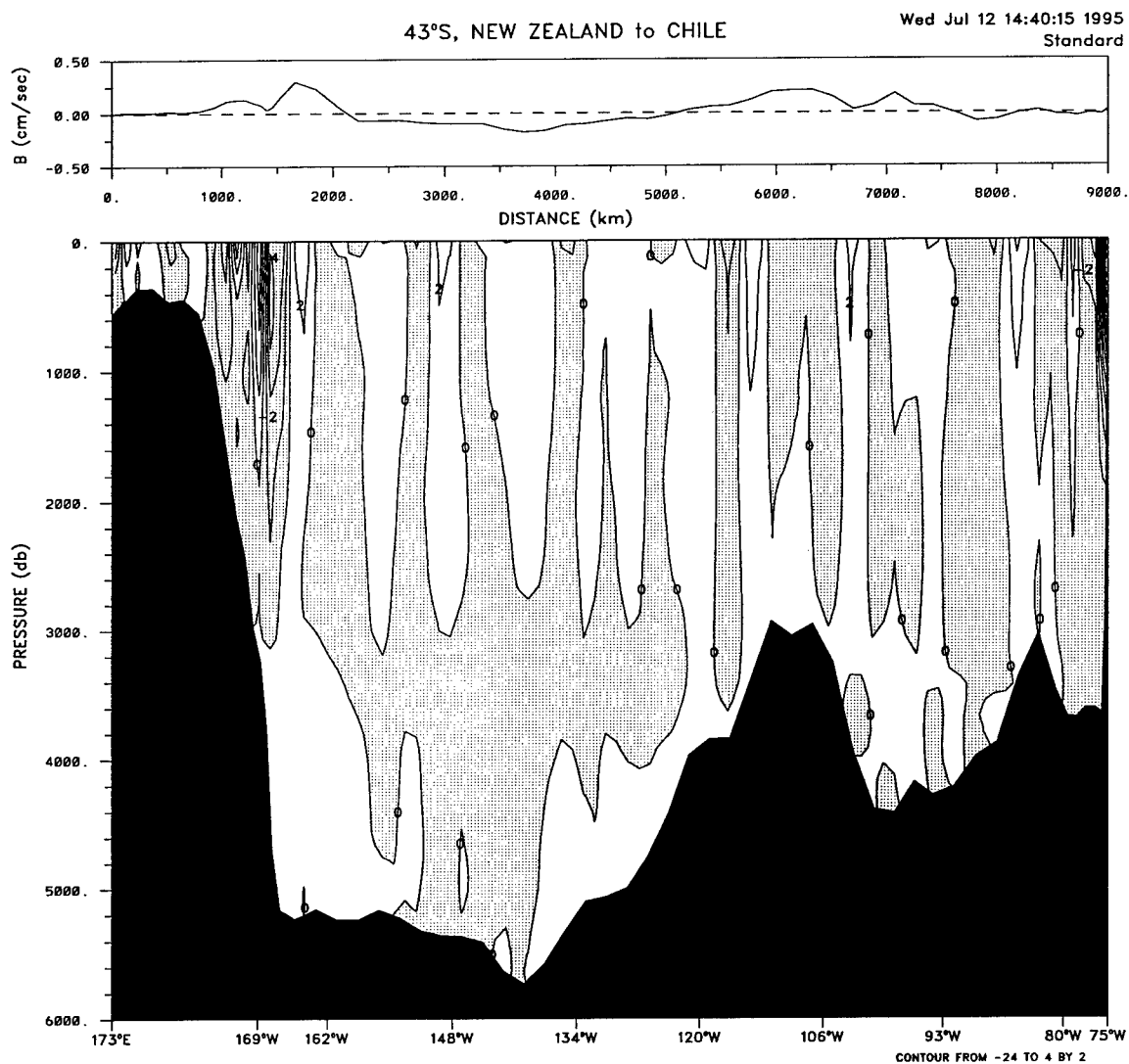


Figure 3.12e: The absolute velocity field across 43°S in the Pacific from New Zealand to Chile, from the standard model. The hydrography comes from the second leg of the Eltanin 28 SCORPIO transect performed in 1967. The reference level velocities at $\sigma_2 = 37.09$ are displayed at the top of the figure.

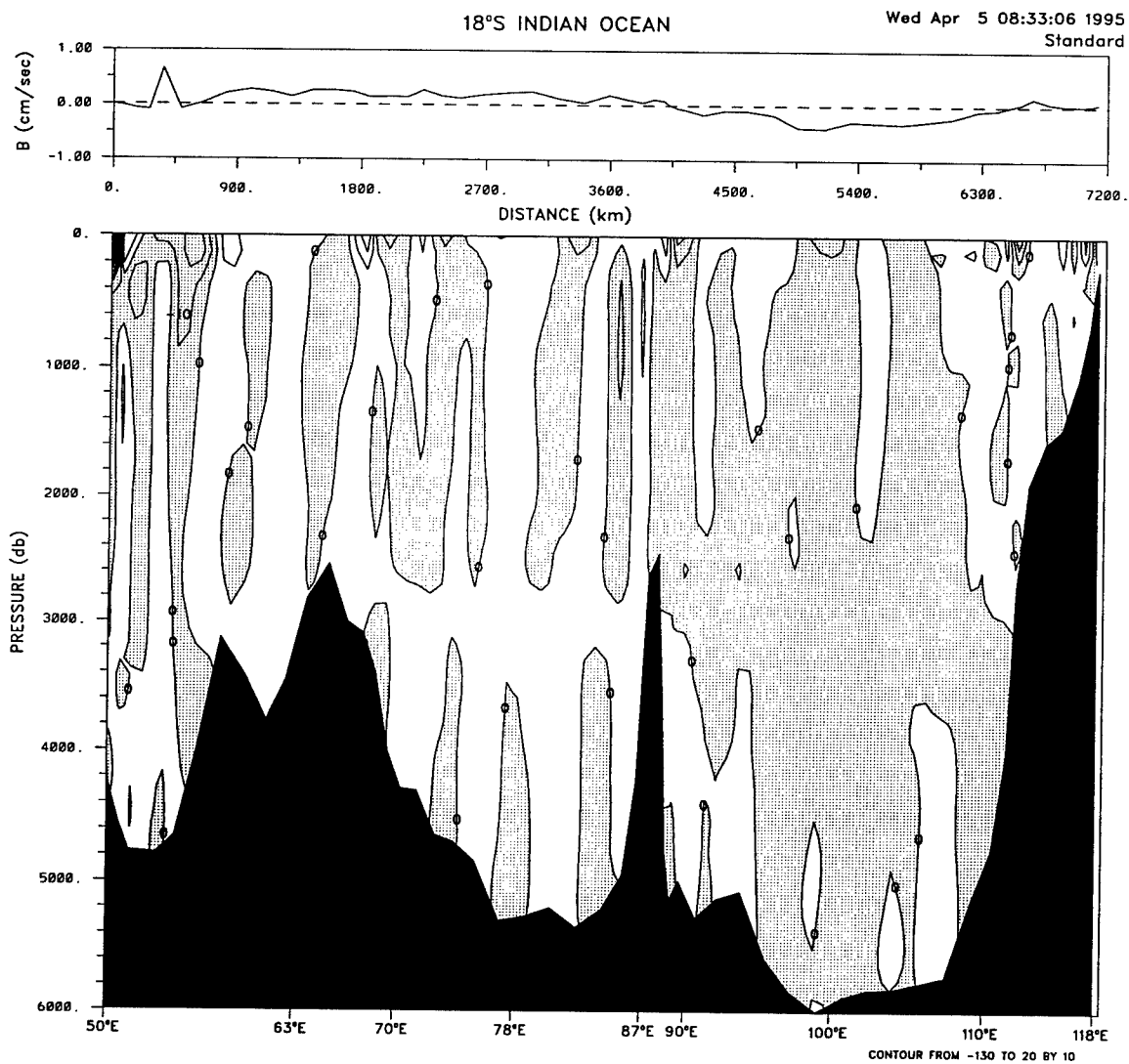


Figure 3.13a: The absolute velocity field across 18°S in the Indian Ocean from the standard model. The hydrography comes from the Atlantis 93, 1976 data set. The reference level velocities at $\sigma_4 = 45.85$ are displayed at the top of the figure.

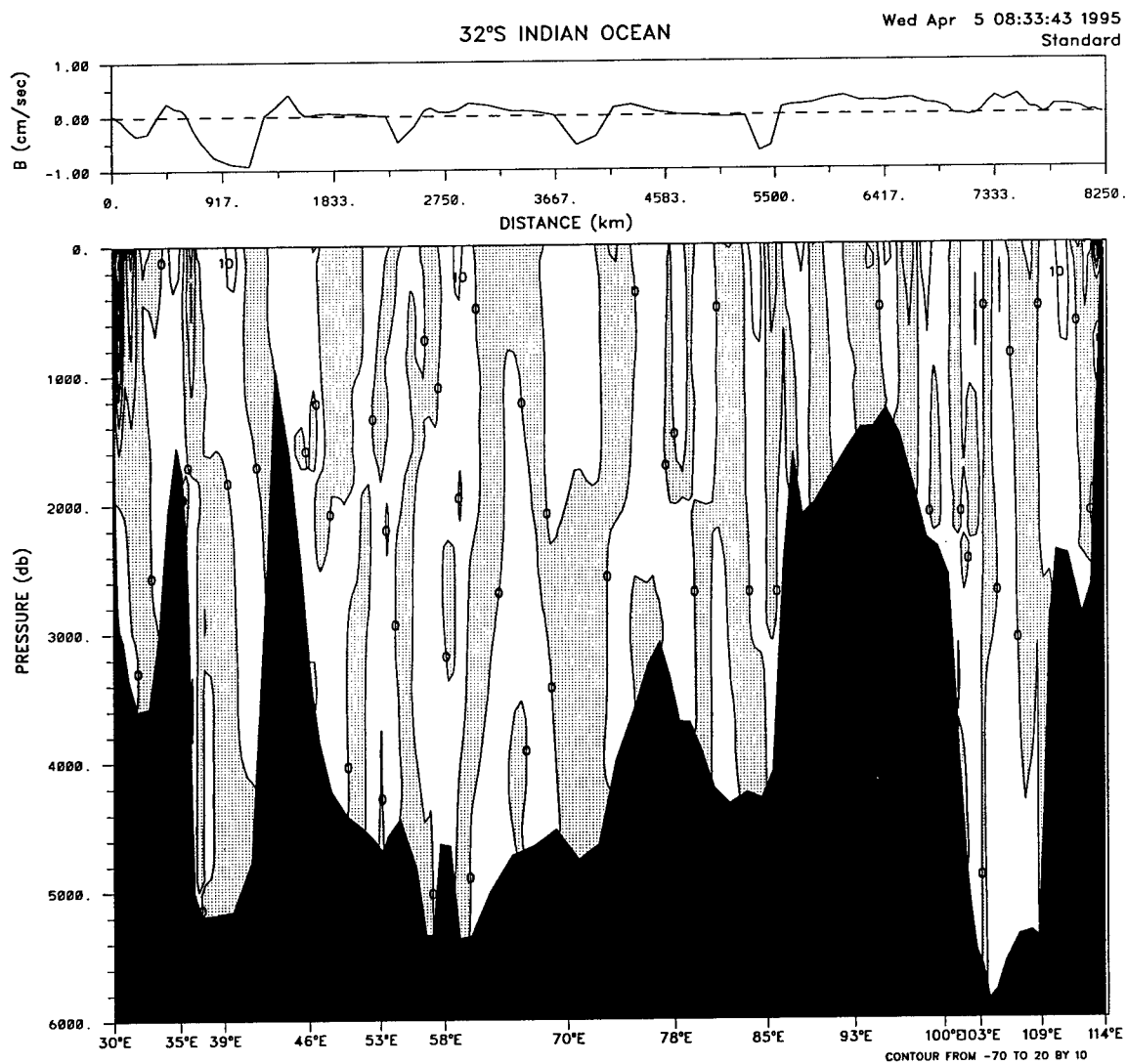


Figure 3.13b: The absolute velocity field across 32°S in the Indian Ocean from the standard model. The hydrography comes from the RRS Charles Darwin 29, 1987 data set.. The reference level velocities at the reference levels supplied by J. Toole (pers comm.) are displayed at the top of the figure.

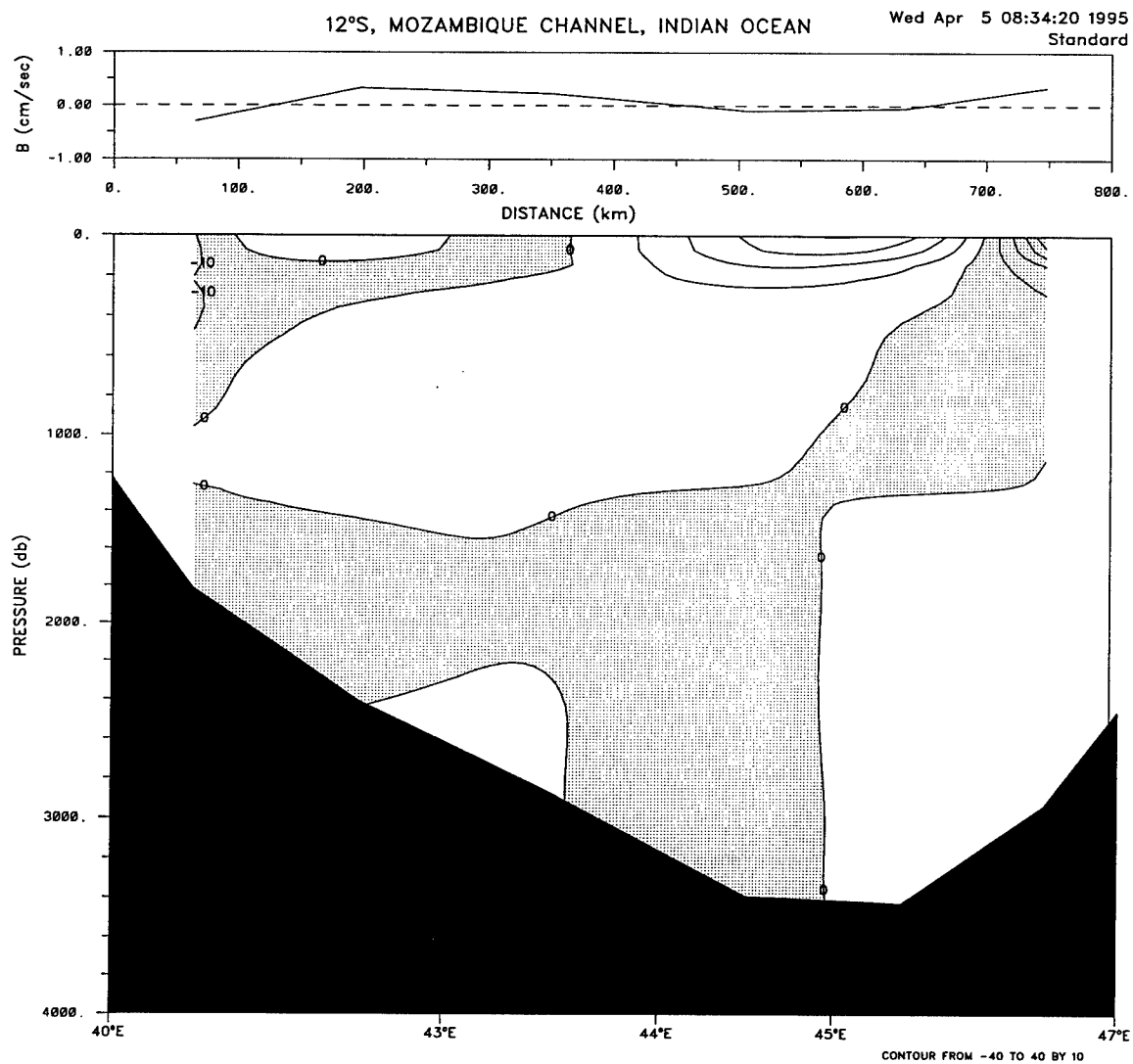


Figure 3.13c: The absolute velocity field across 12°S in the Mozambique Channel from the standard model. The hydrography comes from an Australian NODC data set. These data were taken in 1965. The reference level velocities at $\sigma_1 = 32.16$ (12°S) and $\sigma_0 = 27.4$ (15°S) are displayed at the top of the figures.

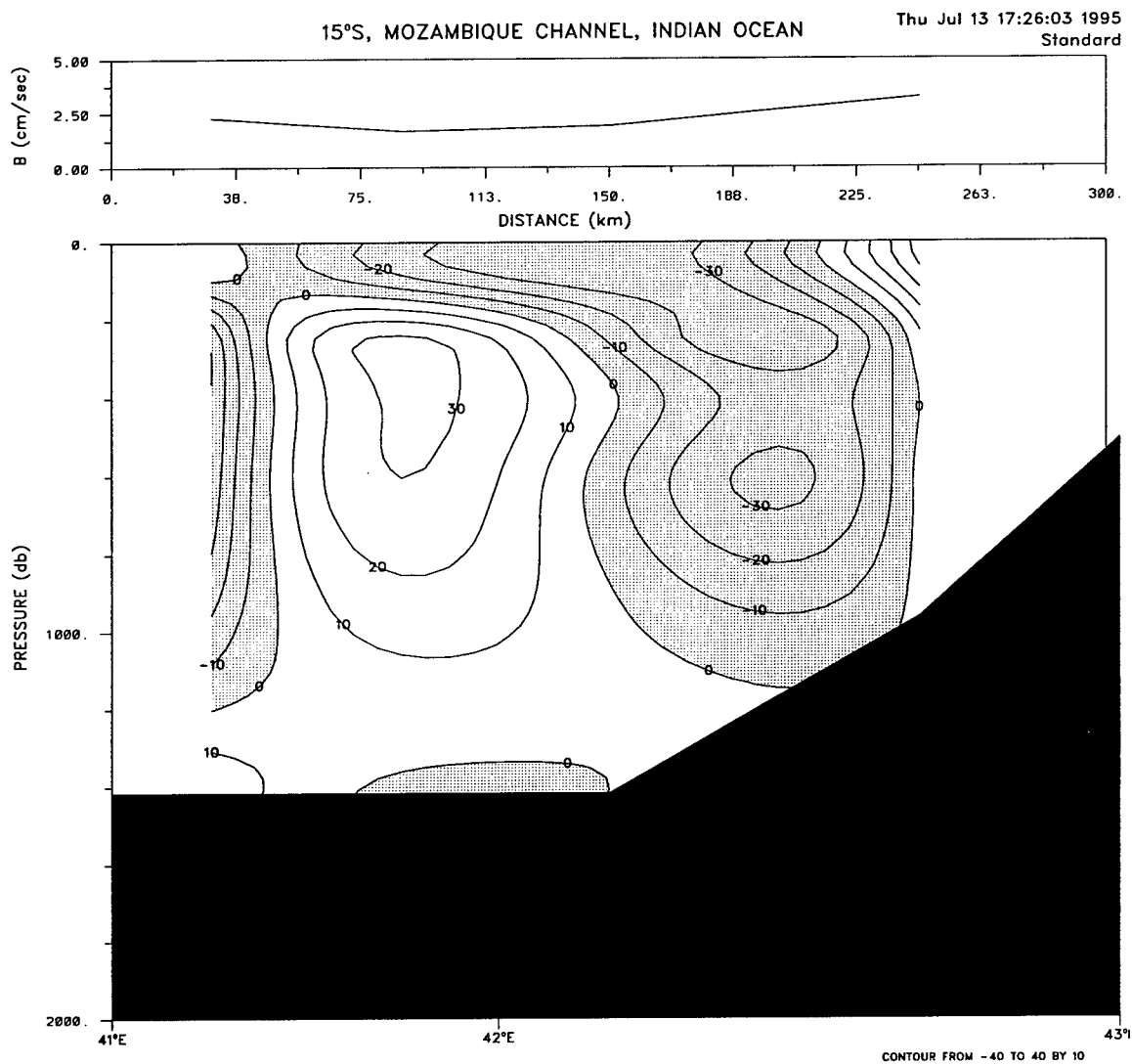


Figure 3.13d: The absolute velocity field across 15°S (bottom) in the Mozambique Channel from the standard model. The hydrography comes from an Australian NODC data set. These data were taken in 1965. The reference level velocities at $\sigma_1 = 32.16$ (12°S) and $\sigma_0 = 27.4$ (15°S) are displayed at the top of the figures.

Section	Mass (10 ⁹ kg/s)	Salt (10 ⁶ kg/s)	Oxygen (10 ⁹ ml)/s	Phosphate (kmol/s)	Silicate (kmol/s)	PO38 (kmol/s)
#A48N	-1.0	-27	-34	-6	-128	-2304
	1.3	45	8	2	26	577
#A36N	-1.0	-27	-73	13	-64	-1420
	1.1	40	7	2	45	495
#Flst	30.1	1085	114	16	171	7303
	0.5	17	2	1	7	138
#A24N	-31.1	-1114	-172	-21	-429	-10540
	1.3	44	8	2	72	514
#A11N	-19.7	-695	-97	-23	-437	-7529
	1.9	65	10	3	74	799
#A11S	-1.1	-27	-9	-13	-322	-2146
	1.2	40	7	2	93	525
#A23S	-0.7	-27	-13	-1.4	-45	-769
	1.1	37	6	3	100	504
#A27S_W	-28.0	-982	-144	-36	-575	-11350
	3.0	105	15	5	153	1354
#A27S_E	27.3	955	133	28	303	9831
	2.8	97	13	5	110	1238
#A57S_W	-4.4	-154	-21	-12	-710	-2571
	11.2	389	60	26	1352	6252
#A57S_E	4.4	153	29	10	694	2719
	11.2	387	58	26	1340	6130
#OE2Afr	142.7	4900	773	311	8674	77410
	4.6	160	23	12	651	2515
#OE_N	167.4	5769	886	341	9485	86590
	5.2	180	27	12	737	2730
#OE_S	0.0	-1	1	-1	-251	-78
	1.0	35	6	2	130	563

Table 3.5: Net horizontally and vertically integrated property fluxes across hydrographic sections, from the standard model. The first row for each section contains the property fluxes with the Ekman component included. These Ekman components are those corrected to balance the salt equations (see Section 3.4.6) and are listed in Table 3.18. The second row contains the uncertainty in transport due to the uncertainty in the reference level velocities. These values should be considered underestimates of the total uncertainty. The standard model heat and temperature transport estimate estimates are given in Table 3.21.

Section	Mass (10 ⁹ kg/s)	Salt (10 ⁶ kg/s)	Oxygen (10 ⁹ ml)/s	Phosphate (kmol/s)	Silicate (kmol/s)	PO38 (kmol/s)
#P47N	0.6	27	-31	12	473	315
	1.4	47	8	4	244	759
#P24N	0.6	27	-37	8	402	-479
	1.3	45	11	5	289	683
#P10N	0.8	27	0	1	278	169
	1.7	60	18	7	268	843
#P28S	9.6	327	93	9	369	5404
	6.9	239	32	16	665	3413
#P43S	9.6	327	82	7	352	4649
	7.1	244	32	16	660	3568
#Mz_N	0.3	10	1	1	87	207
	1.6	55	5	3	126	688
#Mz_S	0.2	6	-6	5	55	386
	1.2	41	4	2	61	488
#I18S	-8.8	-306	-24	4	930	-532
	6.5	227	26	15	684	3167
#I32S	-8.3	-300	1	9	653	1299
	6.7	231	30	14	602	3224
#Drake	141.1	4861	724	304	9203	74290
	3.4	119	17	8	620	1845
#30E	143.7	4945	740	317	10530	76830
	4.7	163	67	24	1546	3032
#132E	151.2	5206	797	309	8346	78180
	7.9	275	42	19	1114	4369

Table 3.5 continued:

3.4 The Standard Model Results

The station pairs in the standard model represent 1600 unknowns. Another 269 unknowns represent the cross-isopycnal transfer between the layer interfaces of the eighteen areas. The constraints described in the previous section provide 973 equations which can be used to solve for the total 1869 formal unknowns, as well as the 973 noise unknowns (Equation 2.3). The solutions are given by Equations 2.15. The resulting reference level velocities and their associated absolute velocity fields are illustrated in the previous section, Figures 3.10 through 3.11.

Although the magnitude and character of the reference level velocities varies from section to section, the rms reference level velocities² for most of the sections are less than the initial order of magnitude estimates (1 cm s^{-1} for most station pairs, 10 cm s^{-1} in the vicinity of strong deep currents). There are two exceptions. The first occurs in the southern section in the Mozambique Channel (Figure 3.13d) where the larger reference level velocity estimates ($b_{rms} = 2.3 \text{ cm s}^{-1}$) are likely an effect of the highly variable currents and shallow topography in the region.

The second place where the reference level velocities ($b_{rms} = 13.9 \text{ cm s}^{-1}$) are somewhat larger than the initial order of magnitude estimate (10 cm s^{-1}) is in the Florida Straits (Figure 3.10c). These larger reference level velocities are a direct result of the flux constraint ($31 \pm 0.5 \times 10^9 \text{ kg s}^{-1}$) placed on the flow. The model produced a transport of $30.2 \pm 0.5 \times 10^9 \text{ kg s}^{-1}$, not quite meeting the specified constraint, but lying well within the $31 \pm 2 \times 10^9 \text{ kg s}^{-1}$ suggested by *Schmitz and Richardson* [1991]. In earlier test models which relaxed the constraint to the $\pm 2 \times 10^9 \text{ kg s}^{-1}$, model transports of about $27 \times 10^9 \text{ kg s}^{-1}$ were obtained, with smaller reference levels velocities ($b_{rms} = 6.7 \text{ cm s}^{-1}$). It is therefore apparent that the Florida Strait reference level velocities

²Rms values for the velocities at the reference levels are only intended to indicate magnitude. They do not imply anything about the statistics of the values.

are extremely sensitive to the initial estimate of net transport through the section. *Rintoul* [1988] used the same data at 24°N, at 36°N and in the Florida Straits and applied a $30 \times 10^6 \text{ m}^3 \text{ s}^{-1}$ constraint to #FlSt transport. He obtained rms reference level velocities for the #FlSt section of 9.8 cm s^{-1} . It appears that his model used increased reference levels velocities at the eastern end of the section to reverse the direction of the southward flow, thereby presumably obtaining the necessary transport to meet the applied constraint. Why the standard model does not do the same is not known, but the reason is likely related choice of model columns weights. Except for the odd station pair in #A57S_E, #0E2Afr and #0EN, none of the sections other than #FlSt and #Mz_S contain reference level velocities which are significantly different from zero.

The initial order of magnitude estimates for the vertical transfer terms were $1 \times 10^{-4} \text{ cm s}^{-1}$ for all areas except area XVIII (between 36°N and 48°N in the Atlantic) which was given an initial estimate of $5 \times 10^{-4} \text{ cm s}^{-1}$. The canonical value for abyssal upwelling is about $1 \times 10^{-5} \text{ cm s}^{-1}$, however, experience tells us that given such a small initial estimate, the final model estimates will tend to be even smaller. Earlier experiments showed that an initial estimate of $1 \times 10^{-5} \text{ cm s}^{-1}$ results in an inability to balance mass in some regions. As mentioned in the previous chapter, earlier experiments also showed that the larger initial estimate for area XVIII was necessary in order to balance mass in the region. The larger estimate is reflected in the model solution where the vertical transfer terms have rms values which range in magnitude from $2 \times 10^{-5} \text{ cm s}^{-1}$ (in area XVI, between 11°N and 24°N in the Atlantic) to $1.0 \times 10^{-4} \text{ cm s}^{-1}$ (in area IV to the southwest of South Africa) and $3.6 \times 10^{-4} \text{ cm s}^{-1}$ (in area XVIII between 36°N and 48°N in the Atlantic). The median rms w^* value for all the areas is $5 \times 10^{-5} \text{ cm s}^{-1}$. The six largest rms values of w^* (greater than 6×10^{-5}) occur in the Atlantic south of 27°S and in the Atlantic and Pacific north of 24°N. Many, though not all the regions have at least some w^* values which are

significantly different from zero. The character of the cross-isopycnal transfer terms will be examined in detail in Chapter 4.

The discussion of the standard model results which follows, is divided into four regions (Atlantic Ocean, Southern Ocean, Indian Ocean and Pacific Ocean). Within each section, a brief description is given of the water masses present in the region and how their characteristics appear in the hydrographic transects used in this study. This description is followed by a discussion of the standard model velocity fields and resulting transports of currents and water masses through and between the basins.

The standard model produces a number of features which run counter to conventional wisdom. Often test models were used to investigate these features. The outcome of these test runs is discussed at the end of the regional descriptions. The reader may skip to the summary at the end of this section (page 204) if not interested in the detailed results of the specific hydrographic transects.

3.4.1 The Atlantic Ocean

This section compares the results of the standard model in the Atlantic Ocean to the results of numerous recent studies. For more detailed summaries of the literature the reader may turn to the review articles of *Schmitz and McCartney* [1993] for the North Atlantic circulation and of *Peterson and Stramma* [1991] for the South Atlantic circulation. The studies of *Reid* [1994] and [1989] give detailed descriptions of the patterns of tracer distributions and provide estimates of the absolute geostrophic flow patterns in the North and South Atlantic, respectively.

The North Atlantic

The North Atlantic polar regions are recognized as formation sites for much of the deep water found within the oceans. Although they are not the only sites of deep water formation, they are often thought of as the source and beginning of the global thermohaline circulation. It therefore, seems reasonable to begin the discussion of the velocity and transport results within the North Atlantic. The northernmost section at 48°N lies just to the south of these regions of deep water formation. The sections, #A36N, #A24N and #A11N lead the discussion into the South Atlantic where the water from all three of the major ocean basins meet.

Figure 3.6 shows the zonally integrated profiles of Θ , S , O_2 and nutrients for the Atlantic sections. At #A48N (Figures 3.6a) the uppermost layer is confined to the western boundary over the shallow Grand Banks and is extremely cold and fresh (0.4°C, 33.3), while the surface layer in the open ocean region exhibits the cold, 11.7°C (relative to more southerly sections) and salty, 35.5, character expected from water which has undergone strong evaporative cooling to the south. Lying at about 700–1000 db, low salinity, high oxygen intermediate water is evident. NADW is recognized between about 1500 and 4000 db as an oxygen maximum, decreasing with depth. Below 4000 db at temperatures less than 2°C and with relatively high oxygen content the water is a combination of the remnant, silica rich Antarctic Bottom Water (AABW) which has become diluted in its northward travels and the low silica Denmark Strait Overflow Water (DSOW) which has moved away from its northern source. *Luyten et al.*, [1993] suggest that the source of NADW³ can be thought of as a combination of these two bottom waters AABW and DSOW.

³Here, we will use the term NADW to denote deep water originating in the North Atlantic before it is incorporated into the ACC as CDW. Likewise, we will only use the term WSBW when referring to the water mass originating in the Weddell Sea, before it is influenced by the ACC and AABW.

Water Mass Name	Model Layer	Temperature Limits (°C) at			
		#A48N	#A36N	#A24N	#A11N
Surface Water	1	****	> 17.3	> 18.5	> 15.5
Thermocline Water	2-4	> 8.1	> 9.8	> 9.3	> 6.4
Intermediate Water	5-6	> 5.2	> 5.9	> 5.4	> 4.5
North Atlantic Deep Water	7-14	> 2.0	> 1.9	> 1.9	> 1.8
Bottom Water	15-17	< 2.0	< 1.9	< 1.9	< 1.8

Table 3.6: Approximate definition of water masses by the model layers in the North Atlantic. Except in the case of the bottom water, the temperature limits are average temperatures across the section of the lower layer boundary. The bottom water temperature limit is defined in terms of the average temperature of the upper layer boundary. Asterisks indicate that no water is contained in the defined layers. The model layers numbers refer to those defined in Table 2.5a.

In profiles to the south (36°N, 24°N and 11°N) the fresh, nutrient rich AAIW water mass becomes increasingly evident. The effect of the high salinity, low silica Mediterranean waters at intermediate depths although visible in the eastern basin, in the unintegrated property fields, is not apparent in Figure 3.6. The silica values of the bottom water begin to increase towards the south as the presence of AABW becomes more apparent.

Crossing the equator to #A11S, it is apparent that the shapes of the property profiles are similar to those found at 11°N. AAIW, NADW and AABW are still distinguishable by their high silica/low salinity, oxygen maximum/nutrient minimum and temperature minimum/nutrient maximum, respectively. As might be expected, the oxygen content of NADW has decreased as it has traveled away from its northern source, while the silica maximum of AABW is more prominent as we approach its southern source region. At #A23S and #A27S these tendencies continue to evolve in the property profiles.

The circulation of these water masses within the Atlantic is illustrated in the velocity fields (Figure 3.10) and transport profiles (Figure 3.14) for these sections.

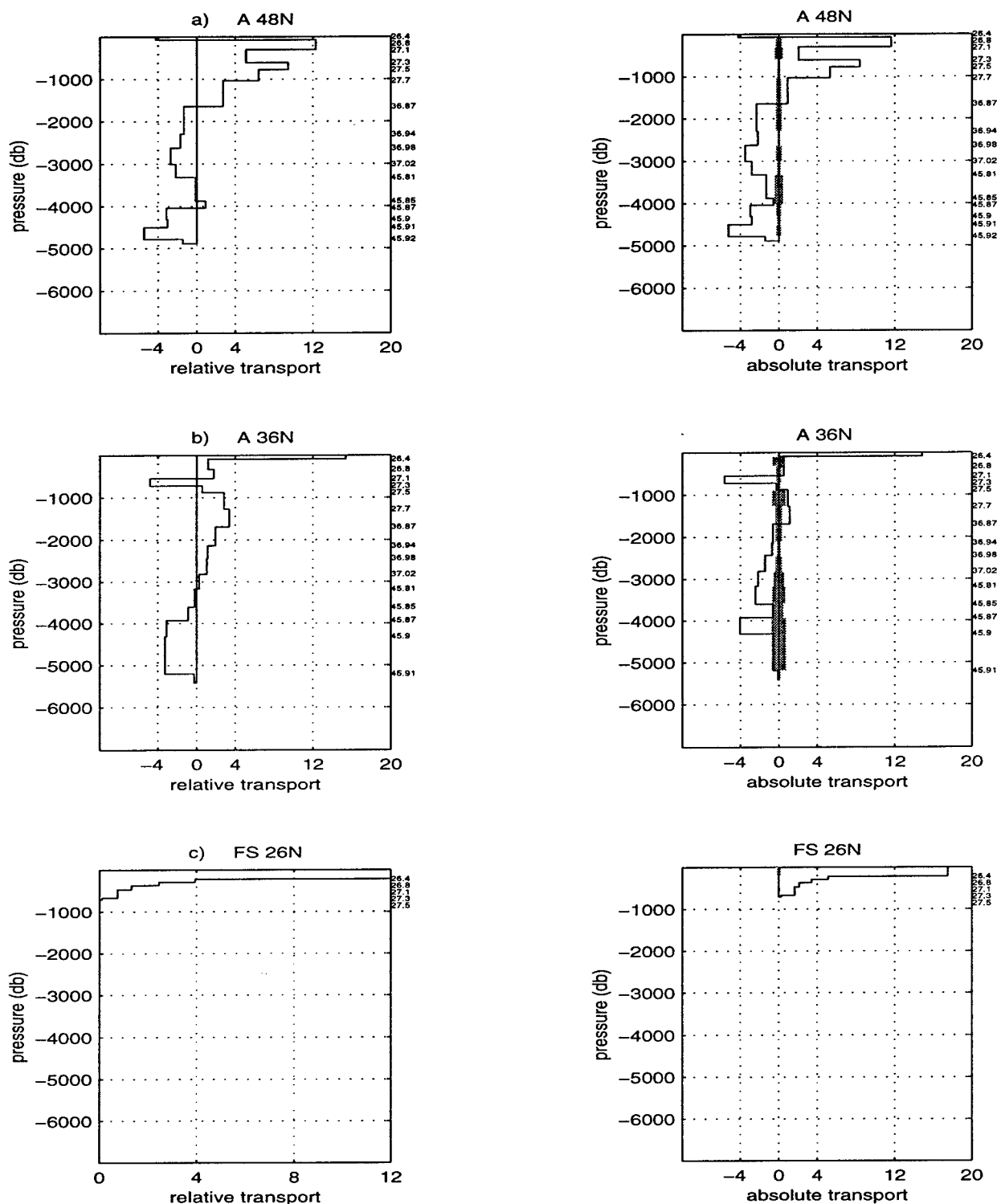


Figure 3.14: The zonally integrated mass transport in potential density layers for the sections: (a) #A48N, (b) #A36N and (c) #F1St. The profiles on the left are based on a zero velocity at the reference level. Those on the right are based on the absolute velocity field computed by standard model. The shaded region indicates the estimated 1 σ uncertainty in the layer transports due to the uncertainty in the reference level velocities. The Ekman transport is included in outcropping layers.

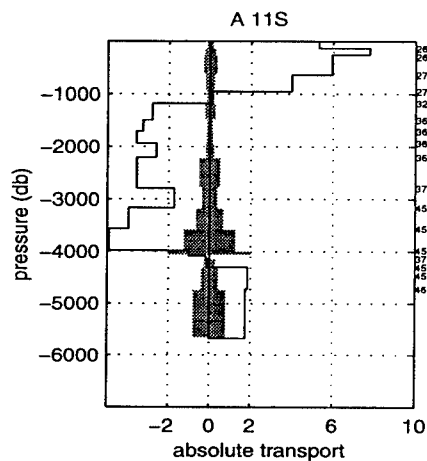
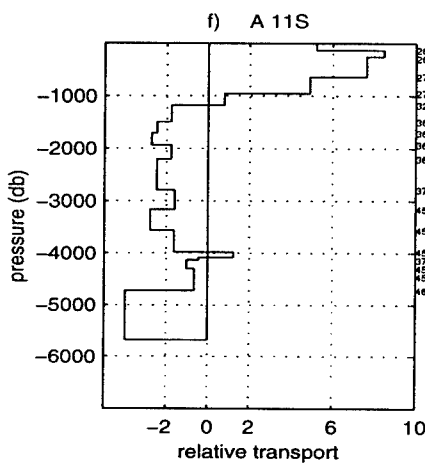
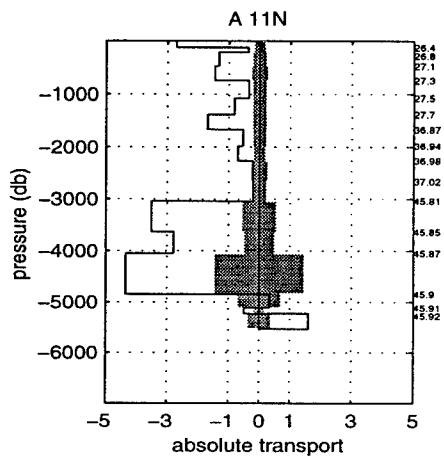
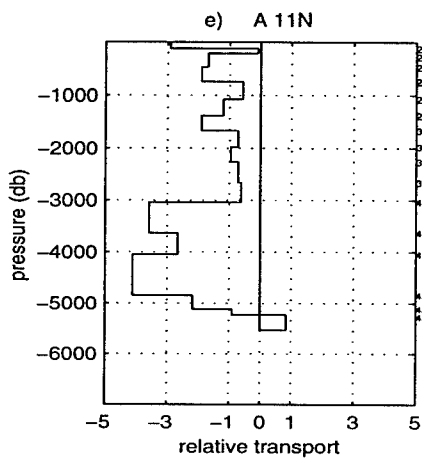
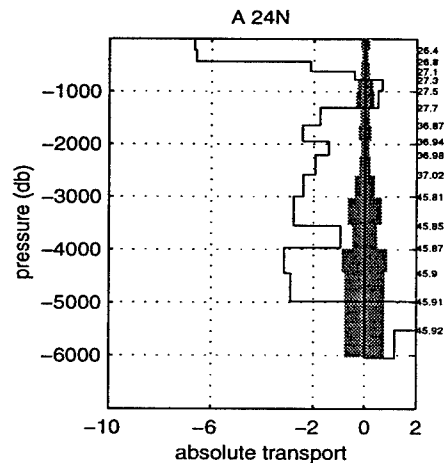
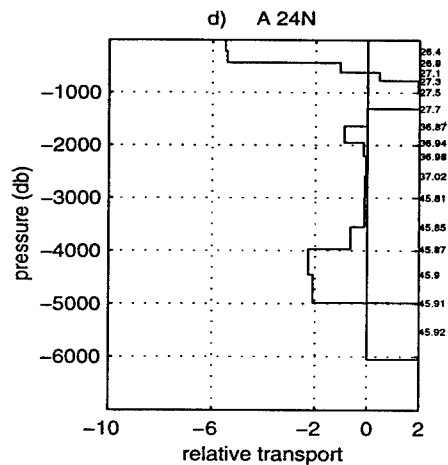


Figure 3.14 continued: The zonally integrated mass transport in potential density layers for the sections: (d) #A24N, (e) #A11N and (f) #A11S.

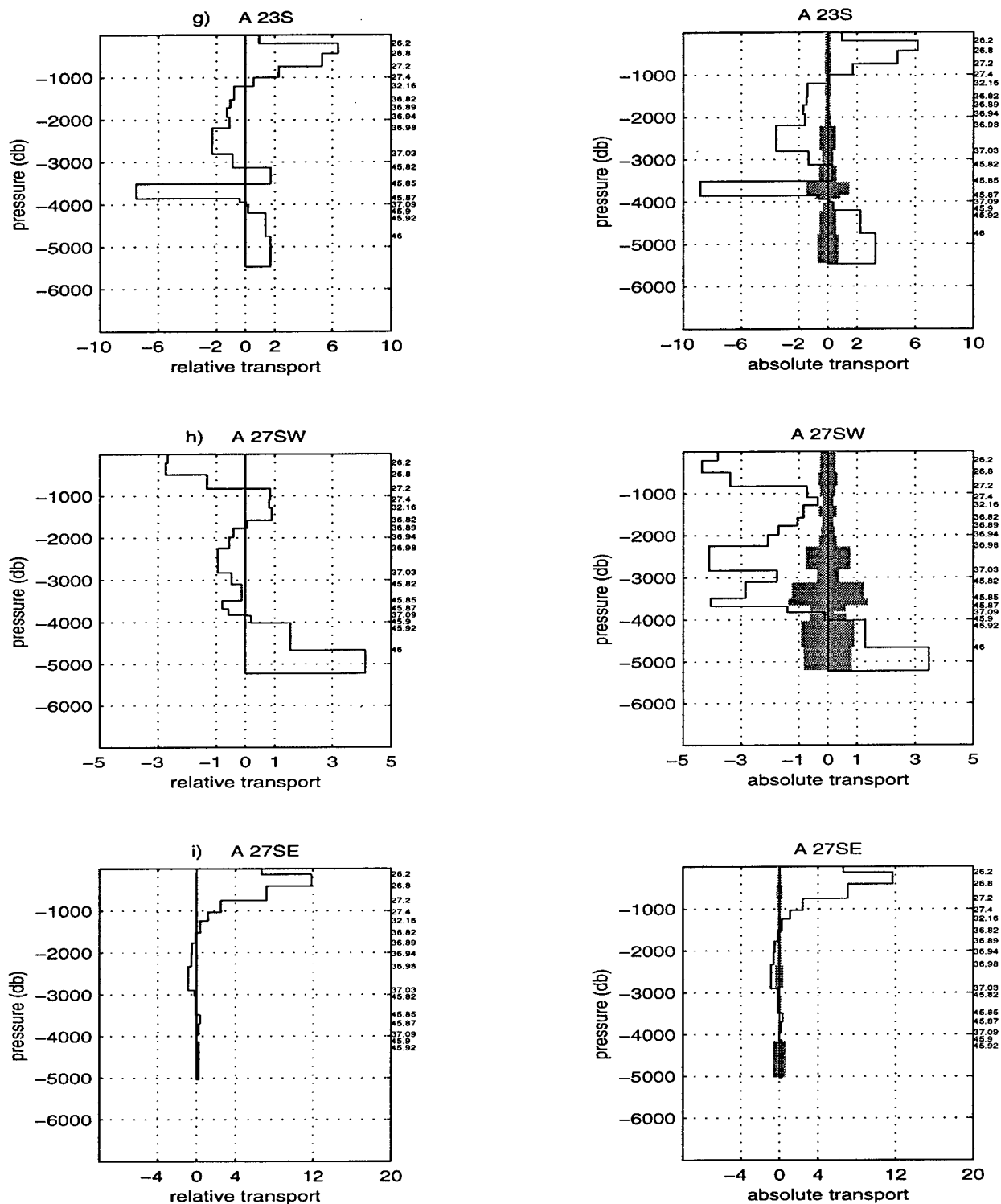


Figure 3.14 continued: The zonally integrated mass transport in potential density layers for the sections: (g) #A23S, (h) #A27S.W and (i) #A27S.E.

To facilitate the discussion of the water mass transports, the isopycnal layers used in the model have been summed according to Table 3.6. The most obvious feature of the absolute velocity fields is the columnar character of the flow which is everywhere evident and which is a result of the eddy field as seen through relative velocities calculated between station pairs, not the addition of the reference level velocities. Most hydrographic sections display this flow characteristic.

The southward flow of deep waters from formation sites to the north, marking beginning of the global overturning cell can be seen in the velocity field to the west of the Mid-Atlantic Ridge at 48°N (Figure 3.10a). Within the first 450 km from the west coast there is a small net southward transport of $-2.2 \pm 0.4 \times 10^9 \text{ kg s}^{-1}$. The deep western boundary current can be seen lying against the coast in the Labrador Basin and carries $-18.0 \pm 1.2 \times 10^9 \text{ kg s}^{-1}$ to west of 40°W. The flow of bottom water is generally to the south in the western basin, especially to the west of 37°W. To the east, the opposing flows within the bottom waters may be indicative of the southern and northern origins of the AABW and the DSOW water masses.

The thermocline and intermediate water circulation is similar to that described by *Schmitz and McCartney* [1993] (S&M henceforth), in that there is an inshore northward transport and the suggestion of a clockwise gyre within the Newfoundland Basin. The strength of the inshore feature in the standard model ($12 \pm 1 \times 10^9 \text{ kg s}^{-1}$) is comparable to that suggested by S&M ($12 \times 10^6 \text{ m}^3 \text{ s}^{-1}$). The strength of the model gyre at $19 \pm 1 \times 10^9 \text{ kg s}^{-1}$ (above about 5°C) is somewhat less than the S&M value of $25 \times 10^6 \text{ m}^3 \text{ s}^{-1}$ (above 7°C). However, it should be noted that the transport estimates for these features are extremely sensitive to choice of station pairs to include in the integration. Here the gyre is defined as a net southward transport between 37.5°W and 35.2°W which is balanced by northward flow between 42°W and 37.5°W. All flow to the west of the gyre and to the east of southward coastal current mentioned above is assumed to be associated with the inshore feature. Since S&M provide no estimate

of the uncertainty in their estimates it is not possible to say whether or not these two values are consistent.

S&M suggest the presence of a strong ($35 \times 10^6 \text{ m}^3 \text{ s}^{-1}$) deep clockwise gyre within the Newfoundland Basin but emphasize that the direction of flow within the region is dependent upon the choice of a bottom reference level. Indeed, in our earlier models which used a deep ($\sigma_4 = 45.85$) reference level, a clockwise gyre of comparable strength was found. However, the deep initial reference level produced a large, $O(60 \times 10^9 \text{ kg s}^{-1})$, initial net mass transport across the #A48N section so the standard model was run with a shallower reference level ($\sigma_2 = 36.87$). In the deeper waters, below about 1000 db and 5°C the standard model finds the strong deep western boundary current mentioned above. To the east, lie flows of alternating direction which produce a net northward transport of $5.3 \pm 4.3 \times 10^9 \text{ kg s}^{-1}$, but there is no evidence in the standard model for a deep gyre. There is a net southward transport in the western basin below 5°C of $-21.8 \pm 4.2 \times 10^9 \text{ kg s}^{-1}$.

The major difference between the S&M circulation and that suggested by the standard model is the transport east of about 32°W . The standard model estimates a net $19.5 \pm 1.6 \times 10^9 \text{ kg s}^{-1}$ poleward transport east of 32°W at temperatures greater than 5°C . About half of this transport occurs over the Mid-Atlantic Ridge region. Another third is associated with the strong velocities seen in Figure 3.10a east of 15°W . This northward flow near the coast of Ireland is consistent with that found by *Martel and Wunsch* [1993] and *Reid* [1994]. However, the standard model circulation in this region is of quite different character from that described by S&M. They suggest that only $1 \times 10^6 \text{ m}^3 \text{ s}^{-1}$ of water warmer than 7°C , emanating from the Mediterranean moves across 48°N within the eastern basin. They estimate $2 \times 10^6 \text{ m}^3 \text{ s}^{-1}$ moving northward across this latitude in the temperature range 1.8°C to 4°C .

We attempted to apply the S&M picture of the eastern basin circulation as constraints on the standard model using an uncertainty of $1 \times 10^9 \text{ kg s}^{-1}$ (see Table 3.1).

Neither constraint was met. East of 24.5°W , in the 1.8°C to 4°C range the standard model found $-0.5 \pm 1.0 \times 10^9 \text{ kg s}^{-1}$, a flow which is at least consistent in the sense that it is small. More surprisingly, the standard model found that the upper layer constraint did not even lie within the realm of possibility as it estimated a net transport in the eastern basin of water warmer than about 5°C of $11.0 \pm 0.7 \times 10^9 \text{ kg s}^{-1}$. The general pattern of strong northward flow east of 32°W is not affected by the choice of reference level. As long as the standard model does not balance mass in the western basin alone, the balance suggested by S&M in the eastern basin cannot be consistent with the standard model solution. A strong northward flow ($13 \times 10^6 \text{ m}^3 \text{ s}^{-1}$) in the upper layers east of 32°W would be consistent with the S&M picture 5° further to the north. However, why the resulting upper layer circulation patterns appear so different at 48°N is not understood.

At 36°N (Figure 3.10b), the Gulf Stream is found at about 71°W . A cold core ring is seen to the east at about 66°W . The standard model suggests a Gulf Stream transport of $91 \pm 3 \times 10^9 \text{ kg s}^{-1}$ down to about 3200 db and a maximum speed of 177 cm s^{-1} . *Rintoul and Wunsch* [1991] (henceforth R&W) found a Gulf Stream transport for this section ranging between $55 \times 10^9 \text{ kg s}^{-1}$ down to 1500 db and $84 \times 10^9 \text{ kg s}^{-1}$ down to 3000 db depending upon their choice of initial reference level. The reference isopycnal used here ($\sigma_4 = 45.81$) lies between about 2500 and 3000 db within the Gulf Stream region. To be consistent with the R&W estimate, the Gulf Stream transport is summed over the region in which the top to bottom transport has the same sign.

Other recent estimates of Gulf Stream transport are given in Table 3.7. Though the lack of uncertainty estimates on some of the values makes it difficult to define a range of consistency, we are led to the same conclusion as R&W. That is, most of the recent direct velocity estimates of Gulf Stream transport appear to be higher than the standard model estimate. However, the range of values indicated by these direct velocity measurements is large and does not lead us to believe that the #A36N

Reference	$10^6 \text{ m}^3\text{s}^{-1}$	Location	Method/Comment
<i>Hall & Bryden</i> [1985]	103	68°W	Current meter data, above 4000 db
<i>Halkin & Rossby</i> [1985]	88±17	73°W	Pegasus profiler, above 2000 db
<i>Joyce et al.</i> [1986]	107±11	74°W	Acoustic doppler combined
	125±6	72°W	with hydrography
<i>Hogg</i> [1992]	94	73°W	Re-evaluating the Halkin and
	96	68°W	Rossby data and using data
	147	60°W	from three current meters
	149	55°W	

Table 3.7: Recent estimates of Gulf Stream transport.

hydrographic estimates are incorrect. In fact, the time dependent nature of the Gulf Stream system would suggest that any or all of the above mentioned transport estimates may be "correct".

Across the section at 36°N the net poleward transport of surface, thermocline and intermediate water is balanced by an equatorward transport of deeper waters, which are mainly confined to the western basin west of 67°W. This result is consistent with the classical picture of the overturning cell and the deep western boundary current. Inshore of the Gulf Stream there is a net southward transport of $-5.8 \pm 2.1 \times 10^9 \text{ kg s}^{-1}$. Beneath it (below 3200 db) there is $-4.8 \pm 1.3 \times 10^9 \text{ kg s}^{-1}$ moving southward, giving a total western boundary current on the order of about $11 \times 10^9 \text{ kg s}^{-1}$. The $4.8 \pm 1.3 \times 10^9 \text{ kg s}^{-1}$ flowing beneath the Gulf Stream is smaller but consistent (where uncertainties are given) with previous estimates ($12 \times 10^6 \text{ m}^3 \text{ s}^{-1}$ below 1000 db at 70°W [*Hogg*, 1983]; $9 \pm 3 \times 10^6 \text{ m}^3 \text{ s}^{-1}$ below 2000 db [*Joyce et al.*, 1986] and $11 \times 10^6 \text{ m}^3 \text{ s}^{-1}$ below 2000 db R&W). To the east of the Gulf Stream and to west of the Mid-Atlantic Ridge there is a net southward transport in the deep layers (Table 3.6) of $-18 \pm 5 \times 10^9 \text{ kg s}^{-1}$, indicating, as has been suggested before [*Reid*, 1981; *Rintoul and Wunsch*, 1991] that much of the southward flux of NADW occurs within the interior of the western basin.

In the eastern basin, the flow patterns are considerably weaker, as would be expected. There is a net southward transport of surface and thermocline waters, consistent with the maps of *Reid* [1994]. The net deep flow is directed northward ($1.2 \pm 1.0 \times 10^9 \text{ kg s}^{-1}$ between 24°W and the coast of Europe), while the net intermediate flow is directed southward ($-1.8 \pm 1.2 \times 10^9 \text{ kg s}^{-1}$). *Rintoul* [1988] found a much stronger circulation in this region, with a net transport of $-9 \times 10^6 \text{ m}^3 \text{ s}^{-1}$ moving southward at intermediate depths between the Mid-Atlantic Ridge and 20°W balanced by a net northward transport between 20°W and the coast. There is no evidence for a balance between such strong flows in the standard model.

There are many differences between the *Rintoul* [1988] model constraints and those of the standard model. The exact cause for the difference in the resulting eastern basin intermediate transport is not known. It is likely that it lies in the choice of reference level and solution. Experimentation has shown that the choice of column scalings which determine how well the cross-isopycnal transfer terms are resolved (see Chapter 4) are also capable of creating such differences. In the deep waters of the eastern basin where *Rintoul* found a net northward transport of $6 \times 10^6 \text{ m}^3 \text{ s}^{-1}$, the disagreement with the standard model is caused by a combination of the standard model requirement for conservation of mass in the deep waters of the eastern North Atlantic, the S&M constraint on the deep flow at #A48N and our choice of w^* weights.

One does not expect the smaller scale features of circulation patterns to necessarily agree, even between two inverse box models. What is perhaps of more interest is the comparatively low estimate of the strength of the overturning cell at this latitude. The standard model estimates that the northward transport of warmer waters which is balanced by the southward transport of colder waters amounts to only $(11 \pm 1.5 \times 10^9 \text{ kg s}^{-1})$ at 36°N . Whereas *Rintoul's* estimate for the transport in the same layers was $17.2 \times 10^6 \text{ m}^3 \text{ s}^{-1}$. A number of test models were run to determine

the cause of this difference. The main result of these tests was that the magnitude of the overturning cell within the standard model has been reduced by

- the net northward bottom water constraints which have an effect of about $3 \times 10^9 \text{ kg s}^{-1}$,
- the assumed $1 \text{ cm}^2 \text{ s}^{-2}$ variance for the reference level velocities which has an effect of about $3 \times 10^9 \text{ kg s}^{-1}$
- and the allowance for a net transport across the section which has an effect of about $1 \times 10^9 \text{ kg s}^{-1}$.

Including the other constraints in the North Atlantic (from #A11N and #A48N) has the effect of increasing the estimate of the magnitude of the overturning cell by about $1 \times 10^9 \text{ kg s}^{-1}$.

In an effort to reproduce the *Rintoul* [1988] result, a test model was run which used only the area XVII constraints, removed the bottom water constraints and allowed a $100 \text{ cm}^2 \text{ s}^{-2}$ variance for the reference level velocities. The b_{rms} approximately doubled to 0.9 cm s^{-1} and the test model produced an overturning cell of $16.4 \pm 5.8 \times 10^9 \text{ kg s}^{-1}$, with $-17.1 \times 10^9 \text{ kg s}^{-1}$ moving southward in layer 7 and below. This estimate is closer to the *Rintoul* [1988] value and different from his because of the estimate of net transport through the section.

The strong effect of the bottom water constraints and the fact that they were not met, leads us to the conclusion that they are neither consistent with the other model constraints nor with what is thought to be known about the North Atlantic circulation. Whether or not larger reference velocities should be expected in the North Atlantic, which is a region of strong circulation, is a judgement call. We leave it to the reader to consider that they are not necessary to meet the requirements of this model, but that they will effect a larger estimate of the overturning cell at this latitude. We conclude that the *Rintoul* [1988] estimate of the magnitude of the overturning cell at 36°N is 0.5 to $1 \times 10^6 \text{ m}^3 \text{ s}^{-1}$ too high because he did not include the effect of a net mass

transport across the section, but this effect is compensated by the lack of data to the north and south in his model. The standard model estimate is at least $3 \times 10^9 \text{ kg s}^{-1}$ too low because it included a certain set of constraints on the bottom water in the North Atlantic, in particular at 24°N and at 36°N . The remaining difference in the estimates is dependent upon how large we believe reference level velocities should be at this latitude. Allowing for larger values of \hat{b} produces a larger estimate of the overturning cell (17.2 compared to 14.3) with a larger estimate in the uncertainty (3.5 compared to 1.5). Reasonable estimates of the overturning cell at this latitude probably lie within this range. The North Atlantic test models used in this discussion are described in relation to the estimated heat flux at this latitude in section 3.4.7.

At 24°N (Figure 3.10d), the net southward flow which compensates for the northward transport within the Florida Straits is overlaid upon a strong eddy field. Much of the southward flow lies to the east of 54°W and although it occurs throughout the water column, most of the net southward flow is concentrated in the surface and thermocline layers. There is a net northward transport of intermediate waters across $\#A24\text{N}$ ($1.2 \pm 0.7 \times 10^9 \text{ kg s}^{-1}$) composed of a net southward transport to the west of 52°W ($-3.2 \pm 0.6 \times 10^9 \text{ kg s}^{-1}$) and a net northward transport to the east ($4.4 \pm 1.1 \times 10^9 \text{ kg s}^{-1}$). This pattern is consistent with the maps of *Reid* [1994] as is the net southward flow of intermediate waters over the Mid-Atlantic Ridge region.

At this latitude the deep western boundary current has narrowed but away from the western boundary there is still net southward transport within the deep water ($-16 \pm 5 \times 10^9 \text{ kg s}^{-1}$ between 71°W and the crest Mid-Atlantic Ridge). There is also a small net northward transport of AABW ($0.4 \pm 0.8 \times 10^9 \text{ kg s}^{-1}$).

The $\#A11\text{N}$ transect (Figure 3.10e) approaches the western boundary at about 5°N . At the coast of South America, the outer portion of the North Brazil Current (NBC) is seen. In the upper three layers (500 db) and inshore of 50.5°W , there is a net northward transport of $7.7 \pm 0.3 \times 10^9 \text{ kg s}^{-1}$. This value is similar to the *Friedrichs*

and Hall [1993] (henceforth F&H) estimate that $7 \times 10^6 \text{ m}^3 \text{ s}^{-1}$ (with no uncertainty given) of the NBC transport are included in the hydrographic section. Balancing mass across the section and assuming the initial estimate of Bering Strait transport ($0.8 \times 10^9 \text{ kg s}^{-1}$) is correct gives an estimated $18.4 \pm 1.9 \times 10^9 \text{ kg s}^{-1}$ for the NBC inshore of the western-most hydrographic station. Combining these two values produces an estimated total mean NBC mass transport of $26.1 \pm 1.9 \times 10^9 \text{ kg s}^{-1}$, which is consistent with the initial constraint ($26.5 \pm 5 \times 10^9 \text{ kg s}^{-1}$). Offshore of the NBC, a strong southward current exists. This countercurrent was also noted by F&H and they surmised that a portion of this flow may be the North Equatorial Countercurrent which was present in the region during the time at which the data were taken [according to Katz, 1993 as noted by F&H]. They also suggest that some of the counter flow may be an eddy originating from the the retroflexion region of the NBC. As in the other sections, the sign of the velocities oscillates across the basin and is indicative of intense eddy activity filling the basin, especially to the west of about 36°W (see Figure 3.10e).

As at 24°N , compensation for the strong poleward boundary current transport is provided by a net equatorward transport across the rest of the 11°N section, at all depths, except in this case in the bottom layers. At this latitude, most of the northward transport of intermediate waters occurs within the western basin. The deep western boundary current extends from about 1000 db to the bottom. It carries $-24.9 \pm 1.8 \pm 1 \times 10^9 \text{ kg s}^{-1}$ between 51°W and 49°W at temperatures less than about 5°C . This value is quite similar to the F&H estimate of $-26.5 \pm 1.8 \times 10^6 \text{ m}^3 \text{ s}^{-1}$. They take the magnitude of the deep western boundary current to be the maximum southward transport of waters with $\Theta < 4.7^\circ \text{C}$ integrated seaward of the western boundary. Other estimates of the deep western boundary transport near this latitude range from about 22 to $26 \times 10^6 \text{ m}^3 \text{ s}^{-1}$ (see Table 3 of F&H).

East of 49°W, the character of deep transport suggested by the standard model differs from the F&H results, even though the initial velocity reference levels for the standard model (see Table A.2) were based upon those used by F&H in their analysis of the #A11N section. The solutions from the two analyses are necessarily different. F&H chose their reference levels to produce "acceptable" western basin AABW transport ($-2.5 \pm 0.7 + 2.6 \pm 0.6 = 0.1 \pm 0.9 \times 10^6 \text{ m}^3 \text{ s}^{-1}$ at $\Theta < 1.8^\circ\text{C}$) and to maximize the net southward transport of NADW ($-7.3 \pm 1.5 \times 10^6 \text{ m}^3 \text{ s}^{-1}$ at $4.7 < \Theta < 1.8^\circ\text{C}$) while simultaneously balancing mass across the section. Their estimate of Ekman transport ($9.1 \pm 1.8 \times 10^6 \text{ m}^3 \text{ s}^{-1}$) is similar to that used in the standard model ($9.3 \pm 1.3 \times 10^9 \text{ kg s}^{-1}$). However, they chose to use an *in situ* estimate of the shallow North Brazil Current of $4.5 \times 10^6 \text{ m}^3 \text{ s}^{-1}$, while we have chosen to use an annual estimate of $19.5 \times 10^9 \text{ kg s}^{-1}$. We therefore begin with a mass imbalance across this section which must be compensated by flow due to the computed reference level velocities.

The only significant difference between the F&H solution and the standard model solution is in the deep water. Within the western basin, F&H find a net southward transport ($-20.6 \pm 2.0 \times 10^9 \text{ kg s}^{-1}$) of NADW west of 46.3°W and a net northward transport ($6.4 \pm 2.8 \times 10^9 \text{ kg s}^{-1}$) to the east. The standard model finds a similar pattern, but the net transport of deep water (between layers 7 and 14) within the western basin is not significantly different from zero. This difference is mainly due to the difference in transport in the F&H region II, between 49°W and 46.3°W which can be seen in the increased magnitude of the reference level velocities between these two longitudes in Figure 3.10e. In this region F&H found a net $-6 \times 10^6 \text{ m}^3 \text{ s}^{-1}$ (between 4.7°C and 7°C), while the standard model estimates a net $2 \times 10^9 \text{ kg s}^{-1}$ (between about 4.5°C and 6.4°C). Most of the remaining difference between their model and ours lies in central region of the basin where there is an equatorward flow of upper deep waters over the Mid-Atlantic Ridge (see Figure 3.10e) which is a strong contributor to the net southward transport of deep water across the section. The model has

placed most of the adjustment for the stronger initial estimate of the North Brazil Current in the deep layers, so that where F&H find a relatively weak overturning cell at this latitude ($5.2 \pm 1.6 \times 10^6 \text{ m}^3 \text{ s}^{-1}$), the standard model estimates a net overturning between layer 7 and the bottom of $12.6 \pm 1.4 \times 10^9 \text{ kg s}^{-1}$.

North Atlantic Summary

In summary the zonally integrated mass transport profiles for the standard model show:

- a net northward surface and thermocline flow in layers 1–4
 - 9.5 \pm $0.6 \times 10^9 \text{ kg s}^{-1}$ across 48°N ,
 - 9.8 \pm $0.8 \times 10^9 \text{ kg s}^{-1}$ across 36°N ,
 - 28.2 \pm $0.4 \times 10^9 \text{ kg s}^{-1}$ in the Florida Straits,
 - 15.8 \pm $0.4 \times 10^9 \text{ kg s}^{-1}$ across 24°N and
 - 12.8 \pm $0.6 \times 10^9 \text{ kg s}^{-1}$ across 11°N (includes NBC estimate),
- a net northward flow of intermediate waters in layers 5–6
 - 13.7 \pm $0.6 \times 10^9 \text{ kg s}^{-1}$ across 48°N ,
 - 0.7 \pm $1.0 \times 10^9 \text{ kg s}^{-1}$ across 36°N ,
 - 1.9 \pm $0.2 \times 10^9 \text{ kg s}^{-1}$ in the Florida Straits,
 - 1.2 \pm $0.7 \times 10^9 \text{ kg s}^{-1}$ across 24°N and
 - 1.2 \pm $2.0 \times 10^9 \text{ kg s}^{-1}$ across 11°N ,
- the net southward flow of deep waters in layers 7–14
 - 14.8 \pm $1.1 \times 10^9 \text{ kg s}^{-1}$ across 48°N ,
 - 10.9 \pm $1.4 \times 10^9 \text{ kg s}^{-1}$ across 36°N ,
 - 16.8 \pm $1.2 \times 10^9 \text{ kg s}^{-1}$ across 24°N and
 - 14.0 \pm $1.6 \times 10^9 \text{ kg s}^{-1}$ across 11°N

- a net southward flow of bottom waters in layers 15–17 across the northern-most sections and a net northward transport across the more southerly sections
 $-9.5 \pm 0.6 \times 10^9 \text{ kg s}^{-1}$ across 48°N ,
 $-0.6 \pm 0.8 \times 10^9 \text{ kg s}^{-1}$ across 36°N ,
 $0.4 \pm 0.8 \times 10^9 \text{ kg s}^{-1}$ across 24°N and
 $1.5 \pm 0.8 \times 10^9 \text{ kg s}^{-1}$ across 11°N

where the uncertainties quoted are only those due to the uncertainty in the reference level velocities.

The standard model upper layer circulation in the North Atlantic is consistent with a mid-latitude anticyclonic gyre and the pattern of circulation described by *Reid* [1994]. The most obvious discrepancy between the results of this model and the results of other studies used for comparison is the strong northward transport of warmer waters across 48°N which in the S&M study appears to occur further to the north. Northward transport of upper layer waters near the coast of Ireland is however, consistent with the maps of *Reid* [1994] and *Martel and Wunsch* [1993], and some northward transport across the Mid-Atlantic Ridge region is consistent with *Reid* [1994]. Without constraints which required conservation of properties in deep eastern North Atlantic, a strong southward transport of deep waters in the eastern basin also appeared at 48°N due to model's inability to recognize the Mid-Atlantic Ridge obstruction. Therefore, standard model included these constraints.

The *Reid* [1994] study describes the deep circulation of the North Atlantic in terms of three gyres. The first lies to the north of the regions covered by these data. The second is the large mid-latitude anticyclonic gyre and the third is a cyclonic gyre lying to the south and east of the mid-latitude gyre. Comparing the standard model results divided into three regions (western basin, over the Mid-Atlantic Ridge and eastern basin), it is found that the sense of the flows suggested by the standard model agrees well with the *Reid* results except in two of regions. These regions are in

Section	Average Θ of $\sigma_\theta = 27.7$ °C	Transport in layers 7-17 10^9 kg s^{-1}	Uncertainty 10^9 kg s^{-1}	Range for Comparison $10^6 \text{ m}^3 \text{ s}^{-1}$
#A48N	5.2	24.2 (24.4)	1.2	
#A36N	5.9	11.4 (14.8)	1.4	12-17
#A24N	5.4	16.4 (19.3)	1.3	16-18
#A11N	4.5	12.6 (12.3)	1.4	10-21

Table 3.8: Estimates of the magnitude of the meridional overturning cell from the standard model. The values in parenthesis come from the test model which did not include the constraints on the bottom water at 24°N and 36°N. Column five contains the range of previous estimates taken from the hydrography estimates of Table 4 of *Friedrichs and Hall* [1993].

the surface waters over the Mid-Atlantic Ridge at 36°N, where the standard model suggests a northward transport ($2.1 \pm 1.5 \times 10^9 \text{ kg s}^{-1}$), and in the intermediate layers of the western basin at 24°N, where the standard models also suggests a net northward transport ($3.6 \pm 0.6 \times 10^9 \text{ kg s}^{-1}$).

In spite of constraints applied as far north as 36°N, #A24N is the northernmost section to maintain a northward transport of bottom water. The bottom water transports are not significantly different from zero at either 36°N or 24°N. Furthermore, it was found that these constraints have the effect of reducing the estimated magnitude of the overturning cell at these latitudes by about $3 \times 10^9 \text{ kg s}^{-1}$. It is concluded that these bottom water constraints are not consistent with either the other standard model constraints or with the what is thought to be understood about the circulation of water masses in this region.

Defining the magnitude of the meridional overturning cell to be the net transport of NADW and AABW as defined in Table 3.6, that is the net transport above and/or below interface 7 ($\sigma_\theta = 27.7$), the standard model suggests a mean magnitude for the overturning cell within the North Atlantic of $16 \pm 6 \times 10^9 \text{ kg s}^{-1}$ ($18 \pm 5 \times 10^9 \text{ kg s}^{-1}$ without the bottom water constraints at 24°N and 36°N) with a fairly broad range

(Table 3.8). The large difference in the estimated magnitudes between #A48N and #A36N is consistent with the large upwelling cross isopycnal transfer found in area XVIII, between the two sections (see Figure 4.2). If one disbelieves either the magnitudes of the transport at 48°N or 36°N, or the magnitude of the w^* terms suggested by the standard model, one might then argue that the #A48N and #A36N data are inconsistent with each another. However, at present, without further knowledge of what to expect between these two latitudes, we see no reason to reject this solution out of hand.

The South Atlantic

South of the equator, the major portion of the zonal boundary of the anticyclonic basin circulation, the South Equatorial Current (SEC) lies to the south of 10°S [Fu, 1981; Tsuchiya, 1986; Reid 1989]. At the South American coast this westward flow splits. The equatorward flow is the southern portion of the NBC and is seen hugging the western boundary at 11°S (Figure 3.10f), with a maximum velocity of 40 cm s^{-1} and a mass transport above 1200 db of $38.5 \pm 1 \times 10^9 \text{ kg s}^{-1}$. The poleward flow of the Brazil Current can be seen the #A23S and #A27S-W sections (Figures 3.10g and 3.10h. respectively). These sections also suggest the countercurrents seen by previous authors [Fu 1981; Zemba 1991]. At 19°S, Miranda and Castro Filho [1982] estimate maximum surface velocities for the Brazil current of about 70 cm s^{-1} (relative to 500 db) producing a transport of $6.5 \times 10^6 \text{ m}^3 \text{ s}^{-1}$. The velocities appear to decrease to the south $50\text{--}60 \text{ cm s}^{-1}$ (relative to 500 db) at 20.5°S [Evans et al. 1983] but the increased depth of the flow produces larger transports (see Table 3.9).

The two sections used here (#A23S and #A27S-W) show maximum velocities of 127 cm s^{-1} and 51 cm s^{-1} and absolute transports of $-12.6 \pm 0.5 \times 10^9 \text{ kg s}^{-1}$ and $-6.4 \pm 0.3 \times 10^9 \text{ kg s}^{-1}$ respectively. It is interesting to note that at the western boundary these two sections are at almost the same location -23.0°S, 40.9°W (#A23S) and

Latitude-	Relative to	Reference	Transport $10^6 \text{ m}^3 \text{ s}^{-1}$
20.5°S	500 & 1000 db	<i>Evans et al.</i> [1983]	-4 & -7
23°S	PEGASUS	<i>Evans and Signorini</i> [1985]	-11
27°S	$\sigma_0 = 27.20$	<i>Zemba</i> [1991]	-12
31°S	$\sigma_0 = 27.10$	<i>Zemba</i> [1991]	-25
34°S	$\sigma_4 = 45.85$	<i>Zemba</i> [1991]	-38
36°S	$\sigma_4 = 45.80$	<i>Zemba</i> [1991]	-80
38°S	1400-1500 db	<i>Gordon and Greengrove</i> [1986] and <i>Gordon</i> [1989]	-19 to -22

Table 3.9: A sampling of the estimates Brazil Current transport from the literature. A more complete listing is given in *Zemba* [1991].

-23.6°S, 41.4°W (#A27S_W) and yet the #A23S section appears to capture more of the current. This is most likely due to the better resolution of the #A23S section near the coast.

Bringing water into the South Equatorial Current, the Guinea Current can be seen flowing southward against the eastern boundary at 11°S while the Benguela Current takes a northwesterly path through the #27S and #23S sections. Although strong northward flow is apparent in #A27S sections (Figures 3.10i and 3.10h), the Benguela Current is diffuse and hard to distinguish from the eddy field in the eastern basin. Between 28°S and 32°S, recent transport estimates for the Benguela Current range between $19 \times 10^6 \text{ m}^3 \text{ s}^{-1}$ and $25 \times 10^6 \text{ m}^3 \text{ s}^{-1}$ [*Fu*, 1981; *Stramma and Peterson*, 1989; *Gordon et al.*, 1992]. Using a comparison to satellite data, *Gordon et al.* [1992] determined that the strong currents seen in the #A27S_E velocity field are two Agulhas eddies which happened to lie in the SAVE leg 4 section during the cruise. The Benguela Current itself lies to the west of these features. The northward transport west of the eddies and east of the 20°W amounts to $23 \pm 10 \times 10^9 \text{ kg s}^{-1}$. This estimate of the Benguela Current transport is consistent with the $25 \times 10^6 \text{ m}^3 \text{ s}^{-1}$ found

by *Gordon et al.* to be flowing to the north of the Benguela–South Atlantic Current front.

Within the South Atlantic, the water mass layers have been defined according to Table 3.10. The zonally integrated mass transport profiles, Figure 3.14 show:

- the characteristic net northward flow of intermediate water in layers 3–4
 - 9.9 \pm 0.6 $\times 10^9$ kg s^{−1} across #11S,
 - 6.5 \pm 0.6 $\times 10^9$ kg s^{−1} across #23S,
 - −4.1 \pm 0.6 $\times 10^9$ kg s^{−1} across #27S_W and
 - 9.4 \pm 0.7 $\times 10^9$ kg s^{−1} across #27S_E,
- the net southward flow of deep water in layers 5–15
 - −27.5 \pm 1.4 $\times 10^9$ kg s^{−1} across #11S,
 - −20.1 \pm 1.2 $\times 10^9$ kg s^{−1} across #23S,
 - −20.3 \pm 2.3 $\times 10^9$ kg s^{−1} across #27S_W and
 - −0.7 \pm 2.1 $\times 10^9$ kg s^{−1} across #27S_E,
- and the net northward flow of bottom water in layers 16–18
 - 3.5 \pm 1.0 $\times 10^9$ kg s^{−1} across #11S,
 - 5.9 \pm 0.9 $\times 10^9$ kg s^{−1} across #23S,
 - 4.6 \pm 0.9 $\times 10^9$ kg s^{−1} across #27S_W and
 - 0.3 \pm 0.7 $\times 10^9$ kg s^{−1} across #27S_E.

Between 27°S and 11°S the intermediate waters have traveled across the basin, with much though not all of the zonal flux presumably occurring in the SEC. At 11°S the intermediate waters are flowing northward mainly on the western side of the basin, as is the case in the sections north of the equator. The east/west split of the section at 27°S clearly shows that most of the equatorward flow of intermediate waters occurs on the eastern side of the basin, whereas most of the deep and bottom water transports are occurring on the western side. This pattern is consistent with the circulation as described by *Reid* [1989] and his figures [17, 20, 24 and 28] of adjusted steric height. Just to the north at 23°S, there is southward transport of intermediate

Water Mass Name	Model Layer	Temperature Limits (°C) at			
		#A11S	#A23S	#A27S_W	#A27S_E
Surface	1	> 16.6	> 15.9	> 15.8	> 15.4
Thermocline	2	> 11.1	> 10.2	> 10.1	> 9.9
AAIW	3-4	> 4.1	> 3.6	> 3.3	> 3.4
UCDW	5-7	> 3.5	> 3.1	> 2.9	> 2.8
UNADW	8-12	> 2.1	> 2.1	> 2.1	> 2.0
LNADW	13-15	> 1.8	> 1.7	> 1.7	> 1.5
AABW	16-18	< 1.8	< 1.7	< 1.7	< 1.5

Table 3.10: Approximate definition of water masses by the model layers in the South Atlantic. Except in the case of the bottom water, the temperature limits are average temperatures across the section of the lower layer boundary. The bottom water temperature limit is defined in terms of the average temperature of the upper layer boundary. The model layers numbers refer to those defined in Table 2.5b.

waters between the Walvis Ridge and the coast of Africa. A quarter of the northward transport of AAIW occurs in the eastern basin, while the other three-quarters of the northward flux occurs to the west of the Mid-Atlantic Ridge. At 11°S, nearly all of the net northward transport of AAIW is carried by the NBC.

At 11°S there is a net southward transport in all the deep layers and although there is a small northward transport in the western basin in layer 5 ($1.5 \pm 0.4 \times 10^9 \text{ kg s}^{-1}$), there is no net northward transport of water in the UCDW layers (5-7). In the eastern basin there is a net southward transport at all depths. All of the net northward transport of bottom water takes place to the west of Mid-Atlantic Ridge. At 23°S most of the northward transport of UCDW (layers 5-7)⁴ and southward transport of UNADW (layers 8-12) occurs in the western basin. However, about half southward transport of LNADW occurs in the eastern basin, to the west of the Walvis Ridge.

At 11°S, the nearly $25 \times 10^9 \text{ kg s}^{-1}$ flowing northward at temperatures greater than about 4°C and the $4 \times 10^9 \text{ kg s}^{-1}$ of northward flowing bottom water are balanced

⁴The origins of UCDW are discussed in the next section

by an equal and opposite flow of deep waters. At 23°S the net southward flow of deep water is reduced to $-19.7 \pm 1.2 \times 10^9 \text{ kg s}^{-1}$. Similar values are found at 27°S.

The results of the standard model within the Atlantic are consistent with the classical view of the overturning cell; warmer waters flowing northward in both basins balanced by a deeper, colder flow moving to the south. Both bottom and intermediate waters flow northward out of the Antarctic region, but only the intermediate layer is visible in the zonally integrated transport profiles of the northern sections. We shall return to the Atlantic results later in the chapter in a discussion of heat and freshwater fluxes and in an overview of the global overturning cell as described by the standard model. For now, we continue to move southward into the Atlantic sector of the Southern Ocean.

3.4.2 The Southern Ocean

The Atlantic Sector

Within the Southern Ocean and within the fronts and zones of the ACC there are a variety of water masses whose characteristics are derived from sources both to the north and the to south of the ACC itself. A brief review of the property values and a calculation of property transports throughout the ACC are given in *Guiffrida* [1985]. The abyssal characteristics are discussed in *Mantyla and Reid* [1983]. *Reid* [1989] describes an estimate of the total geostrophic flow field and the associated tracer distributions within the South Atlantic. *Whitworth and Nowlin* [1987] give a detailed description of the water masses found at 0°E in the South Atlantic. *Locarnini et al.* [1993] discuss the influence of source waters originating in the Weddell Sea Gyre. *Peterson and Whitworth* [1989] review the definitions and characteristics of the waters masses found just to the west of Drake Passage. It is their schematic Figure 3 which

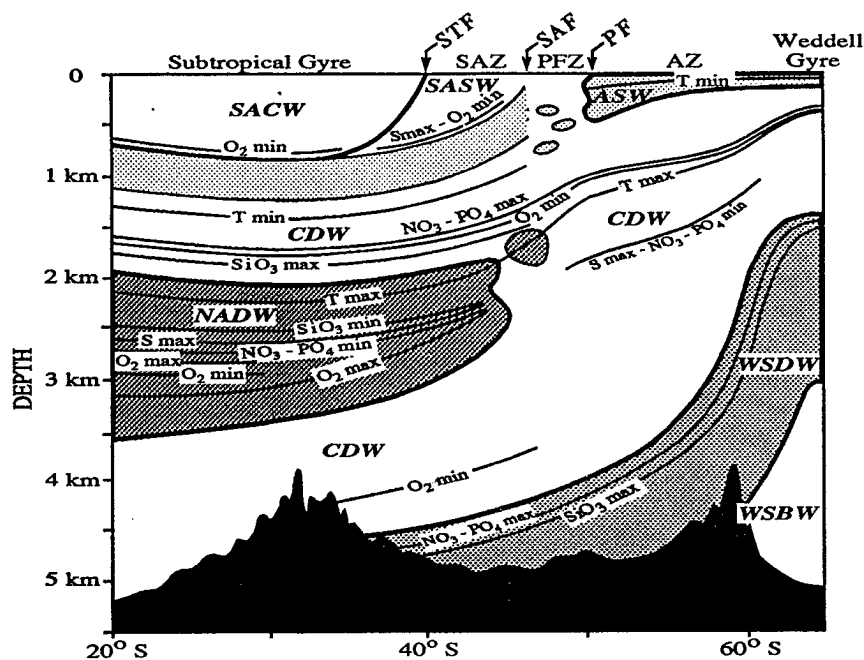


Figure 3.15: Schematic representation of the vertical distribution of the water masses and their identifying features along a north-south line in the South Atlantic to the west of the mid-ocean ridge. The abbreviations for the fronts, zones and water masses are given in the text. From *Peterson and Whitworth [1989]*.

has been reproduced here (Figure 3.15) as an illustration of some of the main water mass characteristics found within the Southern Ocean. The property characteristics for our data set are presented in integrated form in Figure 3.7.

The largest contributor to the abyssal waters of the world ocean is the principle water mass component of the ACC, Circumpolar Deep Water (CDW) [*Mantyla and Reid 1983*]. This water mass whose circumpolar nature attests to its importance within the global thermohaline circulation, is most often identified in the literature in terms of its characteristics relative to other interleaving waters masses. Entering through Drake Passage the upper portion of CDW is characterized by an oxygen minimum and nutrient maxima derived from waters in the Indian and Pacific Basins [*Callahan 1972*]. These extrema are clearly illustrated in the sections which cross the ACC (Figures 3.7a, 3.7d, 3.7g and 3.7h).

CDW derives much of its character from the deep water masses which it meets within the Atlantic Basin. In the 1000 km east of Drake Passage, CDW is ventilated and freshened by Weddell Sea Deep Water (WSDW) as the Polar Front of the ACC flows through the Scotia Sea and meets the northern edge of the Weddell Gyre [Locarnini *et al.*, 1993]. The influence of WSDW extends eastward to the deep water flowing through the South Sandwich Trench and beyond. Locarnini *et al.*, [1993] suggest that WSDW may also flow westward into the Pacific at the southern edge of Drake Passage. There is, however, no evidence of such a flow in the velocity field produced by the standard model (Figure 3.11a).

The ventilation of CDW by the WSDW (defined here as water warmer than -0.7°C and colder than about 0.1°C or 0.2°C [Locarnini *et al.*, 1993]) can be seen in the increased oxygen concentration at depth between Drake Passage (Figure 3.7a) and the Greenwich Meridian (Figures 3.7d) and particularly in the southern section #0E_S (Figure 3.7e). Although it is not obvious in the integrated plots presented here, the freshening has also occurred and is visible in the deep waters between Drake Passage and 0°E . According to the Locarnini *et al.* study, although the ACC inhibits both the northward transport of WSDW into the Argentine Basin and the flux of WSBW out of the Weddell Sea through the South Sandwich Trench, it does not completely block either flow. WSDW is thought to pass directly from the Scotia Sea to the Georgia Basin and to continue northward, primarily through the Georgia Passage, beneath the ACC to eventually become entrained in the deep western boundary current within the Argentine Basin. Once in the Argentine Basin, the water mass which is now identified as CDW meets the deep water, NADW traveling from the North Atlantic.

None of the meridional sections used in this study lie within the Southwest Atlantic region described by Figure 3.15. The influence of NADW is illustrated, however, by a comparison of Figures 3.7a, 3.7d, 3.7e and 3.7g, at #Drake, #0E_N, #0E_S and #30E respectively. NADW is well oxygenated, has large salinities and nutrient

deficiencies compared to CDW. As seen in the previous section, within the western South Atlantic, NADW divides the CDW layer into upper (UCDW) and lower (LCDW) components. Here, UCDW is identified by nitrate, phosphate and temperature maxima, a minimum in oxygen and an increase in the silica concentration with depth. Figure 3.7d, #0E_N illustrates the oxygen and nutrient features of UCDW. The UCDW temperature maximum induced by overlying AAIW and Winter Water (see the low surface temperatures in Figure 3.7e, #0E_S) has been integrated out of #0E_N by the warmer surface waters north of the Subantarctic Front.

The lower component of ACC deep water, LCDW has a salinity maximum and nutrient minima derived from NADW. These features can be seen between about 2500 db and 3500 db in the #0E_N section. Within the Southwest Atlantic, LCDW can also be identified by an oxygen minimum as it overrides the northward spread of WSDW. However, as mentioned before, ventilation through mixing with WSDW occurs over the entire horizontal area provided by the Scotia Sea [*Locarnini et al.*, 1993] with the result that the integrated #0E_N section shows an oxygen maximum in the layers identified as LCDW by their salinity and nutrient characteristics.

On the eastern side of the South Atlantic Basin (see the #30E section illustrated in Figure 3.7g) the Southern Ocean water mass features which are most evident are the oxygen maximum of AAIW in the σ_θ layers between 26.2 and 27.2, the phosphate maximum of UCDW centered just below 1000 db, and the effect on the CDW of low NADW oxygen concentrations. This effect erodes with depth as the ventilated bottom water influences the water above. At 30°E, the LCDW appears to be higher in the water column than at 0°S. The σ_3 layers 37.00 to 37.09 which contain the salinity and oxygen maxima and phosphate minimum of LCDW are centered at about 3000 db in the #0E_N section. These same extrema, relative to the surrounding water mass characteristics are centered at about 2000 db in the #30E section. Between Drake Passage and 30°E (compare Figures 3.7a, 3.7e and 3.7g) the effect of

Weddell Sea Bottom Water (WSBW, with potential temperatures less than -0.7°C) incorporation into the bottom waters of the ACC has been to reduce the temperature and increase the oxygen content of the Antarctic Bottom Water (AABW)

Another interesting feature within the bottom water is the high silica concentration entering through Drake Passage. Thought to originate in the Pacific, Southeast Pacific Deep Water [*Sievers and Nowlin 1984*] with a core concentration of $135.5\text{ }\mu\text{M/L}$ at $\sigma_4 = 46.035$, is evident in the Drake section below $\sigma_3 = 41.63$ with an average concentration in the lowest layer of $136.5\text{ }\mu\text{M/kg}$. This maximum has eroded before reaching the Greenwich Meridian where deep silica concentrations are less than $130\text{ }\mu\text{M/kg}$.

At 132°E (Figure 3.7h), the ACC has passed through the Indian basin. The near surface oxygen maximum of AAIW is still clearly evident. The salinity minimum and phosphate maximum of UCDW are also visible. The oxygen minimum of UCDW evident at Drake Passage and 0°E , but eroded at 30°E , is again strongly apparent, indicating a lack of ventilation with the Indian sector of the Southern Ocean. The salinity maximum and phosphate minimum of LCDW are barely visible, now centered at about 2500 db. The associated oxygen maximum produced by the ventilation from WSBW within the Atlantic, is completely gone. There are still average temperatures in the bottom layer less than 0°C . However, whatever bottom waters may be formed outside of the Atlantic sector of the Southern Ocean must be somewhat warmer than WSBW as the very cold bottom water temperatures (-0.7°C in the lowest layer at 30°E) are eroded somewhat at 132°E (-0.5°C) and are quite a bit warmer at Drake Passage (0.2°C).

For the purpose of discussing the model results, the water masses within the Southern Ocean meridional sections are divided into the 5 water mass layers described in Table 3.11. The water masses which are found within the Southern Ocean to the north of the ACC in relation to the particular sections which are used in the models

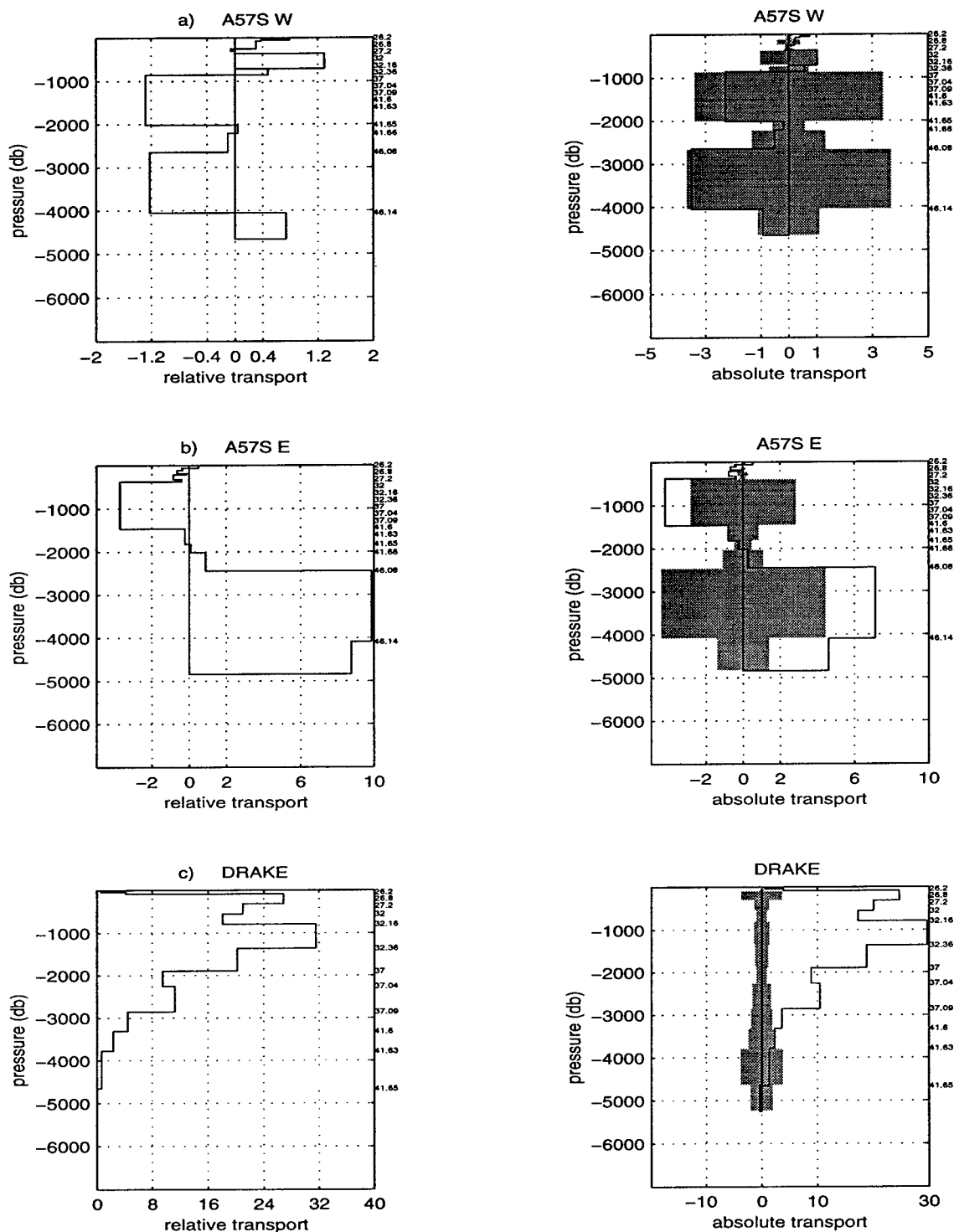


Figure 3.16: The zonally integrated mass transport in potential density layers for the sections: (a) #A57S.W and (b) #A57S.E and the meridionally integrated mass transport for (c) #Drake. The profiles on the left are based on a zero velocity at the reference level. Those on the right are based on the absolute velocity field computed by standard model. The shaded region indicates the estimated 1 σ uncertainty in the layer transports due to the uncertainty in the reference level velocities. The Ekman transport is included in outcropping layers.

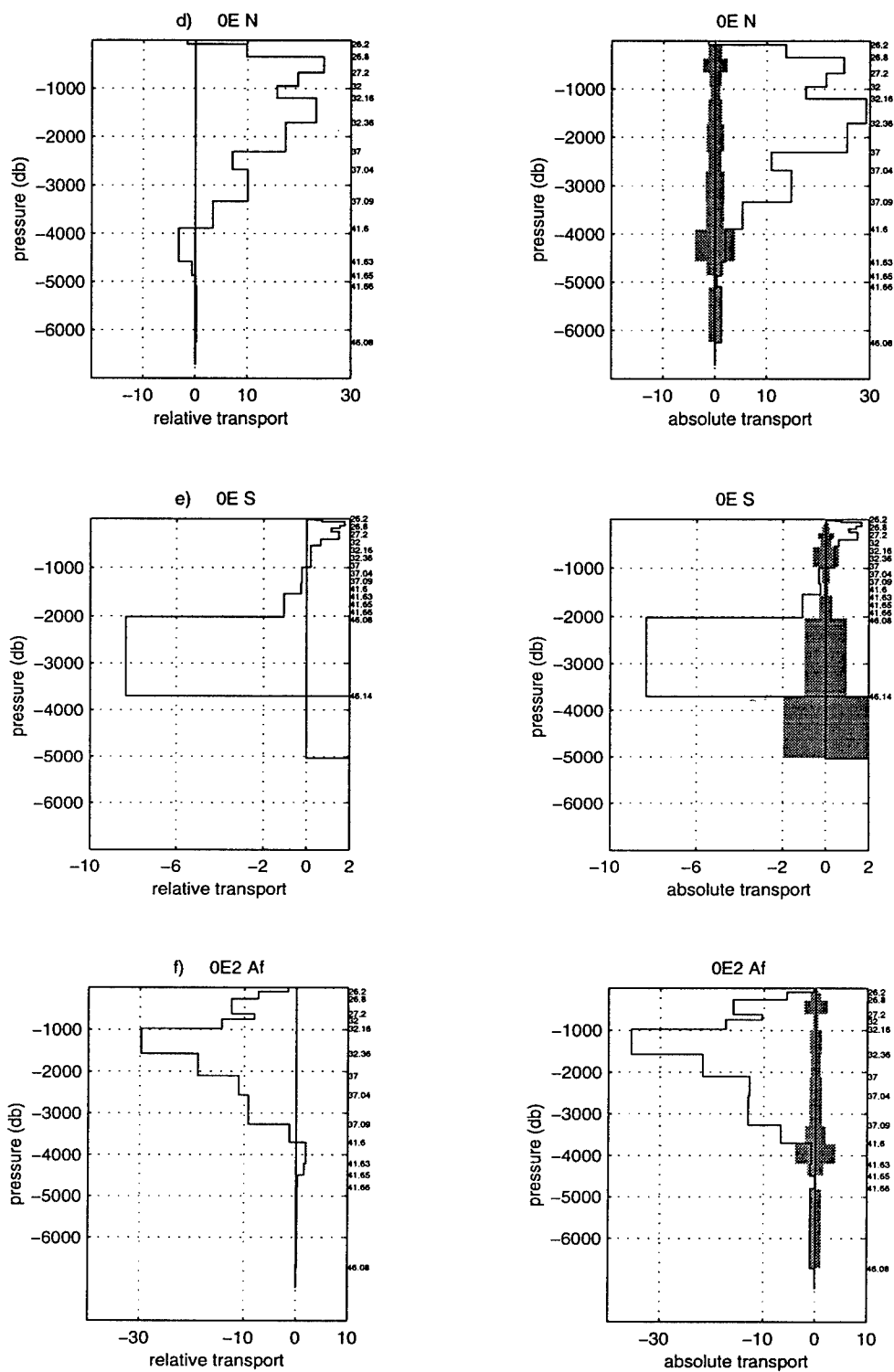


Figure 3.16 continued: The meridionally integrated mass transport in potential density layers for the sections: (d) #0E_N, (e) #0E_S and (f) #0E2Afr. Note that most of the transport across #0E2Afr is moving southeastward.

Water Mass	Layers	Interfaces	Description
Surface	1-2	surface to $\sigma_0 = 26.80$	variable characteristics
AAIW	3-4	$\sigma_0 = 26.80$ to $\sigma_1 = 32.00$	oxygen maximum
UCDW	5-6	$\sigma_1 = 32.00$ to $\sigma_1 = 32.36$	nutrient maximum, decreasing oxygen
LCDW	7-12	$\sigma_1 = 32.36$ to $\sigma_3 = 41.65$	nutrient minimum, increasing oxygen
AABW	13-16	$\sigma_3 = 41.65$ to	temperature minimum, increasing oxygen

Table 3.11: Approximate definition of water masses for sections which cross the ACC, by the Southern Ocean potential density layers (see Tables 2.5c and 2.5d).

are described in *Macdonald* [1991]. The water masses within the South Atlantic were described in the previous section. The water masses with the southern portion of Indian and Pacific Basins (Figures 3.9b, 3.8d and 3.8d) contain variations of the water masses found within the region of the ACC and in particular, also include a layer of central waters whose characteristics are specific to the individual basin. Profiles of mass transport from the standard model, integrated across the sections in the southern ocean are shown in Figure 3.16.

The ACC dominates the circulation pattern of the Southern Ocean. The classic picture of the ACC with two frontal zones delineated by sharp surface temperature gradients is derived from data taken back in the early part of the century, but it still represents our general understanding of the Southern Ocean circulation. The surface flow of the region of ACC is maintained through wind stress forcing. The ACC flows in the same direction as the wind but extends to far greater depths than the direct Ekman influence, as below the wind-driven surface layer the distribution of density maintains a geostrophic equilibrium. The frontal zones (Figure 3.17), now known to extend from the near surface to the bottom [*Nowlin and Clifford* 1982; *Whitworth and Nowlin* 1987] are narrow regions of sharp density gradients and strong currents.

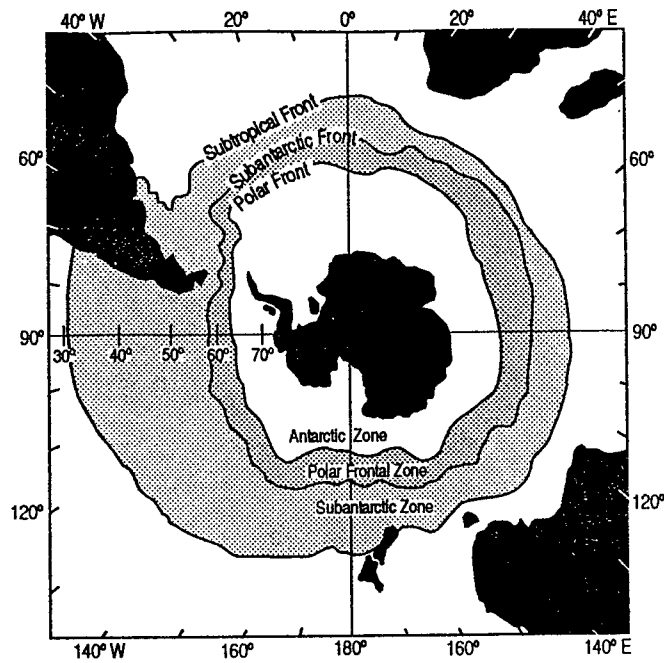


Figure 3.17: Schematic representation of the fronts (Subtropical, Subantarctic and Polar) which divide the waters around Antarctica into separate zones (Subantarctic, Polar Frontal and Antarctic). This figure is adapted from Figure 4 of *Nowlin and Klinck* [1986].

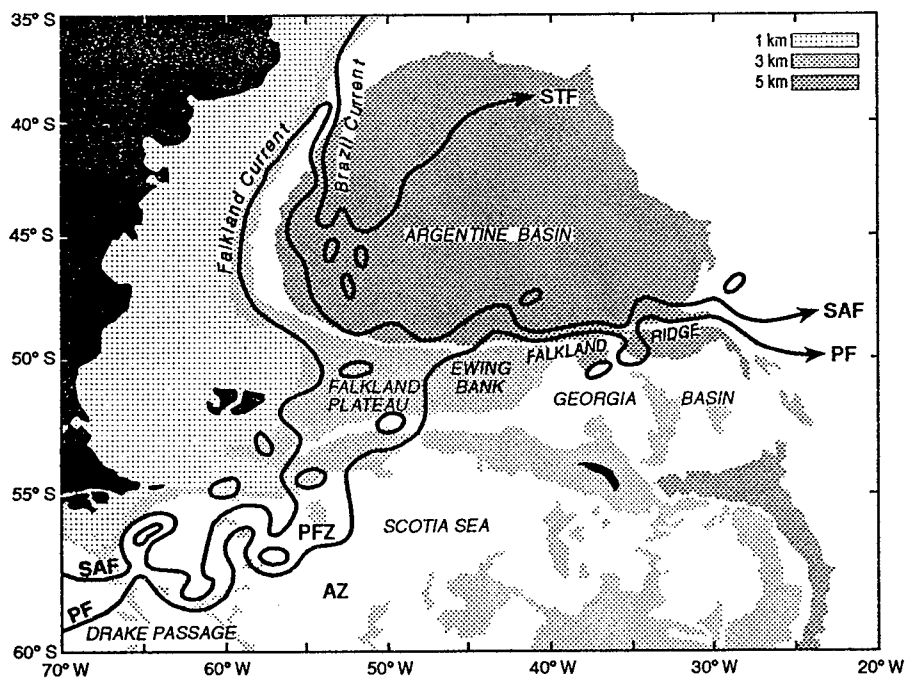


Figure 3.18: A more detailed schematic representation of the Southern Ocean frontal features together with the bathymetry in the western South Atlantic where the ACC exits Drake Passage. This figure is adapted from Figure 2 of *Peterson and Whitworth* [1989].

Nowlin and Clifford [1982] found maximum geostrophic velocities of the order of 30 to 45 cm s^{-1} in Drake Passage. *Peterson and Whitworth* [1989] found surface velocities exceeding 80 cm s^{-1} to the northeast of Drake Passage (north of Ewing Bank) in a region where the Subantarctic and Polar Fronts appear to merge into a single intensified current (Figure 3.18). Nevertheless, the velocities throughout most of the ACC are minimal compared to most western boundary currents with the great majority of the other estimates in the literature being lower, at about 15 cm s^{-1} . It is the great depth of the flow (down to 4000 m) which produces the enormous estimated ACC volume transport, on the order of 130 to $140 \times 10^6 \text{ m}^3 \text{ s}^{-1}$, which is comparable to, if not greater than most western boundary current transport estimates.

The ACC is highlighted in the velocity fields of the meridional sections: #Drake in Figure 3.11a, #0E in Figures 3.11d and 3.11e, #0E2Afr in Figure 3.11f, #30E in Figure 3.11g and #132E in Figure 3.11h. The structure of the absolute velocity field of the ACC at Drake Passage from the Meteor 11/5 data set is characterized by four deep zonal jets with horizontal scales of about 100 km. It is quite similar to the absolute velocity field constructed by *Rintoul* [1991] from the FDRAKE-75 data set although the maximum velocities here are $> 40 \text{ cm s}^{-1}$ compared to the FDRAKE-75 maximum velocities of order 25 cm s^{-1} . The largest velocities are found, as expected [*Peterson and Whitworth* 1989 and *Rintoul* 1991], to the north in the Subantarctic Front.

The velocity field relative to the $\sigma_3 = 41.66$ reference level, which is essentially the bottom, has a transport of $150 \times 10^9 \text{ kg s}^{-1}$. To keep the absolute transport to the $142 \pm 5 \times 10^9 \text{ kg s}^{-1}$ required by the standard model while simultaneously meeting the conservation constraints provided by the areas to the east and west of Drake Passage, the standard model adjusted the reference level velocities so as to decrease the transport in the fastest (northern) jet and to increase it in two out of the other three slower (more southerly) jets. A similar pattern of reference level velocities was

found by *Rintoul* [1988] who use the FDRAKE-75 hydrography in his inverse of the southern South Atlantic. As has been previously found, the jets at 0°E [*Whitworth and Nowlin* 1987] are broader (300 km scale) and slower (maximum velocities less than 25 cm s^{-1}). A little further to the east, the jets as depicted by the #0E2Afr section represent surface to bottom flows. This section also highlights the beginnings of the Benguela Current (as discussed in the previous section) and the intense eddy activity and recirculation emanating from the Agulhas retroflection region. These features are seen again in the #30E velocity field. By the time the ACC has reached 30°E and is entering the Indian Basin, maximum velocities have decreased to less than 20 cm s^{-1} . At 132°E, between the Indian and Pacific Basins, the main jet of the ACC has a meridional scale of about 400 km and maximum velocities are again on the order of 25 cm s^{-1} . It should be noted that at both the 30°E and 132°E the broadening of the jet may be in part artificially induced by the relatively wide station spacing.

In the #0E_S section (Figure 3.11e) the eastward flow to the north and the more southerly westward return flow are associated with the Weddell Gyre. At 57°S, across the northern boundary of the Weddell Sea, an alternating N-S flow is apparent, indicating that deep water is escaping from the Weddell Sea into the Scotia Sea as suggested by *Locarnini et al.* [1993]. The #A57S figures also indicate some northward flow of bottom water through the South Sandwich Trench. Above the trench, near the surface there is what appears to be a jet. This feature may be related to the anticyclonic gyre which was apparent in the AJAX data set at this longitude and which *Rintoul* [1991] suggested might be associated with the trench topography.

The constraint placed on the transport at Drake Passage is met with a value of $141.1 \pm 3.4 \times 10^9 \text{ kg s}^{-1}$. This flow is met by the $20 \pm 1 \times 10^9 \text{ kg s}^{-1}$ of NADW coming from the north through #A27S-W section and the Weddell Sea deep and bottom waters coming through the #A57S sections from the south. The velocity fields in-

Water Mass	Layers	#Drake	#0EN	#0E2Afr	#30	#132E
Surface	1-2	4±1	12±2	6±2	10±4	6±3
AAIW	3-4	45±4	47±3	26±3	29±4	53±7
UCDW	5-6	47±2	47±2	53±2	46±4	44±6
LCDW	7-12	45±6	60±5	56±4	64±6	49±9
BW	13-16	0±2	2±2	1±2	-5±3	-2±1
TOTAL	1-16	141±3	167±5	143±5	144±5	149±8

Table 3.12: Transport of Water Masses for sections which cross the ACC, defined by the Southern Ocean potential density layers (Tables 2.5c and 2.5d) and the water mass definitions (Table 3.11). The Ekman transport is included in the surface layers.

indicate that some Weddell Sea waters are escaping to the north across the western #A57S section, as has been suggested by *Locarnini et al.* [1993]. Most of the northward transport of WSDW (layers 12-15) crossing #A57S.W occurs between 34°W and 28°W. The northward transport of WSDW further to the west is small and not significantly different from zero. The net transport in the WSDW layers across #A57S.W ($-7 \pm 9 \times 10^9 \text{ kg s}^{-1}$) is southward and not significantly different from zero. It is balanced by a net northward transport across #A57S.E ($7 \pm 7 \times 10^9 \text{ kg s}^{-1}$).

The net transport of bottom water across #A57S.W at $-1 \pm 1 \times 10^9 \text{ kg s}^{-1}$ is to the south, but is also not significantly different from zero. It appears that within the #A57S.W section the topography and the ACC are not only doing an effective job of inhibiting the northward flow of WSBW into the South Atlantic just to the east of Drake Passage, but are also moving water (presumably mostly LCDW) into the Weddell Sea. Much of the net transport of WSBW ($4.6 \pm 1.4 \times 10^9 \text{ kg s}^{-1}$) which is moving northward into the South Atlantic is occurring in the eastern section #A57S.E through the South Sandwich Trench.

The large net southward mass flux ($-27 \pm 3 \times 10^9 \text{ kg s}^{-1}$) across #A27.W entering area I combines with the Drake Passage inflow to bring the eastward transport north of the Mid-Ocean Ridge to $167 \pm 5 \times 10^9 \text{ kg s}^{-1}$. The expansion of the ACC as it meets the North Atlantic and Circumpolar deep water masses within the South

Atlantic has been documented by *Whitworth and Nowlin* [1987] and *Locarnini* [1993]. The increase in the net eastward transport is of course, no longer evident across the 20°E section ($143 \pm 5 \times 10^9 \text{ kg s}^{-1}$). Table 3.12 shows that while much of the increase in transport across 0°E occurs in the surface and LCDW layers, the waters which leave the region before crossing 20°E lie in the AAIW layers.

Flow Between the Indian and Atlantic Basins

The transport totals integrated across the sections in area IV give the impression that the excess mass crossing 0°E flows directly from the South Atlantic Current into the flow directed northward up the coast of Africa. However, the intermediate and thermocline waters within and to the east of the Benguela Current are too warm and salty to have come directly from Drake Passage. The waters flowing into the South Atlantic across 27°S are both warmer and saltier than AAIW and some mixing is expected to occur within the southwestern Atlantic. The question is whether Benguela Current waters which will eventually feed the formation process of NADW are only a mixture of subtropical Atlantic water and Drake Passage water (the "cold water" path), or whether there is a significant contribution coming from the Indian Basin (the "warm water" path).

Gordon et al. [1992] suggest that a large portion of the water which eventually forms the Benguela Current (65%, 10 out of $16 \times 10^6 \text{ m}^3 \text{ s}^{-1}$ of the surface and upper thermocline water and 50%, 5 out of $9 \times 10^6 \text{ m}^3 \text{ s}^{-1}$ of the lower thermocline and AAIW) has taken a route which passes from the South Atlantic Current south of the Agulhas Return Current and into the Agulhas recirculation gyre. Within the southwestern Indian Basin this water is warmed and subjected to excess evaporation over precipitation before returning around the southern tip of South Africa, where it is mixed with South Atlantic Current water and eventually flows into the Benguela Current.

Comparing salinities to the north (34.4) and south (34.2) of the Agulhas Front at 33°E and finding little evidence of transfer across the front, *Read and Pollard* [1993] concur with the idea that AAIW continues to flow into the Indian Basin rather than turning immediately north into the South Atlantic. The Agulhas Front is not distinguishable from the Subtropical Front (STF) in the Conrad, #30E section. However, #30E shows similar salinity differences between the intermediate water flowing westward to the north of the STF and eastward to the south of the STF. It also shows some change in the phosphate concentrations across this frontal region ($2.2 \mu\text{M/kg}$ to the north, $2.35 \mu\text{M/kg}$ to the south). AAIW in the #0E2Afr section has lower values of about 2 to $2.2 \mu\text{M/kg}$. The South Atlantic Current in the #0E.N section also has concentrations of about 2 to $2.2 \mu\text{M/kg}$ at the depth of AAIW and up to $2.4 \mu\text{M/kg}$ in the CDW just below. The intermediate waters of the Benguela Current are characterized by low concentrations of about $2.1 \mu\text{M/kg}$ which could be derived from the South Atlantic Current and/or the westward flow through #0E2Afr. These distributions of salinity and phosphate support the argument that some AAIW may be passing into the Indian Basin before heading northward into the Atlantic. They also indicate that there may be some upwelling of CDW across isopycnals within the Agulhas region.

Figures 3.19a and 3.19b describe the transports around area IV in layers 1 to 2 (surface) and 3 to 6 (intermediate). It should be kept in mind that there is some difficulty in comparing the standard model values directly with those of *Gordon et al.* [1992] because of the particular layer definitions used in this study. *Gordon et al.*'s definition of surface and thermocline water was water warmer than 9°C . The definitions used in Figure 3.19a and 3.19b correspond to waters warmer than about $9 \pm 1^\circ\text{C}$ (averaging layer temperatures of each of the sections involved). *Gordon et al.*'s definition of intermediate water was water colder than 9°C but above 1500 db. The standard model definition corresponds to waters warmer than about $2.5 \pm .4^\circ\text{C}$, with a lower boundary of 1600 ± 200 db.

Surface & Thermocline

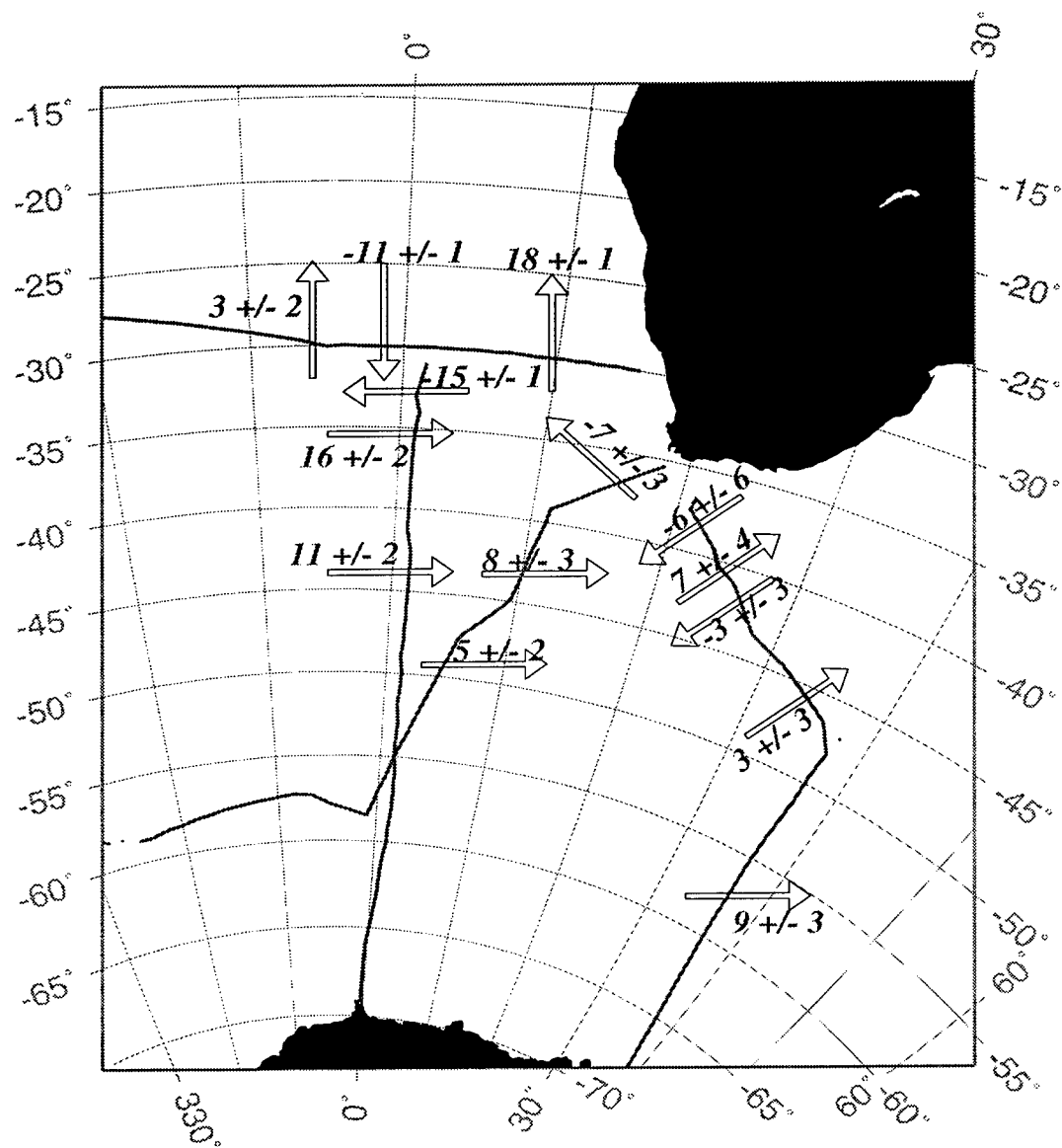


Figure 3.19a: The standard model transport (in units of 10^9 kg s^{-1}) in the surface and thermocline layers as defined in Table 3.11 around the southern tip of Africa, describing the upper layer exchange between the Indian and Atlantic Basins. Ekman transport has been subtracted.

Intermediate Layers

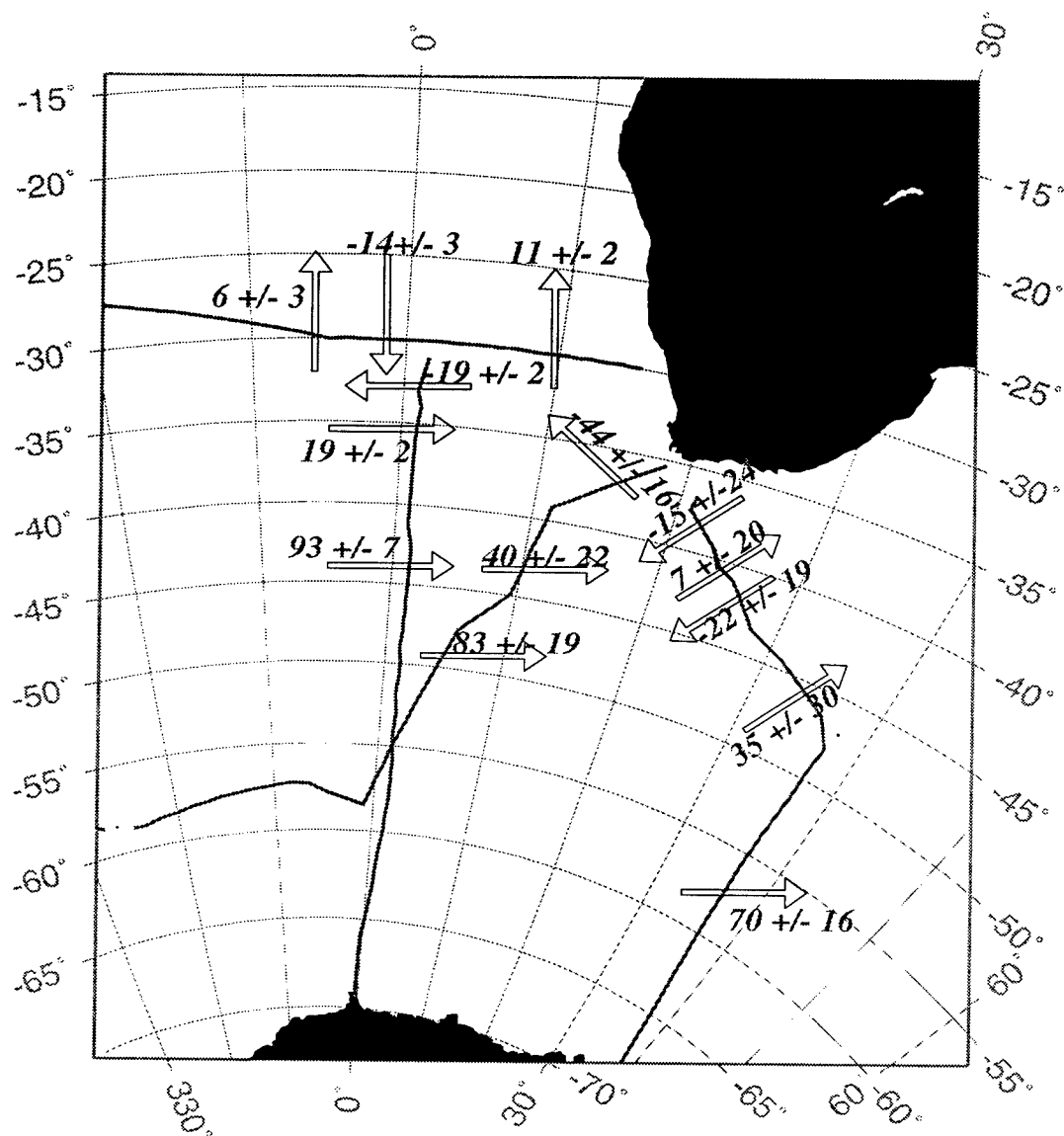


Figure 3.19b: The standard model transport (in units of 10^9 kg s^{-1}) in the intermediate layers as defined in Table 3.11 around the southern tip of Africa, describing the exchange between the Indian and Atlantic Basins.

Within the surface and thermocline layers of the standard model there are two sections of westward flow, carrying a total of about $9 \times 10^9 \text{ kg s}^{-1}$ across the #30E section to the north of 40°S . The westward flow continues with $7 \times 10^9 \text{ kg s}^{-1}$ flowing across #0E2Afr. Within the intermediate layers there are $37 \times 10^9 \text{ kg s}^{-1}$ passing westward through #30E and $44 \times 10^9 \text{ kg s}^{-1}$ continuing to the northwest through the #0E2Afr sections. So it would appear that the standard model finds similar westward transport of surface and thermocline waters (about $8 \times 10^9 \text{ kg s}^{-1}$ compared to $10 \times 10^6 \text{ m}^3 \text{ s}^{-1}$) and a good deal more westward transport of intermediate waters (about $40 \times 10^9 \text{ kg s}^{-1}$ compared to $5 \times 10^6 \text{ m}^3 \text{ s}^{-1}$). These results *may* support Gordon *et al.*'s findings and *may* support the dominant warm water path scenario. However, one must be careful in drawing such conclusions, for although there appears to be significant westward flow across the #0E2Afr section, the westward flow across the #30E section is *not* significantly different from zero in the surface and thermocline layers and is only barely so in the intermediate layers! Furthermore, across the #0E2Afr section most of the westward flow comes from what appears to be a front in temperature and salinity fields, a single station pair containing very strong westward velocities. As there is no documented evidence of strong consistent westward flows in this region, the suspicion is that, this feature is actually a poorly sampled eddy, and that in fact the amount of net westward flow across this section is probably less than what is implied by these numbers.

The main difficulty here is that the model's steady state assumption has become invalid in this region where the eddies moving through one section are unrelated to those moving through the other sections. It would appear from these results that pinning down fractions of water masses which may come from the Indian Ocean (*i.e.* quantifying the relative strengths of the warm and cold water paths) using hydrography is going to require much more data and may not be possible. Repeat sections and perhaps the inclusion of satellite data might provide a reasonable time mean for use with the present model or possibly provide the information necessary for a time

dependent model, either of which would likely be better suited to drawing conclusions about the mean circulation in this region.

Flow Between the Pacific and Indian Basins

Water properties from the Southern Ocean can enter the Indian and Pacific Basins at their southern boundaries. These properties can be modified within basins and are exchanged between them both to the South of Australia and through the Indonesian Archipelago. The standard model places a constraint of $10 \pm 10 \times 10^9 \text{ kg s}^{-1}$ on the flow between the Pacific and Indian Basins (P-I henceforth) through the Indonesian Archipelago. The model produces a throughflow of 9 ± 7 . The most obvious effect of the P-I throughflow within the Southern Ocean is the increased transport between Antarctica and Australia across #132E ($151 \pm 8 \times 10^9 \text{ kg s}^{-1}$) as the waters are carried from the Indian back to the Pacific Basin (Table 3.12). Most of the net southward transport in the Indian Basin across #I32S occurs in the surface (layers 2 and 3) and intermediate layers, while about half of the net northward transport in the Pacific across #P43S and #P28S occurs in the LCDW layers. As might be expected from the Ekman convergence between 43°S and 28°S , the other half occurs in the surface layers across #P43S and in the intermediate layers across #P28S. The model's adjustments to the transport of various water masses are consistent with the mass and property conservation constraints in the region. These adjustments support the view of a net transport of both deep and intermediate waters moving northward into the Pacific. Some of these waters upwell between 28°S and 10°N and may represent a southern source of P-I throughflow water. The next sections look at the circulation in the Pacific and Indian Basins based on the allowed exchange. Chapter 4 looks at the effects upon the regional and global circulation of both varying the reference levels and allowing unconstrained throughflow.

3.4.3 The Pacific Ocean

Reid [1973] gives a detailed description of the characteristics of the South Pacific waters above 2000 m and the review of *Reid* [1986] surveys much of what is currently known about the circulation within the South Pacific. The main features of the circulation are briefly reviewed here. The color plates of *Stommel et al.* [1973] are extremely useful in identifying the features discussed, as are the many sections which illustrate the *Reid* [1986] article. Much of the recent work which has gone on in the Pacific is described in the Joe Reid volume of *Deep Sea Res.*[1991]. The circulation at 24°N is also discussed in *Bryden et al.* [1991] and the circulation to the north of 24°N by *Roemmich and McCallister* [1989]. *Wijffels* [1993] covers the Pacific region between 14°S and 10°N.

The subtropical gyre which describes the surface circulation of the South Pacific is bounded by the South Equatorial Current (SEC), the East Australia Current, the Antarctic Circumpolar Current (ACC) and the Peru Current. It is known that the SEC displays fairly large seasonal variations but retains a consistent westward flow, with most of the seasonal variation due to the monsoons limited to the region north of 10°S. The East Australia Current, on the other hand, is part of an extremely variable region. It appears that not only is the current transient and discontinuous along the coast, but that its southwesterly flow is associated with an offshore northwesterly flow and large (200-300 km) anticyclonic eddies [*Hamon and Golding*, 1980 from *Pickard and Emery*, 1990].

Not surprisingly, the mean transport of the East Australia Current is not well determined. Early estimates were as high as $-57 \times 10^6 \text{ m}^3 \text{ s}^{-1}$, relative to 3500 db at 32°S [*Boland and Hamon*, 1970]. A more recent estimate which came out of an analysis which attempts to better determine the mean, was much lower, only $-9.5 \times 10^6 \text{ m}^3 \text{ s}^{-1}$ at 28°S between the coast and 171°E [*Ridgeway and Godfrey*, 1993].

The poleward flow of the East Australia Current is apparent near the western shore of the velocity sections of the two South Pacific data sets used in this study (Figures 3.12e and 3.12d at 43°S and 28°S, respectively). At 28°S there is a southward transport of $-39 \pm 6 \times 10^9 \text{ kg s}^{-1}$ within 300 km of the coast. Between the coast and 171°E, there is a net transport of -21 ± 11 . At 43°S, within the 700 km east of the shelf there is a net transport of $-21 \pm 7 \times 10^9 \text{ kg s}^{-1}$ southward. Extending the integration eastward, tends to reduce this estimate.

On the eastern side of the Pacific the Peru Current flows equatorward carrying with it the relatively fresh, cool waters of the Southern Ocean. Below and shoreward of this eastern boundary current is the somewhat more saline, poleward flow of the Peru-Chile Current which appears to be of subequatorial origin [Fonesca 1989]. These two currents are also evident in the South Pacific velocity sections.

In the deep waters of the Pacific (described in detail by Warren [1973, 1981a]) one of the most notable features of the cyclonic gyre circulation is the northward flow of the deep western boundary current through the south western Pacific basin⁵, carrying about $20 \times 10^6 \text{ m}^3 \text{ s}^{-1}$ [Warren 1981a]. According to Reid (1986), this flow is not completely confined to the western boundary region but spreads out across the entire central basin. In layers 9–12 of the #P43S section there is a net northward transport of $10 \pm 6 \times 10^9 \text{ kg s}^{-1}$ (Figure 3.20a) of LCDW. There is northward transport of deep water against the western boundary of the western basin. There is also a broad region of weak northward transport of deep waters on the eastern side of the basin, over the East Pacific Rise (Figure 3.12e). At #P28S the deep layers carry $11 \pm 6 \times 10^9 \text{ kg s}^{-1}$ (Figure 3.20b) and while there is ample evidence of the northward flow of deep water across much of the western basin, most of the transport is confined to the deep western boundary current which carries $19 \pm 1.5 \times 10^9 \text{ kg s}^{-1}$ in layers 9

⁵The effective western boundary of the deep South Pacific is not Australia, but New Zealand and the Tonga-Kermadec Ridge.

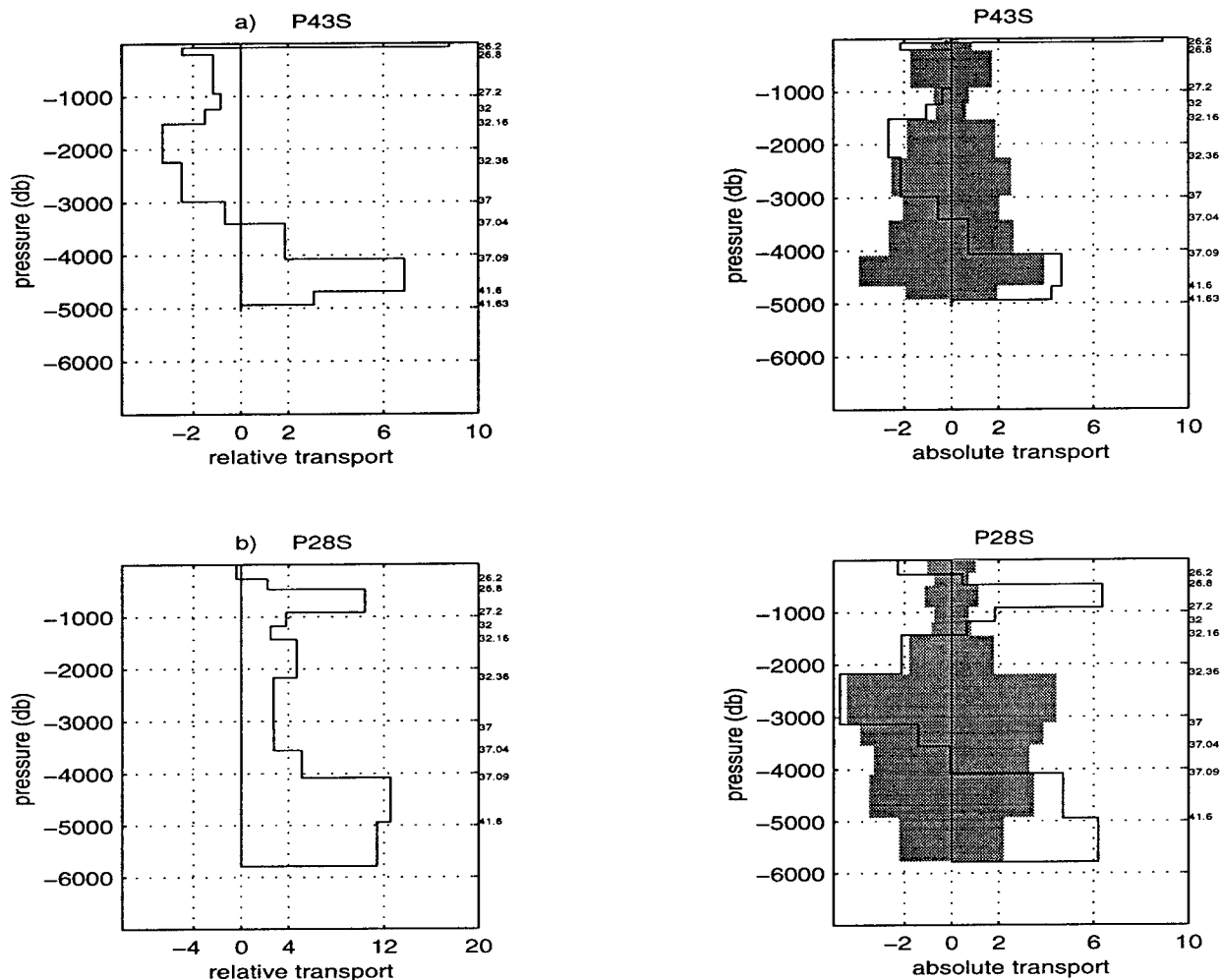


Figure 3.20: The zonally integrated mass transport in potential density layers for the sections: (a) #P43S and (b) #P28S. The profiles on the left are based on a zero velocity at the reference level. Those on the right are based on the absolute velocity field computed by standard model. The shaded region indicates the estimated 1σ uncertainty in the layer transports due to the uncertainty in the reference level velocities. The Ekman transport is included in outcropping layers.

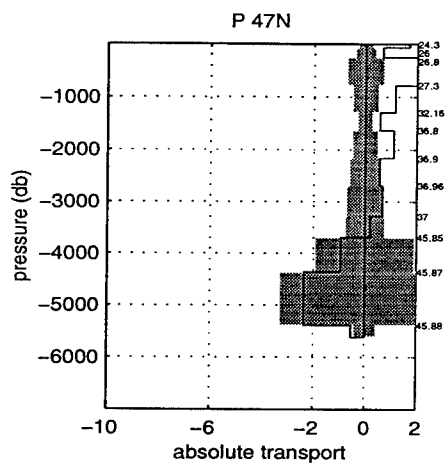
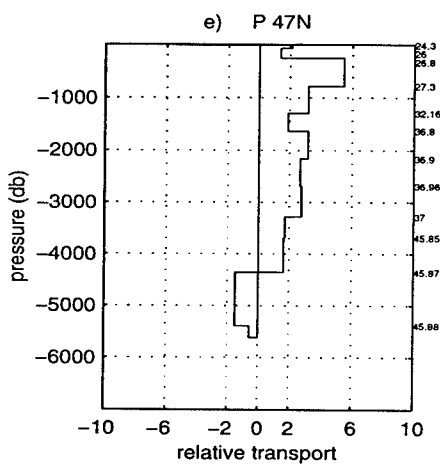
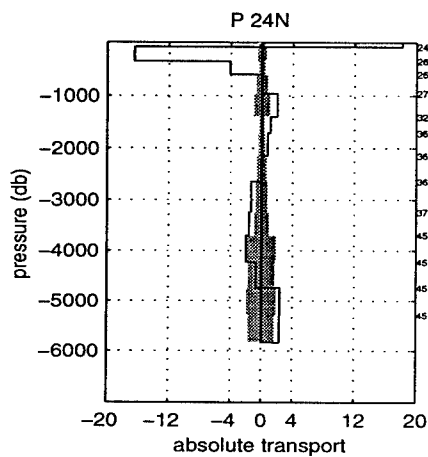
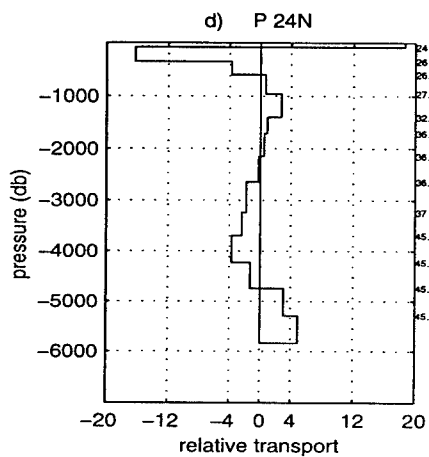
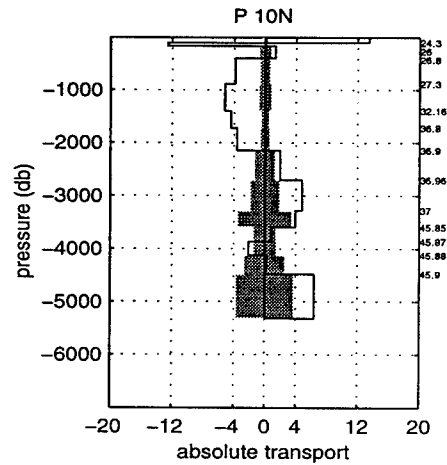
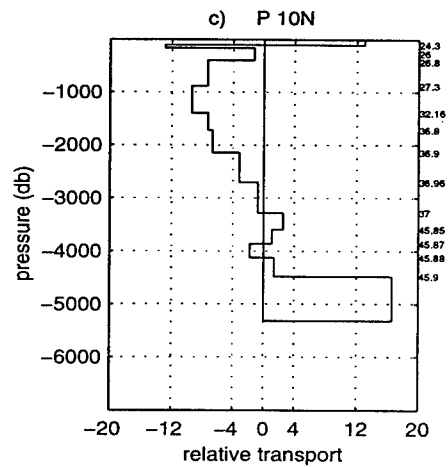


Figure 3.20 continued: The zonally integrated mass transport in potential density layers for the sections: (c) #P10N, (d) #P24N and (e) #P47N.

and below. The East Pacific Rise separates the eastern and western basins and some poleward flow of waters at mid-depths (layers 5–8) also exists east of the East Pacific Rise. The deep Tasman Sea is not a region of deep throughflow as it is closed off to the north at depths greater than 2850 m. The standard model estimate of northward transport of deep and bottom water into the South Pacific is similar to the $7 \times 10^9 \text{ kg s}^{-1}$ suggested by the *Macdonald* [1993] and the $12 \times 10^9 \text{ kg s}^{-1}$ suggested by *Wunsch et al.* [1983].

Although the Pacific is open to the south, *Mantyla and Reid* [1983] point out that the deepest pathway from the Pacific Antarctic lies not into the open South Pacific but along a route eastward into the Drake Passage. Therefore, the bottom water which spreads northward into the Pacific is the least dense of the Antarctic waters, as is evident in Table 2.5c where there is no water below layer 12 at #P43S and none below layer 11 at #P28S.

North of the equator the eddy field of the tropical Pacific is evident in the velocity field for the 10°N section (Figure 3.12c) and is reminiscent of the same rich variability found at 11°N in the Atlantic (Figure 3.10e). Against the west coast at #P10N the southward flow of Mindanao Current carries $-23.5 \pm 0.3 \times 10^9 \text{ kg s}^{-1}$ in the upper 400 db of the water column. This estimate is well within recent estimates, $13\text{--}33 \times 10^9 \text{ kg s}^{-1}$ [*Wijffels*, 1993; *Lukas et al.*, 1991; *Toole et al.*, 1990, *Toole et al.*, 1988]. Good resolution of the Mindanao Current is important as it represents the means of transport for a northern source of P–I throughflow water into the Indonesian Archipelago [*Ffield and Gordon*, 1992].

At 24°N (Figure 3.12b), the Kuroshio lies against the west coast and carries $26.5 \pm 1.6 \times 10^9 \text{ kg s}^{-1}$ northward into the East China Sea, in the upper 1000 m of the water column. This transport estimate is consistent with the initial constraint taken from *Bingham and Talley* [1991]. Beneath the Kuroshio is a small (less than $1 \times 10^9 \text{ kg s}^{-1}$) southward transport. The strong eddy field to the east of the Kuroshio

Water Mass Name	Model Layer	Temperature Limits (°C) at		
		#P10N	#P24N	#P47N
Surface	1-2	> 13.4	> 12.2	> 6.1
NPIW	3-4	> 5.1	> 4.0	> 3.1
AAIW	5-7	> 1.9	> 1.8	> 1.7
NPDW	8-12	> 1.1	> 1.1	> 1.1
AABW	13-14	< 1.1	< 1.1	< 1.1

Table 3.13: Approximate definition of water masses by the model layers in the North Pacific. Except in the case of the bottom water, the temperature limits are average temperatures across the section of the lower layer boundary. The bottom water temperature limit is defined in terms of the average temperature of the upper layer boundary. The model layers numbers refer to those defined in Table 2.5g. Note that at #P47N the upper four layers all outcrop.

noted by *Bryden et al.* [1991] is also quite apparent in the velocity section. Further north at #P47N (Figure 3.12a) the mid-ocean velocity field is somewhat less variable than the fields to the south. The western end of #P47N however, lies within an extremely variable region of the Oyashio and Kuroshio [*Talley et al.*, 1991] and therefore, there is no obvious single western boundary current in the section.

Within the North Pacific, the water masses have been divided according to Table 3.13. The characteristics of the upper 1000 m of the subtropical North Pacific are quite variable as each of the layers represents waters of differing origin [*Roemmich et al.*, 1991]; (surface waters of subtropical origin, North Pacific intermediate waters (NPIW) of subpolar origin and AAIW from the Southern Ocean). NPIW is found at about $26.8 \sigma_\theta$ and is recognized as a salinity minimum across the basin. It is most readily apparent in the #P24N section (Figure 3.8b) at about 800 db. The AAIW water mass which lies below the NPIW layers is associated with an oxygen minimum [*Bryden*, 1991]. This minimum can be seen in all three of the North Pacific sections at about $27.3 \sigma_\theta$. The deep waters of the North Pacific (NPDW) are fairly uniform in T and S, and show increasing oxygen concentrations and decreasing nutrient concentrations with depth. *Bryden et al.* [1991] define NPDW as the waters between

1.9° and 1.05°C, 2000–4700 m at 24°N. The abyssal waters which do make it into the North Pacific from the south have relatively warm temperatures, $\sim 1^\circ\text{C}$.

The zonally integrated transport profiles for the North Pacific sections are shown in Figures 3.20c–e. The northward flow of deep and bottom waters into the North Pacific is balanced by the southward flow of intermediate waters. At #P10N, NPIW is not easily distinguishable from AAIW as both the salinity and oxygen minima lie in the same layer, so not surprisingly, there are indications of both northward and southward flow in the intermediate layers. In the deep layers, although there is some southward transport ($-2.1 \pm 1.5 \times 10^9 \text{ kg s}^{-1}$) in layer 12 ($\sigma_4 = 45.87$ to $\sigma_4 = 45.885$), the net transport of deep water is northward ($9.3 \pm 3.1 \times 10^9 \text{ kg s}^{-1}$) as is the net bottom water transport ($6.5 \pm 3.8 \times 10^9 \text{ kg s}^{-1}$). The northward transport of deep waters is inconsistent with previous findings and the idea that these waters originate to the north. Test models which were used to investigate this feature of the circulation pattern are discussed later (see page 184).

In the North Pacific, the subtropical and subpolar gyres dominate the upper layer circulation, with strong northward transport within the western boundary currents balanced by return flow within the interior [Roemmich and McCallister 1989]. The standard model's $26.5 \pm 1.6 \times 10^9 \text{ kg s}^{-1}$ Kuroshio transport is consistent with the initial estimate of Bingham and Talley [1991] (Table 3.1). Within the western basin (to the east of the Kuroshio, 127°E and to the west of the Izu–Ogasawara Ridge at about 141°E) there is a net northward transport of $12 \pm 5 \times 10^9 \text{ kg s}^{-1}$. The central basin east of Hawaii, carries a net southward transport of $-31 \pm 19 \times 10^9 \text{ kg s}^{-1}$. The eastern basin also supports a net southward transport ($-15 \pm 19 \times 10^9 \text{ kg s}^{-1}$) with $-21.9 \pm 3.4 \times 10^9 \text{ kg s}^{-1}$ in the upper four layers. In fact, all these transport estimates are dominated by the transport which occurs in the upper 1000 db of the water column. All significant northward transport of bottom waters occurs in the central basin east of Hawaii. As in Roemmich and McCallister [1991], at 47°N there is net south-

ward transport west of Emperor Seamounts in all layers while, except for a small net southward transport in the layers 8 to 12, the opposite is true in the eastern basin.

At 24°N, (Figure 3.20b) the net meridional transports from the standard model show,

surface layers.....	$2 \pm 2 \times 10^9 \text{ kg s}^{-1}$
NPIW.....	$-4 \pm 1 \times 10^9 \text{ kg s}^{-1}$
AAIW.....	$4 \pm 2 \times 10^9 \text{ kg s}^{-1}$
NPDW.....	$-6 \pm 3 \times 10^9 \text{ kg s}^{-1}$
AABW.....	$5 \pm 3 \times 10^9 \text{ kg s}^{-1}$.

These transport estimates agree well with the estimates of *Bryden et al.* [1991]: $4.3 \times 10^6 \text{ m}^3 \text{ s}^{-1}$ of AAIW ($4.5^\circ\text{C} > \Theta > 1.9^\circ\text{C}$), $-8.4 \times 10^6 \text{ m}^3 \text{ s}^{-1}$ of NPDW ($1.9^\circ\text{C} > \Theta > 1.05^\circ\text{C}$), $4.9 \times 10^6 \text{ m}^3 \text{ s}^{-1}$ of AABW ($1.05^\circ\text{C} > \Theta$). Changing the definition of NPIW by one layer makes a tremendous difference in the estimate of its transport, *e.g.* using the standard model layers 2–3 produces an NPIW transport of $-21 \times 10^9 \text{ kg s}^{-1}$. The sensitivity of the NPIW transport to its definition is consistent with the findings of *Bryden et al.* [1991] who declined to place an exact estimate on its magnitude. Although similar to the *Bryden et al.* estimate, the standard model estimate of northward moving AABW across 24°N is considerably less than that of *Roemmich and McCallister* [1989]. A model which tests the consistency of the *Roemmich and McCallister* solution with the standard model constraints is discussed in the next section.

North Pacific Test Models: 10°N

Northward transport of deep (NPDW) waters at 10°N in the Pacific as found by the standard model is inconsistent with previous findings and the idea that these waters originate to the north. A number of preliminary models were run to investigate this feature of the circulation. The constraints used in the standard model are a result of these runs.

	<i>Wijffels</i> [1993]		Layers		Test 1	Test 2	Test 3	Test 4	Test 5
Ekman	38.6				24.3	24.3	38.6	38.6	38.6
TC	$\Theta > 11.3$	-36.9	$\Theta > 13.4$	1-2	-37 ± 1	-36 ± 1	-37 ± 1	-37 ± 1	-36.4 ± 0.4
IW	$\Theta > 2.2$	-5.5	$\Theta > 2.5$	3-6	-6 ± 3	-10 ± 2	-12 ± 3	-16 ± 2	-12.3 ± 1.4
NPDW	$\Theta > 1.2$	-5.0	$\Theta > 1.2$	7-10	13 ± 4	5 ± 2	7 ± 4	2 ± 2	-4.2 ± 0.3
LCPW	$\Theta < 1.2$	9.6	$\Theta < 1.2$	11-14	3 ± 5	13 ± 2	5 ± 5	12 ± 2	10.1 ± 0.3
Applied	<i>Wijffels</i> values as Constraints				no	yes	no	yes	yes
b_{rms}					0.22	0.25	0.16	0.17	0.39

Table 3.14: Comparison of the *Wijffels* [1993] buoyancy conserving model results and the standard model results at 10°N in the Pacific in comparable model layers. Test 1 is the same as the standard model in the Pacific except that it uses the ECMWF estimate of Ekman transport. Test 2 uses the ECMWF Ekman transport estimate and the *Wijffels* transport results east and west of 165°E ($\pm 2 \times 10^9 \text{ kg s}^{-1}$) as constraints. Test 3 is the standard model. It is the same as Test 1 except that it uses the *Wijffels* estimate of Ekman transport. Test 4 is the same as Test 2 except that it uses the *Wijffels* estimate of Ekman transport. Test 5 is the same as Test 4 but applies the extra constraints more stringently by using an uncertainty of only $0.2 \times 10^9 \text{ kg s}^{-1}$. All transport values are in units of 10^9 kg/s . Velocities are in cm s^{-1} .

The first model, which was the original one and which we shall call Test 1, used the ECMWF winds to compute the Ekman transport across the #P10N section. Table 3.14 compares the #P10N zonally integrated transport estimates of the *Wijffels* [1993] buoyancy conserving model (column 2) with those of Test 1 (column 4) in comparable layers. The thermocline and intermediate layer values compare well; disagreement, however, occurs in the magnitude of the transport carried by the LCPW layers, and in the magnitude and direction of the transport associated with the NPDW layers. The *Wijffels* model broke the net southward transport of NPDW across 10°N into $6 \times 10^9 \text{ kg s}^{-1}$ flowing northward across the section to the west of 165°E and $-10.5 \times 10^9 \text{ kg s}^{-1}$ flowing southward to the east of 165°E . The Test 1 estimates are similar in the west ($3 \pm 10 \times 10^9 \text{ kg s}^{-1}$) and of opposite sign in the east ($11 \pm 10 \times 10^9 \text{ kg s}^{-1}$). The same pattern of discrepancy appears to a lesser degrees in the LCPW layers where *Wijffels* found $4.1 \times 10^9 \text{ kg s}^{-1}$ in the west and $5.7 \times 10^9 \text{ kg s}^{-1}$ in the east and the Test 1 model found $5 \pm 6 \times 10^9 \text{ kg s}^{-1}$ in the west and $1 \pm 7 \times 10^9 \text{ kg s}^{-1}$ in the east.

Although using the #P10N section, the *Wijffels* model is quite different from the one used here. It uses both other data and different model constraints. One advantage that it may hold over the our model in this region is that it makes use of a mean⁶ meridional line of hydrographic data to break the Pacific into eastern and western boxes at 165°E. These data allow the application of conservation constraints to either side of this line and so regulate a different (more constrained) adjustment of flows from those used by our models. We wanted to ask whether or not our model could support the *Wijffels* flow field. To answer this question, a number of further tests were run.

Test 2 simply attempted to constrain the flow in the NPDW and LCPW layers according the results of *Wijffels* to the west and east of 165°E. An uncertainty of $\pm 2 \times 10^9 \text{ kg s}^{-1}$ was used. The results are shown above in column 5 of Table 3.14. Increasing the northward transport of LCPW was easily accomplished. However, with transports of $10 \pm 2 \times 10^9 \text{ kg s}^{-1}$ and $-5 \pm 2 \times 10^9 \text{ kg s}^{-1}$ to the west and east of 165°E, respectively, the model was unable to produce a southward transport of NPDW.

To produce the results shown, the model doubled the magnitude of the velocities at the reference levels to west of 148°E and decreased and in some case reversed the of direction the reference level velocities to east of 103°W. Larger reference level velocities in the west may not be unreasonable as the reference levels supplied and used by *S. Wijffels* were intended for use with a mean of a number of repeat sections taken to the west of 141.5°E [*Wijffels* 1993], rather than with the #P10N data alone. However, under the assumption that these reference level velocities would have to be increased even more for the model to produce a net *southward* transport of NPDW, it was concluded that a net southward transport of deep water at 10°N in the Pacific was inconsistent with the model constraints as they existed. We then took the inves-

⁶The *Wijffels* [1993] line at 165°E is a mean of 23 hydrographic sections taken between 1984 and 1989 created for use with the #P10N section (1989) and another section at 14°S (1987).

tigation one step further to look at the effect of the initial Ekman estimates on the resulting flow field.

The estimates of Ekman flux used in the *Wijffels* model and our first two test models are substantially different. In balancing mass across this section the difference in Ekman flux has been taken up mainly in the NPDW layers in Test 1 (column 4 of Table 3.14) and spread more evenly throughout the water column below the thermocline in Test 2 (column 5 of Table 3.14). The ECMWF wind stress estimates are known to be low in the tropics [*Trenberth et al.* 1990] so to answer the question as to whether or not the northward transport in NPDW layers is a result of a low initial estimate of the wind stress, two further tests was run. Test 3 which turned out to be the standard model, applies the *Wijffels* buoyancy conserving model estimate of the Ekman transport ($38.6 \times 10^9 \text{ kg s}^{-1}$). The results (column 6 of Table 3.14) show that the constraints in the areas bounded by the 10°N section are met with somewhat smaller reference level velocities than those calculated by Test 1, which may indicate that a larger Ekman transport is more suitable for these data. However, although the increased estimate of Ekman transport reduces the estimate of northward transport in NPDW layers, it does not reverse the sign. Test 3 exhibits the same general pattern of circulation as Test 1, except that there is increased transport of intermediates waters and decreased transport of deep waters. The increase in intermediate flow is a move away from the profile suggested by *Wijffels*.

Test 4 includes both the extra constraints of Test 2 and the *Wijffels* estimate of Ekman transport across 10°N . The results (column 7 of Table 3.14) show a solution which includes increased estimates of both LCPW and IW transport and a net northward transport of NPDW which is not significantly different from zero. Although the rms value of \hat{b} has scarcely changed, a similar rearrangement of the reference level velocities has occurred as discussed above for the Test 1 versus Test 2 cases.

One further model was run. Test 5 is the same Test 4 except that the uncertainty applied to extra constraints has been reduced to $\pm 0.2 \times 10^9 \text{ kg s}^{-1}$. This extremely stringent application of the *Wijffels* solution to our model finally produces a net southward transport within the NPDW layers. To produce this solution still larger reference level velocities have been employed and although these reference level velocities are not so large (maximum $\hat{b} = 2.2 \text{ cm s}^{-1}$) as to be disbelieved, the solution is not acceptable as the model is now unable meet the top to bottom mass transport constraint. It might be possible to still further constrain this solution by applying the top to bottom constraint more stringently or perhaps by forcing a reduction in the net transport of intermediate waters, however, doing so will likely produce still larger reference level velocities.

Certainly a net southward transport of NPDW across the section would appear to be a more sensible solution in light of what is thought to be known about the origins of this water mass. However, the existence of a net northward transport in these layers at any one time can not be considered an impossibility. Whether or not the *Wijffels* or the Test 5 solutions are the "correct" ones remains in doubt. The Test 3 constraints (*i.e.* the *Wijffels* Ekman transport but no forcing of flow in the NPDW and LCPW layers) have been used in the standard model as 1) there is reason to doubt the accuracy of the ECMWF wind estimates in this region, 2) the net northward transport of NPDW is reduced and 3) the transport of LCPW is consistent with the *Wijffels* solution to within our computed uncertainty. The extra constraints of Tests 4 and 5 have not been used as their solutions are no more satisfactory.

So although it may be possible to produce a net southward transport of NPDW, we see that the circulation in this region is affected by more than just the input estimate of Ekman transport. Indeed, the deep and bottom transports in the Pacific are also affected by the *a priori* assumptions which have been made about the strength of cross-isopycnal transfer in the region (see Section 4.4, page 264). One is left to

wonder about the effect of each of the many differences between the *Wijffels* model and the standard model upon the solutions. In particular, consideration should be given to the effect of the the other data used in our models, as well as the effect of the mean meridional line of data at 165°E used in the *Wijffels* model and the suitability of the steady state assumption at the points where the meridional and zonal lines meet. If the reader is unwilling to accept a net northward transport in the deep waters at 10°N in the Pacific, then he/she is at liberty to conclude that the #P10N section is inconsistent with the standard model data and constraints. We would like to remind the reader that a southward transport is seen in standard model's deep layer 12 and suggest that further investigation is necessary to decide whether or not a true inconsistency exists and to discover its source.

North Pacific Test Models: 24°N and 47°N

Table 3.15 compares the zonally integrated results of the standard model with those of *Roemmich and McCallister* [1989] (R&M henceforth). Note, that no uncertainties were provided for the R&M values. The results agree quite well except that at 24°N the net northward transport of abyssal waters is reduced by half in the standard model. The difference in transport in the bottom layers is made up at mid-depths where the standard model's transport estimate is larger and in the opposite direction from that suggest by R&M. Keeping in mind that the R&M data set in the North Pacific also made use of meridional lines to constrain an inverse box model, we once again ask whether or not the standard model constraints are consistent with the previous findings.

The final column in Table 3.15 shows the zonally integrated results of the test model which used both the *Wijffels* [1993] and the R&M transport estimates as constraints. This is the same model as Test 4 in Table 3.14. An uncertainty of $\pm 2 \times 10^9 \text{ kg s}^{-1}$ was applied to each constraint equation. The model has little trouble in

#P24N	R&M	Std. Model	Test Model
surface - $\sigma_0 = 26.80$	-11.4	-10.9 ± 1.3	-10.9 ± 1.2
$\sigma_0 = 26.80 - \sigma_0 = 27.30$	-0.4	0.0 ± 0.8	-0.5 ± 0.7
$\sigma_0 = 27.30 - \sigma_2 = 36.96$	-0.7	3.9 ± 2.0	1.0 ± 1.3
$\sigma_2 = 36.96 - \sigma_4 = 45.885$	-7.5	-5.7 ± 2.7	-7.0 ± 1.5
$\sigma_4 = 45.885 - \text{bottom}$	9.6	4.5 ± 2.7	8.7 ± 1.5

#P47N	R&M	Std. Model	Test Model
surface - $\sigma_0 = 26.80$	2.9	2.1 ± 0.7	2.1 ± 0.4
$\sigma_0 = 26.80 - \sigma_0 = 27.30$	2.5	3.2 ± 0.7	3.3 ± 0.4
$\sigma_0 = 27.30 - \sigma_2 = 36.96$	3.4	3.4 ± 1.9	3.4 ± 1.1
$\sigma_0 = 36.96 - \sigma_4 = 45.885$	-4.1	-2.4 ± 3.1	-3.1 ± 1.6
$\sigma_4 = 45.885 - \text{bottom}$	0.7	-0.5 ± 0.5	-0.4 ± 0.4

Table 3.15: Comparison of the *Roemmich and McCallister* [1989] (R&M) North Pacific model (Ia) and the standard model geostrophic transport results at 24°N and 47°N. The last column contains estimates obtained from a model which uses R&M transport results as constraints. The R&M values are in units $10^6 \text{ m}^3/\text{s}$. The standard model values are in units of 10^9 kg/s .

meeting the new constraints at #P47N with the rms reference level velocity changing by less than 0.02 cm s^{-1} . At #P24N, there are large ($> 1 \text{ cm s}^{-1}$) changes in the reference level velocities in the west but these are not necessarily unacceptable as the affected pairs are associated with the Kuroshio Current in which we have allowed an *a priori* uncertainty estimate of 10 cm s^{-1} . The rms reference level velocity outside this region has changed by less than 0.01 cm s^{-1} between the standard model and the test model.

Wijffels [1993] and R&M find about $10 \times 10^9 \text{ kg s}^{-1}$ of bottom water flowing northward across #P10N and #P24N, respectively. R&M find that most of this water has upwelled before crossing the #P47N section. Although the standard model suggests that about half as much bottom water is flowing northward into the North Pacific, it also suggests that this water has upwelled south of 47°N. The test model finds no inconsistency in a larger upwelling between 24°N and 47°N.

Two conclusions are evident. First the solutions of *Wijffels* [1993] and *Roemich and McCallister* [1989] are consistent (to within the $\pm 2 \times 10^9 \text{ kg s}^{-1}$ applied) with one another in the lowest, LCPW layers. That is, they both suggest the large inflow of bottom waters into the North Pacific. Second, the standard model solution which is consistent with the *Bryden et al.* [1991] results at 24°N and the R&M results at 47°N , differs from the R&M results at 24°N . Nevertheless, the R&M #P24N solution is not inconsistent with our model data as we can constrain the solution to be consistent with theirs. The larger R&M estimate of total geostrophic transport across the #P24N section suggests that initial estimate of Ekman transport may play a role in determining the net bottom transport across this latitude as it did at 10°N . However, we are left with the same conclusion as before, that the standard model left to its own devices suggests a smaller net inflow of bottom water into the North Pacific of about $5 \times 10^9 \text{ kg s}^{-1}$.

Pacific Summary

The northward Ekman transports across the #P10N and #P24N sections are balanced within the upper few layers of the standard model. In the standard model at 10°N the deep waters entering from the south are returned below the thermocline ($\sigma_0 = 26.0$). At 24°N the return flow occurs for the most part in the deep layers and was supplied by inflow of AABW and AAIW. In the South Pacific at 28°S latitude the deep inflow is returned at depths greater than 2000 db. These patterns are consistent with previously published results [*Bryden et al.* 1991; *Wijffels* 1993] in their suggestion of two overturning cells within the Pacific: one shallow, one deep and little communication between the two.

The standard model suggests that about half the abyssal waters entering from the south are upwelled out of the lowest layers between 28°S and 10°N . The other half upwells between 24°N and 47°N . Strong upwelling of abyssal waters was also

found by *Roemmich and McCallister* [1989]. Left to its own devices, the standard model produces an estimate of the magnitude of the northward transport of abyssal waters from the Southern Ocean into the South Pacific which is similar to previous studies [*Wunsch et al.* 1983; *Macdonald* 1993], that is $10 \pm 6 \times 10^9 \text{ kg s}^{-1}$. The standard model's estimate for the continued northward transport of these waters into the North Pacific ($5 \pm 5 \times 10^9 \text{ kg s}^{-1}$) is lower than some previous estimates, in particular those of *Roemmich and McCallister* [1989] and *Wijffels* [1993]. However, at 24°N , the standard model estimate is consistent with the findings of *Bryden et al.* [1991].

Test models have shown that the larger estimate of abyssal inflow is also consistent with the model data and other model constraints. So, the amount of abyssal waters entering the North Pacific is still in question. For the purposes of this thesis, the standard model solution in the Pacific will be left as is, without constraints which attempt to force it to look like previously estimated circulation patterns. Suffice it to say that the standard model can reproduce the particular features in the circulation discussed above when constrained to do so. The one exception found was the southward transport of NPDW at 10°N , which could only be produced in conjunction within an overall mass imbalance across the section.

3.4.4 The Indian Ocean

The recent paper by *Toole and Warren* [1993] includes a detailed discussion of the topography and patterns of flow and transport within the South Indian Ocean. This work is based on the 32°S Charles Darwin section and references the older 18°S section. Both these data sets are used in this study. The absolute velocity fields for the 18°S and 32°S sections are illustrated in Figures 3.13a and 3.13b.

The anti-cyclonic surface circulation of Southern Indian Ocean has its northern limit at $\sim 10^\circ\text{S}$ [*Tchernia* 1980]. The southern limit is the ACC. In February this

southern boundary reaches to 38°S, but in August it is limited to about 30°S [*Lutjeharms and Valentine* 1984]. At 18°S there are two effective western boundaries for the surface flow in the Southern Indian Ocean. The westernmost is the coast of Africa. The island of Madagascar creates the second. According to *Warren* [1981b] the northward mid-ocean transport at 18°S of upper layer waters of about $20 \times 10^6 \text{ m}^3 \text{ s}^{-1}$ is largely balanced by the southward flow along the east coast of Madagascar. The model section #I18S carries $19 \pm 3 \times 10^9 \text{ kg s}^{-1}$ southward in the upper 2000 db within 300 km of the east coast of Madagascar and nearly $-50 \times 10^9 \text{ kg s}^{-1}$ within 700 km of the coast. At 32°S (Figure 3.13b), the Agulhas Current is clearly evident on the western boundary with maximum velocities reaching nearly 2 m s^{-1} .

The geostrophic mass flux attributable to the Mozambique Current is highly uncertain. *Sætre and De Silva* [1984] concluded that there is no consistent flow at all between Madagascar and Africa while *Fu* [1986] and *Harris* [1972] found net southward transports of $-6 \times 10^6 \text{ m}^3 \text{ s}^{-1}$ and $-10 \times 10^6 \text{ m}^3 \text{ s}^{-1}$, respectively. Recent output from the Semtner and Chervin $\frac{1}{4}^\circ$ model [*Tokmakian and Semtner*, pers comm., 1995] shows a mean volume transport at 17.15°S in the Mozambique Channel of $-10 \pm 7 \times 10^6 \text{ m}^3 \text{ s}^{-1}$. The model transport ranges between about 6 and $-30 \times 10^6 \text{ m}^3 \text{ s}^{-1}$ over the two year period beginning in January 1987. The standard model finds no significant net flow in the Mozambique Channel. In the upper layers of the northern section, the equatorward movement of water on the western and eastern sides of the channel is balanced by an equal and opposite flow through the center of the channel. In the lower layers the circulation is in the opposite sense. The southern section, which contains only four station pairs shows alternating flow direction in all the pairs. Given the range in previous estimates and the variability suggested by the Semtner and Chervin model, almost any result in this region would have to be deemed acceptable.

On the eastern side of the southern Indian Ocean, the Leeuwin Current off the west coast of Australia complicates the simple picture of the basin wide surface anti-cyclonic gyre. The Leeuwin Current does not flow equatorward like the eastern boundary currents in the Pacific and Atlantic, but rather flows towards the pole. It carries about $5 \times 10^6 \text{ m}^3 \text{ s}^{-1}$ of warm, fresh water, low in oxygen and high in nutrients to depths of about 250 m [Smith *et al.* 1991], southward against the prevailing winds. Weaver [1990] suggests that its poleward character relies upon the existence of the Pacific-Indian throughflow, which maintains very high steric heights off northwestern Australia through the piling up warm equatorial Pacific waters. In this view, the Leeuwin Current is driven by a deep alongshore density gradient which in turn drives an onshore geostrophic flow which turns southward upon meeting the coast of Australia and the steric height differential maintained by the Pacific-Indian throughflow. The current does express seasonal variations which appear to be due to variations in the wind stress rather than variations in the alongshore pressure gradient or the magnitude of throughflow [Weaver 1990]. Below the Leeuwin Current is an equatorward flow also of about $5 \times 10^6 \text{ m}^3 \text{ s}^{-1}$ [Thompson 1984] which carries the more saline, oxygen rich and nutrient poor South Indian Central water northward, closing the main anti-cyclonic gyre. Both northward and southward flows are in evidence near the eastern boundary of the #I32S section in Figure 3.13b.

In the deep Indian Ocean, the Central Indian Ridge and Ninety-East Ridge divide the flow originating in the Antarctic into three distinct circulation systems. In the Mascarene and West Australian Basins, the equatorward flow of the western boundary currents appears to be associated with a weaker, poleward flow to the east of the boundary. The Central Indian Basin is closed off below about 3500 m. Deep water which exists at depths greater than this finds its way into the Central Basin through passages in the Ninety-East Ridge from the West Australian Basin [Warren, 1981a]. The deep water from the Antarctic travels into the Indian Ocean not only from the west, but also from the east around southwest Australia.

Water Mass Name	Model Layer	Temperature Limits (°C) at			
		#I32S	#I18S	#Mz_N	#Mz_S
Surface	1-3	> 12.7	> 12.8	> 12.4	> 12.6
Intermediate	4-7	> 2.3	> 2.4	> 2.7	< 12.6
Deep	8-11	> 1.4	> 1.4	< 2.7	-
Bottom	12-13	< 1.4	< 1.4	-	-

Table 3.16: Approximate definition of water masses by potential density layers in the Indian Ocean. Except in the case of the bottom water, the temperature limits are average temperatures across the section of the lower layer boundary. The bottom water temperature limit is defined in terms of the average temperature of the upper layer boundary. The model layers numbers refer to those defined in Table 2.5e.

The zonally integrated profiles mass transport are shown in Figure 3.21. The model division for the water masses of the Indian Basin are defined in Table 3.16. Within these layers the net meridional transports found by the standard model show:

	#I32S	#I18S
surface layers	$-15 \pm 2 \times 10^9 \text{ kg s}^{-1}$	$-16 \pm 2 \times 10^9 \text{ kg s}^{-1}$
intermediate layers	$-9 \pm 4 \times 10^9 \text{ kg s}^{-1}$	$-3 \pm 4 \times 10^9 \text{ kg s}^{-1}$
deep layers	$12 \pm 4 \times 10^9 \text{ kg s}^{-1}$	$3 \pm 5 \times 10^9 \text{ kg s}^{-1}$
bottom layers	$5 \pm 2 \times 10^9 \text{ kg s}^{-1}$	$7 \pm 4 \times 10^9 \text{ kg s}^{-1}$

Consistent with the existence of a warm water flow from the Pacific to the Indian Basin through the Indonesian Archipelago, there is a net southward transport above about 2000 db at both 18°S and 32°S. There is a net northward flow of AAIW in layer 4 at 18°S ($1.4 \pm 0.8 \times 10^9 \text{ kg s}^{-1}$). The same layer at 32°S carries -0.1 ± 1.4 , a transport which is not different from zero or small positive values. The lack of a net northward transport of AAIW at 32°S is not a result of the P-I throughflow requirement as this net northward flow has also been suggested by previous studies [Toole and Warren, 1993; Macdonald, 1991]. The Agulhas Current dominates the southward transport of intermediate waters ($-51 \pm 2 \times 10^9 \text{ kg s}^{-1}$ in layers 4 through 7) across 32°S. The time variability of the flow has not been included in the uncertainty

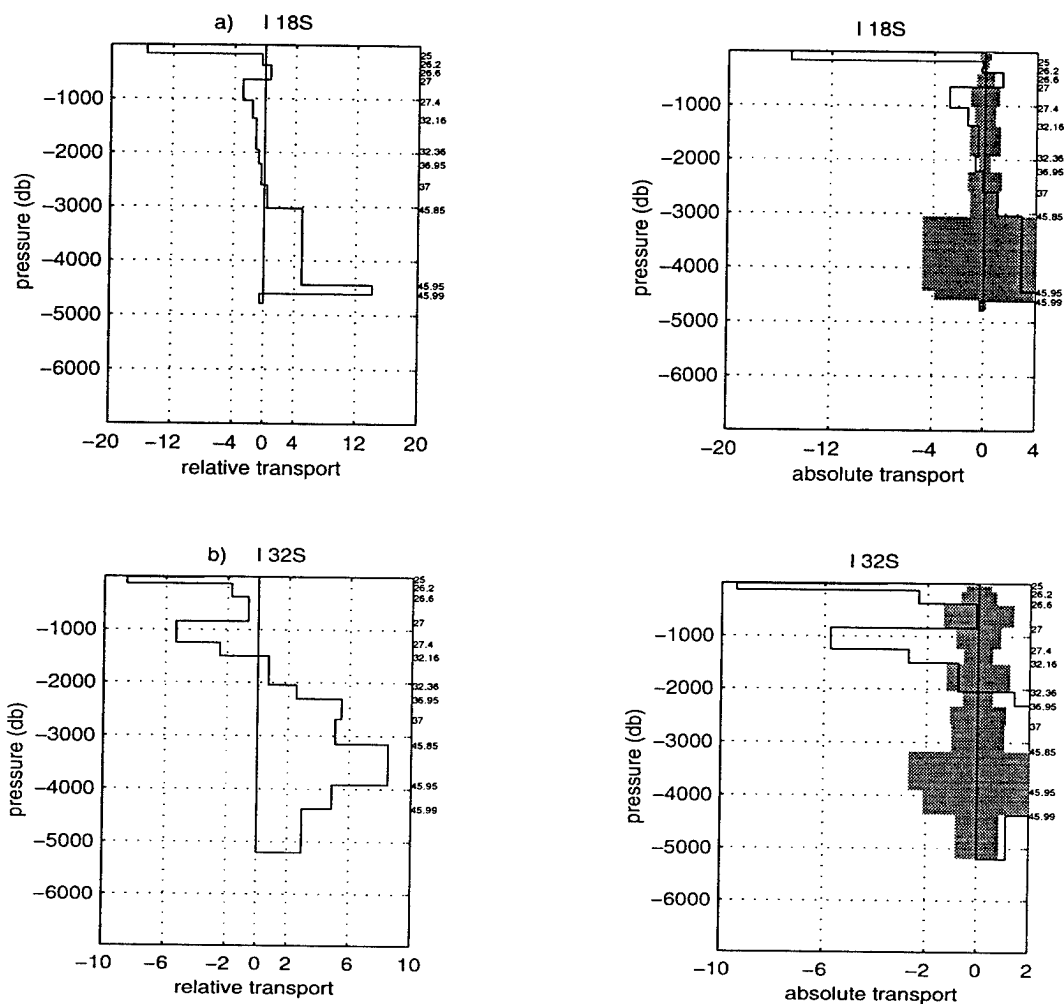


Figure 3.21: The zonally integrated mass transport in potential density layers for the sections: (a) #I18S and (b) #I32S. The profiles on the left are based on a zero velocity at the reference level. Those on the right are based on the absolute velocity field computed by standard model. The shaded region indicates the estimated 1σ uncertainty in the layer transports due to the uncertainty in the reference level velocities. The Ekman transport is included in outcropping layers.

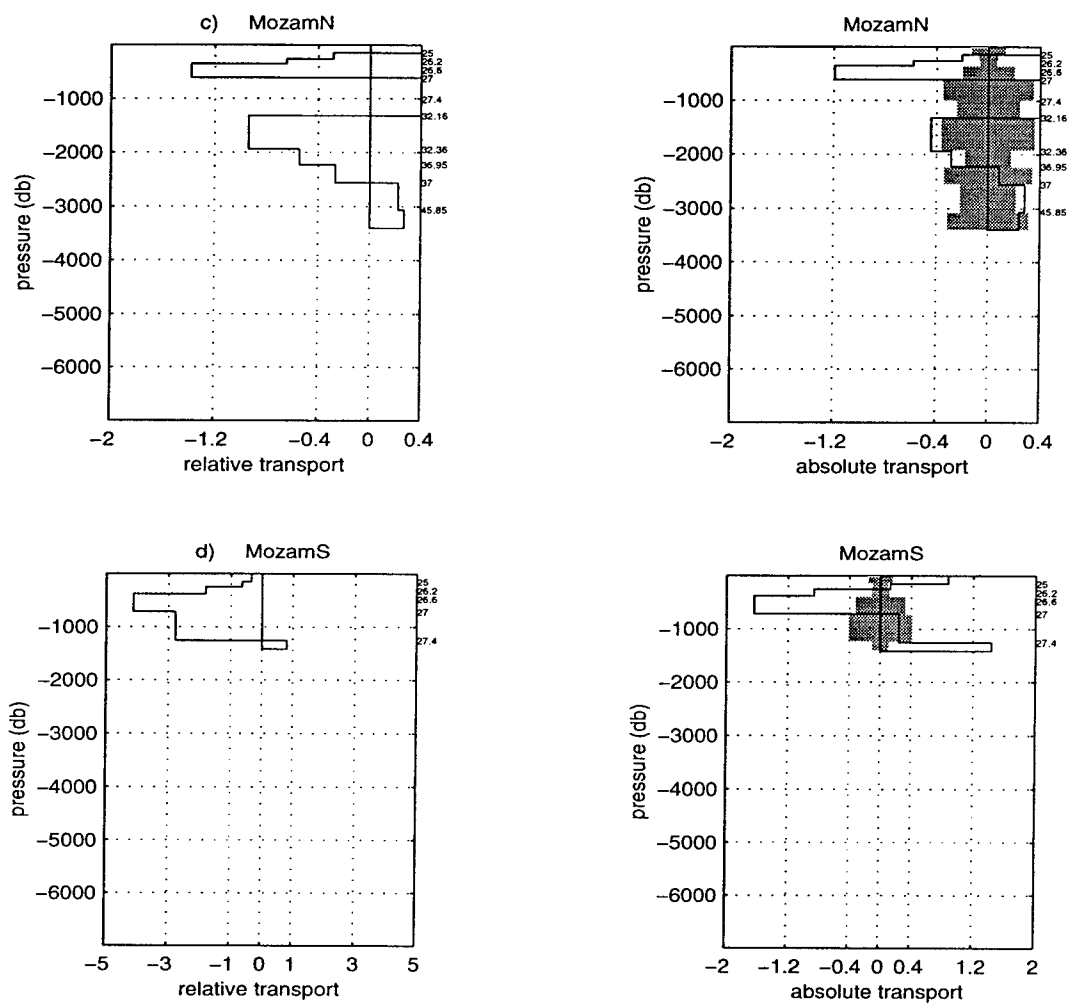


Figure 3.21 continued: The zonally integrated mass transport in potential density layers for the sections: (c) #Mz_N and (d) #Mz_S.

estimates quoted here. It should be noted that it would only take a 3% change over time of the layer 4 intermediate water transport in the Agulhas Current to reverse the sign of the net flow within the layer across the section and to make it significantly different from zero. At both latitudes, there is a net southward transport of surface and intermediate waters across the entire section, but a net northward flow in the central basin. The Agulhas Current carries a total of $93 \pm 2 \times 10^9 \text{ kg s}^{-1}$ of surface and intermediate waters southward at 32°S . There is also strong southward transport in the western basin at 18°S , but significant southward transport also exists in the intermediate layers of the West Australian Basin.

Circumpolar Deep Waters are seen moving northward through both sections. Most of the net northward transport of deep waters occurs in the Crozet Basin at 32°S and in the western and central basins at 18°S . The estimated net transport of $16.5 \pm 5 \times 10^9 \text{ kg s}^{-1}$ at 32°S (below layer 7, about 2050 db) is considerably less than the $27 \times 10^6 \text{ m}^3 \text{ s}^{-1}$ below 2000 db estimated by *Toole and Warren* [1993]. Below layer 9 (about 2600 db) at 18°S , the standard model suggests a northward transport of $11 \pm 5 \times 10^9 \text{ kg s}^{-1}$, a value which is quite a bit more than the $3.6 \times 10^9 \text{ kg s}^{-1}$ below 2000 m suggested by *Fu* [1986]. It may be that the requirement of mass balance between the two sections (in potential density layers with a fixed estimate of the magnitude of the diapycnal transfer) has tended to reduce the larger estimate and increase the smaller one. Within the depth range of the deep water there are upwelling diapycnal transfers of between 2 and $6 \times 10^9 \text{ kg s}^{-1}$. The associated model estimated w^* terms range between about 1 to $4 \times 10^{-5} \text{ cm s}^{-1}$.

Using the GFDL model [*Cox* 1984] and its adjoint in an enclosed⁷ Indian Ocean north of 31°S , *T. Lee* [*pers. comm.* 1995] finds an even smaller estimate of deep Indian Ocean inflow. At 29°S , *Lee* finds a net northward transport of waters below 1850 m

⁷The *T. Lee* [*pers. comm.* 1995] model includes sponge layers at the southern boundary and the Indonesian Passages in which the temperature and salinity are estimated as part of the solution.

of only $4.5 \times 10^6 \text{ m}^3 \text{ s}^{-1}$ and concludes that the major overturning in the Indian Basin occurs above 2000 m depth. The apparent discrepancy among the *Toole and Warren* results, the *Lee* results and those of the standard model is not understood and should be investigated further. *Lee* suggests that the effects of both the sponge layers and the seasonal cycle on his model solution should be studied. He also suggests that poor resolution may play a role in producing the small deep overturning cell. For our part, a more detailed study on the effect of the chosen reference levels might be enlightening. Beyond this, should the necessary data become available, it would be interesting to investigate the effects of the seasonal cycle upon the inverse model solution.

The stronger the east-west flux is between the Pacific and Indian basins through the Indonesian Archipelago, the weaker the resulting northward transport of deep water is across the Indian Ocean sections⁸ in the model. The throughflow is thought to exhibit annual variations [*Meyers*, 1995]. Whether or not the instantaneous deep flow can be affected by such variations is questionable. However, the deep transport in these models is connected through mass conservation to the strength of the P-I throughflow. The #I18S data were taken during a season associated with strong throughflow, while the #I32S data were taken during a season associated with weaker throughflow. Therefore, one might expect that the deep transport estimate obtained through the combination of these two data sets, would be different those found using either one of the sections alone.

Indian Ocean Test Models

The net transport of water within the bottom layer of the standard model is moving northwards across the 32°S section in the Indian Ocean, while the transport within

⁸The effect of varying the magnitude of the P-I throughflow on the deep Indian Ocean transport is discussed in Chapter 4, page 249.

#I32S Ekman = 0.5	Std. Model Global Constraints	Test Model Global Constraints	Test Model Just Indian Constraints	Test Model Ind + S. Ocean Constraints
surface to $\sigma_2 = 32.36$	-25.2 ± 4.1	-24.8 ± 4.2	-27.6 ± 4.3	-26.7 ± 4.2
$\sigma_2 = 32.36$ to $\sigma_4 = 45.99$	15.3 ± 4.9	16.4 ± 4.9	18.5 ± 5.1	17.3 ± 4.9
$\sigma_0 = 45.99$ to bottom	1.1 ± 0.9	-1.3 ± 1.7	0.7 ± 2.2	-1.0 ± 1.7
surface to bottom	-8.3 ± 6.7	-9.2 ± 6.7	-7.9 ± 7.0	-9.9 ± 6.7

#I18S Ekman = -15.3	Std. Model Global Constraints	Test Model Global Constraints	Test Model Just Indian Constraints	Test Model Ind + S. Ocean Constraints
surface to $\sigma_2 = 37.01$	-4.5 ± 5.9	-4.4 ± 5.9	-7.2 ± 6.1	-7.5 ± 6.0
$\sigma_2 = 37.01$ to $\sigma_4 = 45.99$	11.3 ± 4.9	10.5 ± 4.9	14.9 ± 5.2	13.1 ± 5.1
$\sigma_0 = 45.99$ to bottom	-0.3 ± 0.3	-0.5 ± 0.3	-0.5 ± 0.3	-0.5 ± 0.3
#Mz_N surface to bottom	0.3 ± 1.6	0.3 ± 1.6	0.2 ± 1.6	0.2 ± 1.6
total surface to bottom	-8.5 ± 6.4	-9.4 ± 6.4	-8.0 ± 6.7	-10.1 ± 6.4

Table 3.17: Comparison of the transports in the Indian Ocean in models which do (standard model) and do not (test model) include constraints on the bottom water flow into the Indian Basin. Column 2 gives the results for the standard model. Column 3 gives the results for the test model using the entire global data set. Column 4 gives the results for the test model using only data and constraints from the Indian Basin. Column 5 gives the results for the test model using data and constraints from the Indian Basin and the Southern Ocean.

the bottom layer at 18°S is directed southwards but is small ($-0.3 \times 10^9 \text{ kg s}^{-1}$) and not significantly different from zero. This solution is a result of the standard model constraints which require the flow to be directed northwards in lowest layer. Without these constraints the model produces southward transport in the lowest layer of both sections. Such a circulation feature was felt to be undesirable as it is not believed that bottom water can be formed in the northern Indian Ocean.

A test model was run using the same basic set of constraints as the standard model but without the bottom layer constraints. Table 3.17 compares the zonally integrated transport results of the standard model to those of the test model. When the test model was run using only the data within the Indian Basin a small ($-0.5 \pm 0.3 \times 10^9 \text{ kg s}^{-1}$) net southward across the 18°S section in the lowest layer still resulted. However, when the test model was run using the entire global data set it

showed that the southward transport of bottom water across the 32°S section in the standard model is an effect of the larger data set, not the Indian Ocean data. The larger models also produced a slightly reduced estimate of the inflow of deep waters. The southward flow of bottom water was not present in the models of *Macdonald* [1991] which combined the #I18S, #I32S, #P28S and #P43S transects, suggesting that the most likely sources of this effect are the meridional sections to the south (#30E and #132E) as they ultimately determine how much bottom water gets into and out of the Indian Basin. This suggestion is supported by the results of the test model when run using only the Southern Ocean and Indian Ocean constraints (column 5 of Table 3.17).

Finding a singular value decomposition solution which includes resolution matrices would allow confirmation of this hypothesis. Although this test has not yet been performed, an experiment was run which used only the southern ocean regions (C and D, see Figure 2.3) and the Indian Ocean region (E). This model also produced a net southward transport in the lowest layer of the #I32S section, which does not tell us exactly what is causing the effect of southward bottom water flow but does at least confirm that it relates to information coming from the Southern Ocean.

As discussed earlier in the chapter, the #30E section is attempting to represent the mean circulation in an eddy rich region which is by no means in a steady state within the time scale provided by a single hydrographic section. It is therefore, a likely cause of "questionable" circulation features. Until such time as an svd solution is computed and the resolution matrices are examined it must suffice to say that even without the bottom layer constraints (which are included in the standard model), the net southward flow at 18°S is very small ($-0.5 \pm 0.3 \times 10^9 \text{ kg s}^{-1}$) and though the transport at 32°S is larger, at $-1.3 \pm 1.7 \times 10^9 \text{ kg s}^{-1}$, it is not significantly different from zero.

Since it is possible to meet the conservation constraints provided by the #30E and #132E sections without producing unacceptably large solutions (\hat{b} 's), the determination as to whether or not these two sections are consistent with each other and with the model in general rests upon whether or not we accept the circulation patterns they produce. For instance, should we definitively determine at some time in the future that it is one or the combination of both of these sections which is producing the southward transport of bottom waters within the Indian Basin (a result which is not consistent with our understanding of the mean circulation) we could then conclude that they are inconsistent with each other and the model and seek some alternate form of constraint in the Southern Ocean. However, we must be careful not to throw out every piece of data which produces an unexpected feature in the circulation pattern. Some of these features may be inconsistencies in the data set. Others may represent gaps in our understanding of the mean and/or time varying circulation.

Indian Ocean Summary

The standard model produces a surface circulation pattern within the southern Indian Basin in which waters move generally northward away from the western boundary, consistent with a subtropical gyre. There is evidence of both northward and southward flows in the West Australian and Perth Basins with a net convergence between the sections at 18°S and 32°S in the surface waters of this eastern region. The intermediate circulation pattern is similar. Deep and bottom waters move northward along the numerous western boundaries, with most of the net deep northward transport occurring in the Crozet Basin at 32°S and in the Central Indian Basin at 18°S. Most of the net northward bottom water transport occurs to the east of the Ninety-East Ridge, a result which is consistent with the findings of *Warren* [1981a].

The character of the cumulatively integrated meridional transport (Figure 3.22) across #I32S, above and below $\sigma_2 = 32.36$ (~ 2000 db) is similar to that found by

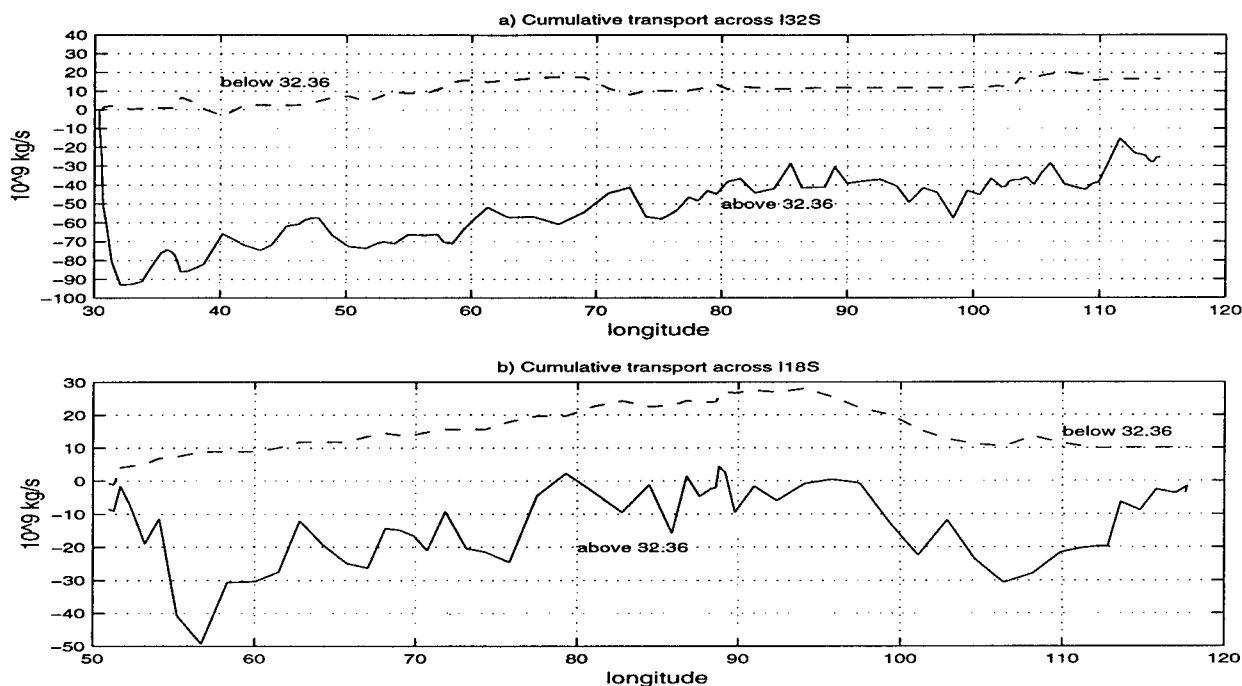


Figure 3.22: Standard model estimates of cumulative meridional transport above and below $\sigma_2 = 32.36$ (approximately 2000 db) across a) #I32S and b) #I18S. Ekman transport is not included.

Toole and Warren [1993], above and below 2000 db. However, the standard model estimate of net deep northward transport of $17 \pm 5 \times 10^9 \text{ kg s}^{-1}$ across #I32S is only a little more than half that estimated by Toole and Warren [1993]. At 18°S , the estimated net northward transport of deep and bottom waters ($11 \pm 5 \times 10^9 \text{ kg s}^{-1}$) is about twice that estimated by Fu [1986]. This tendency for the 32°S section to exhibit stronger northward transport of deep water than the section at 18°S suggesting that there is more deep water crossing the more southerly section and upwelling occurring between the two. Such a scenario would be consistent with the strong Indian Ocean upwelling suggested by Toole and Warren [1993]. It is however, inconsistent with the model results of Lee [pers. comm. 1995] who finds little evidence upwelling below 2000 db.

3.4.5 Summary

The standard model transport results are summarized in Figures 3.23 and 3.24. Note that in Figures 3.24a–3.24d, the vectors are placed geographically midway between the stations have which been used in the integration of transport values. However, in Figures 3.23a and 3.23b the placement of the surface, intermediate, deep and bottom transport vectors is arbitrary. It is also important to note that these plots are only useful for comparison of values within the individual regions as described in Figure 2.3. The layer (surface, intermediate, deep and bottom) definitions are given in the tables indicated.

The model produces an average overturning cell of $18 \pm 4 \times 10^9 \text{ kg s}^{-1}$ ⁹. The standard deviation of $4 \times 10^9 \text{ kg s}^{-1}$ on the estimated magnitude of overturning cell in the Atlantic is indicative of the large changes in the estimates from section to section. These changes are made possible by the vertical transfer allowed by the model. Between 36°N and 48°N the model found it necessary to implement large diapycnal transfers $O(4 \times 10^{-4} \text{ cm s}^{-1})$ in order to meet the model conservation constraints. These transfers resulted in an estimated overturning magnitude of $25 \times 10^9 \text{ kg s}^{-1}$ at 48°N and only $16 \times 10^9 \text{ kg s}^{-1}$ at 36°N. There are at least two possible explanations for this large change, both related to the fact that this region which contains the Gulf Stream and its northern extension into the North Atlantic Current is associated with strong variations both in space and time. The first is that within the presence of the strong currents there really are such strong diapycnal transfers. The second is that the diapycnal transfers are actually smaller, but the temporal variability of the region makes the two hydrographic sections incompatible.

⁹To avoid confusion over the different layer definitions in the North and South Atlantic, the magnitude of the overturning cell is taken here, as the maximum north–south exchange of waters across each zonal section, averaged over all the Atlantic sections.

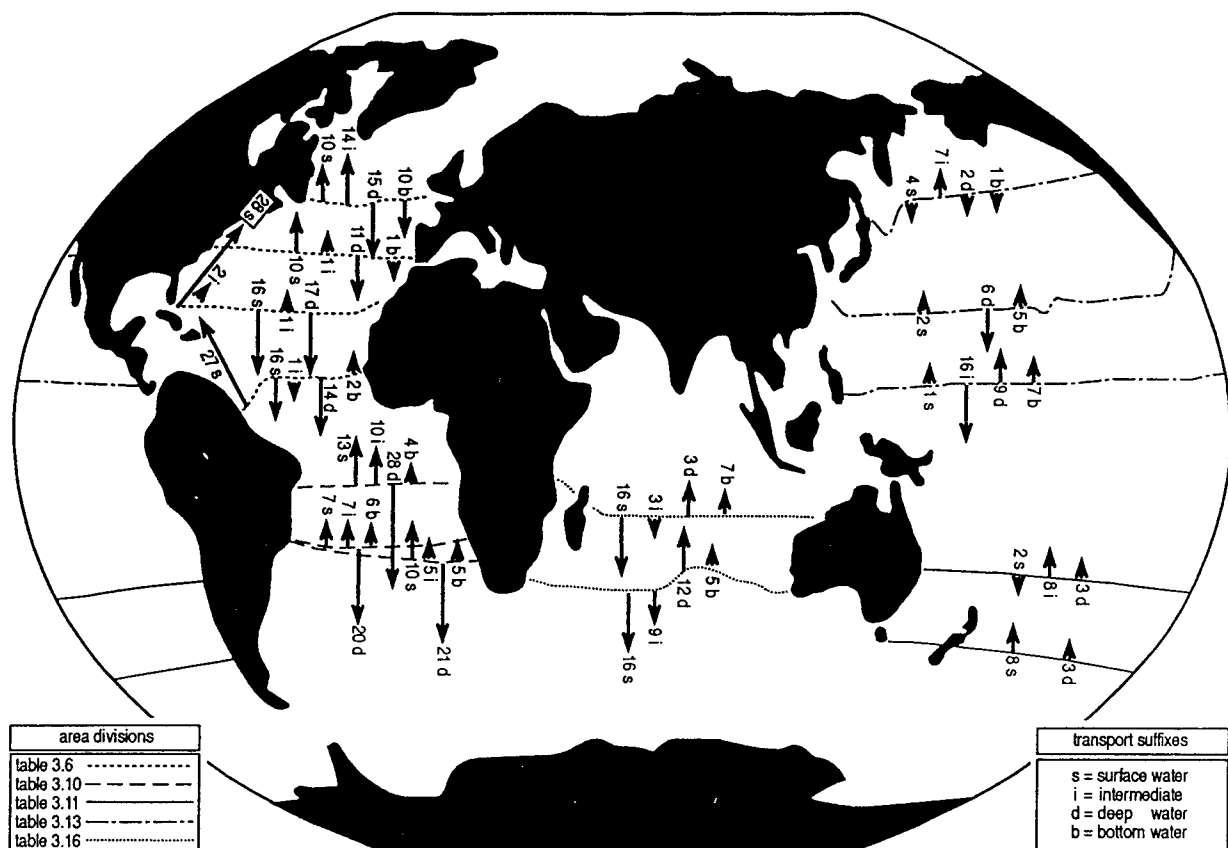


Figure 3.23a: Standard model zonally integrated mass transport in potential density layers describing surface waters (s), intermediate waters (i), deep waters (d) and bottom waters (b), from left to right, respectively. The definitions of the divisions for each of the areas are given in the tables indicated. The Ekman transport (Table 2.4) is included in outcropping layers. The transports within the Southern Ocean are shown in the accompanying Figure 3.23b.

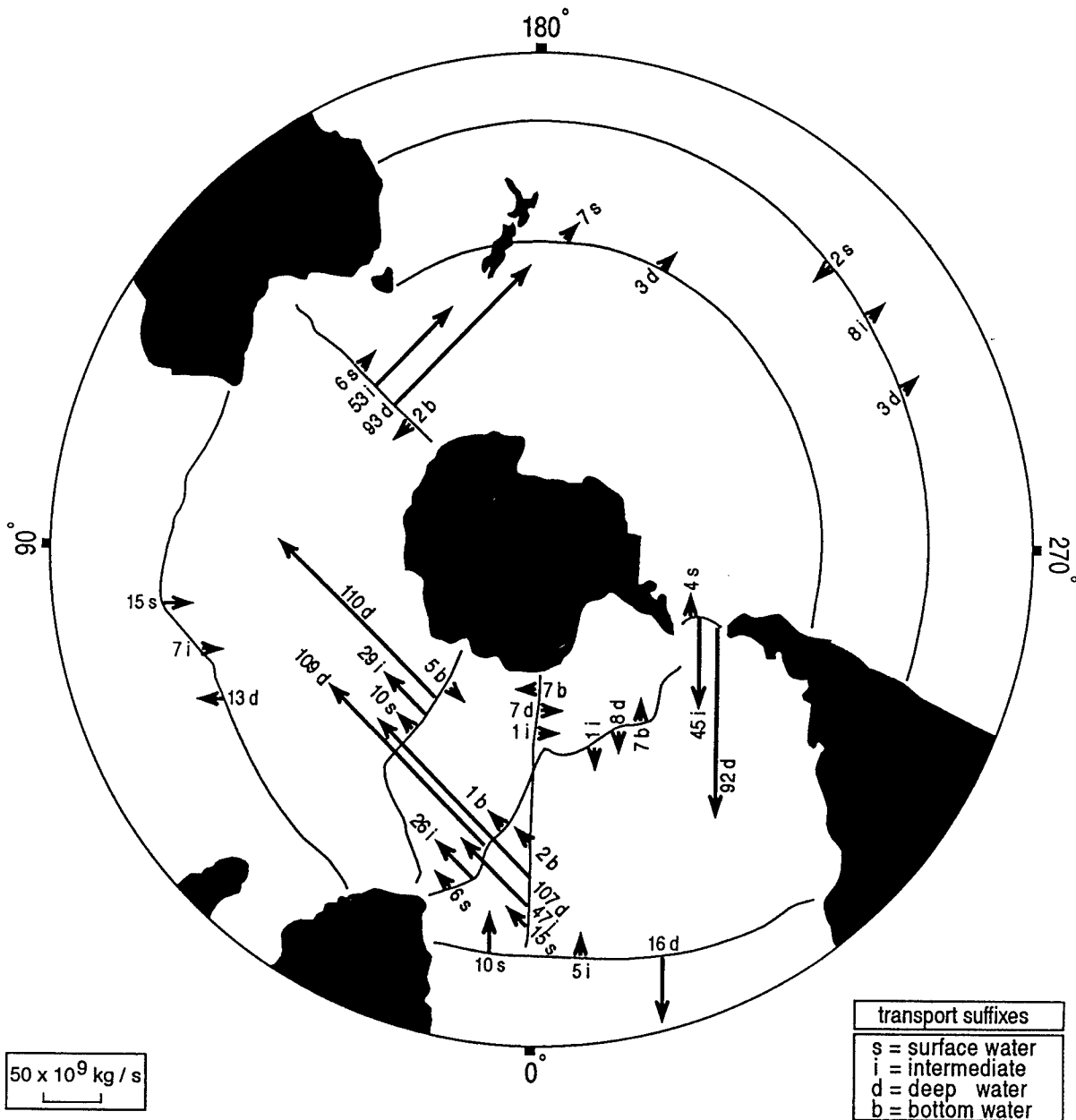


Figure 3.23b: Standard model horizontally integrated mass transport within the Southern Ocean in potential density layers describing surface waters (s), intermediate waters (i), deep waters (d) and bottom waters (b), from left to right, respectively. The definitions of these divisions are given Table 3.11. The Ekman transport is included in outcropping layers.

surface mass transport

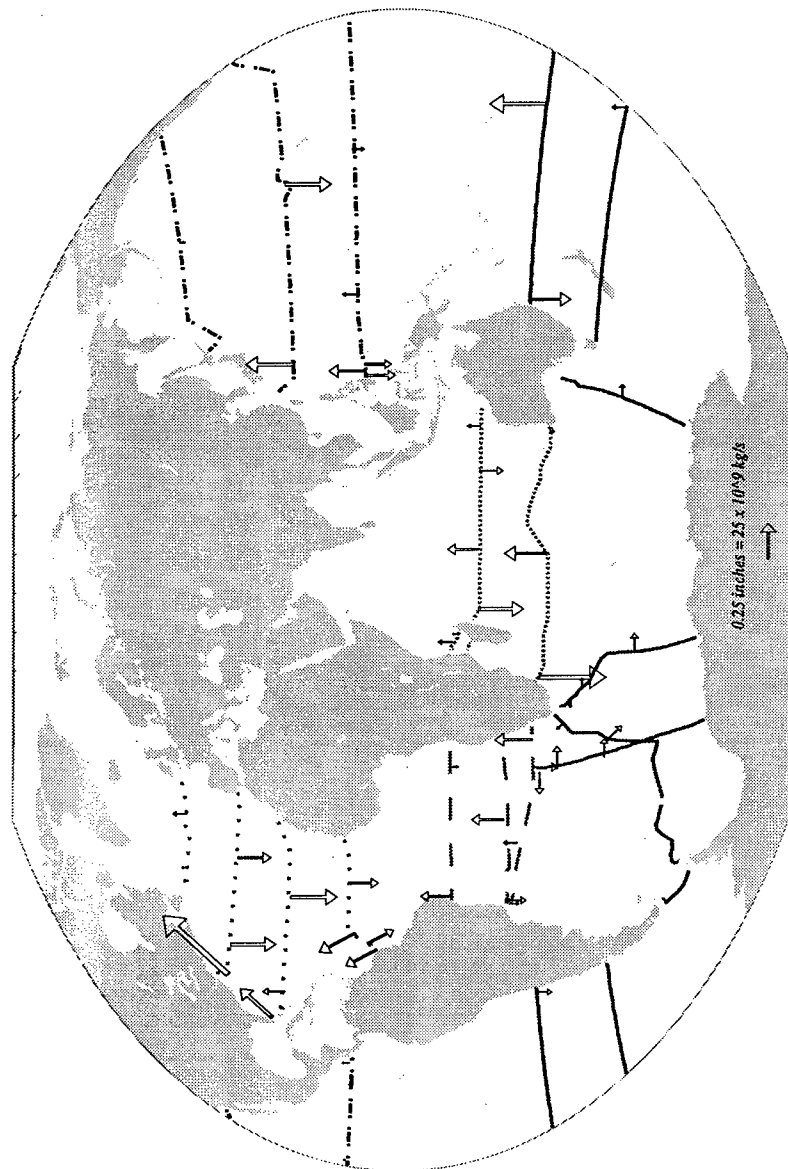


Figure 3.24a: The zonally integrated mass transport in potential density layers describing surface and thermocline waters in the standard model. The definitions of these divisions for each of the areas are given in: Tables 3.6 for the spaced dotted line; 3.10 for the dashed lines; 3.11 for the solid line; 3.16 for the close dotted lines and 3.13 for the chain dash-dot lines. The Ekman transport is included. The vectors are placed geographically midway between the stations which have been integrated to obtain the transport values.

intermediate mass transport

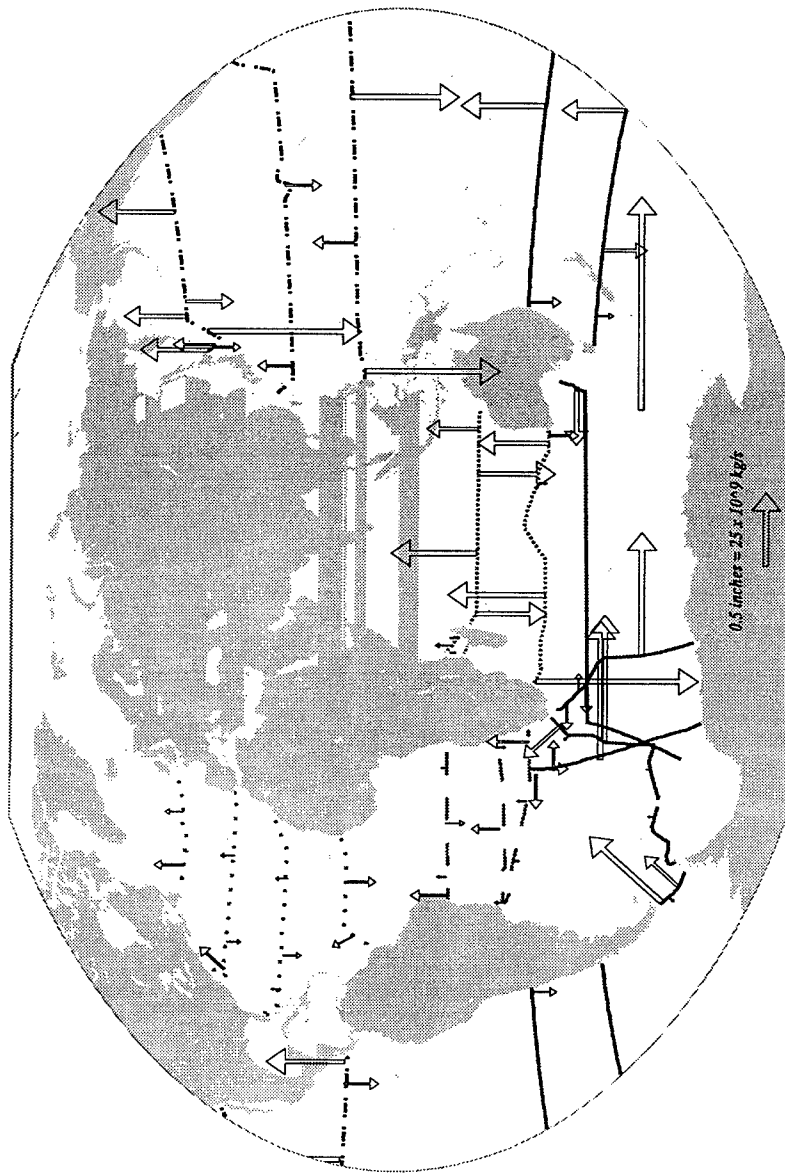


Figure 3.24b: The zonally integrated mass transport in potential density layers describing intermediate waters for the standard model. The definitions of these divisions are given in the tables listed in Figure 3.24a. The vectors are placed geographically midway between the stations which have been integrated to obtain the transport values.

deep mass transport

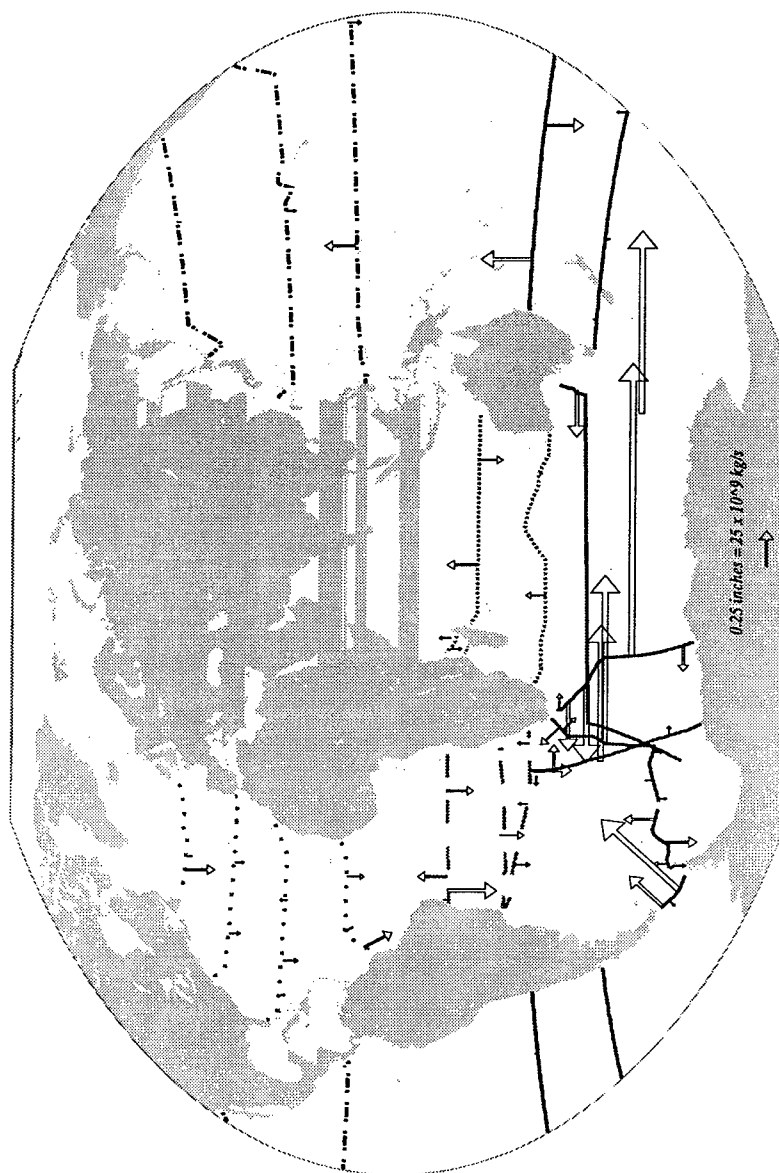


Figure 3.24c: The zonally integrated mass transport in potential density layers describing deep waters for the standard model. The definitions of these divisions are given in the tables listed in Figure 3.24a. The vectors are placed geographically midway between the stations which have been integrated to obtain the transport values.

bottom mass transport

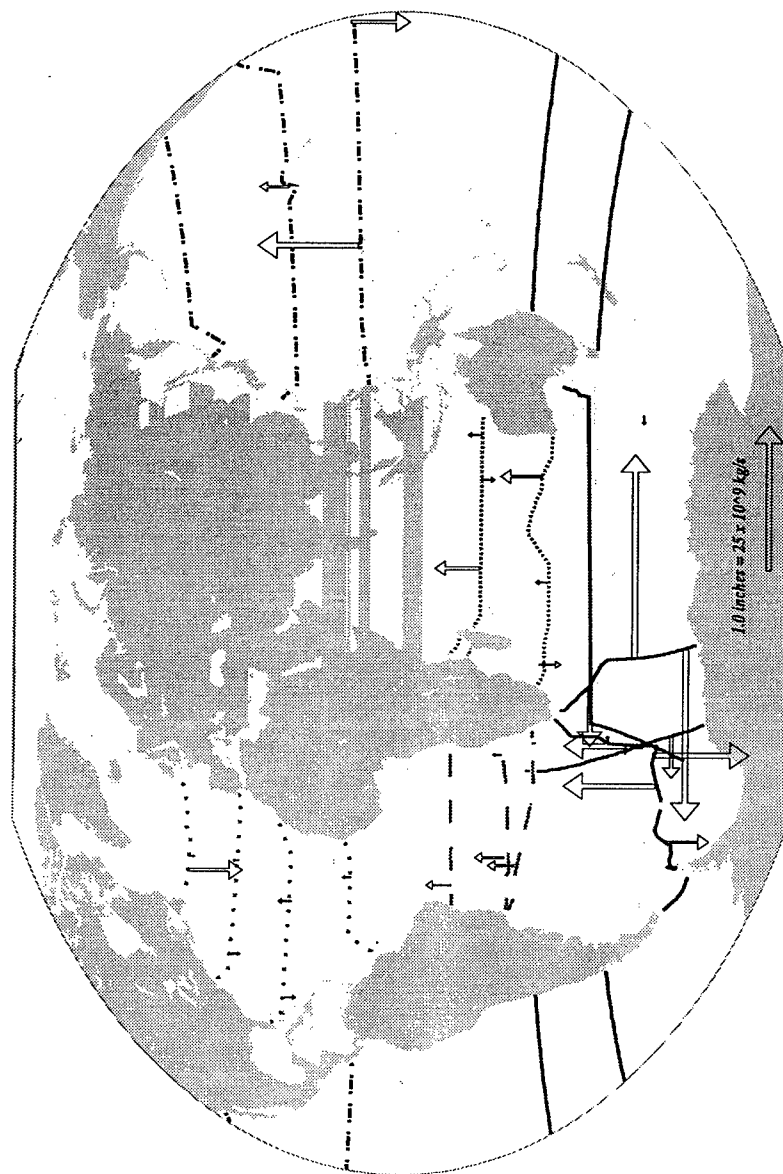


Figure 3.24d: The zonally integrated mass transport in potential density layers describing bottom waters for the standard model. The definitions of these divisions are given in the tables listed in Figure 3.24a. The vectors are placed geographically midway between the stations which have been integrated to obtain the transport values.

The other region where a large change in the magnitude of the overturning cell occurs in the equatorial Atlantic. The vertical transfers terms in the Atlantic between 11°S and 11°N are large, $O(5 \times 10^{-5} \text{ cm s}^{-1})$, but not unduly so. However, it is not possible to balance the mass constraints in this region without allowing for vertical transfer. The increase in the estimated magnitude of the overturning cell across the equator in the Atlantic may be related to the specific estimate of the North Brazil Current transport used in the model. But the particulars of the relation between the two estimates are not understood and warrant further investigation.

The warm waters feeding the formation of NADW, flow northward in the eastern basin of the South Atlantic and cross over to the western basin south of the equator. The deep return flow occurs mainly in the western basin but is not always confined to the western boundary. The net transport of intermediate waters is northward across all the Atlantic sections except #A11N. In the South Atlantic, bottom waters flow northward away from their Antarctic source regions and are directed northward as far north as 24°N . At 36°N the net bottom water transport is not significantly different from zero and at 48°N , it is directed southward. The transport of bottom waters across the South Atlantic sections are consistent with the input estimates which came from *Speer and Zenk* [1993] with 4.7 ± 0.9 , 4.1 ± 1.0 and 2.1 ± 1.2 crossing #A27S-W, #A23S and #A11S to the west of 13.7°W .

Within the Southwest Atlantic, the intermediate and deep waters which enter through Drake Passage combine with the deep waters arriving from the north (NADW) and the south (WSDW). South of 35°S , at the Greenwich Meridian there is a net eastward transport on the order of $170 \times 10^9 \text{ kg s}^{-1}$. Across the #0E2Afr section, the net transport is reduced to about $140 \times 10^9 \text{ kg s}^{-1}$ as required by mass conservation. There is both eastward and westward transport across the two sections lying to the south of South Africa. So although some of the water (presumably that within the South Atlantic Current) turns northwestward, west of 15°E , some portion of the

eastward currents continues to flow into the Agulhas Retroflexion region. Of this, part turns around and returns westward but most continues eastward, further to the south, into the Indian and Pacific Basins.

The standard model shows that it is likely that some portion of the northward flow of surface, thermocline and intermediate waters within and to the east of the Benguela Current at 30°S is coming from the Indian Basin. The pattern of flow and property values also indicate that some of this water may originate in the South Atlantic Current, pass into the Agulhas recirculation gyre and then return westward around the southern tip of South Africa, in a short-circuited "warm water" path. However, the model was unable to place precise (or even imprecise) estimates on the fraction of NADW feed water which takes this route, as the temporal resolution provided by the sections used in this study are not adequate for modeling this region which is dominated by a rich eddy field. Hydrography alone is unlikely to provide a good estimate of the mean field in this region. The strong and steady source of upper and intermediate waters available from the Southwest Atlantic and the "cold water" path support the argument that this is the dominant or at least most consistent source of NADW feed water. Nevertheless, the sections which surround the southern tip of South Africa and the "warm water" path connection are consistent in the *suggestion* that there is westward flow of waters within the eddies originating in the Agulhas Retroflexion region and that this flow may be an important source of the feed for the eventual formation of deep waters in the north. The fact that the eddies themselves are a combination of South Atlantic and Indian Ocean waters may complicate controversy regarding the strengths of the "warm" and "cold" water paths, as the "warm water" path may be dependent upon the "cold water" path for its own form of feed (South Atlantic Current) water.

Within the North Pacific, the shallow meridional cell suggested in the literature is evident as the Ekman transport is more than compensated for in the model surface

and thermocline layers. The deep and bottom waters which flow northward into the Pacific from the Southern Ocean are returned below these uppermost layers. The Southern Ocean region layer definitions (Table 3.11) are not particularly appropriate for describing transport across the two South Pacific sections. Redefining deep and bottom waters as layers 9–12, gives an estimate of $10\text{--}11 \times 10^9 \text{ kg s}^{-1}$ moving into the Pacific below $\sigma_2 = 37.04$. This value is reduced to about $5 \times 10^9 \text{ kg s}^{-1}$ crossing 24°N , all of which is upwelled south of 47°N . It was shown that a doubling of this transport within the North Pacific is also consistent with the standard model constraints. So while the standard model suggests a fairly small net northward transport of abyssal waters into the North Pacific, the possibility of a larger net transport cannot be ruled out. The standard model was unable to produce a southward transport of deep waters at 10°N in the Pacific and balance mass across the section simultaneously. This result may be construed as an inconsistency among the Pacific Ocean sections and warrants further investigation.

The standard model contains a constraint placing a limit on the throughflow of $10 \pm 10 \times 10^9 \text{ kg s}^{-1}$, from the Pacific to the Indian Basin. The model produces a throughflow of $9 \pm 7 \times 10^9 \text{ kg s}^{-1}$. Northward flow enters the Pacific Basin predominantly in the intermediate and deep layers and exits the Indian Basin mostly in the intermediate and surface layers. There is a net southward transport in the surface and intermediate layers across #I18S east of the Ninety–East Ridge and a net northward transport of these waters across #I32S. However, there is adequate southward transport east of Ninety–East Ridge across both these sections to account for the southward transport due to P–I throughflow. There is a strong southward transport within the Mindanao Current at 10°N in the Pacific and upwelling of deep and intermediate waters between 28°S and 10°N . These features of the circulation pattern are evidence for both southern and northern sources of the Indonesian Passage throughflow waters and suggest that the magnitude of the throughflow itself is not of integral importance to the global thermohaline overturning cell. The sensitivity of

the throughflow to the model constraints and the connection of the throughflow to the global circulation will be further investigated in the next chapter.

3.4.6 The Standard Model Freshwater Fluxes

Estimates of freshwater fluxes from the standard model are illustrated in Figure 3.25. These figures compare the model estimates to the *Baumgartner and Reichel* [1975] and *Schmitt et al.* [1989] values with an integration reference point at the Bering Strait (see the discussion in Chapter 2). The model estimates are made in the following manner. Mass conservation gives:

$$T_g + T_{ek} = T_{bs} + T_{pi} + T_{fw} \quad (3.1)$$

$$(\rho\bar{v})_g + (\rho\bar{v})_{ek} = (\rho\bar{v})_{bs} + (\rho\bar{v})_{pi} + T_{fw} \quad (3.2)$$

where T indicates mass transport, the v, velocity, and the subscripts the subscripts *g*, *ek*, *bs*, *pi* and *fw* denote the geostrophic, Ekman, Bering Strait, Pacific-Indian and freshwater transports respectively. The overbar is defined on page 28, Equation 2.5. Assuming that the $\bar{v}'\bar{S}'$ terms for the Bering Strait, Indonesian Passage and Ekman components are negligible, salt conservation gives:

$$T_{S_g} + T_{S_{ek}} = T_{S_{bs}} + T_{S_{pi}} \quad (3.3)$$

$$(\rho\bar{v}\bar{S})_g + (\rho\bar{v}\bar{S})_{ek} = (\rho\bar{v}\bar{S})_{bs} + (\rho\bar{v}\bar{S})_{pi} \quad (3.4)$$

where T.S represents the salt transport. The model results give an estimate of the absolute geostrophic field. The data give the salinities of the geostrophic and Ekman components (the Ekman component is assigned the mean salinity of the surface layer). Initial estimates of the Ekman, freshwater and Bering Strait transport were included in the model constraints (see Table 3.1). Assuming that \bar{S}_{bs} and \bar{S}_{pi} are known, leaves 2 equations (3.2 and 3.4) and 3 (and at some latitudes 4) possible unknowns (T_{fw} , \bar{v}_{ek} , \bar{v}_{bs} , \bar{v}_{pi}).

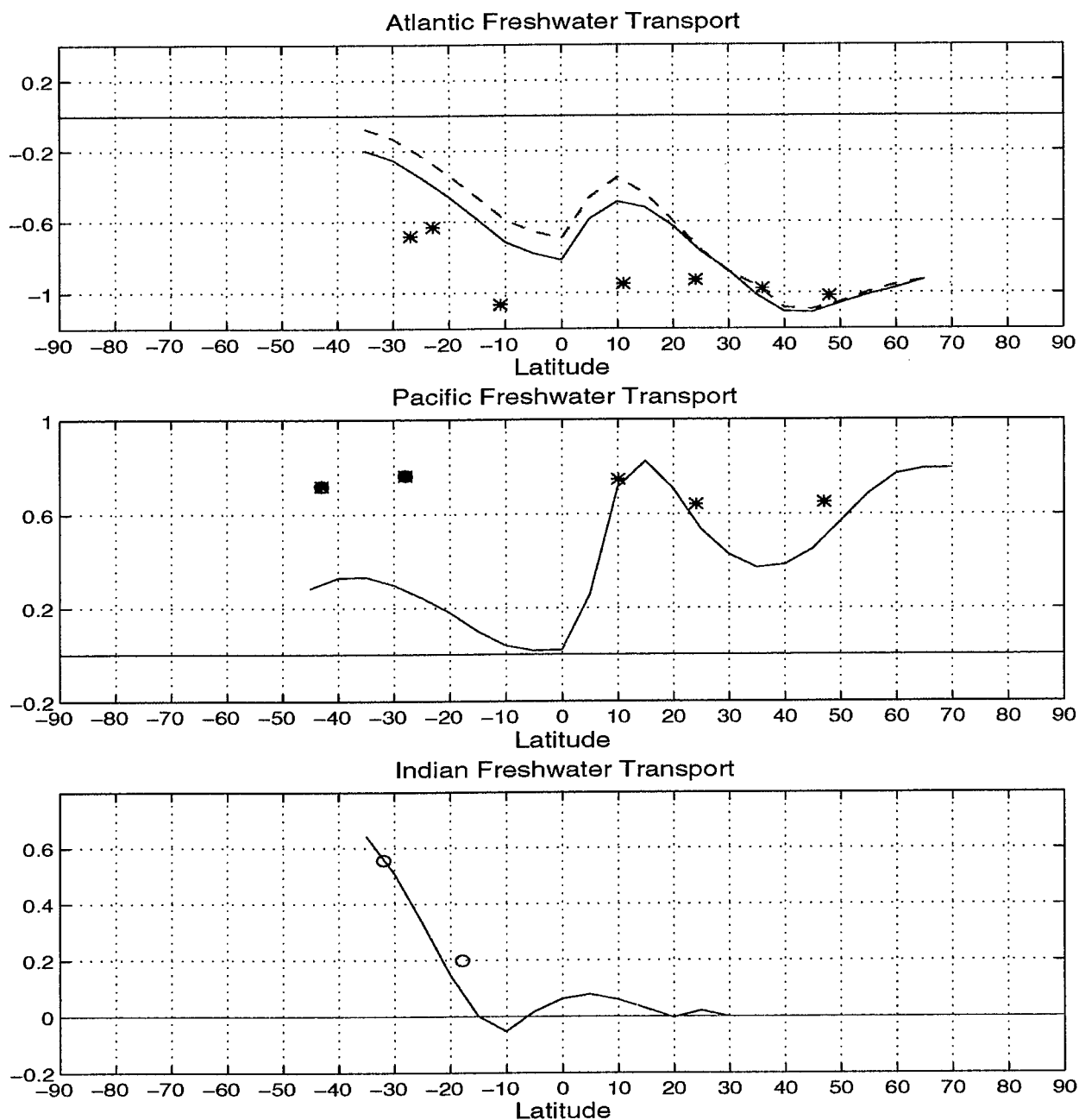


Figure 3.25: Estimates of northward meridional freshwater transport within the Atlantic, Pacific and Indian Basins ($10^6 \text{ m}^3/\text{s}$). The solid green curves represent the *Baumgartner and Reichel* [1975] P-E+R estimates which were used to initialize the model in the Pacific and Indian Basins. The dashed line represents the *Schmitt et al.* [1989] values used to initialize the model in the Atlantic. Both these curves use the same Bering Strait starting reference. The asterisks are the model estimates assuming that the initial estimate of Bering Strait throughflow is correct and recalculating the Ekman transport at each latitude. The circles are a reminder that an estimate of the Pacific/Indian throughflow has been used. Note: none of these values are considered significantly different from zero. A discussion of the associated uncertainties begins on page 217.

Section	Ekman Transport	Uncertainty	Section	Ekman Transport	Uncertainty
#A48N	-4.2	1.3	#A57S_W	1.1	11.2
#A36N	-2.8	1.1	#A57S_E	0.9	11.2
#Flst	0.1	0.5	#P47N	-5.1	1.4
#A24N	4.2	1.3	#P24N	8.5	1.3
#A11N	8.7	1.9	#P10N	38.3	1.7
#A11S	-12.8	1.2	#P28S	-5.3	6.9
#A23S	-4.1	1.1	#P43S	9.2	7.1
#A27S_W	-0.8	3.0	#Mz_S	-0.7	1.2
#A27S_E	-0.2	2.8	#I18S	-15.3	6.5
#0E_S	-0.4	1.0	#I32S	0.4	6.7

Table 3.18: Standard model estimates of Ekman transport computed to balance the mass and salinity transports across the sections (see the discussion in section 3.4.6). The Ekman transports across the following sections were not corrected: #Drake, #30E, #0EN, #0E2Afr, #132E and #Mz_N. Uncertainties are taken from the uncertainty in the top to bottom transport across the sections. All values are in 10^9 kgs^{-1} . Positive values are northward and eastward.

In Figure 3.25 the standard model freshwater estimates indicated by asterisks are computed assuming that the initial estimate of the Bering Strait throughflow [Coachman and Aagaard, 1988] is correct and recalculating the Ekman transport at each latitude so that the overall mass balance is exactly met. The new estimates of Ekman transport are listed in Table 3.18. All but four of the recomputed Ekman transports are consistent with the initial estimates to within the 1σ uncertainties quoted in Table 2.4. Of the remaining four (#A24N, #A11S, #A27S_W and #0ES) only #0ES is different by more than 2σ . This difference is not considered particularly worrisome, as it is thought that reliable wind stress estimates are not yet available at such high southern latitudes [Mestas-Nuñez et al., 1994]. The freshwater flux estimates in the Indian and South Pacific are computed using the mean estimate of the PI throughflow from the Indian Ocean sections assuming that the initial Ekman transport is correct. The #A11N estimate has assumed that the initial North Brazil Current estimate (Table 3.1) is correct.

Ignoring the uncertainties for a moment, there are a number of comments which can be made about Figure 3.25. The model estimates of freshwater transport agree, at least in sign, with the initial estimates. The particularly good agreement in the North Pacific may be fortuitous but is likely technical and due to the relative lack of constraints for the large number of unknowns in the region. Regions G and F (Figure 2.3) have ratios of $\frac{\text{number of equations}}{\text{number of unknowns}}$ of 0.2 and 0.1 respectively, compared to ratio 0.5 and 0.6 in Areas A and B. With the large number of unknowns in the Pacific, the model has little trouble producing solutions with small residuals in the net top to bottom flux constraints. Since these equations contain the initial freshwater water flux estimates and since the equation residuals are small, the final freshwater flux estimates tends to be very similar to the initial ones. In the Indian Basin the model freshwater transport estimates are similar to the *Baumgartner and Reichel* [1975] values and the suggested flux divergence, loss of freshwater to the atmosphere over the region is similar. The model estimates in the Atlantic are difficult to analyze. They are of the same sign as the P-E+R estimates but this is mainly due to the integration reference point. The flux divergences are quite different and lead to a discussion of the uncertainties involved in the calculation.

Basing the uncertainties of the freshwater fluxes upon the model estimate of the uncertainty in the top to bottom mass flux equations (*i.e.* the model estimate of the uncertainty in the mass balances across a section based on the covariance the reference level velocities) results in a range in uncertainty of 1.1 to $7.1 \times 10^9 \text{ kg s}^{-1}$. Even if the sections affected by the PI throughflow are ignored, the mean top to bottom uncertainty based on the uncertainty in the reference level velocities is $1.3 \times 10^9 \text{ kg s}^{-1}$, a value which is larger than any of the freshwater flux estimates. Historically it has always been difficult to compute freshwater fluxes from hydrographic data because they have been taken as the residual of a set of larger numbers. This same technique has been used here and leads us to question our ability to compute freshwater fluxes from hydrography.

A number of questions arise concerning the formulation of the problem which tend to confuse the estimation of freshwater flux uncertainty. What is the effect of the uncertainty in the individual elements used in the equations just presented on the uncertainty of the whole? Can we do better by assuming that we know the total balance better than the individual elements, and how well do we think we know this total balance? Can we can utilize the fact that there is no net divergence of salt flux within the oceans? Can the uncertainties be reduced through the use of salinity anomaly conservation?

What is the effect of the uncertainty in the individual elements used in the Equations 3.1 and 3.2 to the uncertainty of the whole?

The uncertainty in the mean Bering Strait throughflow does not appear to contribute a great deal to the uncertainty in the freshwater flux estimate. The quoted uncertainty in the Bering Strait volume flux value was 0.6 Sv. The equations above can be rewritten:

$$\rho \bar{v}_g - \rho \bar{v} \bar{S}_g / \bar{S}_{ek} - \rho \bar{v}_{bs} \times (1 - \bar{S}_{bs} / \bar{S}_{ek}) = T_{fw} \quad (3.5)$$

The term $(1 - \bar{S}_{bs} / \bar{S}_{ek})$ would range between 0.165 to 0.025 for a very large allowance in the possible range of uncertainty in the mean salinity of the Bering Strait throughflow (30 to 35). So a six tenths of Sverdrup difference in the Bering Strait volume flux, even associated with a 2.5 difference in salinity would only result in a $0.1 \times 10^9 \text{ kg s}^{-1}$ change in the model T_{fw} estimate.

On the other hand, as already discussed, the estimated uncertainties in the geostrophic component of meridional mass flux, based upon the computed uncertainty in the model reference level velocities, are alone enough to swamp most of the freshwater flux estimates. The uncertainties associated with the time variance in the relative velocity field, which we are not in a position to include in our uncertainty estimates, are also likely to be capable of swamping the freshwater flux estimates.

The models used the variance in a certain set of annual average winds to account for the uncertainty in the Ekman component of transport. These initial estimates almost certainly under-represent the variance in the true field.

Using the individual elements within the equations to compute the uncertainty of the oceanic freshwater flux, leads one to conclude that the biggest obstacle remaining in computing the freshwater flux from hydrographic lines is the inability of these data, in combination with wind data, to compute absolute mean mass flux across lines of latitude to an accuracy greater than the magnitude of the freshwater fluxes.

Can we do better by assuming that we know the total balance better than the individual elements and how well do we think we know this total balance?

In setting up this problem we defined weights for our equations based upon how well we thought we could balance the conservation equations using hydrographic measurements. We chose to use a base value of $2 \times 10^9 \text{ kg s}^{-1}$ for the top to bottom equations. Other studies have used similar values: $3 \times 10^9 \text{ kg s}^{-1}$ [Roemmich, 1983], $2 \times 10^9 \text{ kg s}^{-1}$ [Rintoul and Wunsch, 1991] and computed from the variance of the station pair transports, around $1 \times 10^9 \text{ kg s}^{-1}$ [Wijffels, 1993]. If we assume that the standard model's estimate of $\sigma_{\bar{v}_g}$ is equivalent to an uncertainty in the net mass balance (*i.e.* the uncertainty in the other components has already been included in our initial equation weighting), we get the range of values mentioned above (1.1 to $7.1 \times 10^9 \text{ kg s}^{-1}$). These estimates will not allow the calculation of freshwater flux to go forward.

On the other hand, satellite measurements suggest that the actual balance between the various components in Equation 3.2 is better than the model estimates. After removal of seasonal steric effects, sea level computed from TOPEX/POSEIDON data in the Pacific, averaged over ten degree bands displays a dominant variation of 2 cm over a 10 day period [D. Stammer pers. comm.]. This value can be divided

by the area over which it is computed (about 10,000 km X 1000 km) to give a rough estimate of its implied net mass balance.

$$\left(\frac{2 \times 10^{-2} \text{ m}}{10 \text{ days}}\right) (1 \times 10^{13} \text{ m}^2) = 2 \times 10^5 \text{ m}^3/\text{s} \quad (3.6)$$

An uncertainty of $0.2 \times 10^9 \text{ kg s}^{-1}$ in the net mass balance would certainly make the calculation of freshwater fluxes and flux divergences appear more feasible. However, a hydrographic section is made up of point measurements taken over a one to three month period. The sampling statistics of such a measurement technique make it hard to believe that our balances are subject to such a small uncertainty.

Can we can utilize the fact that there is no net divergence of salt flux within the oceans?

Dividing the oceanic salt flux across a section, $\overline{VS} = \iint vS \, dx dz$, into a mean and a variation about that mean,

$$\overline{VS} = \overline{V} \overline{S} + \overline{V'S'}, \quad (3.7)$$

using the knowledge that there is no divergence of salt flux within the oceans,

$$\overline{VS}^A - \overline{VS}^B = 0, \quad (3.8)$$

and stating that the divergence of the mass flux between two sections is expected to balance the divergence of freshwater,

$$\overline{V}^A - \overline{V}^B = (P - E + R)_a, \quad (3.9)$$

allows us to compute the freshwater flux divergence in the following manner,

$$(P - E + R)_a = \overline{V}^A \left(\frac{\overline{S}^B - \overline{S}^A}{\overline{S}^B} \right) + \frac{(\overline{V'S'}^A - \overline{V'S'}^B)}{\overline{S}^B}. \quad (3.10)$$

Does this formulation allow us to compute freshwater flux divergences which are significantly different from zero? Consider the hydrographic sections and areas in the North Atlantic by way of example. Table 3.19 contains estimates of the each the

Section	\bar{V}	\bar{S}	$\bar{V}\bar{S}$	$\bar{V}\bar{S}'$	$\bar{V}'\bar{S}'$
#A48N	-1.043	35.023	-26.66	-36.529	9.87
#A36N	-1.001	35.202	-26.69	-35.237	8.55
#A24N	-0.960	35.520	-29.00	-34.099	5.10
#A11N	-0.940	35.254	-26.30	-33.406	6.84
source:	model	data	model	model&data	equ. 3.7

Section	$\sigma_{\bar{V}}^2$	$\sigma_{\bar{S}}^2$	$\sigma_{\bar{V}\bar{S}}^2$	$\sigma_{\bar{V}\bar{S}'}^2$	$\sigma_{\bar{V}'\bar{S}'}^2$
#A48N	1.65	0.05	2016	2024	4040
#A36N	1.27	0.19	1579	1574	3153
#A24N	1.18	0.63	1722	1489	3211
#A11N	3.49	0.05	4268	4348	8606
source:	model	data	model	model&data	err. prop.

Table 3.19: The standard model values and uncertainties making up Equation 3.10. The row labeled source indicate the origin of the value. Note that the $\bar{V}'\bar{S}'$ term is computed from Equation 3.7 and its associated uncertainty is derived through error propagation of the terms in the equation.

elements of Equation 3.10 and their associated uncertainty for the standard model run in the North Atlantic. The \bar{V} and $\bar{V}\bar{S}$ terms are based on the model's absolute velocity field. The uncertainty in these terms is derived from the final covariance, matrix (see section 2.4.3). The \bar{S} and $\sigma_{\bar{S}}$ are computed from the data. The $\bar{V}'\bar{S}'$ term and its uncertainty are computed from Equation 3.7.

Table 3.20 contains estimates of the two terms on the right hand side of Equation 3.10 for the three areas in the North Atlantic. The first term in Equation 3.10 is, not surprisingly, quite small, less than $0.01 \times 10^9 \text{ kg s}^{-1}$. Its associated uncertainty is twice as large. The second term in the equation dominates, but is also subject to large uncertainties when computed from hydrographic data. If one believes that $\sigma_{\bar{V}}$ is $O(0.1 \times 10^9 \text{ kg s}^{-1})$, rather than the model estimate of $O(1 \times 10^9 \text{ kg s}^{-1})$, this uncertainty is reduced by half, with the model computed variance of the salt transport then dominating. If one goes a step further to say that the uncertainty estimate in the salt transport balance should be reduced by the same factor as that in the mass

	Area XVIII	Area XVII	Area XVI
Term 1	-0.005 ±0.016	-0.009 ±0.021	+0.008 ±0.018
Term 2	-0.037 ±2.4	-0.097 ±2.2	+0.049 ±4.3
(P-E+R) _a	-0.04 ±2.4	-0.11 ±2.2	+0.06 ±4.3

Table 3.20: Estimates from the North Atlantic areas of terms one and two on the right hand side of Equation 3.10 which computes freshwater divergence, (P-E+R)_a. Area XVIII is bounded by #A48N and #A36N. Area XVII is bounded by #A36N, #A24N and #Flst. Area XVI is bounded by #A24N, #Flst and #A11N. All values are in 10⁹ kg/s.

transport balance, then the estimated uncertainty in the second term in Equation 3.10 goes down by a factor of 10. Although this method produces uncertainties which are quite a bit smaller, even with this reduction none of the model freshwater divergence estimates could be considered significant.

If one believes that the smaller estimates of the uncertainty in \bar{V} are closer to the true values than the model estimated uncertainty then significant freshwater fluxes are within our grasp. However, as stated above, it would seem reasonable to believe that these estimates are too optimistic and are not realistic for calculations made with hydrographic data. The problem is that instead of measuring $\overline{V'S'}$, it is computed and is therefore, subject to a propagation of errors which renders it insignificant. The estimated uncertainty in $\overline{V'S'}$ as computed here assumes that there is no correlation between $\bar{V}\bar{S}$ and $\bar{V}'\bar{S}'$. This is clearly a worst case scenario. An estimate of the correlation between these two terms would allow for a reduced estimate of the uncertainty in $\overline{V'S'}$ and possibly a significant freshwater flux divergence estimate.

Can the uncertainties be reduced through the use of salinity anomaly conservation?

It has been suggested [T. McDougall, 1991] that the use of salinity anomaly conservation constraints as opposed to salt conservation constraints would add enough independent information to the system to reduce the uncertainties in the transport

due to the reference level velocities to levels acceptable for computing freshwater fluxes. The method works in the following manner.

The model equations are written in form given in Equation 2.3. Defining the elements of \mathbf{E} as $\mathbf{E}_{ij} = \int_B^T \rho_{ij} \mathbf{a}_{ij} dp$, mass conservation becomes

$$\mathbf{E}\mathbf{b} + \mathbf{n}_{mass} = -\Gamma. \quad (3.11)$$

Salt conservation is then written as

$$\mathbf{E}\mathbf{S}\mathbf{b} + \mathbf{n}_{salt} = -\Gamma\mathbf{S}. \quad (3.12)$$

Multiplying Equation 3.11 by a suitable mean salinity and subtracting it from Equation 3.12 gives an equation for the conservation of salinity anomaly,

$$\mathbf{E}(\mathbf{S} - \mathbf{S}_o)\mathbf{b} + (\mathbf{n}_{salt} - \mathbf{S}_o\mathbf{n}_{mass}) = -\Gamma(\mathbf{S} - \mathbf{S}_o). \quad (3.13)$$

If the expected value of $(\mathbf{n}_{salt} - \mathbf{S}_o\mathbf{n}_{mass})$ is zero, then we have created a perfect (noiseless) equation. The hope is that the noise in the anomaly equation (3.13) has at the very least, been reduced relative to the noise in the original equation (3.12), allowing for smaller residuals and therefore, smaller uncertainties in the solution.

In Chapter 4, a model which uses salinity anomaly constraints is described. In the tests which were run, we were unable to significantly improve the uncertainty in the solution. However, as will be discussed in the next chapter, further changes to the model may yet make this approach feasible.

3.4.7 The Standard Model Heat Fluxes

There is net transport of mass across all the sections used in this model. It is assumed in the heat flux estimates that the approximately $0.8 \times 10^9 \text{ kg s}^{-1}$ due to the Bering Strait throughflow which crosses all the sections in the Atlantic and

Pacific can be considered negligible compared to the uncertainty in the mass balance across the sections. The fluxes computed at those sections which are affected by P-I throughflow (#P43S, #P28S, #I18S, #Mz_N, #Mz_S, #I32S and #I32E) and those affected by ACC transport (#DRAKE, #0E_N, #0E2Afr, #30E and #I32E) are temperature fluxes based on a 0°C reference temperature. Table 3.21 lists the heat and temperature transports computed from the standard model. The heat flux estimates include both the mean and the spatially vary components. The contribution from the Ekman component has been estimated as the Ekman mass transport times the mean temperature of the uppermost model layer. Column 4 gives the heat flux estimates which have been computed with the Ekman components corrected to balance the salt conservation constraints (listed in Table 3.18) as described in the previous section. As a reference, Column 3 gives the heat fluxes which have been computed using the initial estimates of Ekman transport (Table 2.4). Unless otherwise indicated all references will be made to the column 4 values.

The table also gives the model estimated uncertainty in these values based upon the uncertainty in the reference level velocities. For the sections affected by the ACC the mean uncertainty in temperature transport is 0.22 PW. For those sections affected by the P-I throughflow the mean uncertainty is 0.14 PW. The mean uncertainty in the heat transport values for the other sections is only 0.05 PW. These uncertainties are *small*, probably too small. To come up with a more sensible estimate of the uncertainties in the heat transport, a number of factors other than just the uncertainty in the reference level velocities ought to be considered.

Using data from a number of different transects in the South Atlantic between 11°S and 30°S, *Holfort* [1994] compares results from several different inverse model runs and a calculation based upon the method of *Hall and Bryden* [1982] to determine those factors which most strongly contribute to the uncertainty in the estimated heat transports. Having considered the influence of the choice of level of no motion,

Section	Net Mass transport (10^9 kg/s) final	Heat/ Θ transport (PW)		Uncertainty due to σ_b (PW)	Total Estimated Uncertainty (PW)
		initial	final		
#A48N	-1.0 ± 1.3	0.65^\dagger	0.65	0.04	0.25
#A36N	-1.0 ± 1.1	1.02^\dagger	0.88	0.06	0.26
#Flst+#A24N	-1.0 ± 1.2	1.14^\dagger	0.93	0.05	0.26
#A11N+NBC	-0.9 ± 1.9	1.33^\dagger	1.34	0.05	0.26
#A11S	-1.1 ± 1.2	1.02	0.88	0.04	0.25
#A23S	-0.7 ± 1.1	0.31	0.33	0.04	0.25
#A27S	0.7 ± 1.2	0.33	0.50	0.05	0.26
#A57S	0.0 ± 1.9	-0.03	-0.03	0.02	0.25
#P47N	0.6 ± 1.4	-0.10	-0.08	0.04	0.25
#P24N	0.6 ± 1.3	0.47	0.45	0.09	0.27
#P10N	0.8 ± 1.7	0.47	0.44	0.07	0.26
#Mz_N	0.3 ± 1.6	—	0.03	0.05	0.26
#Mz_S	0.2 ± 1.2	0.06	0.01	0.05	0.26
#0E_S	0.0 ± 1.0	0.03	0.03	0.01	0.25
#0E_N	167.4 ± 5.2	—	1.85	0.14	0.29
#0E2Afr	142.7 ± 4.6	—	0.90	0.18	0.31
#Drake	141.1 ± 3.4	—	1.40	0.10	0.27
#30E	143.7 ± 4.7	—	1.16	0.31	0.40
#132E	151.2 ± 7.9	—	1.73	0.35	0.43
#P28S	9.6 ± 6.9	-0.07	-0.05	0.16	0.30
#P43S	9.6 ± 7.1	0.28	0.25	0.12	0.28
#I18S	-8.8 ± 6.5	-1.51	-1.45	0.16	0.30
#I32S	-8.3 ± 6.7	-1.29	-1.30	0.13	0.28

Table 3.21: Standard model estimates of heat and temperature fluxes. Column three (initial) contains the heat flux based on the initial input estimate of Ekman transport (Table 2.4). Column four (final) contains the heat flux based on the Ekman component which has been corrected to balance the salt equations as described in Section 3.4.6 (Table 3.18). See text for a discussion of the uncertainties.

[†] These values are taken from the test model which removed the bottom water constraints at 24°N and 36°N.

the layer definitions, the box definitions, the prescribed flux constraints, additional conservation constraints, the use of bottle versus CTD data, the choice of wind field and the temporal variability of temperature field, *Holfort* determines that the net uncertainty for the heat transport estimates in this South Atlantic region is on the order of 0.25 PW. He further determines that the largest contributing factor is the uncertainty arising from the temporal variability of the temperature in the upper ocean, $O(0.18 \text{ PW})$.

In our global analysis as it will be shown shortly, at some latitudes the effect of the uncertainty in the estimated Ekman transport plays a greater role in contributing to the net uncertainty in the heat transport estimates than it does in the South Atlantic region discussed by *Holfort* [1994]. In some regions the effect of prescribed flux (western boundary transport) constraints plays a greater role. The data are not yet available to determine the contribution of the ocean's temporal variability on the global scale, but the fact that the data sets used in the standard model span both seasons and decades and yet do not represent a climatology, is reason enough to believe that the net uncertainty in the standard model heat transport estimates is quite a bit larger than the 0.05 PW suggested by the uncertainty in the reference level velocities. For this reason, the uncertainty which we will ascribe to the heat and temperature transport estimates for the standard model (column 6 of Table 3.21) will be taken as that due to the uncertainty in the reference level velocities (column 5 of Table 3.21) combined with the average uncertainty suggested by *Holfort* for his South Atlantic sections (0.25 PW). It is understood, that in some regions this method will likely result in an over-estimate in uncertainty (*e.g.* #A57S), while at others it may represent an under-estimate (*e.g.* #P10N).

The zonally integrated values of heat and temperature flux across the lines of latitude described by the standard model are broadly compared to previous estimates in Figure 3.26. The model values within the Atlantic are consistent with many of the

previous estimates to within expected uncertainties and fall within the seasonal range provided by *Hsiung et al.* [1989]. The estimates at 24°N and 36°N are lower than some of the previous estimates and will be discussed shortly. The equatorward flux of heat within the South Atlantic, a consequence of a vertically overturning cell which carries warmer waters equatorward and colder waters poleward, is well illustrated by all the estimates.

The flux of heat within the Indian Basin is expected to be southward as much of the Indian Ocean lies at latitudes where surface warming rather than cooling occurs and there is no exit for this build up of heat to the north. Within the South Indian Ocean, model poleward temperature fluxes increase with increasing estimates of P-I throughflow, as the throughflow is associated with the southward mass transport of surface and intermediate waters in this basin. Likewise, in the South Pacific, model estimates of temperature flux become more equatorward as throughflow estimates increase. The net heat transport across 30°S in the Indian and Pacific Basins is not significantly affected by changes in the throughflow transport.

Figure 3.27 provides the zonally integrated values of heat flux across the lines of latitude and meridionally integrated values of temperature flux across lines of longitude described by the standard model. This map illustrates the loss of heat throughout the North Atlantic. The values of 1.3 PW at 11°N is extremely sensitive to the choice of North Brazil Current transport as most of the warmer waters are carried northward in the boundary current at this latitude. The North Brazil Current transport estimates range from $10.8 \times 10^6 \text{ m}^3 \text{ s}^{-1}$ in the April/May to $35 \times 10^6 \text{ m}^3 \text{ s}^{-1}$ in the July/August [*W. Johns* pers. comm., 1994]. It is therefore expected that the heat flux at this latitude is also subject to a strong seasonal variability. *Friedrichs and Hall* [1993] found that varying North Brazil Current transport estimate from the synoptic March value to an annual average value produced variations in heat transport of 0.8 PW. The heat transport estimates of all sections which contain strong boundary

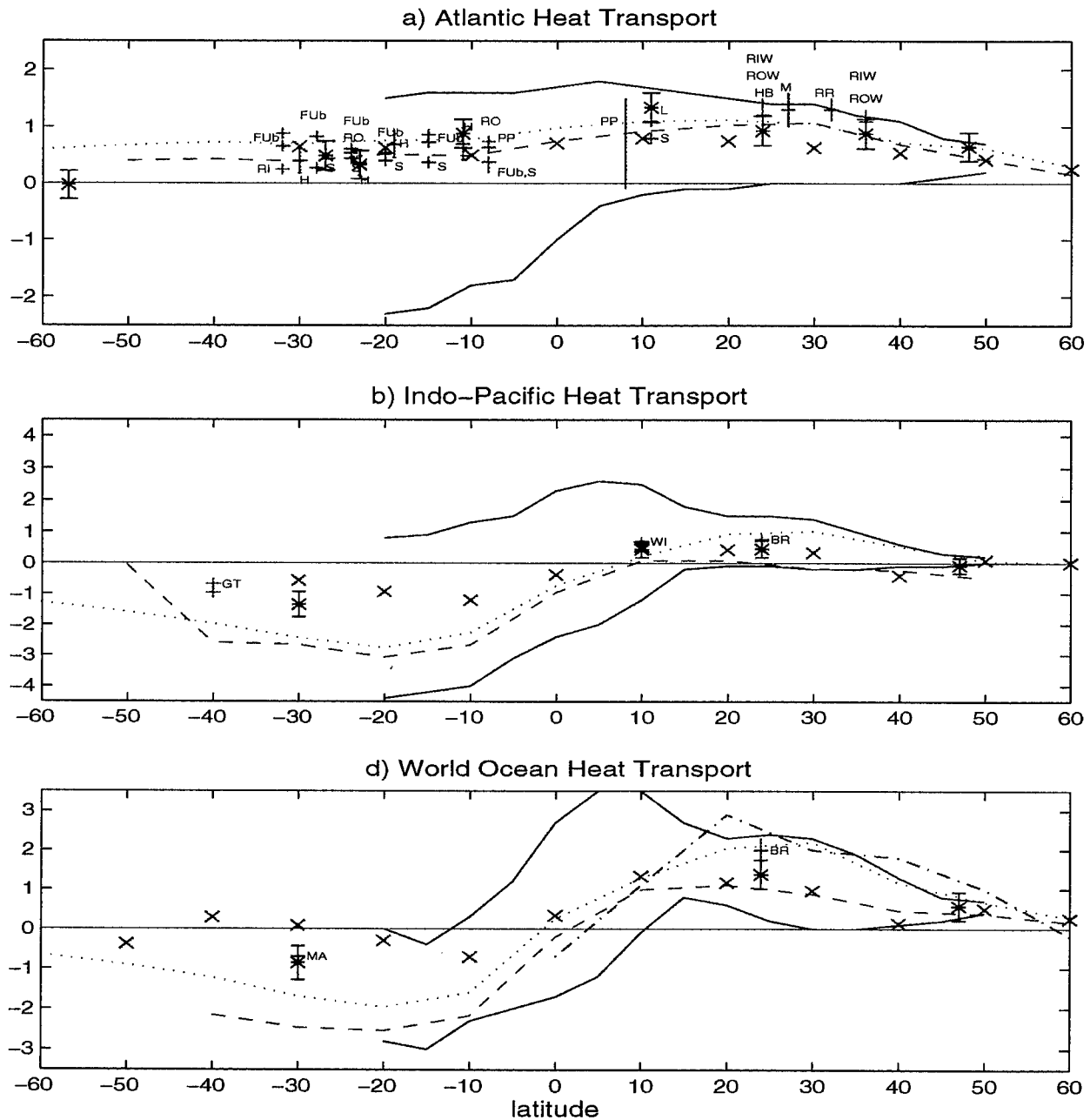


Figure 3.26: Comparison of standard model meridional heat flux estimates (asterisks with error bars) with previous values. Figures a), b) and c) represent the Atlantic, Indo-Pacific and World Oceans respectively. Solid curves: *Hsiung et al.* [1989], Dotted Curve: *Hastenrath* [1982], Dashed curve: *Talley* [1984], dash dot curve: *Oort and Van der Haar* [1976] and x's: *Semtner and Chervin* [1992]. The reference initials are described in Figure 1.1. The values and the uncertainties due to the uncertainty in the reference level velocities are listed in Table 3.5. All values are in PW.

currents will be sensitive to the estimated transport in the currents. However, the influence of the boundary currents is not always this dramatic. *Holfort* [1994] found that reasonable variations in the estimated transport of the Brazil Current resulted in variations of only 0.03 PW in the South Atlantic heat transport. The estimated magnitude of boundary currents on the meridional heat transport estimates is tied to the expected range in reasonable mass transports for the boundary currents and the temperature difference between the boundary current and interior flows.

At three places (47°N, 24°N and 30°S), the model produces heat flux estimates across complete latitudinal circles. At 30°S, the standard model estimate of heat flux -0.9 ± 0.4 PW is dominated by a large (>1 PW) poleward temperature flux in the Indian Basin. At 47°N, the net poleward heat flux of 0.6 ± 0.4 PW is dominated by the northward transport into polar regions within the Atlantic Basin. At 24°N there is a net heat transport of 1.4 ± 0.4 PW. This value is lower than the *Bryden et al.* [1991] estimate of 2 PW. The *Bryden et al.* value was obtained from individual estimates which used the same hydrographic transects in the Atlantic and Pacific as studied here. Their own value of 0.76 ± 0.3 PW for the Pacific section is higher but not significantly different from that found here, 0.5 ± 0.3 PW. The standard model Atlantic value 0.9 ± 0.3 PW is also low, but consistent with the *Hall and Bryden* [1982] value of 1.2 ± 0.3 PW, used by *Bryden et al.*

It has been suggested that the lower estimate in the model heat flux values at 24°N may be due to a general over-estimate of the Ekman transport based on the ECMWF winds (see *Mestas-Núñez et al.* [1994]). However, in neither the Atlantic nor the Pacific do our estimates of Ekman transport appear to have been over-estimated. In the Pacific, the difference in heat flux estimates is certainly due to a difference in the expected Ekman contribution used for the two studies. This difference, however, constitutes a possible under-estimate on the part of the ECMWF winds ($8.8 \pm 1.3 \times 10^6 \text{ m}^3 \text{ s}^{-1}$) or an over-estimate by *Bryden et al.* ($12 \times 10^6 \text{ m}^3 \text{ s}^{-1}$ from

heat & temperature transport

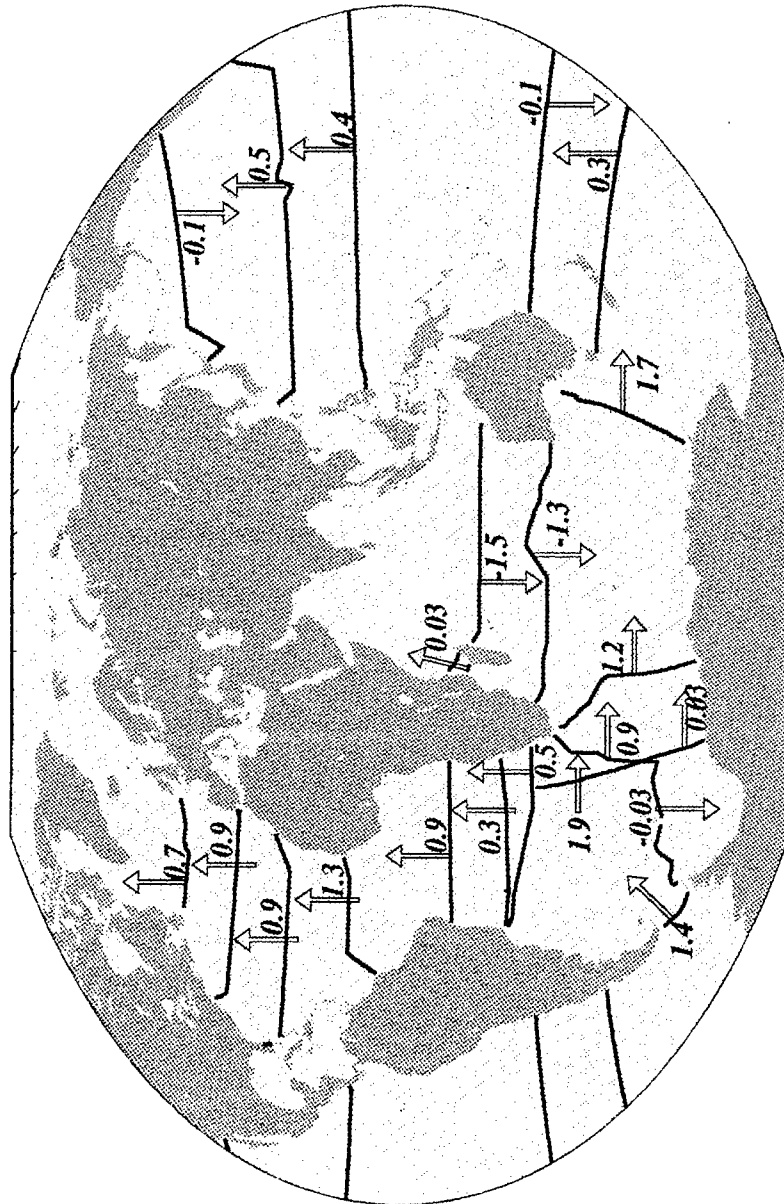


Figure 3.27: Map of standard model meridional and zonal heat (blue) and temperature (red) flux estimates. All values are in PW. The estimated uncertainties associated with these values are listed in Table 3.21.

Hellerman and Rosenstein [1983]). The reasons for the lower estimate of heat transport across 24°N in the Atlantic are discussed below.

#A24N Test Models

At 24°N and 36°N the standard model estimates of 0.9 ± 0.3 PW are somewhat lower than most of the previous estimates (at 24°N: 1.2 ± 0.3 [*Hall and Bryden*, 1982] (H&B henceforth) and 1.2 ± 0.2 [*Rintoul and Wunsch*, 1991] (R&W henceforth) and at 36°N, 1.3 ± 0.2 [R&W]). Although all the values are technically consistent with one another the following discussion looks at the detailed differences between the R&W model heat flux and the standard model heat flux in an effort to emphasize how choices in model construction and analysis methods can affect the resulting values.

There are a number of possible reasons for the standard model's lower estimate of heat transport at 24°N in the Atlantic:

- the standard model's Florida Strait transport
- the calculation of the Ekman transport
- and the bottom water constraints at 24°N and 36°N.

At 24°N in the Atlantic the low estimate of heat transport may be partially due to the standard model's inability to produce a full $31 \times 10^9 \text{ kg s}^{-1}$ flowing through the Florida Straits. An increase in the Florida Straits transport of $1 \times 10^9 \text{ kg s}^{-1}$ at the mean temperature of the section, which returns across #A24N at the mean temperature of that section results in an increase in the net heat transport of 0.05 PW. It should however, be noted that H&B used an estimate of $29.5 \times 10^6 \text{ m}^3 \text{ s}^{-1}$ in the Florida Straits, while R&W used an estimate of $30 \times 10^6 \text{ m}^3 \text{ s}^{-1}$ to produce the same net heat flux. So while the Florida Straits transport may account for some of the difference with R&W estimate, it does not account for the difference with H&B.

The initial estimate of the Ekman transport across #A24N used in the standard model, $5.4 \pm 0.7 \times 10^6 \text{ m}^3 \text{ s}^{-1}$ is similar to the $5 \times 10^6 \text{ m}^3 \text{ s}^{-1}$ used by H&B [from

Leetmaa and Bunker, 1978], and is not significantly different from the R&W value of $6 \pm 2 \times 10^6 \text{ m}^3 \text{ s}^{-1}$ [from *Hellerman and Rosenstein*, 1983]. However, the corrected model estimate of $4.2 \times 10^9 \text{ kg s}^{-1}$ is at the low end of the range. A difference of $2 \times 10^9 \text{ kg s}^{-1}$ in the Ekman transport given the temperature of the surface layer compensated by a return flow at the mean the temperature of the section, results in a difference in the net heat transport of 0.13 PW. Applying the uncorrected ECMWF estimate of Ekman transport to the standard model produces a heat transport estimate at 24°N of 1.04 PW.

The temperature which is chosen to be associated with the Ekman component at this latitude is also partially responsible for the difference in the total heat flux estimates. R&W chose to use the average temperature of the sea surface temperature, 26.8°C . In this analysis we have chosen to use the average temperature of the surface layer, 22.1°C . For a $5.5 \times 10^9 \text{ kg s}^{-1}$ Ekman component this represents a difference of 0.1 PW. The R&W value is probably a bit too high, ours a bit too low.

As discussed earlier the bottom water constraints which were applied to the standard model and which have since been determined to be inconsistent with the model, have the effect of reducing the magnitude of the overturning cell at 24°N and 36°N . Removing these constraints from the model increases the estimated heat flux at both latitudes by another 0.1 PW. The heat flux at 24°N in the Atlantic listed in column 3 of Table 3.21 of 1.14 PW comes from the test model which did not include the bottom water constraints and is computed using the uncorrected Ekman flux. It represents the maximum heat flux found at this latitude in the test models.

Given a slightly greater Florida Straits transport, an increased estimate in the Ekman transport and the removal of the bottom water constraints, a heat transport estimate of 1.2 PW could be obtained. However, it should be noted that

- the standard model was not able to obtain a larger Florida Straits transport estimate and

- it was the requirement of mass balance across #A24N which produced the reduced Ekman transport estimate. This requirement is not unreasonable in light of the desire to compute freshwater and heat flux estimates, therefore it shall be retained.

The final model estimates of heat flux at 24°N and 36°N are 1.1 ± 0.3 PW and 1.0 ± 0.3 PW, respectively. These estimates come from the model which did not attempt to constrain the flow of bottom water in the North Atlantic beyond 11°N.

#A36N Test Models

At 36°N neither the temperature of nor the correction to the Ekman transport is at issue. The rather low estimate of heat transport is in part related to the low estimate in the strength of the overturning cell at this latitude which has been caused by the inclusion of constraints on the flow of bottom water. Several test models were run in an attempt to reproduce the 1.3 PW best estimate value obtained by R&W. These tests included models which ran only the North Atlantic region, only area XVII, only area XVII with the total silica conservation constraint used by R&W and models which allowed for larger estimates of the reference level velocities. None produce a larger heat flux. In comparing the layer by layer temperature transports of the R&W best estimate model and our test models it became apparent that it is the zonally varying component of the temperature flux that is source of the discrepancy.

Multiplying the layer average temperature by the transport in each layer and summing, produces temperature fluxes of about 1.1 PW for the models without upweighted \hat{b}_s and 1.2 PW for those with upweighted \hat{b}_s and for the R&W model (see Table 3.22). The implied zonally varying component of heat flux is quite different for our models and the R&W model, and accounts for the difference in the estimated totals. This result is interesting because R&W used this same argument to account for

Model	Total T_{Θ}	Ekman	$\sum T\bar{\Theta}$	$T'\Theta'$
R&W (3000 db)	1.34	-0.18	1.22	0.30
Standard	0.89	-0.21	1.07	0.03
Test	1.04	-0.21	1.19	0.06

Table 3.22: A Comparison of the components of heat flux, T_{Θ} across #A36N computed from Tables 3.1 and 5.2 of *Rintoul* [1988], the standard model and a test model intended to mimic the *Rintoul* model which used only area XVII, did not include any bottom water constraints and allowed for larger reference level velocities. All values are in PW.

the difference between their heat flux value at 36°N and that of *Roemmich and Wunsch* [1985] (0.8 PW) who used a smoothed data set. The difference is that whereas the *Roemmich and Wunsch* model produced horizontal correlations of velocity and temperature whose sum was of the opposite sign of R&W's, the models used here simply find very little contribution at all from the zonally varying component of the heat flux. Why these estimated contributions should be so different is not yet understood, but it certainly warrants further investigation as it represents a continuing source of uncertainty in all heat flux estimates at this latitude.

#P10N Test Models

In the Pacific the standard model heat transport estimate of 0.44 ± 0.3 PW at #P10N is consistent but lower than the *Wijffels* [1993] estimates of 0.61 and 0.66 PW. At this latitude the heat flux estimates are extremely sensitive to the choice of Ekman transport. *Wijffels* [1993] looked at three estimates of mean annual Ekman flux across this latitude; $43.3 \times 10^9 \text{ kg s}^{-1}$ from *Hellerman and Rosenstein* [1983], $37.4 \times 10^9 \text{ kg s}^{-1}$ from the Florida State University wind analyses of *Goldenburg and O'Brien* [1981] and $32.6 \times 10^9 \text{ kg s}^{-1}$ from *Harrison* [1989], all of which are higher than ECMWF estimate of $24.3 \pm 2.7 \times 10^9 \text{ kg s}^{-1}$. The final value used by *Wijffels* for this #P10N section was $38.6 \times 10^9 \text{ kg s}^{-1}$, based on the FSU winds and adjusted to obtain conservation of salt in her model. The standard model used this estimate of Ekman transport initially

and afterwards adjusted it to $38.3 \times 10^9 \text{ kg s}^{-1}$ to balance its own salt budget. The test model (Test 1 of Table 3.14 see page 3.4.3) which used the ECMWF winds produced a large net heat transport in the opposite direction, -0.74 PW . At this latitude the choice of using or not using the ECMWF winds can have a profound effect upon the resulting estimate of heat transport. In fact any estimate of heat transport at this latitude will be highly dependent upon the associated estimate of Ekman transport simply because the range in estimated wind stress values integrated across the width of the Pacific creates a large range in Ekman transport estimates.

Heat Convergences

Figure 3.28 illustrates the pattern of oceanic heat convergence and divergence within the boxes of the standard model. Although some of these values are not significantly different from zero, their pattern is recognizable. Again the heat loss over the ocean in the North Atlantic is well illustrated, as is heat loss over the North Pacific. Heat gain around the equatorial regions and loss throughout much of the Southern Ocean is also shown. The gain of heat within the Indo-Pacific region would decrease with a decreased estimate of the Ekman transport across #P10N. Likewise the estimated gain of heat to the north (between 10°N and 24°N in the Pacific) increases with a decreased estimate of the Ekman transport across #P10N.

In spite of differing estimates of ACC mass transport, the pattern of the implied heat loss and gain (to/from both the atmosphere and the to the north) from the region of the ACC suggested by the standard model is similar to that suggested by *Georgi and Toole* [1982] and *Guiffrida* [1985] (henceforth G&T and GF). The standard model suggests a loss of heat within the Atlantic and Pacific sectors of $0.2 \pm 0.3 \text{ PW}$ and $0.3 \pm 0.4 \text{ PW}$ respectively, and a net gain of heat within the Indian sector $0.6 \pm 0.5 \text{ PW}$. G&T found net losses in the Atlantic and Pacific sectors of $0.3 \pm 0.3 \text{ PW}$ and $0.3 \pm 0.4 \text{ PW}$ respectively and GF found losses of 0.4 and 0.3 PW.

heat convergence

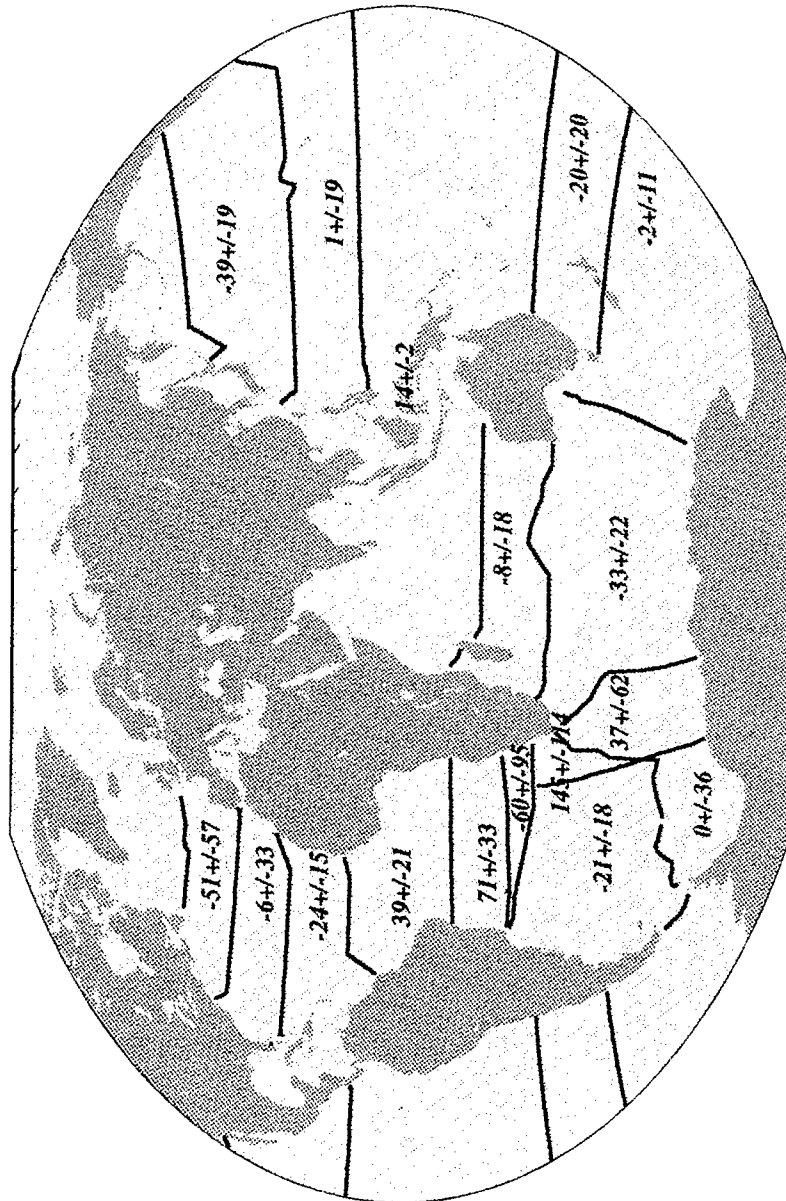


Figure 3.28: Map of the standard model oceanic heat flux convergence (blue: less than 0) and divergence (red: greater than 0) estimates. A convergence represents a net heat loss to the atmosphere. All values are in W/m^2 .

Within the Indian sector G&T found the same value as we do and GF's value of 0.7 PW is also similar.

The standard model results differ from these previous solutions in their implied atmospheric exchange rates. In the Indian sector of the southern ocean the net heat loss to the atmosphere of 0.7 ± 0.4 PW is consistent with, but larger than, that used by G&T (0.4 PW) and that used by GF (0.3 PW). In the Pacific sector, the standard model suggest a loss of 0.1 PW but with an uncertainty of 0.3 PW the value is not significantly different from zero. G&T and GF used values 0.2 PW and 0.3 PW. Again, these differences do not appear to be significant in light of the uncertainty in the standard model values and the difficulties involved in obtaining air-sea exchange data available in the Southern Ocean.

In the South Atlantic, air-sea exchange values used by G&T and GF suggested net losses to the atmosphere of 0.1 and 0.2 PW, respectively, while the standard model suggests a net heat gain of 0.3 ± 0.1 PW. This difference may be due to the larger area covered by the standard model. G&T and GF were looking at the air-sea exchange rates to the south of 40°S , whereas the standard includes the area between 30°S and 40°S . While the standard model does suggest a gain of heat in area III which extends to the far south, it is not significantly different from zero. The strong heat gain occurs in area IV and though we are not in a position to say where within the region most of the gain is occurs, it is possible that it happens to the north of 40°S . The *Bunker* [1988] atlas shows some heat loss over much of area IV, but also strong heat gain ($> 150 \text{ W/m}^2$) in the area IV region near the coast, so the standard model value does not appear unreasonable.

The uncertainty estimates include the 0.25 PW factor which was used in the heat transport uncertainty estimates (see page 226) and which was expected to be dominated by the uncertainty due to variability in the upper ocean and uncertainty in Ekman transport estimates. In the convergence calculation, this 0.25 PW has been

used once for each area¹⁰, rather than once for each section, as it is expected that variations affecting neighboring sections will be correlated.

As a final note on the heat flux estimates, two points should be made. The first is that estimates of the uncertainties in heat flux estimates rarely include the uncertainty due to the specific construction of the model, be it an inverse with a chosen set of layers, reference levels, and solution or a "direct" calculation which is also made with a set of assumptions about the movement of waters masses, topographic obstructions *etc.* Secondly, we should remember that when uncertainties are given at a 1σ level it should be expected that a third of all other estimates should lie outside this range. Also if we quote values of say 0.2 to 0.3 PW as 1σ uncertainties, we should mean it, *i.e.* 1.3 ± 0.2 PW and 0.9 ± 0.3 PW are consistent. So as we enter a stage where we are trying to pin down the oceanic contribution to the global heat balance, we would do well to continue to consider that pinning down the contributions to the uncertainty in these oceanic fluxes is just as important.

Having presented the mass, heat and freshwater transport results of the standard model, the next chapter discusses the steps in model development which brought about the set of requirements and weights used to constrain the standard model.

¹⁰The uncertainties in the heat convergence values are computed as $(\sum_i^{\text{sections}} \sigma_{T_{\theta i}}^2 + 0.25^2)^{1/2}$, where $\sigma_{T_{\theta}}$ is the uncertainty in heat transport due the uncertainty in the reference level velocities.

Chapter 4

Alternative Models

4.1 Introduction

Chapter 3 described the results of the standard model. To reach the set of constraints which defined this solution, a number of alternatively constrained models were first run. Rather than presenting the reader with a chronological account of the model development, this chapter simply presents a few of the models and results which laid the groundwork for deciding which constraints to include in the standard model and how to include them. It extends the discussion by describing the results of some more recent runs of models whose prescribed constraints are somewhat different from the those of the standard model.

The first section looks at the very first models run. These models (A and B) were used to examine the effect upon the circulation patterns of changing the initial velocity reference levels. It includes a discussion of the predicted Indonesian Passage throughflow and its sensitivity to the choice of reference level. This discussion continues in the next section which describes the effect upon the Pacific and Indian circulation when the P-I throughflow is varied (models C₁, C₂ and C₃). The third

section looks at the terms describing the transfer across the isopycnal interfaces of the standard model, considers the effect of better resolving these vertical transfer terms (model D₂) and also examines the solution of a model which allows no cross-isopycnal transfer (model D₁). The fourth section summarizes the past, present and possible future incarnations of the model and discusses some of experimental runs which have been made since choosing the constraints for the standard model. It also discusses some of the changes which could be made to further improve the model.

4.2 Shallow versus Deep Reference Levels

Shallow: Model A (*a.k.a.* SRL) and Deep: Model B (*a.k.a.* DRL)

To arrive at the set of geostrophic velocity reference levels used in the standard model (column 2 of Table 3.2, p. 58), a comparison was made between the solutions using a set of relatively shallow reference levels, model A (columns 3 and 4 of Table 3.2) and the solutions using a set of deeper reference levels, model B (columns 5 and 6 of Table 3.2). These levels were chosen to represent estimates of the approximate depths of the interfaces between oppositely directed water masses or to represent near bottom layers in which it was expected that the waters were moving relatively slowly. Many of the levels tested were taken from the literature. For each section, a subjective judgement was made concerning the suitability of each of the reference levels. The procedure involved an examination of the solution size (assuming smaller reference level velocities indicate a better choice of initial reference level), the solution residuals and the structure of the final zonally integrated transport profiles compared to the initial profiles (using only the relative velocity fields), as well as to profiles provided by previous studies.

For several, but not all the sections, the magnitude of the resulting reference level velocities was strongly affected by the choice of the initial reference level. In particular, this was the case in the South Atlantic at 11°S and 23°S where the rms reference level velocities (b_{rms}) for the deeper reference level model (DRL) were twice as large as for the shallow reference level model (SRL). The same held true in the Mozambique Channel sections. At #A48N, the b_{rms} of the SRL model (chosen as an estimate of the interface between Mode and Mediterranean waters) was twice as large as the DRL b_{rms} . Throughout the Southern Ocean meridional sections, the SRL rms reference level velocities were also, not surprisingly, considerably larger than the DRL ones.

The final choice of reference level usually sided with the smaller rms reference level velocity, as it was assumed that the other reference level (the one with the larger b_{rms}) was either not a good guess of a zero velocity level or that a zero velocity level in that part of the water column simply did not exist consistently across the entire section. At #A48N a third reference level was chosen which lay between the deep and shallow levels. This level was chosen to reduce the large, $O(60 \times 10^9 \text{ kg s}^{-1})$, net imbalances across the #A48N and within area XVIII.

It turned out that all the available station-specific reference levels (see Appendix A) were used. In the cases of #I32S and #A11N they were used because there was not a great deal of difference between the model A and B solutions. Therefore, it seemed reasonable to use the levels provided by previous research for the sake of consistency in comparison of results. For #P10N, the station-specific reference level velocities were used instead of either the deep or shallow isopycnals because the resulting circulation of bottom water seemed to make more sense. In all sections, the pattern of the circulation was also examined before making the decision between reference levels.

In the majority of cases, the structure of the zonally integrated absolute mass transport profiles and therefore, the solution residuals, were not significantly affected by the choice of reference level. In particular, the magnitude of the overturning cell within the Atlantic was not affected by the choice. The major exception occurred in the sections affected by the flow through the Indonesian Passage. The DRL model produced an east-west transport through the Indonesian Passage of about $26 \times 10^9 \text{ kg s}^{-1}$, while the SRL model produced a west-east (from the Indian Basin to the Pacific) transport of about $12 \times 10^9 \text{ kg s}^{-1}$.

Comparing the transport profiles of these sections with previous estimates [Wunsch *et al.*, 1983 for #P28S and #P43S; Fu, 1986 for #I18S, Toole and Warren, 1993 for #I32S and Macdonald, 1993 for all four sections], it was found, not surprisingly, that the SRL model with the smaller (albeit west-east) P-I throughflow (henceforth T_{PI}) compared more favorably with previous findings associated with small T_{PI} estimates: that is, in the South Pacific:

- a convergence between the two latitudes of surface waters;
- an equatorward flow of intermediate waters
- a poleward flow at mid-depths,
- an equatorward flow of bottom waters,

and in the South Indian Ocean:

- and a net poleward transport of surface waters.
- a small equatorward transport of intermediate waters
- a poleward transport at around 1000 db,
- a net equatorward transport of deeper waters,

The DRL transport profiles were overwhelmed by the large east-west T_{PI} , which caused nearly all the water to flow northward across the Pacific sections and considerably diminished the northward transport of deep waters within the Indian Basin while effecting a southward transport of shallower waters. Both models produced an unexpected (albeit small) poleward transport within the lowest layer of the

Indian Ocean sections. It was unexpected as there is no known source of bottom water within the Indian Basin. This feature eventually led to the standard model constraints which require northward flow of bottom waters within the Indian Basin.

It was decided to use the deeper reference levels even though the DRL transport profiles in the Indo-Pacific region were not as similar as the SRL profiles to those suggested by previous studies. The rationale for this decision was that the reference level velocities were smaller and the throughflow, although large, was in the expected direction. The next section looks at the effect upon the standard model of varying the T_{PI} estimate within the range of previous estimates ($0-20 \times 10^9 \text{ kg s}^{-1}$).

4.3 Unconstrained and Constrained T_{PI}

Models C_1 , C_2 and C_3

The results of models A and B, along with the reasoning that the Indo-Pacific region, area V, is the least well constrained of all the areas in the models and so is not well equipped to produce reliable estimates of the Pacific-Indian throughflow led to the decision to include a constraint on the P-I throughflow in the standard model. It turns out however, that left to its own devices the standard model produces a perfectly reasonable estimate of T_{PI} , about $11 \times 10^9 \text{ kg s}^{-1}$.

The standard model is quite different from the models A and B as a fair number of changes have taken place since the initial reference level tests. The changes include:

- the inclusion of constraints on
 - the heat flux into the Weddell Gyre (area II) region,
 - the flow in the eastern North Atlantic,
 - the flow of bottom water in the Indian and Atlantic,
- changes to the constraints on the Florida Straits transport, the Drake Passage transport and the North Brazil Current transport,

- changes to the expected order of magnitude of the cross-isopycnal transfer terms,
- and changes to the column and row weighting of the model which has changed how the solutions are chosen.

Not all these changes are likely to have had much of an effect upon the P-I throughflow estimate. Exactly which of these changes is responsible for bringing the T_{PI} estimate within the range of previous estimates has not been determined. Suffice it to say, that it is the last change which has probably had the strongest effect. The T_{PI} estimate which is produced by the unconstrained model is not significantly different from zero, however, it is interesting to look at how the number is limited.

Model C_1 is defined by the same constraints as the standard model but does not include any constraint on T_{PI} . Table 4.1 gives the net transport across the zonal sections affected by the throughflow for each of the steps in the recursion, beginning with the second step. The table illustrates how final the throughflow value is limited by each set of data and constraints included in the model. When the model uses only the data and constraints from the Southern Ocean sections a large throughflow value of 23 to $26 \times 10^9 \text{ kg s}^{-1}$ is obtained. Including the constraints from the Indian Ocean sections reduces this estimate to between 15 and $18 \times 10^9 \text{ kg s}^{-1}$. Including the Indo-Pacific region reduces it still further to between 11 and $15 \times 10^9 \text{ kg s}^{-1}$. The inclusion of the North Pacific sections brings the Indian and Pacific estimates closer together. The constraints in this region which are most likely responsible for the limiting effect upon the South Pacific T_{PI} estimates are those which require conservation of mass and salt across the #P10N section. The final estimate for T_{PI} which is produced by the fifth step in the recursion is about $11 \pm 14 \times 10^9 \text{ kg s}^{-1}$. The large uncertainty suggests that the standard model is capable of supporting both larger and smaller throughflows which brings us to the question of how it might do so. To answer this question two alternative models were run. Model C_2 included a constraint for zero throughflow. Model C_3 included a constraint for a $20 \times 10^9 \text{ kg s}^{-1}$ throughflow.

Using Regions	Indian 18°S	Indian 32°S	Pacific 43°S	Pacific 28°S
C & D	-	23.2±20.2	26.3±20.3	26.4±20.3
C, D & E	14.6±13.6	14.8±13.9	18.1±14.5	18.2±14.6
C, D, E & F	10.9±13.5	11.2±13.7	14.3±14.3	14.7±14.4
C, D, E, F & G	10.7±13.5	10.7±13.7	11.1±13.7	11.1±13.6
B, C, D, E, F & G	10.7±13.5	10.7±13.7	11.0±13.7	11.0±13.6
A, B, C, D, E, F & G	10.7±13.5	10.7±13.7	11.0±13.7	11.0±13.6

Table 4.1: Estimates of the magnitude of the Pacific-Indian throughflow from model C_1 containing no P-I throughflow constraint. The different rows contain solutions from each successive step in the recursion. All values are in 10^9 kg s^{-1} . The Ekman transport from Table 3.18 has been subtracted and $0.8 \times 10^9 \text{ kg s}^{-1}$ Bering Strait throughflow has been subtracted from the Pacific sections. The region definitions are given in Figure 2.3.

It is expected that the waters flowing from the Pacific to the Indian Basin are relatively warm and lie in the upper portion of the water column. Therefore, the T_{PI} constraints are placed upon the upper six layers of the #I32S section and are included as a net top to bottom flux across the combined #I18S and Mozambique Channel sections. The models are free to balance mass within the combined Pacific-Indian sections (area X) in any way they choose.

Model C_2 produces an estimated throughflow of about $0.3 \times 10^9 \text{ kg s}^{-1}$. Model C_3 produces an estimated throughflow of about $17 \times 10^9 \text{ kg s}^{-1}$. To account for this difference the rms reference level velocities for the sections involved change by less than 0.1 cm s^{-1} (20%). Figure 4.1 and Table 4.2 illustrate how these models adjusted transport estimates in the vertical to compensate for the different throughflow requirements. As expected none of the adjustments exceed the uncertainty on the standard model transport values.

In the Indian Basin, although the constraints were placed in the upper 6 layers of the model at 32°S, the surface layer transports are not greatly affected by the net throughflow. About 40% of the difference in transport between the models is carried

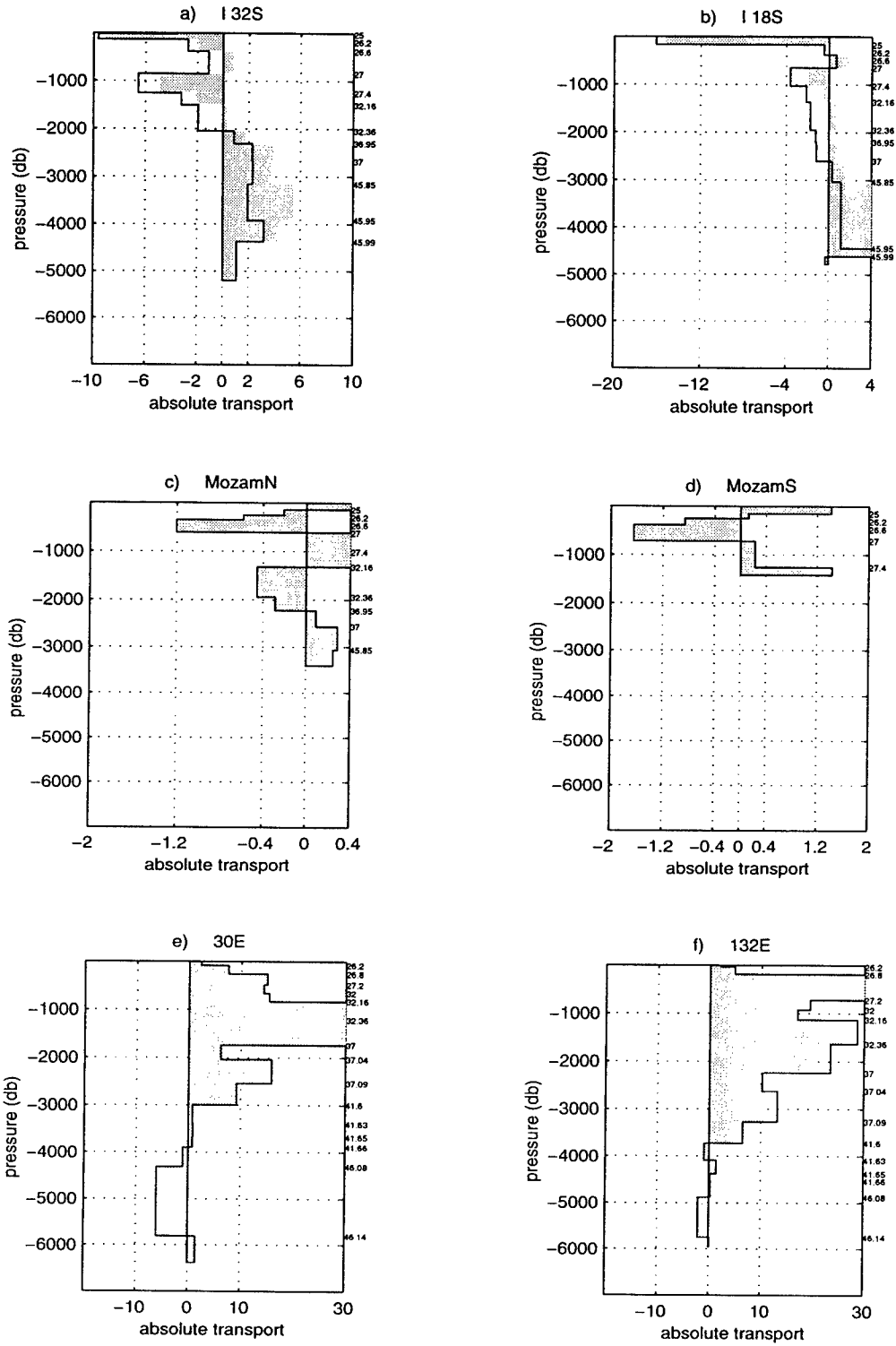


Figure 4.1: Comparison of the zonally integrated mass transport profiles resulting from models C_2 , $T_{PI} = 0 \times 10^9 \text{ kg s}^{-1}$ (shaded) and C_3 , $T_{PI} = 20 \times 10^9 \text{ kg s}^{-1}$ (solid line), for sections: (a) #I32S, (b) #I18S, (c) #MZ_N, (d) #MZ_S, (e) #30E and (f) #132E. The Ekman transport is included in outcropping layers.

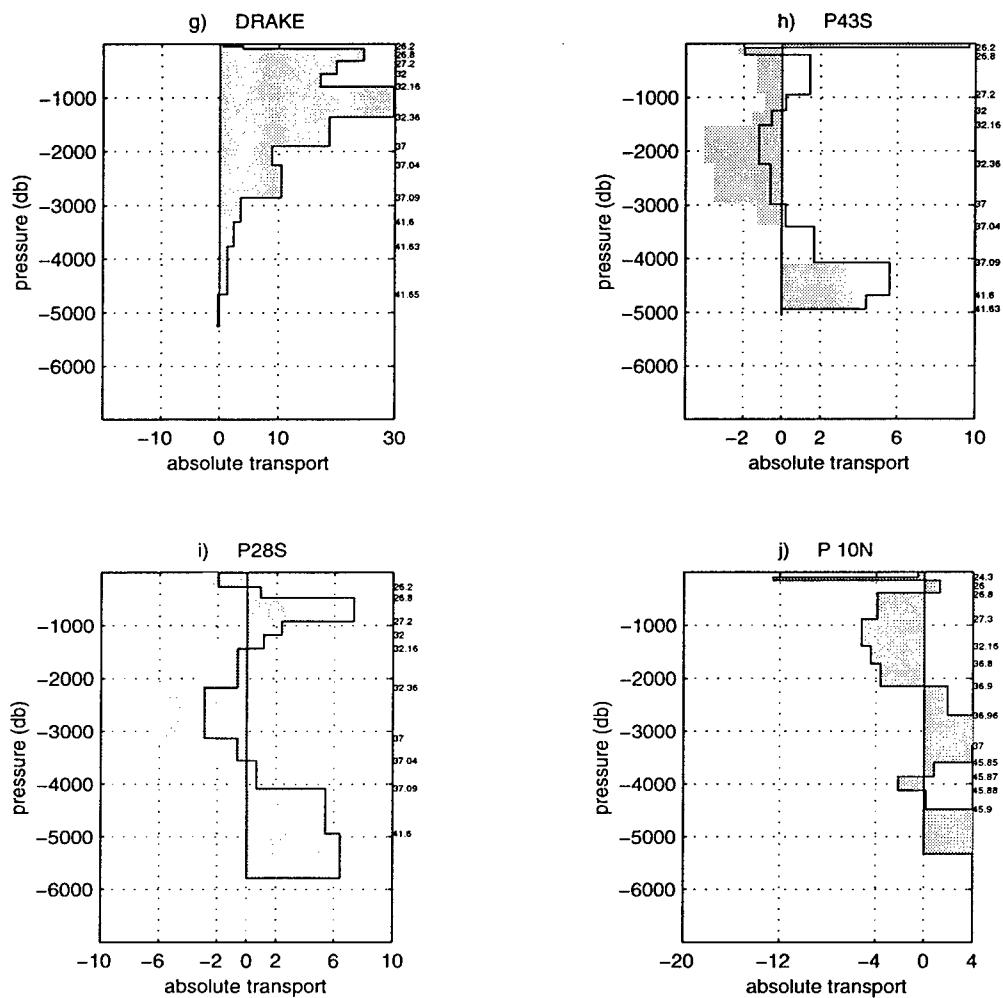


Figure 4.1 continued: Comparison of the zonally integrated mass transport profiles resulting from models C_2 , $T_{PI} = 0 \times 10^9 \text{ kg s}^{-1}$ (shaded) and C_3 , $T_{PI} = 20 \times 10^9 \text{ kg s}^{-1}$ (solid line), for sections: (g) #DRAKE, (h) #P43S, (i) #P28S, and (j) #P10N.

	Indian Layers	Standard Model	No T_{PI} constraint ΔC_1	$T_{PI} = 0$ ΔC_2	$T_{PI} = 20$ ΔC_3
#I18S	1-3	-15.6 ± 1.0	0.3	-0.6	0.6
	4-7	-3.3 ± 3.6	1.2	-3.3	3.5
	8-11	3.0 ± 5.1	0.8	-3.8	4.1
	12-13	7.1 ± 3.9	-0.1	-0.4	0.5
#I32S	1-3	-15.4 ± 1.1	0.3	-0.6	0.9
	4-7	-9.4 ± 3.6	1.4	-3.4	3.5
	8-11	11.5 ± 4.2	0.7	-3.8	3.9
	12-13	5.0 ± 2.3	0.0	-0.4	0.5
#MZ.N	1-3	0.1 ± 0.3	0.0	0.0	0.0
	4-7	-0.1 ± 1.1	0.1	0.0	0.1
	8-11	0.3 ± 0.8	0.0	0.0	0.0
	Pacific Layers	Standard Model	No T_{PI} constraint ΔC_1	$T_{PI} = 0$ ΔC_2	$T_{PI} = 20$ ΔC_3
#I32S	1-3	-18.5 ± 2.3	1.0	-1.9	2.5
	4-5	-5.4 ± 1.1	0.5	-0.9	1.0
	6-8	6.2 ± 3.0	0.7	-3.1	3.0
	9-12	9.5 ± 3.9	0.3	-2.8	3.0
	13-16	0.0 ± 0.7	0.0	0.1	-0.1
#I32E	1-3	40.8 ± 8.6	-0.7	1.7	-1.8
	4-5	35.4 ± 4.7	-0.3	1.1	-1.1
	6-8	59.0 ± 7.4	-0.9	3.1	-3.3
	9-12	17.6 ± 8.6	-0.4	2.4	-2.6
	13-16	-1.5 ± 2.9	0.0	0.0	0.0
#P43S	1-3	6.8 ± 2.6	-0.5	1.7	-1.8
	4-5	-1.5 ± 1.5	-0.3	1.0	-1.2
	6-8	-5.4 ± 4.9	-1.0	3.6	-3.8
	9-12	9.6 ± 5.6	-0.5	1.9	-2.1
#P28S	1-3	4.5 ± 2.6	-0.5	1.9	-2.0
	4-5	2.5 ± 1.6	-0.2	1.0	-1.0
	6-8	-8.3 ± 5.7	-1.1	3.9	-4.1
	9-12	10.9 ± 6.1	-0.3	1.6	-1.6

Table 4.2: Variation in potential density layer transports across Indian sections with varying T_{PI} constraints. Δ is the difference between the standard model and the alternate model, i.e. the standard model transport minus the Δ value is the alternate model transport. The Indian layers are defined in Table 2.5e. The Pacific layers are defined in Tables 2.5c and 2.5d. All values are in 10^9 kg s^{-1} . The Ekman transport from Table 3.18 has been subtracted. No estimate of Bering Strait throughflow has been subtracted.

in the intermediate layers lying between about 400 and 2000 db. Another 40% to 50% is carried in the deep layers. The northward transport of bottom waters is minimally affected.

Nearly all the difference in net transport at #I32S between the standard model and models C_2 and C_3 occurs within the Crozet Basin (70%) and in the eastern basin just to the east of the Ninety-East Ridge (30%). The Agulhas transport and the flow in the Mozambique Basin are not affected at all. To the north at 18°S, 70% of the difference occurs in the Central Basin and 15% in the East Australian Basin. Without meridional constraints on the east-west flow, we must be careful not to interpret the rearrangement of transport as a basis for a dynamical explanation of where the throughflow waters themselves circulate. The important point here is that the model does not find it necessary to adjust the flow in the Agulhas region to account for larger or smaller P-I throughflow estimates.

At #132E, most of the difference in net transport between the two models occurs between 450 and 2300 km south of the coast of Australia (*i.e.* within and to the north of the ACC). The lack of differences further to the south is notable as 30% of the eastward transport across this section occurs further to the south. Although little change is evident in the surface layers of the #132E section, about 50% of the difference in transport is carried in the upper 1500 db of the water column. There is little difference in transport below about 3700 db ($\sigma_3 = 41.6$).

Within the South Pacific, all the net transport difference occurs to the east of the East Australia Current at 43°S, with about two-thirds to the west of the East Pacific Rise. 70% is carried below 1500 db. At 28°S, the difference has approximately the same spread in the vertical and lies between the Kermadec Ridge and East Pacific Rise. Table 4.2 show that at 32°S in the Indian Basin, there is an even split between the difference carried in the mid-depth layers 6-8 and the deep layers 9-12. Following the difference around Australia, through the #132E, #P43S and #P28S sections

shows more of the difference being carried in the mid-depth layers (which incidentally deepen from about 2800 db at #I32S to 4000 db at #P28S) and less in the deeper layers.

The differences in layer transports between model C_2 and C_3 at #30E, #P10N and #DRAKE are extremely small. The greatest change is $0.4 \times 10^9 \text{ kg s}^{-1}$ less eastward (more westward) flow across #30E in layers 2 to 10 in the $20 \times 10^9 \text{ kg s}^{-1}$ throughflow case. The #P10N sections shows a $0.1 \times 10^9 \text{ kg s}^{-1}$ increase in the southward flow above layer 10 balance by a decrease in the northward abyssal transport. Although we have already seen that the presence of the #P10N section has a limiting affect upon the T_{PI} estimate, the lack of change in the circulation at this latitude is indicative of the looseness of constraints in area X. It also indicates that an increased P-I throughflow does not necessarily imply an increase in the northern source of throughflow water as the estimated transport in the Mindanao Current is the same for model C_2 , C_3 and the standard model.

Using the difference between the net transports associated with P-I throughflow in models C_1 and C_2 as a method of tracing the possible pathways affected by throughflow transport (not the pathway of throughflow transport itself), it appears that the effects of the throughflow although spreading westward within the Indian Basin as far as the Madagascar, have no discernible effect upon the Agulhas Current and retroflexion region. Therefore, the "warm water" path of waters feeding the formation of NADW appears to be independent of magnitude of the P-I throughflow. Also, the effects of increased throughflow do not spread strongly enough to the east in the Pacific sector of the South Ocean to affect the make up of the Drake Passage throughflow and the "cold water" path. The circulation of P-I throughflow in these models is disconnected and independent of the global overturning cell.

4.4 Cross-Isopycnal Transfer

The cross-isopycnal transfer terms in the model equations (w^* in Equation 2.1) represent the integrated movement of mass across layer interfaces due to all physical processes which might be responsible for its existence, including advection, diffusion and outcropping. The standard model made the initial assumption that the cross-isopycnal transfer terms were of the order of $10^{-4} \text{ cm s}^{-1}$ in all the boxes. The only exception was in area XVIII in the North Atlantic where the initial order of magnitude estimate was raised to $5 \times 10^{-4} \text{ cm s}^{-1}$ to obtain layer mass balances between the #A36N and #A48N sections.

Profiles of the standard model cross-isopycnal transfer terms are illustrated in Figure 4.2 and the rms w^* values for each of the model areas are listed in column 4 of Table 4.3. Many of the estimates are not significantly different from zero, particularly in the Southern Ocean. Significant estimates do appear in the upper layers of South Indian and South Pacific areas and over most of the water column in the equatorial and northern areas of the Pacific and Atlantic.

The magnitude of the expected Ekman convergence in each area is given in column 3 of Table 4.3. For 12 out of the 18 areas the sign of the w^* terms in the surface layer(s) agrees with that which might be expected from wind forcing. Of the six which don't agree, only two, area XI (between 10°N and 24°N in the Pacific) and area XVII (between 24°N and 36°N in the Atlantic) are significantly different from zero. Almost all the profiles show upwelling from the lowest layer.

Within the Indian and Pacific sectors of the Southern Ocean there is downwelling throughout most of the water column. The *Stommel and Arons'* [1960] theory of abyssal flow suggests that once away from regions of deep water formation, upwelling should be prevalent throughout most of the water column. The South Indian (VIII) and South Pacific (VII) areas show upwelling through potential density inter-

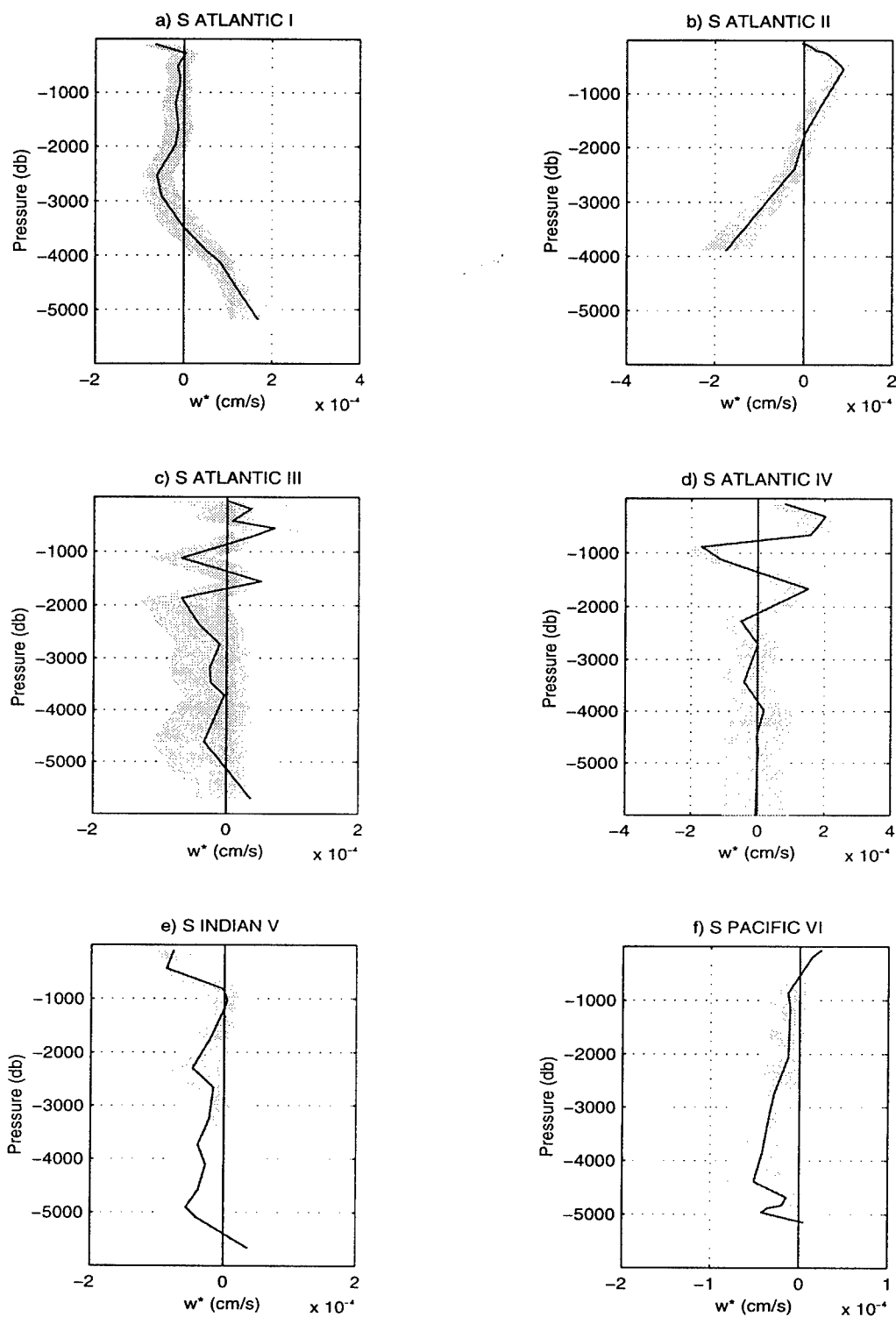


Figure 4.2: The transfer rate across potential density interfaces (w^*) for the standard model areas I through VI. The shading illustrates the standard model estimate of the uncertainty in w^* terms.

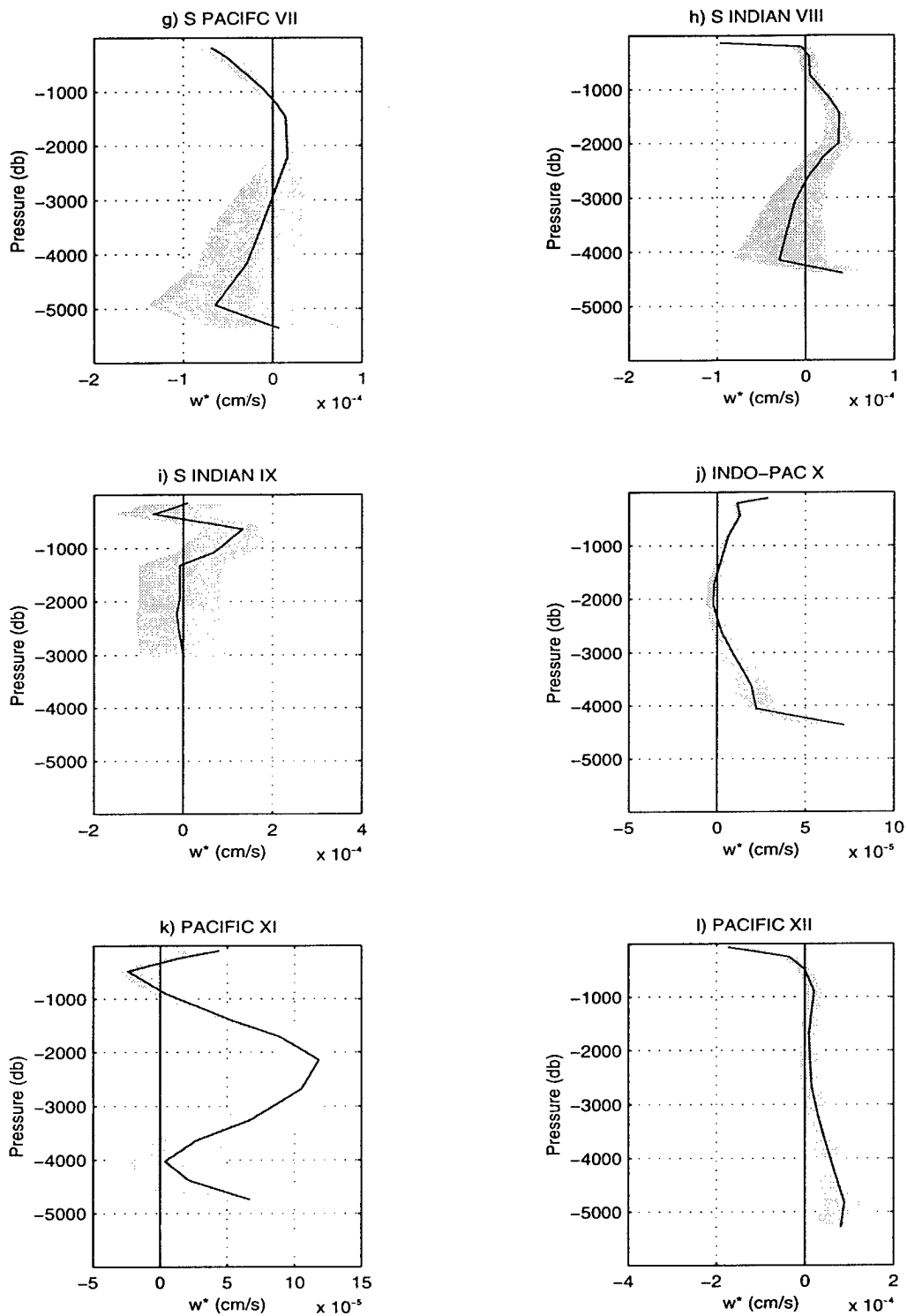


Figure 4.2 continued: The transfer rate across potential density interfaces (w^*) for the standard model areas VII through XII.

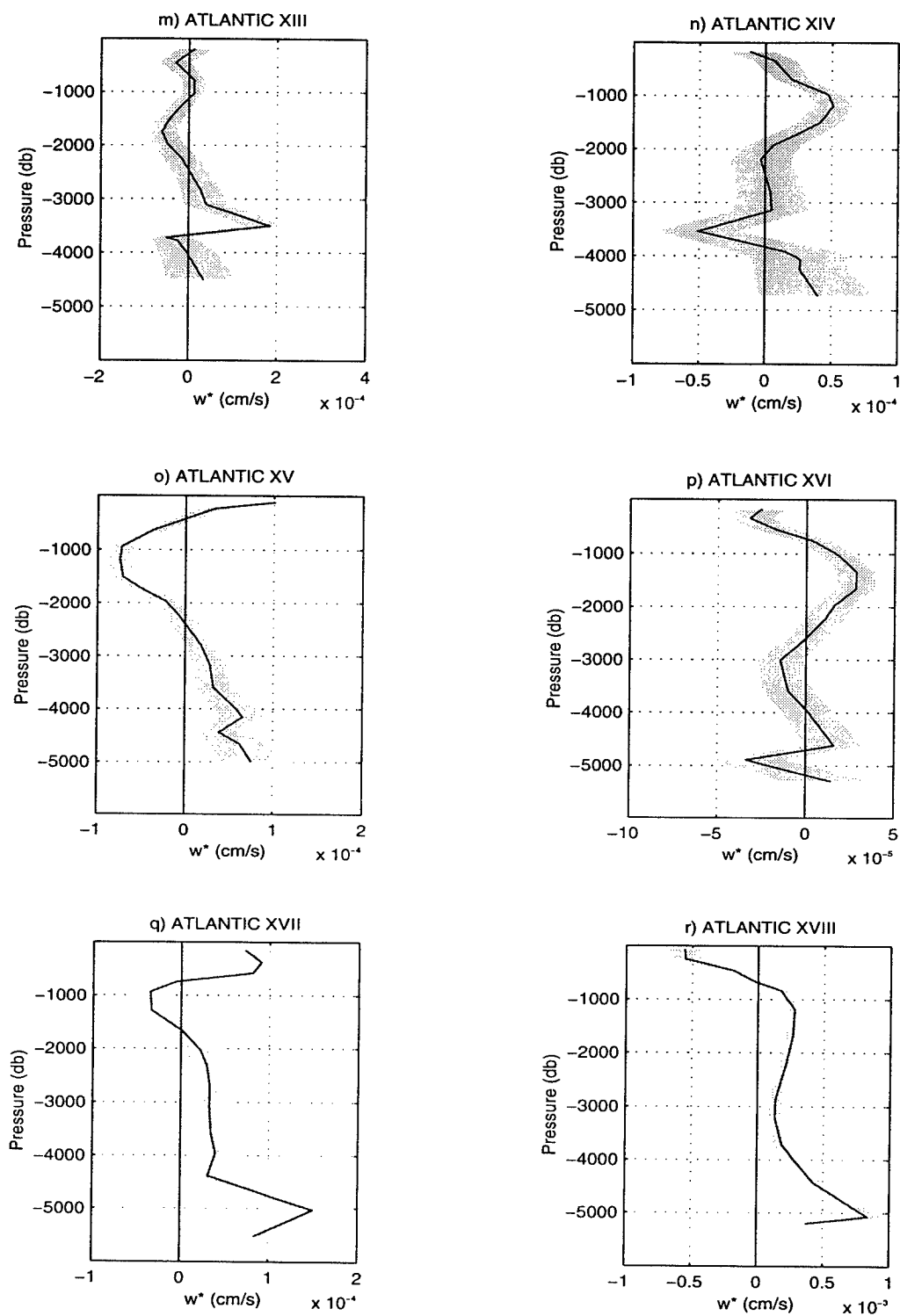


Figure 4.2 continued: The transfer rate across potential density interfaces (w^*) for the standard model areas XIII through XVIII.

Area		Ekman	Standard	Model D ₂
Name & Id Number		Convergence	rms w*	rms w*
Southwest Atlantic	I	1.2	6.5	15.9
Weddell Scotia	II	-2.3	6.0	11.6
South of South Africa	III	1.3	4.0	11.9
West of South Africa	IV	1.3	9.7	31.4
Indian Southern Ocean	V	0.2	4.2	6.0
Pacific Southern Ocean	VI	-8.0	2.7	3.2
Pacific 43°S-28°S	VII	15.3	3.0	6.8
Indian 32°S-18°S	VIII	16.4	3.7	4.1
Mozambique Channel	IX	0.5	4.8	65.9
Indo-Pacific	X	-60.0	2.4	3.1
Pacific 10°N-24°N	XI	29.8	5.9	9.0
Pacific 24°N-47°N	XII	14.5	6.2	10.8
Atlantic 23°S-27°S	XIII	4.3	5.5	12.1
Atlantic 23°S-11°S	XIV	6.9	2.9	3.6
Atlantic 11°S-11°N	XV	-20.5	5.6	6.3
Atlantic 11°N-24°N	XVI	3.7	2.0	2.6
Atlantic 24°N-36°N	XVII	8.3	6.1	11.8
Atlantic 36°N-48°N	XVIII	1.1	35.9	39.9
Initial Estimate			10 [†]	100

Table 4.3: Cross isopycnal transfer results for each of the model areas in units of $10^{-5} \text{ cm s}^{-1}$. Column 3 gives the Ekman convergence (greater than 0) within each of the model areas (10^9 kg/s) according to the values in Table 2.4. Columns 4 and 5 contain the resulting rms values of w^* for the standard model and model D₂, respectively.

[†] The initial estimate for area XVIII was $5 \times 10^{-4} \text{ cm s}^{-1}$.

faces above about 3 km and downwelling below this depth. To the north in these basins, the model produces mainly upwelling. In the Atlantic the picture presented by the model is more complicated and difficult to categorize.

In the Southwest Atlantic (area I), there is an upwelling of the bottom waters as they move northward and a downwelling through all the layers above in which water masses of various origins are thought to be interleaving. Area II, covering the Weddell Gyre region shows a pattern of upwelling through the upper layers which are in contact with the atmosphere and down to about 2000 db, and downwelling with larger uncertainty below this depth. The near surface upwelling is perhaps not what might be expected in a region of deep water formation. However, it should be remembered that this structure is only consistent with the available data and that data bounds the Weddell Sea to the north and east and does not include any direct information about what is occurring to the south. Areas III and IV to the south of South Africa, show particularly random behavior in their w^* terms and are thought to be not well enough resolved to allow discussion.

Moving northward in the Atlantic, area XIII, between #A27S and #A23S also displays a fairly random character with a tendency towards downwelling above about 2500 db and upwelling beneath. Between #23S and #11S, upwelling is evident throughout most of the water column, as might be expected for a region which is further from the sources of deep and bottom water formation. Across the equator, the profile flips. Upwelling still exists at depth, but above about 2500 db the model invokes significant downwelling. The w^* profile flips again in area XVI and again in area XVII. In areas XIV and XVI the w^* estimates below about 2000 db are barely significantly different from zero, so this flipping of sign may be due to a lack of resolution rather than some physical process. The strong vertical transfer terms which were required to balance mass between #A36N and #A48N are associated with downwelling in the upper waters above about 800 db, consistent with a general

sinking due to evaporation. Below this depth, upwelling is apparent throughout the water column.

Given that many of the standard model cross-isopycnal transfer terms are smaller than the initial estimates, and given the random character of some of the w^* profiles and the general lack of significant values, two questions come to mind. The first is whether or not it is possible to produce a globally consistent model which does not allow for any cross-isopycnal transfer. The second is whether anything can be learned from allowing the w^* terms to be even better resolved than they are in the standard model.

No Cross-Isopycnal Transfer, Model D₁

Model D₁ is an attempt to run with the same constraints as the standard model but with no cross-isopycnal transfer terms. The resulting reference level velocities are larger, as are the associated uncertainties. On average, the model D₁ rms reference level velocities are two and half times as large as the reference level velocities determined for the standard model. The smallest increase occurs across the #Mz_S section, 0.04 cm s^{-1} . The largest increase occurs across the #0E_N section, 7.9 cm s^{-1} . Although it happens that in only one section, #0E_S the increase in b_{rms} goes beyond the initial order of magnitude estimate, there are six areas in which the top to bottom mass and salt conservation constraints cannot be met. These areas are areas I and IV in the Atlantic sector of the Southern Ocean, areas V and VI in the Indian and Pacific sectors of the Southern Oceans, area VII in the South Pacific and area X which crosses the equator in the Indo-Pacific region. Area XV which crosses the equator in the Atlantic, area XIV just to the south and XVIII in the far north Atlantic cannot meet the conservation constraints in a third of the individual layers. There are another four areas in which conservation is not possible in three or more individual layers. All of these areas lie in the North Pacific and North Atlantic. So it

appears that some allowance for transfer across isopycnal interfaces is necessary near the polar regions, across the equator and within the eddy field bounding the Agulhas and Cape Basins.

The zonally integrated mass transport profiles for model D₁ are shown in comparison to the standard model profiles in Appendix B, Figure B.1. It is difficult to assess the changes in the global ocean circulation for model D₁ because the pattern is interrupted by the regions where mass conservation does not hold. However, a few things can be said. First the average magnitude of the overturning cell within the Atlantic cell has been somewhat reduced, as has the range of estimates given by the individual section. Using the definition for the overturning cell given on page 204, model D₁ finds an average magnitude of $16 \pm 4 \times 10^9 \text{ kg s}^{-1}$ which is smaller compared to the $18 \pm 4 \times 10^9 \text{ kg s}^{-1}$ of the standard model, but not significantly so. The variation in the estimated magnitude of the overturning cell at the different latitudes remains. However, whereas the standard model employed diapycnal exchanges to balance the layer equations, model D₁ simply fails to meet these constraints. None of the standard model bottom water constraints could be met as model D₁ produced smaller northward transports of AABW in the Atlantic and net southward transports in the lowest layer of both the South Indian sections. The transport of both NADW and AABW virtually disappeared below 2900 db in the South Atlantic box of the *Macdonald* [1993] model which used no w^* terms. The presence of sections to the north effectively forcing the southward transport of NADW and the constraint on the AABW water mass prevents their disappearance in model D₁. Without vertical transfer, the northward transport of deep waters into the South Indian Basin is reduced and as found by *Macdonald* [1993], the deep waters in the South Pacific flow poleward. At $134 \times 10^9 \text{ kg s}^{-1}$, the transport at Drake Passage is low compared to the initial constraint. The transports across the other Southern Ocean meridional lines vary somewhat as they are affected by the lack of mass conservation. The

sections affected by the P-I throughflow produce net transports of between 7 and $14 \times 10^9 \text{ kg s}^{-1}$.

Many of the more significant differences in the circulation patterns of the standard model and model D₁ appear in the deep waters. The overall pattern of heat and temperature fluxes are therefore similar for the two models. The only heat flux estimate which actually reverses sign is that across #A57S going from -0.03 to 0.01 PW. The biggest change in the estimated heat fluxes occurs at 10°N in the Pacific where the model D₁ value is 0.4 PW greater than that produced by the standard model. Across the sections which carry the ACC, the model D₁ temperature fluxes range between being 0.2 PW less than the standard model estimates to being 0.3 PW greater (a change of about 20%). The temperature flux estimates across those sections affected by the P-I throughflow are also different by 0.1 to 0.2 PW, except at #P28S where the estimates are virtually identical in spite of the difference in net transport. The region least affected by the lack of cross-isopycnal transfer is the tiny one in the Mozambique Channel. This result comes as no surprise as its standard model solution was dominated by large reference level velocities at #Mz_S. All other sections either directly bound one of the areas which cannot meet the initial constraints or lie in an area adjacent to one of these areas. A globally consistent solution without cross-isopycnal transfer is not possible.

Better Resolved Cross-Isopycnal Transfer, Model D₂

Having seen that the removal of cross-isopycnal transfer from the model equations can produce profound changes in the solution, the experiment was taken a step further to determine what happens to the solution when the w^* terms are allowed to be better resolved. The hope is that the random character, where it exists, of the standard model w^* profiles would be lessened and that the any remaining structure in the standard model residuals would be removed.

Model D₂ uses the same constraints as the standard model but uses an initial order of magnitude estimate for the cross-isopycnal terms of $1 \times 10^{-3} \text{ cm s}^{-1}$ for all the areas. Profiles of the resulting cross-isopycnal transfer terms for model D₂ are shown in relation to the standard model results in Figure 4.3. The cross-isopycnal transfer terms are greater in model D₂ as would be expected from the better resolution. The greatest overall difference occurs in area IX in the Mozambique Channel where the magnitude of the w^* terms increases tenfold. Compare columns 4 and 5 of Table 4.3. Interestingly enough, two of the smallest overall changes occur right next door in the South Indian area VIII and the Indo-Pacific area X.

The better resolution of the w^* terms is, of course, at the expense of the resolution of the reference level velocities. The rms values of the reference level velocities have decreased for all but two of the sections (#Mz_N and #FlSt). Half of the sections have received reductions of b_{rms} of a third or more. The sections hit the hardest by this loss of resolution in reference level velocities are those in the Atlantic which carry the ACC, #0EN, #0E2Afr, #30E and #Drake. All these sections have model D₂ b_{rms} values of 1 to 3 cm s^{-1} less than the standard model values. Not surprisingly, given the large increase in the magnitude of the w^* terms in area IX, the b_{rms} estimate for the model D₁ #Mz_S section has also decreased by 1 cm s^{-1} . This decrease produces a b_{rms} for the section of 1.2 cm s^{-1} which is more in line with the initial order of magnitude estimate and indicates that a larger initial estimate for the w^* terms in area IX may be appropriate. It is difficult to tell though, for as we have already discussed, this is a region of strong variability.

The overall structure the w^* profiles have not changed, except in region IX, where model D₂ has invoked strong upwelling. In a few areas, I, II, IV and XIII there are significant changes which have tended to enhance the structure already suggested by the standard model; that is, the deep upwelling in the Southwest Atlantic, the downwelling in the Weddell Scotia region, the near surface upwelling in the region to

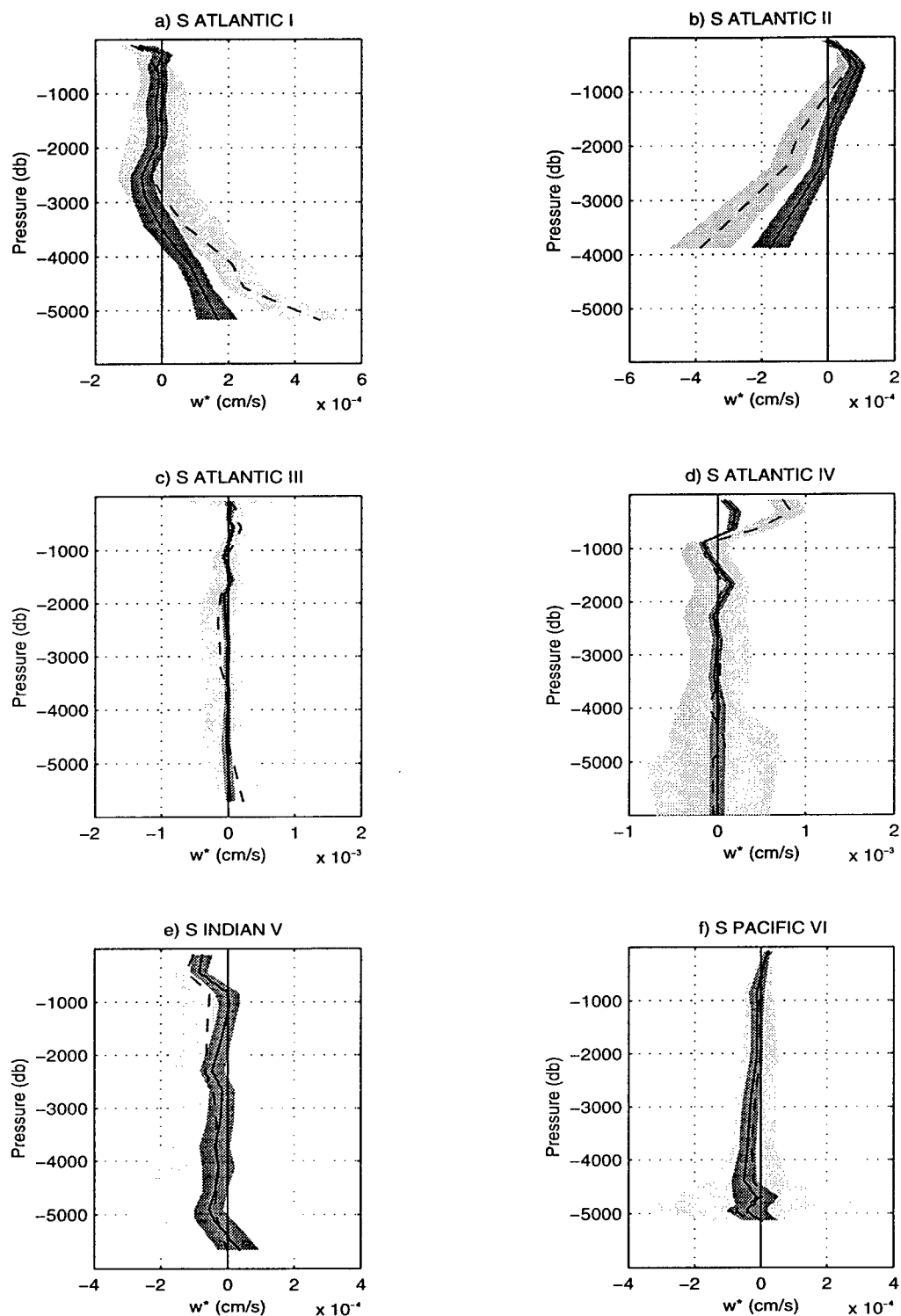


Figure 4.3: Comparison of the transfer rate across potential density interfaces (w^*) for the standard model (solid line) and model D₂ (dashed line) for areas I through VI. The dark shaded region illustrates the standard model estimate of the uncertainty in w^* estimates. The light shaded region illustrates the same for the model D₂ estimates. Model D₂ allows for larger w^* terms.

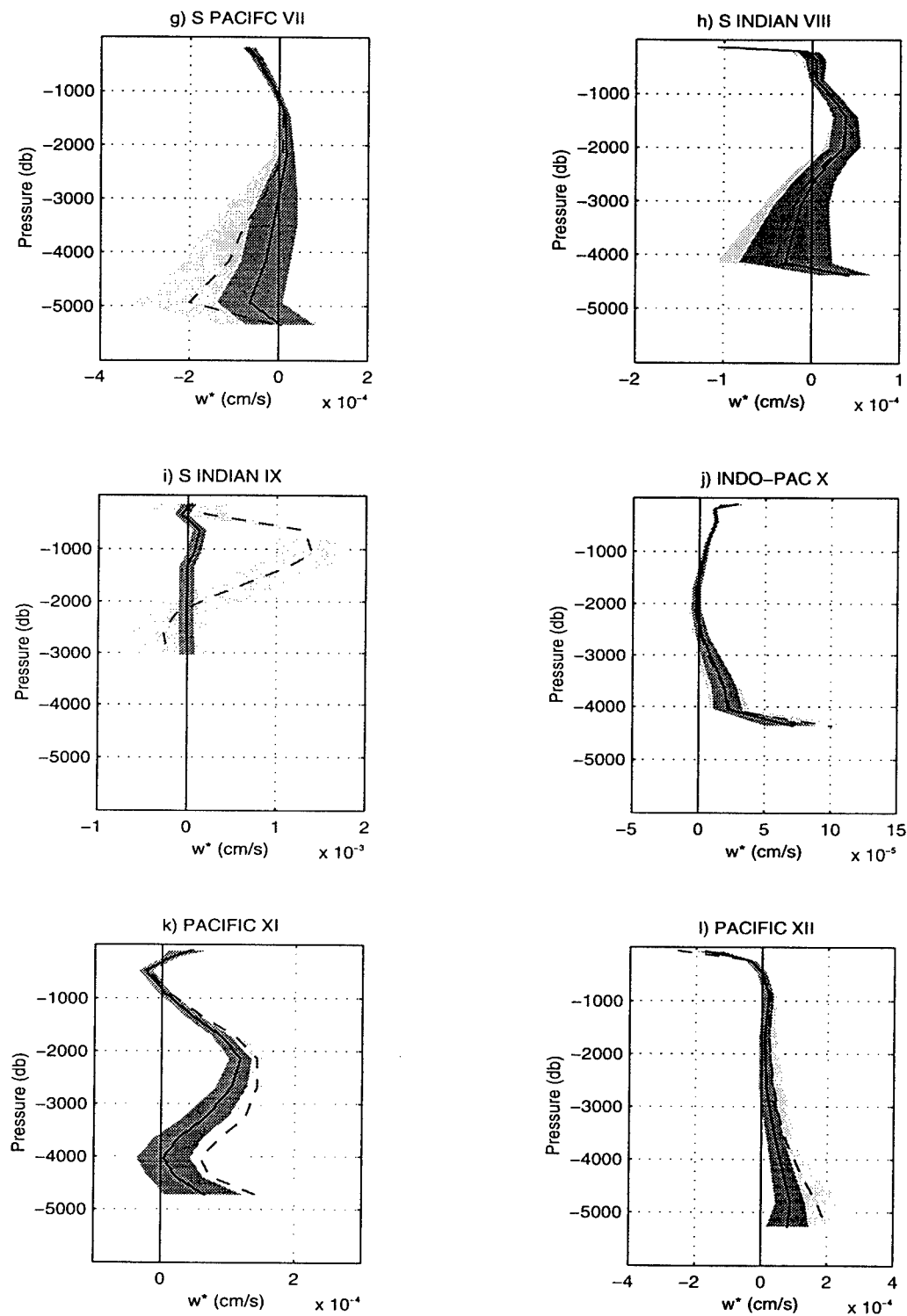


Figure 4.3 continued: Comparison of the transfer rate across potential density interfaces (w^*) for the standard model (solid line) and model D₂ (dashed line) for areas VII through XII.

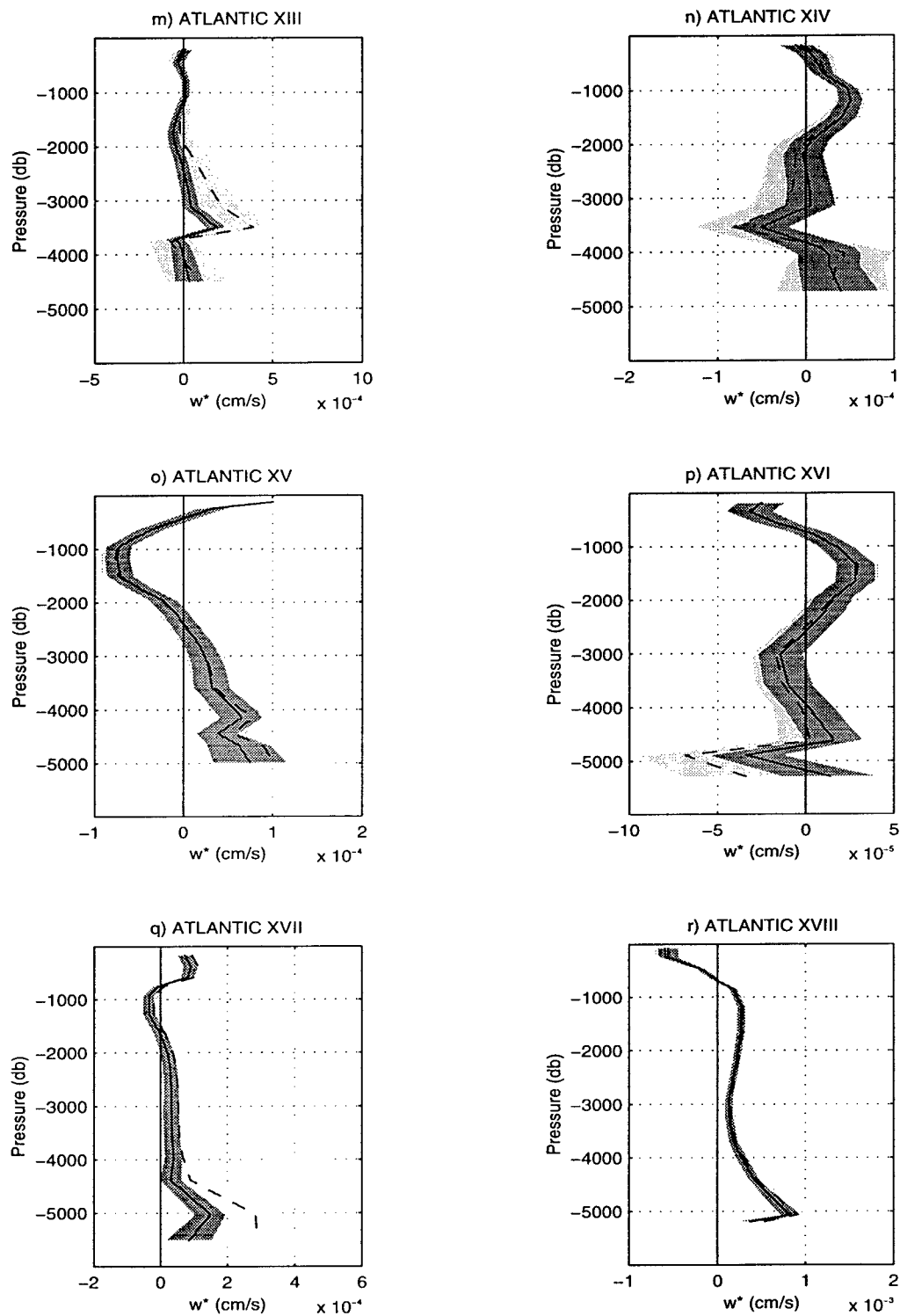


Figure 4.3 continued: Comparison of the transfer rate across potential density interfaces (w^*) for the standard model (solid line) and model D_2 (dashed line) for areas XIII through XVIII.

the southeast of South Africa where some of the warm waters are turning northward to feed the formation of NADW and the upwelling of waters at depth between #A27S and #A23S. Model D₂ suggests stronger downwelling in the Indian sector of the Southern Ocean which appears to be associated with a slightly weaker downwelling in the Pacific sector. Model D₂ also suggests a stronger downwelling of deep waters the South Pacific between #P43S and #P28S and stronger upwelling at depth in the North Pacific. The flipping of sign is still prevalent in the North Atlantic as most the increase in w^* in this region occurs below about 4000 db. There is little change to the w^* profile for area XVIII, which is to be expected as the initial order of magnitude estimate was only doubled for this region. Figure 4.4 further illustrates these changes in profiles of the cross-isopycnal transport associated with the w^* terms.

The structure of the zonally integrated mass transport has not changed a great deal in model D₂ (see Figure B.2) except, as expected, in the Mozambique Channel which now supports a southward mass transport of $4.5 \times 10^9 \text{ kg s}^{-1}$, about half the estimated P-I throughflow. However, in spite of retaining the overall structure in the zonally integrated mass transports, there are never the less, dramatic changes in the magnitude of these flows in the deep Pacific. The larger estimates of w^* which resulted in stronger Pacific upwelling have allowed for stronger transports of deep water.

section	depth range	standard	model D ₂
#P43S	below $\sigma_2 = 37.040 \sim 3400 \text{ db}$	9.6 ± 6.1	10.8 ± 6.2
#P28S	below $\sigma_2 = 37.040 \sim 3600 \text{ db}$	10.9 ± 6.1	17.4 ± 7.8
#P10N	below $\sigma_4 = 45.885 \sim 4100 \text{ db}$	6.5 ± 3.8	15.2 ± 5.6
#P24N	below $\sigma_4 = 45.885 \sim 4700 \text{ db}$	4.7 ± 2.7	8.9 ± 4.1
#P47N	below $\sigma_4 = 45.850 \sim 3700 \text{ db}$	-3.8 ± 3.2	-5.2 ± 3.6

Thus, the strength of the deep and bottom circulation patterns in the Pacific are strongly bound to the *a priori* assumptions made about the strength of cross-isopycnal

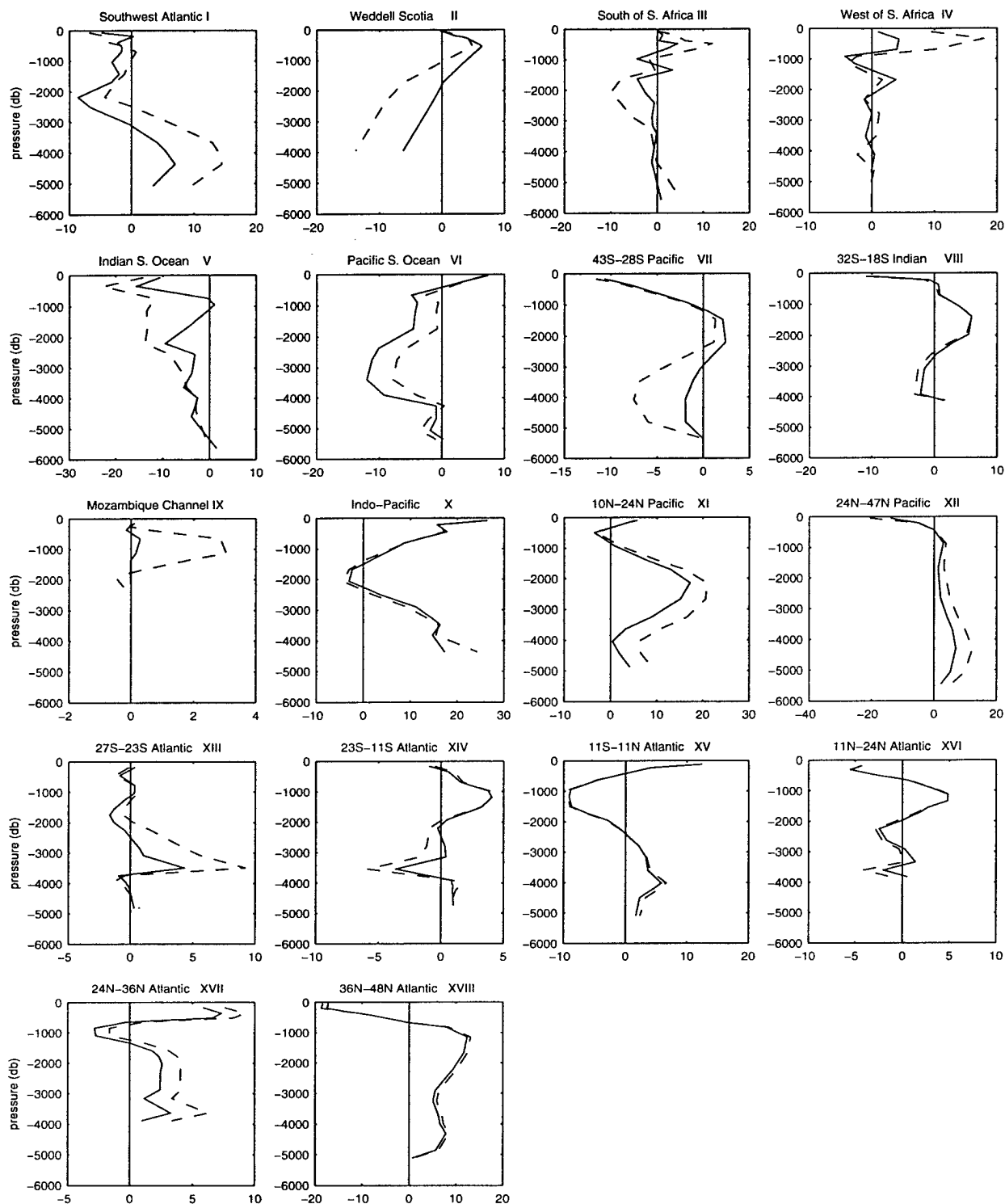


Figure 4.4: Comparison of the profiles of mass transport across potential density interfaces for the standard model and model D_2 for each of the areas I through XVIII.

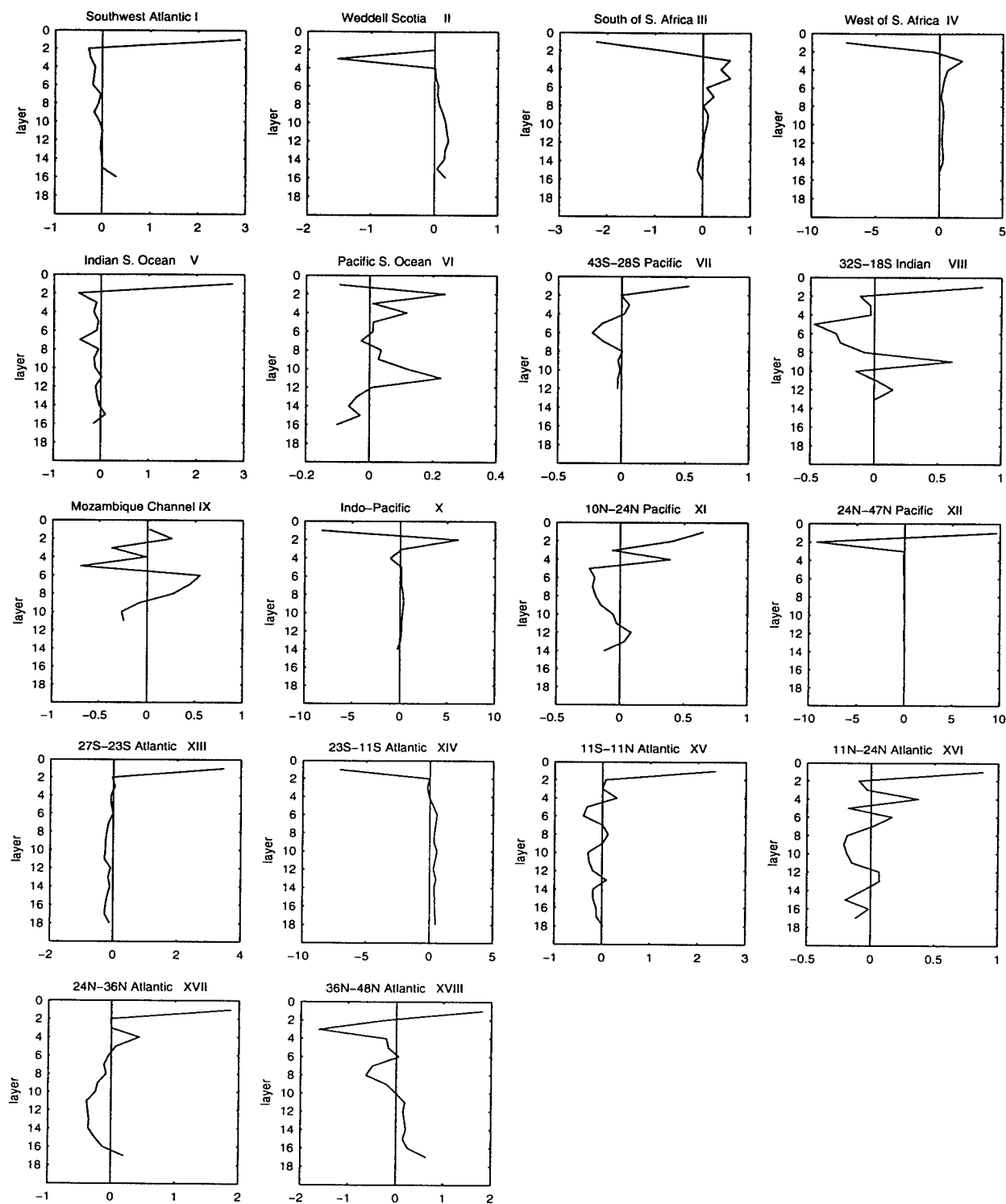


Figure 4.5a: Profiles of the standard model mass residuals in potential density layers for each of the areas I through XVIII. The Ekman transport has been included in outcropping layers. Units are 10^9 kg s^{-1} .

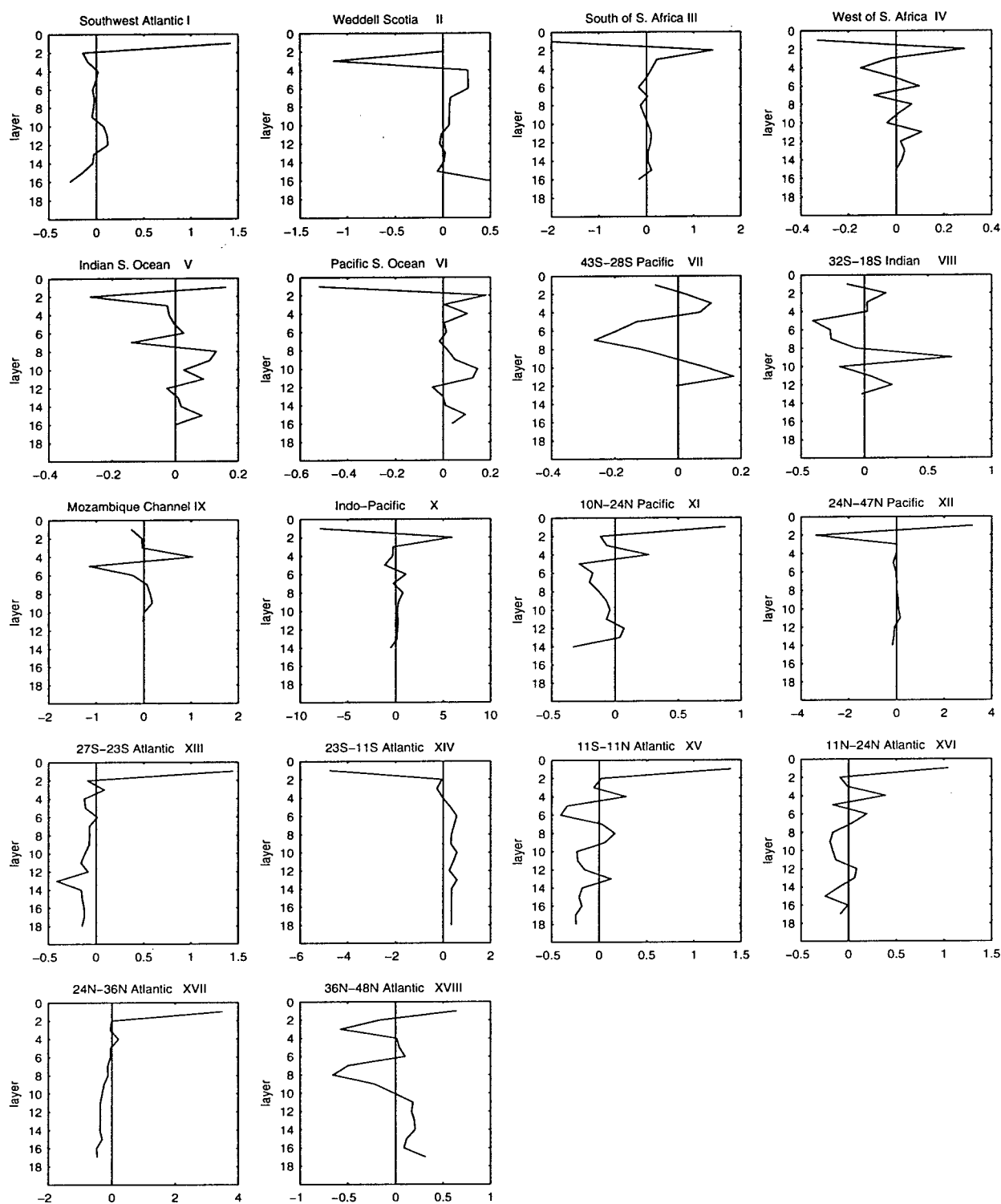


Figure 4.5b: Profiles of the model D_2 (upweighted w^* terms) mass residuals in potential density layers for each of the areas I through XVIII. The Ekman transport has been included in outcropping layers. Units are 10^9 kg s^{-1} .

transfer. We are once again reminded of the uncertainty surrounding the various estimates of northward transport of deep waters into this basin.

Returning to the original reasons for running this model, that is the expectation of more structure in the profiles of w^* which appear to have a random character and of an associated removal of structure from the residuals, it is evident in Figure 4.3 that the first objective does not seem to have been obtained. The most random/oscillatory w^* profiles (areas III, IV, XIV and XVI, see Figure 4.2) in the standard model hardly appear to be less so in model D_2 and are associated with larger uncertainties in model D_2 .

The standard model mass residuals are shown in Figure 4.5a. The largest residuals are in the surface layers because of the weighting scheme (see Section 2.5.3) which weighted outcropping layers by the magnitude of the Ekman component. Below the surface layers the residuals are small, less than about $1 \times 10^9 \text{ kg s}^{-1}$. In some areas (*eg.* XV and XVI) they appear to be completely random in character. In others (*eg.* II, III, IV, XIII and XIV) they still retain some structure. Most of the profiles appear neither to be completely random or completely structured.

The residuals for model D_2 (Figure 4.5b) are smaller than those for the standard model. In some cases, *eg.* areas III and IV and at depth in area II, structure seems to have been removed. In others, *eg.* areas XIII and XIV, it has not. The Mozambique Channel residuals are larger in model D_2 than in the standard model. These results would indicate that the standard model actually does a fairly good job, in most regions of resolving the w^* terms. That is, it resolves them almost as well as it can and better resolution would require stronger constraints.

The overall tendency of the increased w^* terms is to reduce the residuals in the surface layers by taking up the Ekman convergence or divergence, and to allow for stronger abyssal circulations. Model D_2 does better resolve the cross-isopycnal trans-

fer terms than the standard model, but only at the expense of the terms describing the reference level velocities. There are a number of sections¹ where it appears obvious from the magnitude of the reference level velocities that the model D_2 circulation is one which balances mass *etc.* almost solely through cross-isopycnal transfer. The rms values of w^* listed in column 5 of Table 4.3 can probably be taken as an upper limit on the magnitude of the cross-isopycnal transfer in each of the model areas.

Early inverse box models (*e.g.* Wunsch *et al.* [1983]) which did not explicitly include the cross-isopycnal terms within the model constraints, suggested that the structure which remained in the residuals could be explained by the missing model physics associated with the exchange across isopycnals. Later models which did include these terms within the model equations found, as we have here, that although they are capable of reducing the magnitude of and removing some structure from the residuals, their results do not necessarily match the classic [Stommel and Arons, 1960] assumption of upwelling over the vast expanse of the oceans interior away from isolated sinking regions.

It is here that we must remind ourselves that these areas of downwelling may not only be isolated convection regions but may also include boundary currents [Warren 1976]. As has been pointed out previously [Wunsch *et al.*, 1983], if there is upwelling in the ocean interior with strong downwelling in limited regions outside the interior, in say, the western boundaries, then it is quite likely that the horizontally integrated values (*i.e.* w^*) will appear random or at the very least not reflect a generalized interior upwelling. There is no way within this model to separate the two regions. It has also been suggested [Edwards and Pedlosky, 1995] in more recent modeling efforts that the character of the interior flow can depend upon the location of the sources of deep water and that the picture provided by Stommel and Arons

¹#A27S, #A57S-W, #0ES, #P43S, #P28S, #I18S, #P10N, #A23S and #A24N all have rms reference level velocities of less than 0.2 cm s^{-1} .

was simplified by the assumptions made in the original models. This reasoning could explain why the models were able to find consistent upwelling in the Pacific but not in the Atlantic.

A further possibility is that by using a single term to describe both the primarily advective transfer of mass and the essentially diffusive transfer of properties across isopycnals that neither is well described. Separating these two terms produces a great number of additional unknowns. However, it has been suggested [McDougall, 1991] that the solutions for these new unknowns often more clearly describe the expected dynamics than the w^* terms used here. Wijffels [1993] did separate diapycnal advection and diffusion in her cross-equatorial inversion. She concluded that although it was not possible to find solutions in which all the diagnosed diffusivities were distinguishable from zero and non-negative², the buoyancy (salinity and heat anomaly) constraints which used them added useful information to the system. Separating the diapycnal terms in the standard model would almost double the number of unknowns in the system; nevertheless it is an experiment which should be done in the future if only to see if the resulting solutions do more clearly describe the expected dynamics.

The range in circulation patterns illustrated in Appendix B is quite large and perhaps a little unsettling. However, without independent measurements of horizontally integrated cross-isopycnal transfer or alternatively basin wide estimates of absolute velocities, the choice of balance between the importance of the horizontal advective and the cross-isopycnal transfer terms in the conservation constraints, remains a subjective one. It should be noted that separating advection from diffusion in the equations will not make the choice of solution any more objective.

²The character of the Wijffels' [1993] diffusivities closely resembled that of the diagnosed vertical velocities.

4.5 Model Summary

Past

Chapter 3 presented the results of the standard model. The present chapter discusses possible variations on the standard model results through a series of alternatively constrained models. The geostrophic velocity reference levels for the standard model were chosen by first looking at models which used both shallower (Model A) and deeper (Model B) reference levels and then making a subjective decision as to which appeared more appropriate for each individual section. Based on the results of these early reference level testing models, it was decided to include the requirement that the flow through the Indonesian Archipelago not exceed $10 \pm 10 \times 10^9 \text{ kg s}^{-1}$. However, although earlier models had produced throughflow estimates which lay outside the bounds of all previously published estimates, it was later found that the standard model, left to its own devices, could produce a perfectly reasonable estimate of the throughflow ($11 \pm 7 \times 10^9 \text{ kg s}^{-1}$) which was limited by the constraints provided by the surrounding areas.

The work which lead up to the standard models tells us, that the model estimates of P-I throughflow are sensitive to the choice of reference levels, data sets and solution and noise covariance estimates. Future models could be better constrained in these region through the inclusion of more data. However, experience would indicate that the seasonality (see page 193) and overall variance in estimates from different measurement techniques will dictate that a single hydrographic data set at or near the archipelago is unlikely to produce a good estimate of the mean transport between the basins, as is required by this model. The hydrographic WOCE program proposed in the Indian Ocean [*U.S. WOCE*, 1993] will supply much better coverage than presently available and may allow even simple models such as these to say something about the consistency of using hydrography from different seasons and decades in this region.

Many of the flux and topographic constraints included in the standard model are the result of previous experiments which indicated that their presence was necessary to produce sensible solutions. The most obvious of these constraints is the one which requires conservation in the deep eastern North Atlantic and so allows the model to recognize the obstruction presented by Mid-Atlantic Ridge. Also included in the standard model was a constraint based upon the idea that a poleward oceanic flux of heat is necessary for bottom water formation in the Weddell Sea. This constraint required a net input of heat into the model area II. Such a constraint was also used by *Rintoul* [1991]. Although without this constraint there was a minimal (not significantly different from zero) advective export of heat from the region, the inclusion of the constraint produced only a net balance, not a net import of heat into the region. Tests indicate that it did, however, increase the net northward transport of deep and bottom waters out of the Weddell Sea and allowed a net northward transport of bottom waters to be seen north of the equator. Future experiments might include an analysis to judge the sensitivity of bottom water production and circulation to the oceanic transport of heat into area II.

Present

In choosing the constraints for the standard model, rather than simply trying to reproduce the results of previous authors, we attempted to choose the most reasonable (or perhaps middle of the road) constraints and hope that the reader will not dismiss all the results associated with some of the more extreme models which have been presented in this chapter. Comparison among these alternative models has shown:

- that the models solutions are quite sensitive in some regions to the choice of the initial velocity reference levels,
- that it is not possible to produce a globally consistent circulation pattern without allowing for cross-isopycnal transfer,

- that the w^* terms in standard model are for the most part, as well resolved as possible without severely reducing the resolution of the reference level velocities and producing a circulation which balances mass primarily through cross-isopycnal transfer,
- that the small northward transport of warmer waters across the mid to eastern Atlantic at 48°N as suggested by *Schmitz and McCartney* [1989] is inconsistent with the other model constraints,
- that the net north transport of bottom water across 24°N and 36°N in the Atlantic is inconsistent with what is thought to be known about the magnitude of overturning cell and the heat flux at 24°N ,
- and finally that the magnitude of the P-I throughflow does not affect the global ocean circulation pattern (*i.e.* the strength of the *warm* and *cold* waters paths which feed the formation of abyssal waters in the Atlantic). Rather the models suggest a pattern of circulation in which effects of the throughflow are confined to the Pacific and Indian Basins.

Future

One would like to have the most highly constrained model possible. However, determining the "best" possible set of constraints is difficult. Chapter 3 presented instances where in the detailed analysis of results it was determined that in some cases different constraints, and in other cases additional constraints were necessary to produce solutions which more closely resembled expected circulation patterns (*e.g.* using a different estimate of Ekman transport at 10°N in the Pacific and requiring the northward transport of bottom waters into the South Indian Basin). Although never intending to simply reproduce previous findings, Chapter 3 also presented instances where it was useful to use some specific flux constraints (*e.g.* specification of deep transport in the North Pacific and specification of upper layer transport in the eastern North Atlantic) to determine whether or not the results of previous research were

consistent with the standard model. These constraints were used in test models, but were not included in the standard model. However, the standard model did include some flux constraints such as those on the transport through Drake Passage and the Florida Straits, which kept the model from straying too far from acceptable solutions. It was found that the Drake Passage transport was reduced by two-thirds without the added constraint. Why this happened was not determined and further investigation is warranted. The model was never run without the Florida Strait constraint. The standard model also included constraints on the flow of bottom water within the Atlantic and it was determined that the constraints requiring a net northward flow of bottom waters across 24°N and 36°N were not consistent with expected circulation patterns.

The inclusion of specific flux constraints always leaves the question as to what happens without the constraint and why. Clearly, it is more desirable to constrain the system with more data, be it new hydrography or updated topography or some other type of information, rather than to simply limit certain flows through the use of previously determined estimates. Two such possibilities for improving the standard model are the use of different wind data and the use of property anomaly conservation rather than property conservation.

Choice of Wind Field

It has already been shown (Section 3.4.3) that initial estimates of Ekman flux can affect the pattern of deep transport, as well as the surface transport produced by the model. Clearly, the choice of wind field is not to be taken lightly. However, choosing the best wind field is at best, problematic. At the time this dissertation was begun, the global coverage offered by the ECMWF 1980–1986 climatology made it a good choice for use with this model. Since that time, however, the ECMWF analysis procedures have been improved so that for instance, its estimates of wind stress in the tropics are considered somewhat more reliable [Halpern *et al.*, 1994].

Other global data sets are, of course, available and in certain regions, especially those where more data is available, other wind fields would likely provide better estimates. One is caught between choosing a single consistent data set which may provide poor estimates in some regions and choosing among a number of more regional data sets which probably don't provide a consistent global picture. Further complicating the choice one finds that estimates are constantly changing and improving.

Two model experiments would be useful. One would allow for a larger estimate of the uncertainty in the Ekman transport than was used for the standard model. This uncertainty might be based upon the variation found in the available wind fields. The second experiment would use a different wind field altogether to estimate the Ekman transport. Together, these model runs would give some idea as to how sensitive the model's global circulation patterns are to the specific wind field used.

Salinity Anomalies

It has been suggested that inverse box models such as the one presented here have suffered from an unnecessary reduction in rank because the tracer equations and in particular, the salinity equations are linearly dependent upon the continuity equation [McDougall, 1991]. It has been further suggested that removal of this dependency can be achieved through the subtraction of a mean value from the tracer conservation equations thereby creating tracer anomaly constraints. Two test models were run to determine whether or not it would be possible to reduce the uncertainties in the solution through the inclusion of constraints requiring conservation of salinity anomaly rather than salt. The mean value used to compute the anomalies was computed as an areal mean of all the sections used in the model (34.738).

Two runs were made because it is not particularly clear how these salinity anomaly equations should be weighted, that is we do not have a good understanding of the expected noise in these equations. Wijffels [1993] chose to use an estimated

uncertainty based upon the magnitude of the convergence of the property, computed as the amount advected through the horizontal layer interfaces by a transport equal to the uncertainty in the layer equations. The first test run used a slightly simpler formula which produced uncertainties which were likely somewhat larger than the *Wijffels* estimates. This formula took the uncertainty in the anomaly equations to be the uncertainty in the mass equations times the local rms anomaly.

It was found with this first run that although the new equations did offer some new independent information to the system, not only were many of the salinity anomaly constraints not met, but also the uncertainties were not reduced. Under the assumption that this first test had failed because the uncertainties ascribed to the new equations were too large and to assure that the salinity anomaly constraints were met, the second test run reduced the estimated uncertainties by a factor of 10. The results of this test were also unsatisfactory. In attempting to meet the new constraints it became impossible to meet a good number of mass constraints, including the top to bottom mass balances across several sections. The magnitude of the unknowns was increased, in some instances outside the bounds of the prescribed estimates, and yet it still was not possible to significantly reduce the estimated transport uncertainties. This behavior would indicate that the salinity anomaly equations are not consistent with the rest of the model constraints. The anomaly equations may simply be too noisy to offer to allow enough information to be gleaned from them to significantly reduce the resulting uncertainties. The other possible reason for the inability of the model to fully utilize these equations may be the compound character of the model's w^* terms.

Subtraction of a mean property value from the tracer conservation equations removes the dominating effect of the noise in the continuity equation allowing the advective/diffusive balances to be extracted [*McDougall*, 1991]. The standard model however, has no diffusive terms. *McDougall* [1991] and *McDougall and You* [1990]

argue that while there is no problem in combining the advective and diffusive processes in a model which uses only thermal wind and continuity, these processes must be separated in models which include property conservation equations. By making the salinity anomaly constraints independent of the mass constraints, it is argued that the advective and diffusive terms must be separated to allow a balance to take place.

The anomaly constraints in the test model would appear noisy if the physics necessary to meet them were not available in the model. It would therefore be reasonable to change the model to include vertical diffusion and to repeat the experiment of including anomaly constraints. One might then hope to not only increase the rank of the system, but also to produce a more understandable set of vertical transfer terms.

Chapter 5

Summary and Conclusions

The “warm” and “cold” water paths of *Gordon* [1986] and “conveyor belt” of *Broecker* [1987, 1991] have brought the overturning nature of the thermohaline circulation into the public eye, especially as it relates to global climate. Much of the ongoing work which attempts to model the effects man has had and will have on the course of nature uses the “conveyor belt” schematic of the ocean circulation as a given. The assumption that the global oceanic circulation is known and understood is a source of concern, as there is much disagreement within the physical oceanographic community over not only the quantitative aspects of the thermohaline circulation: how much deep water is formed, how much heat does the ocean carry, how much freshwater exchange exists *etc.*; but also over the basic qualitative aspects of the picture: *e.g.* the importance of the flows through Drake Passage, through the Indonesian Passage and through the Bering Strait, the importance of the individual ocean basins to the global picture and even how real or useful a mean or general picture of the global circulation is.

The purpose of this thesis has been to create a globally consistent picture of the general circulation from a selection of modern hydrographic data sets with the

primary emphasis upon the quantitative aspects of the circulation. It is a basic result of this thesis, which could not be taken as a foregone conclusion, that it is indeed possible to create such a globally consistent model, in spite of the twenty five year time span and the lack of seasonal consistency among the data.

Following the introduction in the first chapter of this thesis, the second chapter presented the formulation of the model equations and the hydrography used in the research. Much of the initial effort in the development of the models presented, went into obtaining and formatting the data sets used and into building the tools necessary for handling the large amount of data available. Although a number of the data sets were obtained from the same source, each of the sections presented their own unique "interesting features" making the task of processing the data into a single format a less than trivial exercise. As more and more data, and different kinds of data are becoming available within the oceanographic community, the task of making the information generally accessible and usable is becoming more important. The existence of data sets which give global scale coverage necessitates the accessibility of the data from more regional studies for comparison and combination.

Chapter 3 provided the detailed results of the standard model. This model used constraints which included conservation of mass, salt, silica and PO₃₈ (phosphate-oxygen combination). It was found that, as with local or regional inverse solutions, the model results could be sensitive to the choice of the geostrophic velocity reference levels, the choice of initial covariance estimates, the choice of particular flux constraints and choice of the initial estimates of the Ekman component (the source of the wind estimates used, as well as the choice of annual versus cruise monthly means). The inclusion of different data sets could affect the results and the influence of some of the choices mentioned above, sometimes extended beyond the local region which was intended to be directly affected. It should be noted that all these choices will affect the solutions, regardless of whether or not an inversion is used to solve the

problem. The two choices which most affected the zonally integrated mass transport results of the standard model were the constraint set upon the flow from the Pacific to the Indian Basin through the Indonesian Archipelago and the initial estimate of the magnitude of the cross-isopycnal transfer terms.

The standard model, although globally consistent (*i.e.* displayed consistency between the model data and physics), not surprisingly, suggested a number of features in the circulation which appeared to counter conventional wisdom and/or previously published results. In particular, the standard model suggests

- a strong flow of warmer waters across the middle and eastern portions of the #A48N section,
- only a very small southward flow of North Pacific Deep Water across #P10N,
- a weaker overturning cell and somewhat lower heat flux across #A24N and #A36N than heretofore suggested.

The first and second of these features could not be removed even when constraints requiring their removal were employed. There is, of course, the possibility that some other constraint is working to maintain their existence, as is the case with the third feature. It was found that the strength of the overturning cell and the heat transport across the two North Atlantic sections could be increased when the constraints requiring a net northward transport of bottom waters across the sections were removed. It was determined that these constraints were inconsistent with both the model and conventional wisdom. They will not be included in future runs of the model.

The development and analysis of the standard model and its comparison to numerous test models presents a picture of the thermohaline circulation which is illustrated in cartoon form in Figure 5.1 and in more detail in Tables 5.1 and 5.2. Note that the values in this figure and these tables are taken from a run of the standard model which did not include the bottom water constraints across #A24N

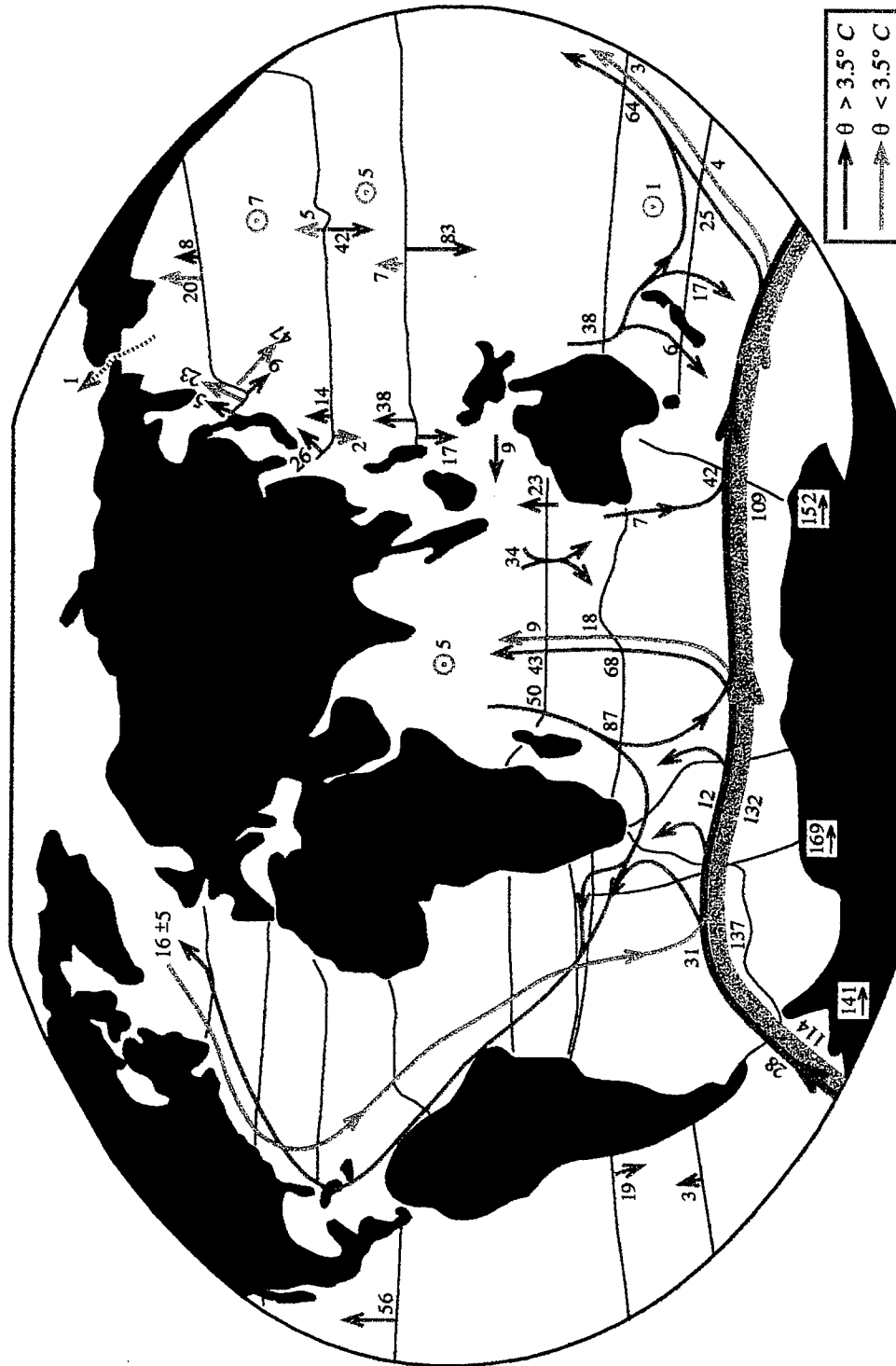


Figure 5.1: Schematic of the global ocean circulation taken from the run of the standard model which did not include the bottom water constraints across #A24N and #A36N. Red arrows indicate the flow of water which is greater than 3.5°C . Blue arrows indicate the flow of water which is less than 3.5°C . Transport values are given in 10^9 kg/s .

and #A36N¹. The schematic shows an overturning cell of the waters greater and less than 3.5°C of $16 \pm 5 \times 10^9 \text{ kg s}^{-1}$ within the Atlantic Basin. The uncertainty quoted here is the standard deviation of the values making up the average and indicates the variation in the estimates across the different sections. A discussion of these variations was given in Section 3.4.5. The presence of the flow through the Arctic from the Pacific, means that the average $16 \times 10^9 \text{ kg s}^{-1}$ of northward flow at temperatures greater than 3.5°C is balanced by an average of $-17 \times 10^9 \text{ kg s}^{-1}$ southward transport of waters less than 3.5°C. The estimated magnitude of the Atlantic overturning cell does not appear to be severely affected by the choice of velocity reference levels or the resolution of the cross-isopycnal transfer terms. Earlier tests have indicated that it is sensitive the choice of the flux constraint placed upon the North Brazil Current at 11°N and although it has not been tested, the magnitude of the overturning cell is also likely to be affected by the choice of the flux constraint placed on the Florida Straits transport.

Many, though not all the features of the Atlantic cell are similar to those seen in previous schematics of the circulation. Relatively warm waters flow northward in the eastern South Atlantic and cross over to the western basin south of the equator. The oceanic loss of heat within the North Atlantic was seen in Figures 3.27 and 3.28 and its effects were illustrated in Figures 3.24a and 3.24b where the northward transport became more obvious in denser potential density layers as the waters continued towards the northern polar regions. The southward flow of deep waters although generally seen in the western basins was not always tightly constrained to the western boundary. The standard model produced an unexpectedly strong northward transport of upper layer waters across the northernmost section in the North Atlantic.

¹The zonally integrated mass, heat and freshwater transports for the standard model without the bottom water constraints at #A24N and #A36N, are not significantly different from those of the standard model. However, for the sake of completeness, they are compared to the standard model results in Appendix C.

Section	$\Theta > 7.0^{\circ}\text{C}$	$\Theta < 7.0^{\circ}\text{C}$ $\Theta > 3.5^{\circ}\text{C}$	$\Theta < 3.5^{\circ}\text{C}$ $\Theta > 1.8^{\circ}\text{C}$	$\Theta < 1.8^{\circ}\text{C}$
#A48N	22	4	-21	-5
#A36N	11	5	-15	-1
#A24N	-13	-2	-13	-2
#Flst	29	1	0	0
net 24N	16	-1	-13	-2
#A11N	-5	-3	-13	4
NBC	19	0	0	0
net 11N	14	-3	-13	4
#A11S	15	1	-23	3
#A23S	10	3	-20	4
#A27S.W	-10	-2	-21	5
#A27S.E	22	5	-1	0
net 27S	12	3	-22	5
#A57S.W	0	0	1	-6
#A57S.E	0	0	1	3
net 57S	2	0	2	-2
#P47N	-4	9	3	-7
#P24N	-1	0	3	0
#P10N	2	-8	-9	16
#P28S	0	6	-2	5
#P43S	1	4	-3	7
#I18S	-15	-3	-2	11
#I32S	-19	-7	8	10
#Mz.N	-1	2	-1	0
#Mz.S	-2	2	0	0
#Drake	3	24	37	77
#0E.N	10	21	81	56
#0E.S	0	0	0	0
#0E2Afr	-12	21	90	44
#30E	-2	14	34	98
#132E	3	39	50	59

Table 5.1: Transport in potential temperature layers for the standard model. Positive values are north and east. The Ekman component has been subtracted from the surface layer. The lower bound on the uncertainty of these values for most of the sections is $2 \times 10^9 \text{ kg s}^{-1}$. For the sections which carry the ACC or which are affected by P-I throughflow the estimated uncertainty is of the order of $5 \times 10^9 \text{ kg s}^{-1}$.

Area		from $\Theta < 1.8^{\circ}\text{C}$	from $\Theta < 3.5^{\circ}\text{C}$	from $\Theta < 7.0^{\circ}\text{C}$
Name & Id Number		to $\Theta < 3.5^{\circ}\text{C}$	to $\Theta < 7.0^{\circ}\text{C}$	to $\Theta > 7.0^{\circ}\text{C}$
Southwest Atlantic	I	14	-7	-1
Weddell Scotia	II	2	-	-
South of South Africa	III	-54	2	9
West of South Africa	IV	-12	4	-1
Indian Southern Ocean	V	29	1	-17
Pacific Southern Ocean	VI	-25	-9	2
Pacific 43°S - 28°S	VII	2	1	-1
Indian 32°S - 18°S	VIII	-1	9	3
Mozambique Channel	IX	-	1	1
Indo-Pacific	X	-	4	17
Pacific 10°N - 24°N	XI	16	4	-4
Pacific 24°N - 47°N	XII	7	7	-2
Atlantic 23°S - 27°S	XIII	1	-1	-1
Atlantic 23°S - 11°S	XIV	1	4	6
Atlantic 11°S - 11°N	XV	-1	-11	-7
Atlantic 11°N - 24°N	XVI	6	6	4
Atlantic 24°N - 36°N	XVII	-1	1	-5
Atlantic 36°N - 48°N	XVIII	4	10	11
Northern Polar Region		-12	-30	-17

Table 5.2: Transport between potential temperature layers in each area (see Figure 2.2), deduced from the horizontal mass transport values given in Table 5.1, integrating from the bottom up. Positive values indicate conversion from colder to warmer waters. Negative values indicate conversion from warmer to colder waters.

This feature of the circulation could not be removed even by direct restrictions on the flow in this region and warrants further investigation.

Within the Southwest Atlantic the deep waters from the north and south combine with the predominantly deep and intermediate waters coming through Drake Passage from the Pacific. The expected increase in net transport between Drake Passage and the Greenwich Meridian is apparent across the 0°E section in Table 5.1 at potential temperatures less than 3.5°C . The question which arises is, does the water within the Benguela Current which eventually feeds the formation of deep water to the north, flow directly from Drake Passage into the South Atlantic Current and turn northward east of 0°E (the "cold water" path) or does it continue into the Indian Basin and possibly into the Pacific Basin, before returning to the Atlantic around the southern tip of South Africa (the "warm water" path)?

The models show (Table 3.12 and Table 5.1) evidence of a strong northward transfer of surface and intermediate waters in the eastern South Atlantic between the Greenwich Meridian and the southern tip of South Africa. The models also show (Figures 5.1, 3.19a and 3.19b) that there is ample evidence of water flowing westward to the south of the southern tip of South Africa and that this water is similar to that found within the Benguela Current. Taking the strength of the flow between the Indian and Atlantic Basins suggested by the sections used in these models as typical, would imply that the "warm water" path is at least as important as the "cold water" path in supplying a source for the deep water formation in the north. However, the uncertainties associated with the westward transport are large, as this "warm water" flow is carried by a few strong eddy features. The variability of the region makes hydrography a poor estimator of the relative strengths of the "warm" and "cold" paths, especially in models such as these which rely upon the assumption of a steady state. Such models are biased (as this one certainly is) by the particular data sets included in the studies. So while the models presented here suggest that

both pathways may be important to the global overturning cell, repeat sections and perhaps the inclusion of satellite and other forms of data would improve further investigation.

The second question of importance to the idea of a global overturning cell is how important the strength of the Indonesian Passage throughflow is to the strength of the "warm" and "cold" water scenarios. The pattern of flow and property values within the South Atlantic and South Indian Basins suggests that some portion of the NADW feed water originates in the South Atlantic Current, passes into the Agulhas recirculation gyre and then returns westward around the southern tip of South Africa, as in the short-circuited "warm water" path of *Gordon et al.* [1992]. In support of this suggestion, the comparison of models with both stronger and weaker P-I throughflow transports indicates that the effects of P-I throughflow are disconnected and independent from the global overturning cell. The picture developed from the models is not so much of a single global overturning cell as two cells, one which connects the Atlantic to the ACC and the deep waters of the Southern Ocean, and one which connects the Pacific and Indian Basins to the north and south of Australia.

Within the first cell, as in the classical picture, the warmer waters flowing northward within the Atlantic are converted to deep water in the north before returning to the south. These northern deep waters are met within the southwest Atlantic by the deep and bottom waters of the Weddell Gyre region, and deep and intermediate waters entering from the Pacific through Drake Passage. Some of these waters turn northward and upwell within the eastern basin where there is a large gain of heat by the ocean from the atmosphere. Some the waters flow into the Agulhas region of the Indian Basin where they also upwell and return westward into the Atlantic in form of eddies. Most of these combined abyssal waters (mostly CDW with some AABW) move into the Indian and Pacific Basins within the ACC. According to Table 3.12 the major modification of the deep waters flowing eastward

within the southern ocean is the loss of LCDW which occurs in mainly in the Indian sector but also, to a lesser degree in the Pacific sector. In its passage through the Indian and Pacific basins, it appears that about $20 \times 10^9 \text{ kg s}^{-1}$ of LCDW is replaced with intermediate water before returning once again to the Atlantic through Drake Passage.

Within the Indian Basin much of the deep water which enters along the numerous western boundaries is returned within the Agulhas Current. There is a conversion from cold to warmer waters both between 32°S and 18°S , and to the north of 18°S .

Within the South Pacific $8 \times 10^9 \text{ kg s}^{-1}$ enters at potential temperatures less than 3.5°C . Across the equator at 10°N , there is an increased northward flow of deep waters, all of which occurs at temperatures greater than 1.8°C . Much of the conversion from cold to warm waters appears to occur well below the thermocline between 10°N and 24°N in the Pacific. This cold to warm conversion also occurs to a lesser degree to the north of 24°N latitude.

The large transport of abyssal waters across 10°N in the Pacific is not due to the creation of bottom waters within the basin, but is rather due to a deficiency in the model constraints in the Indo-Pacific region. The standard model Indo-Pacific constraints would be improved with constraints requiring conservation of deep waters in the individual basins. It is known that neither the Indian nor the North Pacific circulations are greatly changed when the model only uses the data from the individual basins. Therefore, it is suspected that the inclusion of a constraint on the deep flows in the Indo-Pacific would result in stronger inflows of abyssal waters into the South Pacific and lesser changes to the Indian and North Pacific circulations.

The second cell, which appears to be independent of the first, sees thermocline waters from the Pacific flowing into the Indian Basin through the Indonesian Archipelago. The models indicate that there is adequate southward flow of surface

and intermediate waters in the eastern South Indian Ocean to account for flow entering through the Indonesian Archipelago. The convergence of surface and intermediate waters between 18°S and 32°S suggests that some of these upper layer waters recirculate within the Indian Basin, but the Figure 5.1 cartoon illustrates the result of the models that the P-I throughflow has no discernible effect upon the flow within the Agulhas Current nor upon the return flow around the southern tip of South Africa. In accordance with this argument, *Schmitz* [1995] in his synthesis of previously published results is led to conclude that only $2 \text{ to } 4 \times 10^6 \text{ m}^3 \text{ s}^{-1}$ of warm water flow around the southern tip of South Africa is connected to Indonesian Passage throughflow (estimated at $O(10 \text{ Sv})$). Meridional hydrographic lines in the Pacific and Indian Basins (although problematic to include) would be useful in better determining how far the effects of P-I throughflow extend in the zonal direction. For the moment however, our models indicate that regardless of the magnitude of the throughflow, it is disconnected from the global pattern and so does not affect the relative strengths of the "warm" and "cold water" pathways.

Along with the mass transports, heat and freshwater fluxes were also computed. The models produced estimates of the heat flux across complete latitudinal circles at three positions: 47°N, 24°N and 30°S. At 30°S, the standard model estimate of heat flux $-0.9 \pm 0.4 \text{ PW}$ is dominated by a large ($>1 \text{ PW}$) poleward temperature flux in the Indian Basin. This value did not appear to be significantly affected by the magnitude of the P-I throughflow. At 47°N, the net poleward heat flux of $0.6 \pm 0.4 \text{ PW}$ is dominated by the northward transport into polar regions within the Atlantic Basin. The standard model estimate of $1.4 \pm 0.4 \text{ PW}$ calculated at 24°N is lower than, and only just consistent with the $2 \pm 0.3 \text{ PW}$ of *Bryden et al.* [1991]. One cause for the low estimate was determined to be the inclusion of the bottom water constraints in the North Atlantic. Removal of these constraints in the North Atlantic raises this estimate to $1.5 \pm 0.4 \text{ PW}$. This value is our "best" estimate. Most of the remaining

discrepancy between this value and the *Bryden et al.* value occurs in the Pacific and is due to differing estimates of Ekman transport.

The heat flux estimates tended to be some of the most robust estimates to come out of the models, being insensitive to many of the choices which affected the other transport estimates. They were, however, quite sensitive to the initial estimates of the Ekman transport. In particular, the standard model heat flux estimates at 10°N in the Pacific were strongly affected by the choice of wind field used to compute the Ekman transport. The computed flux uncertainties are considered to be small as they only represent the uncertainty in the absolute transport due to the uncertainty in the reference level velocities. In the case of the heat fluxes, an additional 0.25 PW was included in the quoted values of uncertainty to account for that portion which arises from the assumption that our data set represents a climatology.

Freshwater fluxes were computed from the model results and compared to the E-P+R estimates of *Baumgartner and Reichel* [1975] and *Schmitt et al.* [1989] as computed by *Wijffels et al.* [1992] with an integration reference point at the Bering Strait. Unfortunately, it was found that the models were unable to produce results accurate enough to be used to calculate freshwater fluxes which would be significantly different from zero. The models were unable to cast any light upon the the significance to the global circulation of the northern mass, heat and freshwater connection between North Pacific and Atlantic Basins through the Arctic. Their failure to do so was due to the looseness of the constraints in the northern polar region. Although in this work it was not possible to compute freshwater fluxes which were significantly different from zero, future inclusion of salinity anomaly constraints along with terms describing vertical diffusion may yet make it possible to compute significant freshwater flux estimates from hydrography.

The models presented here suggest a global circulation pattern which is in some ways similar to the classical picture and in some ways different. In conclusion

we should ask what is necessary to improve either these results or our general base of knowledge. It is the suspicion of this author that simply *more* data will not be enough to fill in the gaps in our understanding. Certainly, there are obvious holes where more hydrographic measurements would be useful (*e.g.* the North Indian Ocean and around the ACC in locations other than Drake Passage), however, there are a number of other places where the inclusion of different kinds of data or data from repeat sections would provide better insight. In particular, those places where it is unlikely that the hydrography is providing a useful time mean, such as the Indian Ocean and the Indonesian Archipelago where seasonal variations are large and around Cape Agulhas where it is suspected that the eddy field is carrying much of the mass and heat transfer between the Indian and Atlantic Basins. Some data sets already exist (*e.g.* XBT data in the Indonesian Archipelago and current meter data in Drake Passage) and could be included in the model constraints. However, it should be kept in mind that studies of P-I throughflow continue to produce conflicting estimates [*Fieuz et al.*, 1994; *Meyers et al.*, 1995; *Wijffels* 1993] and although the present model does not find the throughflow to be an integral choke point in global circulation picture, it is definitely a feature which calls for further investigation.

Along with including different model constraints it would be useful to test the model's dependency upon some of the constraints which already exist. In particular, further investigation is warranted into its dependency upon the specific flux estimates (*eg.* Florida Straits and Drake Passage) and Ekman transport estimates used. There is also the need to properly test the advantages of using tracer anomaly conservation through the inclusion of diffusive terms in the equations. Constraining the system more stringently with available tracer information might provide a better test of the consistency of combining data sets spanning three decades in the same model.

The possibilities for further constraining the current model are essentially infinite and are limited only by the time and data available for this research. There

are numerous local regions in which the detailed circulation might be further constrained or examined. However, the main goal of this work, is to look at the global scale circulation and to that end some of the more interesting extensions would be to include new hydrographic data as it becomes available, to replace some of the older lines with more recent (better sampled) data sets and to include other types of data in the constraints. These extensions would give some idea of how much the particular circulation pattern found is a result of the particular data sets used.

The greatest limitation of the current setup is its inability to determine the effects of the steady state assumption, but with enough data it might be possible to at the very least compare decadal or perhaps seasonal global circulation patterns. It has already been seen that some of the most important connections between the basins are not readily modeled by a steady state system. It may well be that the comparison of results using different data sets will result in the conclusion that the "mean" circulation at these connection points is not as important to our understanding of the global circulation pattern as the time varying component.

There is much room for improvement within the standard model, so rather than it being considered an end point, it should be considered a stepping off point for the creation of better, differently and/or more highly constrained models. It does not replace the regional analyses, but can complement them by placing their results in a global perspective. The greatest advantage of the setup presented here is that it allows the fairly straight forward inclusion of these new constraints (new data and ideas) and provides a simple method of checking the consistency of new constraints with previous ones.

Appendix A

Station-Specific Reference Levels

This appendix lists the station-specific reference levels used in the standard model, supplied in one case, by the literature (#A11N) and in the other two (#I32S and #P10N) through personal communication.

Starting Station Pair	Ending Station Pair	Starting Longitude	Ending Longitude	Reference Level (db)
1	8	30.4°E	31.2°E	2000
9	9	31.2°E	31.6°E	2500
10	13	31.6°E	35.0°E	3000
14	21	35.0°E	39.5°E	1750
22	25	39.5°E	44.5°E	6000
26	30	44.5°E	48.3°E	1750
31	34	48.3°E	52.8°E	2000
35	35	52.8°E	53.2°E	4000
36	37	53.2°E	54.1°E	2000
38	38	54.1°E	55.8°E	2500
39	39	55.8°E	57.0°E	1750
40	41	57.0°E	58.2°E	1400
42	42	58.2°E	58.9°E	2000
43	45	58.9°E	62.0°E	2250
46	48	62.0°E	68.0°E	3500
49	53	68.0°E	76.0°E	2250
54	54	76.0°E	77.0°E	2500
55	55	77.0°E	77.7°E	2750
56	60	77.7°E	82.0°E	2000
61	61	82.0°E	83.5°E	3250
62	62	83.5°E	85.0°E	2000
63	36	85.0°E	86.0°E	4750
64	64	86.0°E	86.9°E	2000
65	70	86.9°E	93.4°E	6000
71	85	93.4°E	104.5°E	2250
86	86	104.5°E	105.0°E	3250
87	88	105.0°E	106.5°E	3500
89	91	106.5°E	109.2°E	4000
92	103	109.2°E	114.8°E	2500

Table A.1: Station-specific reference levels used for the #I32S section. Values originate from *J. Toole* (pers. comm.) and have been converted to the standard depths used in creating the model equations.

Starting Station Pair	Ending Station Pair	Starting Longitude	Ending Longitude	Reference Level (db)
1	6	-17.7°E	-50.2°E	1100
7	22	-50.2°E	-46.3°E	2750
23	79	-46.3°E	-17.7°E	2000

Table A.2: Station-specific reference levels used for the #A11N section. Values originate from *Friedrichs and Hall* [1993] and have been converted to the standard depths used in creating the model equations.

Starting Station Pair	Ending Station Pair	Starting Longitude	Ending Longitude	Reference Level (db)
1	71	126.6°E	169.3°E	3250
72	83	169.3°E	176.3°E	3000
84	112	176.3°E	200.5°E	3750
113	178	200.5°E	255.5°E	1750
179	208	255.5°E	274.3°E	3000

Table A.3: Station-specific reference levels used for the #P10N section. Values originate from *S. Wijffels* (pers. comm.) and have been converted to the standard depths used in creating the model equations.

Appendix B

Alternative Model Mass Transport Profiles

This appendix illustrates the differences between the standard model described in Chapter 3 and some of the alternative models discussed in Chapter 4.

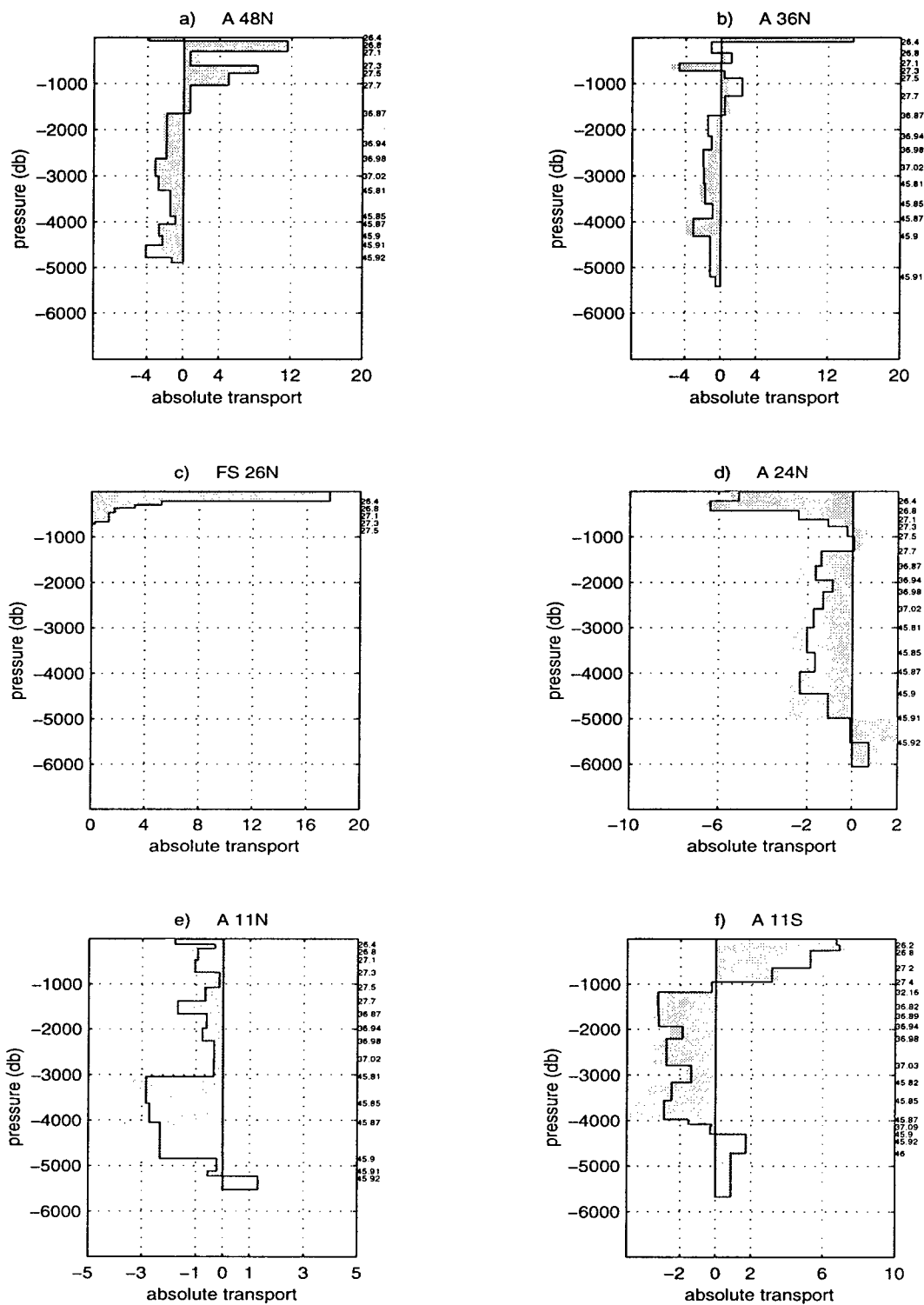


Figure B.1: Comparison of the zonally integrated mass transport profiles resulting from the standard model (shaded) and model D₁ (solid line), for sections: (a) #A48N, (b) #A36N, (c) #F1St, (d) #A24N, (e) #A11N and (f) #A11S. Model D₁ does not allow for any vertical transfer. The standard model does. The Ekman transport is included in outcropping layers.

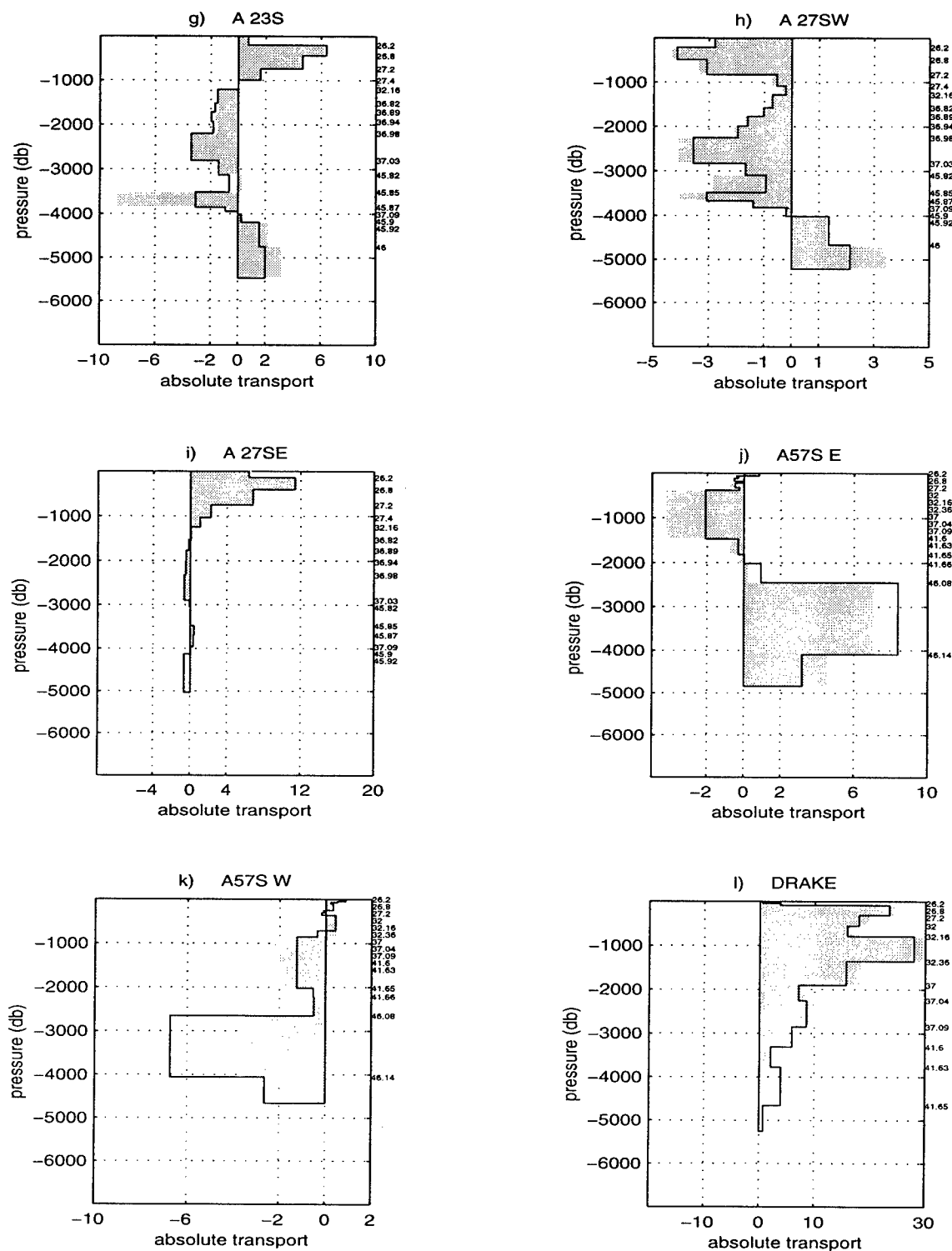


Figure B.1 continued: Comparison of the zonally integrated mass transport profiles resulting from the standard model (shaded) and model D_1 (solid line), for sections: (g) #A23S, (h) #A27S-W, (i) #A27S-E, (j) #A57S-W, (k) #A57S-E and the meridionally integrated profile for (l) #Drake. Model D_1 does not allow for any vertical transfer. The standard model does.

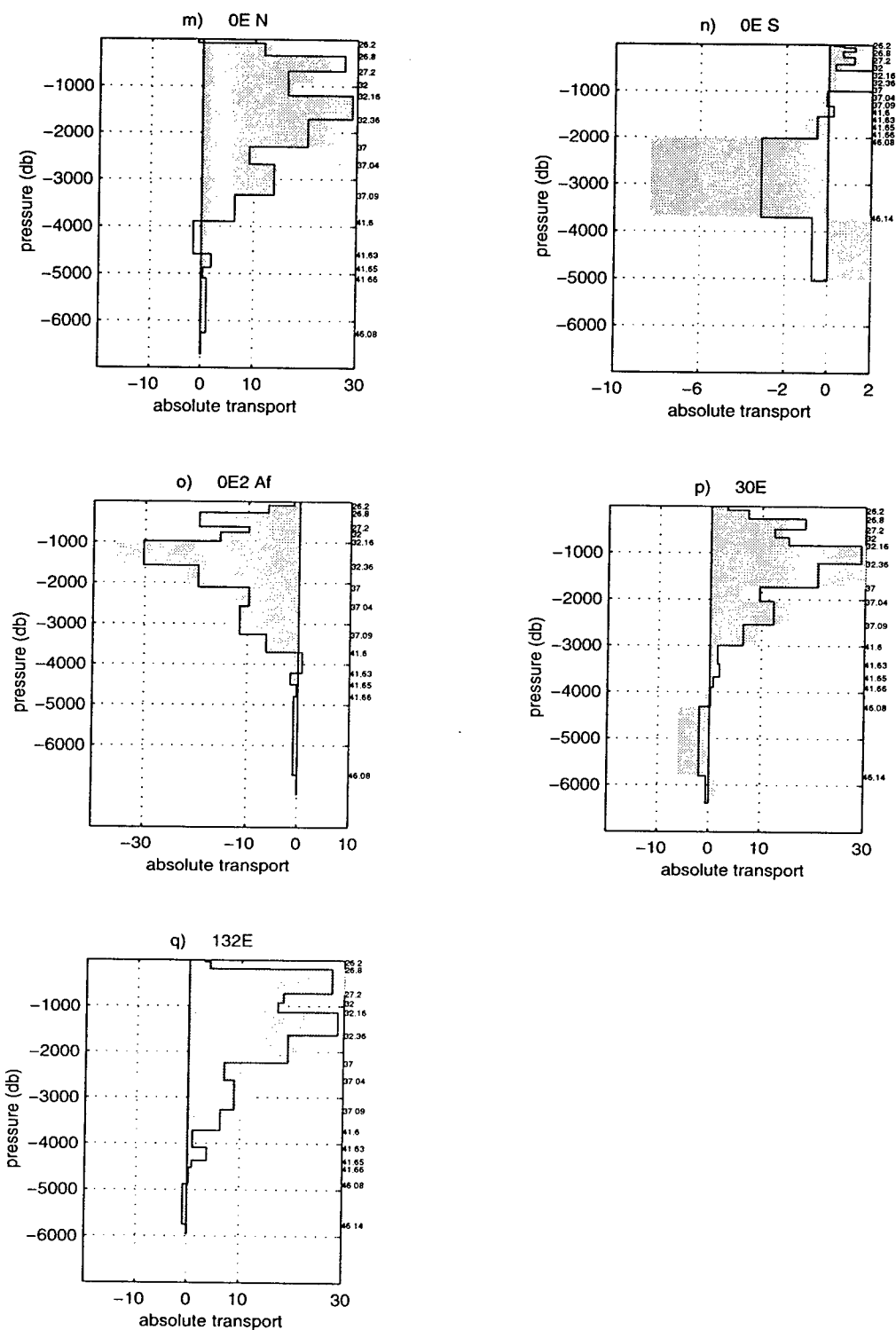


Figure B.1 continued: Comparison of the meridionally integrated mass transport profiles resulting from the standard model (shaded) and model D₁ (solid line), for sections: (m) #0E.N, (n) #0E.S, (o) #0E2Afr, (p) #30E and (q) #132E. Model D₁ does not allow for any vertical transfer. The standard model does.

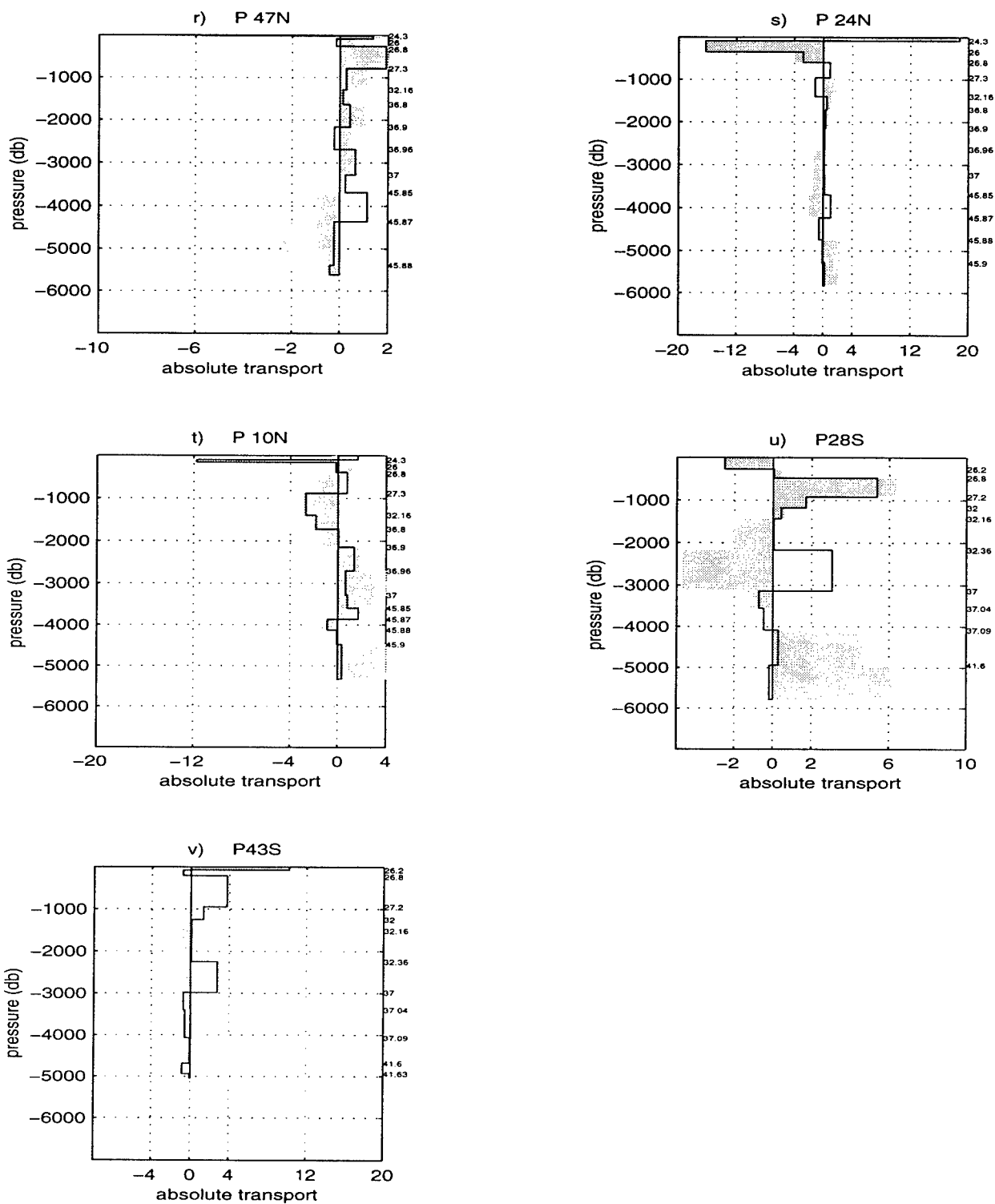


Figure B.1 continued: Comparison of the zonally integrated mass transport profiles resulting from the standard model (shaded) and model D₁ (solid line), for sections: (r) #P47N, (s) #P24N, (t) #P10N, (u) #P28S and (v) #P43S. Model D₁ does not allow for any vertical transfer. The standard model does.

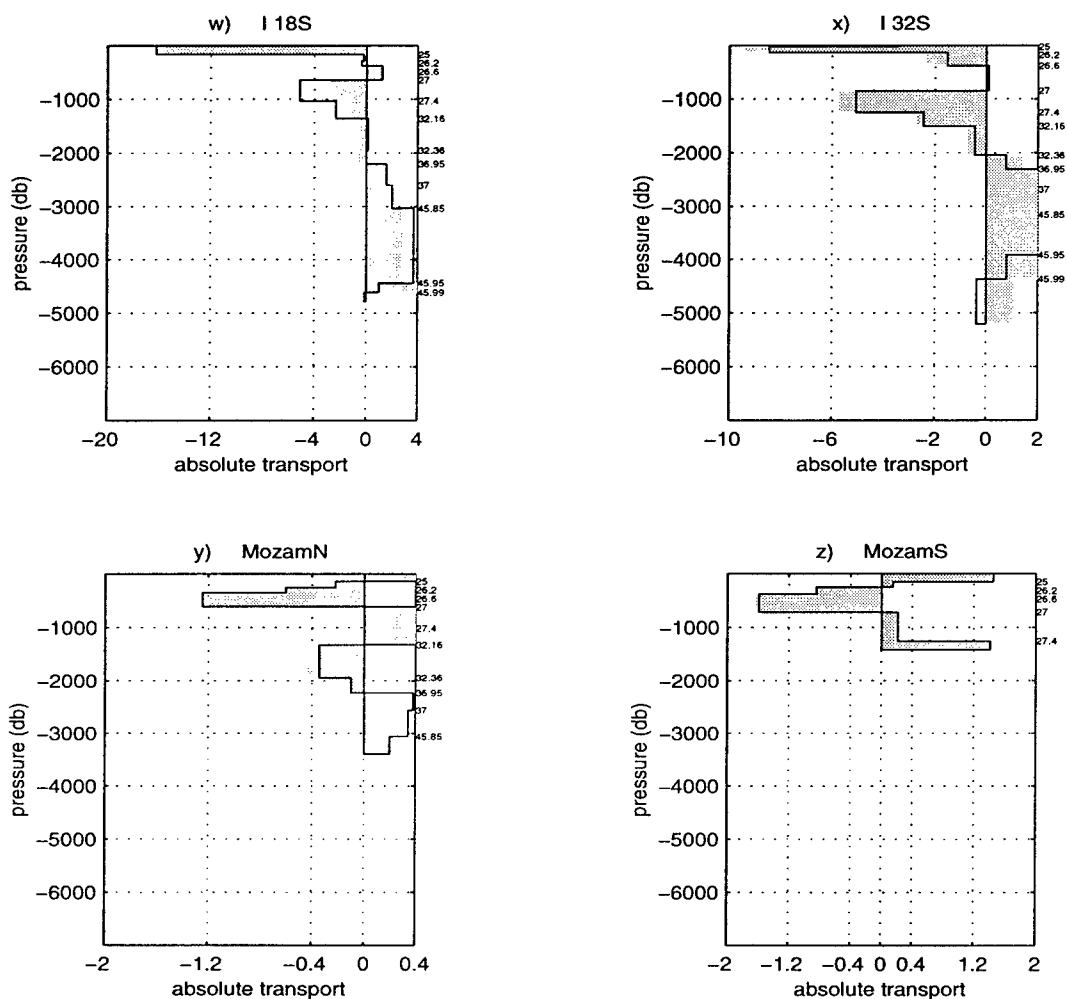


Figure B.1 continued: Comparison of the zonally integrated mass transport profiles resulting from the standard model (shaded) and model D₁ (solid line), for sections: (w) #I18S, (x) #I32S, (y) #Mz_N, and (z) #Mz_S. Model D₁ does not allow for any vertical transfer. The standard model does.

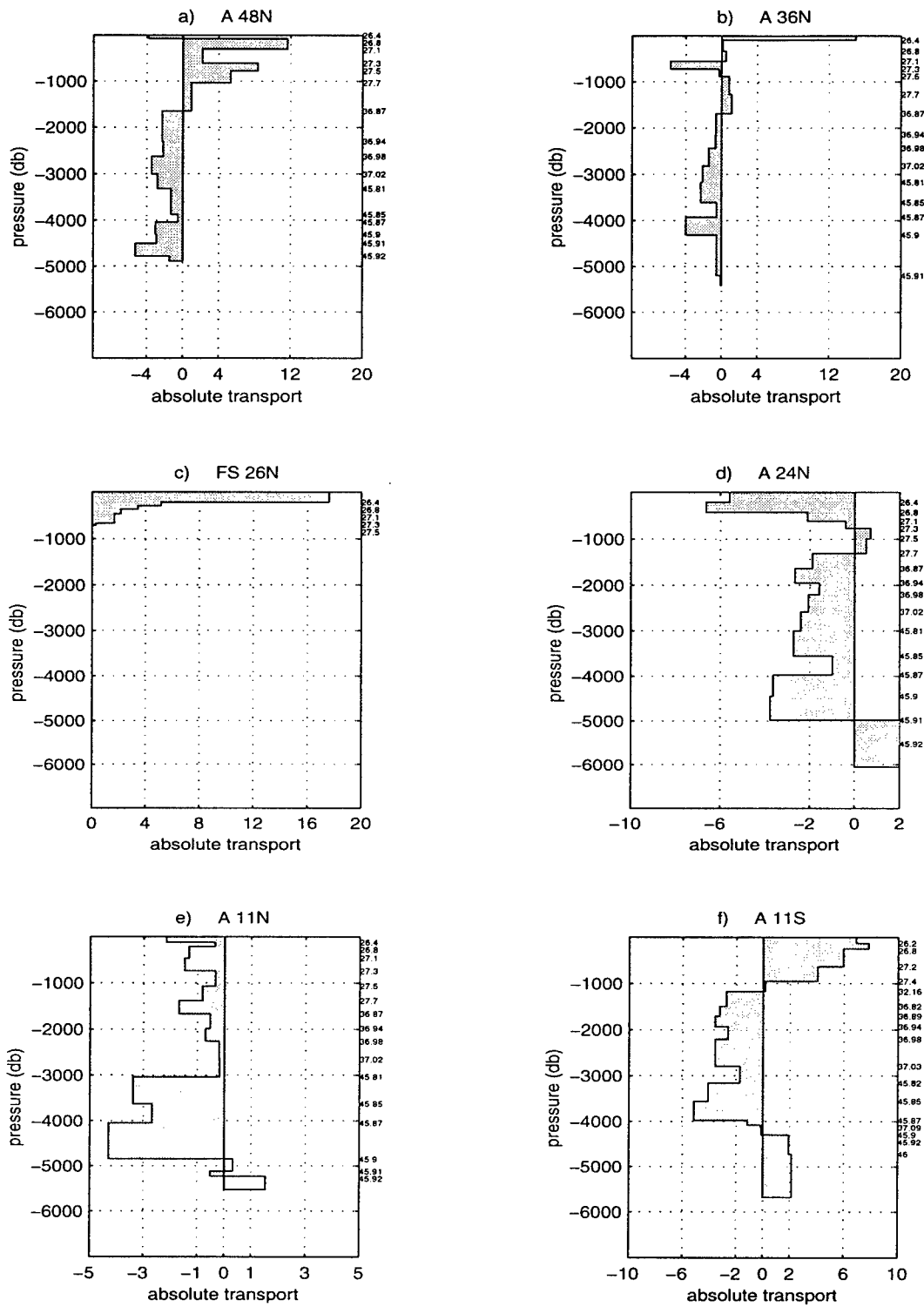


Figure B.2: Comparison of the zonally integrated mass transport profiles resulting from the standard model (shaded) and model D_2 (solid line), for sections: (a) #A48N, (b) #A36N, (c) #F1St, (d) #A24N, (e) #A11N and (f) #A11S. Model D_2 allows for larger vertical transfers (see Table 4.3). The Ekman transport is included in outcropping layers.

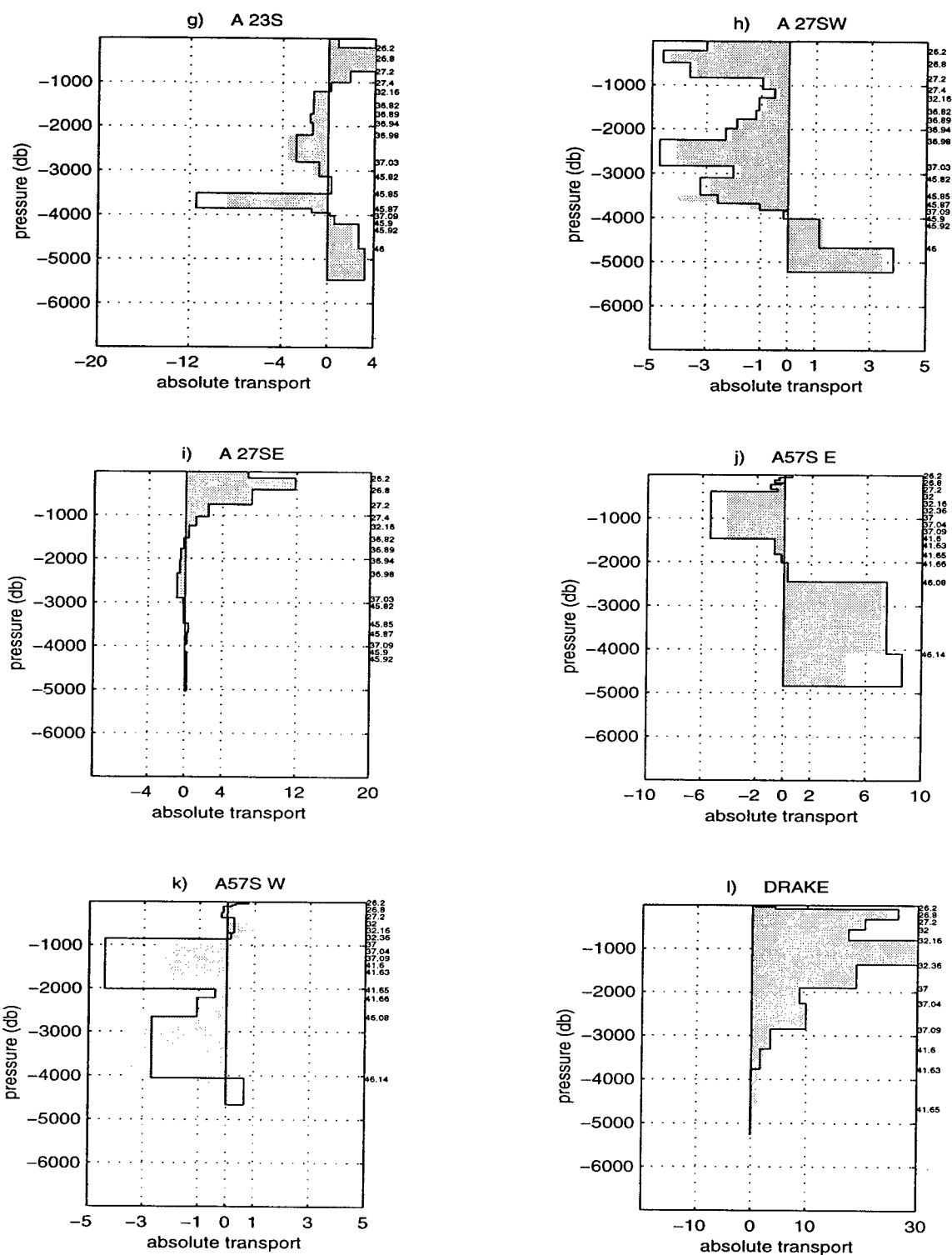


Figure B.2 continued: Comparison of the zonally integrated mass transport profiles resulting from the standard model (shaded) and model D₂ (solid line), for sections: (g) #A23S, (h) #A27S-W, (i) #A27S-E, (j) #A57S-W, (k) #A57S-E and the meridionally integrated profile for (l) #Drake. Model D₂ allows for larger vertical transfers (see Table 4.3).

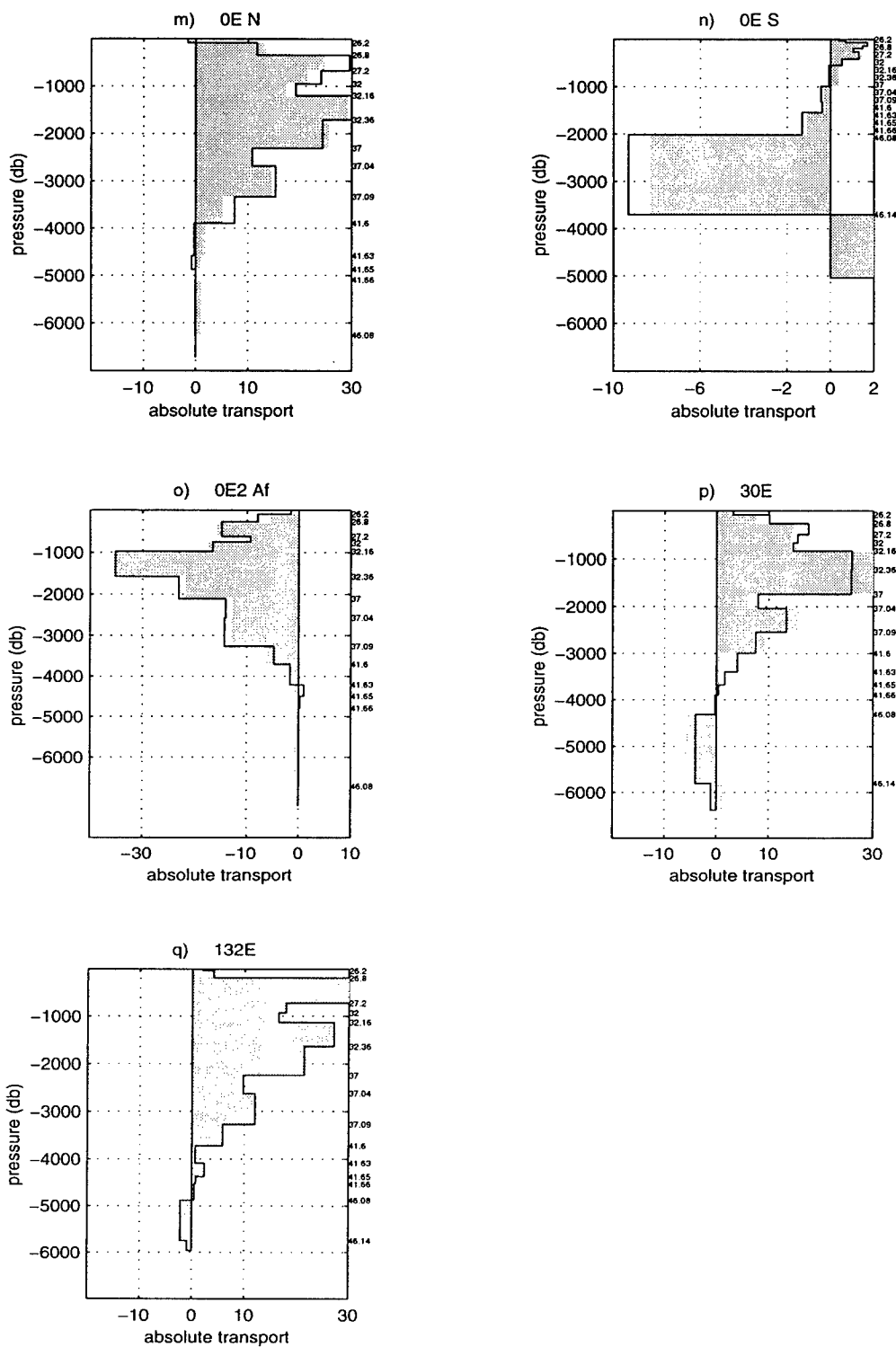


Figure B.2 continued: Comparison of the meridionally integrated mass transport profiles resulting from the standard model (shaded) and model D₂ (solid line), for sections: (m) #0E_N, (n) #0E_S, (o) #0E2Afr, (p) #30E and (q) #132E. Model D₂ allows for larger vertical transfers (see Table 4.3).

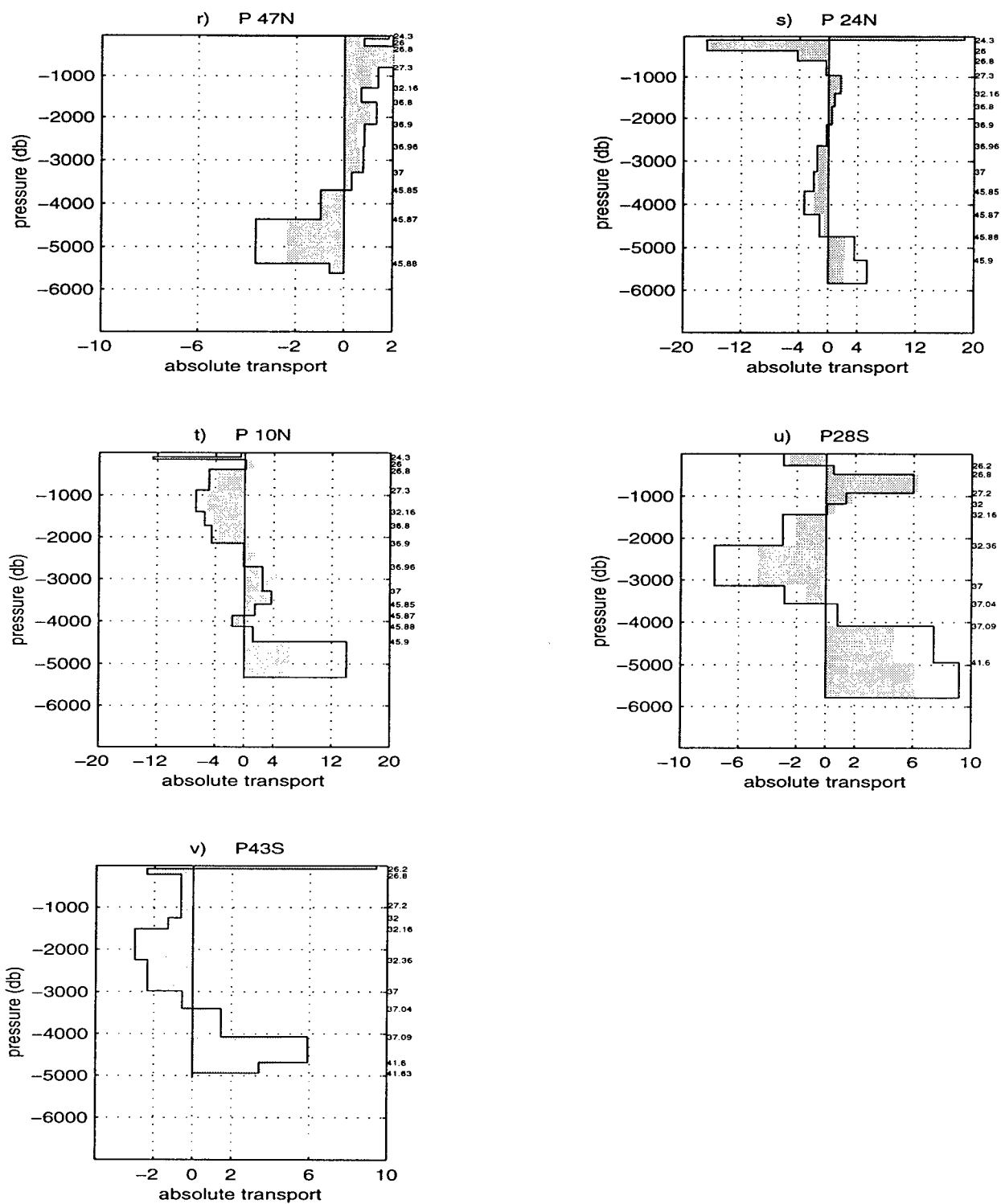


Figure B.2 continued: Comparison of the zonally integrated mass transport profiles resulting from the standard model (shaded) and model D₂ (solid line), for sections: (r) #P47N, (s) #P24N, (t) #P10N, (u) #P28S and (v) #P43S. Model D₂ allows for larger vertical transfers (see Table 4.3).

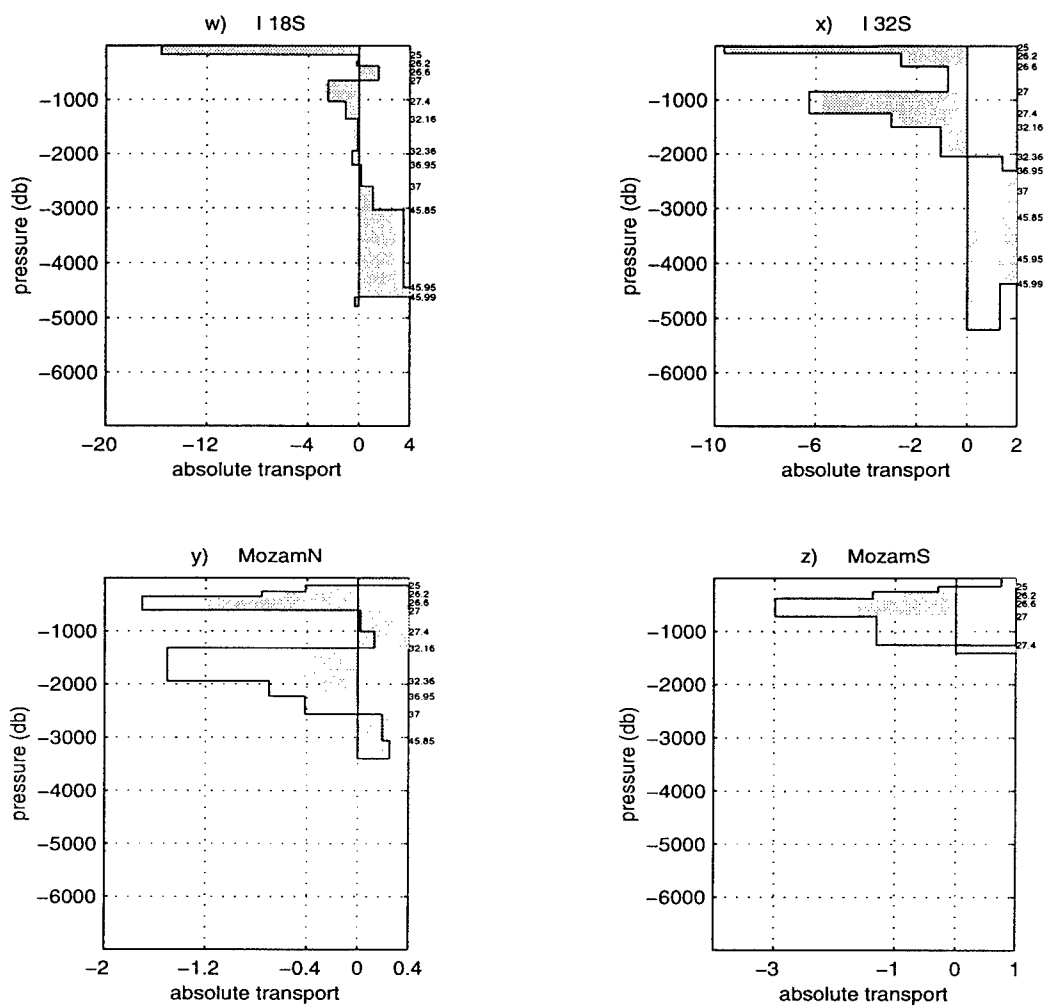


Figure B.2 continued: Comparison of the zonally integrated mass transport profiles resulting from the standard model (shaded) and model D₂ (solid line), for sections: (w) #I18S, (x) #I32S, (y) #Mz.N, and (z) #Mz.S. Model D₂ allows for larger vertical transfers (see Table 4.3).

Appendix C

Comparison of the Standard Model and Model NBW

This appendix compares the results of the standard model as described in Chapters 2 and 3 and the “best” estimate version of the standard model which does not constrain the bottom water flow to the north of 11°N in the Atlantic. The bottom water constraints at 24°N and 36°N in the Atlantic, used in the standard model were determined to be inconsistent with the other model constraints and the expected circulation patterns in the region. The most obvious difference in the solutions is the magnitude of the overturning cell across #A24N and #A36N (see Figure C.1 and the discussion on page 146). The heat flux estimates at these two latitudes are also slightly affected (see discussion in section 3.4.7). The primary purpose of this appendix is to illustrate how similar this solution is to the standard model solution beyond the #A24N and #A36N sections.

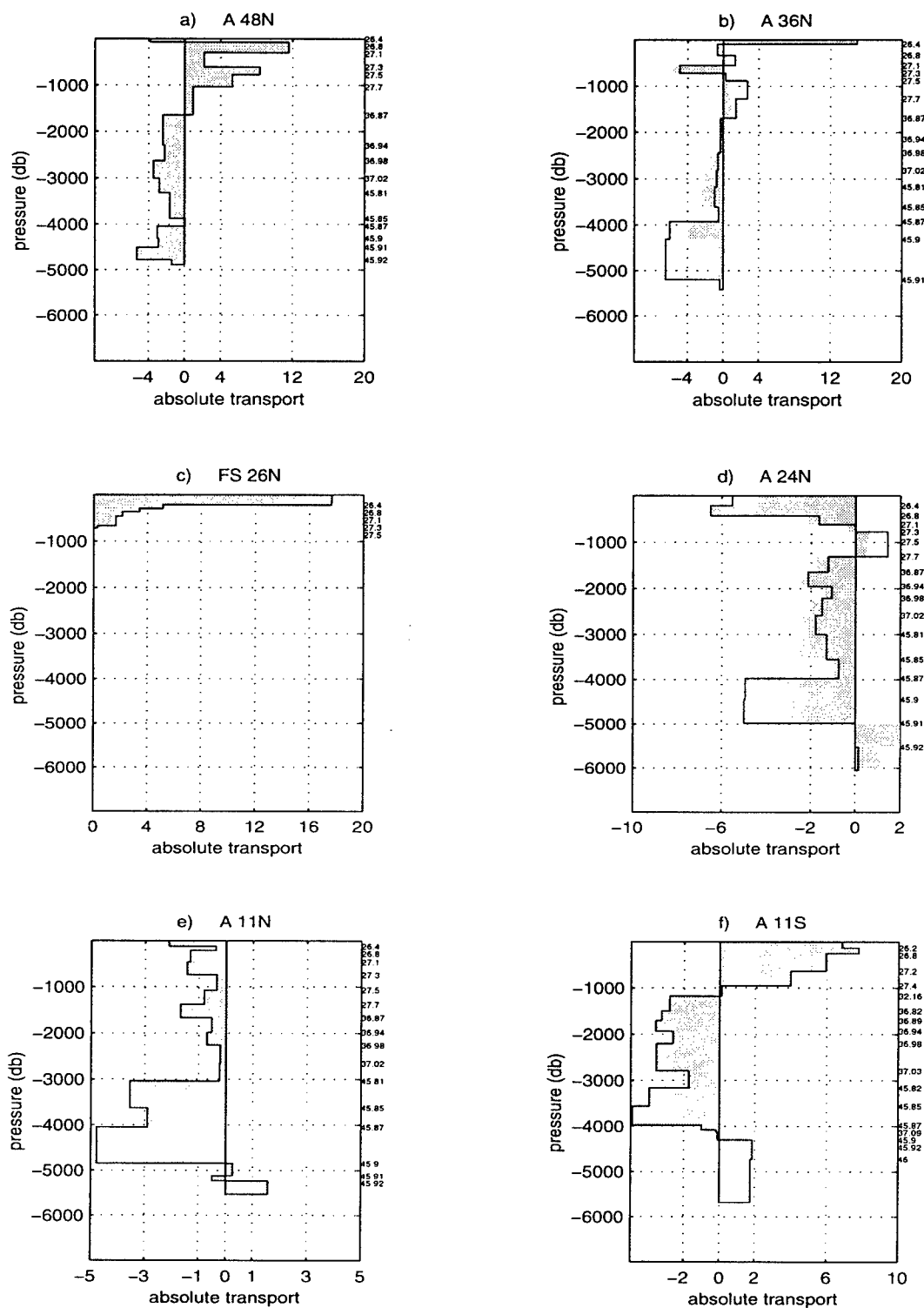


Figure C.1: Comparison of the zonally integrated mass transport profiles resulting from the standard model (shaded) and standard model without the bottom water constraints at #A24N and #A36N (solid line), for sections: (a) #A48N, (b) #A36N, (c) #F1St, (d) #A24N, (e) #A11N and (f) #A11S. The Ekman transport is included in outcropping layers.

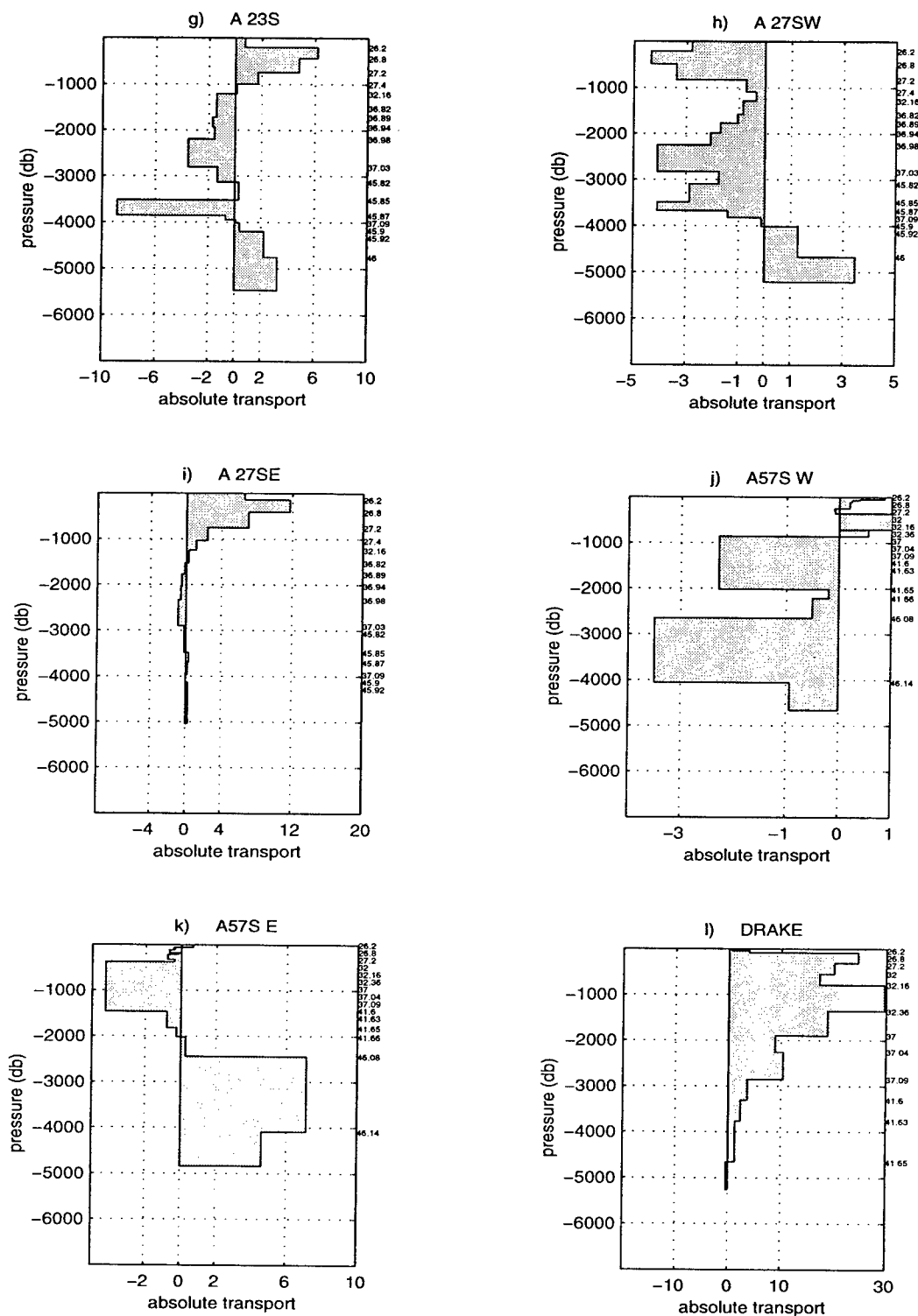


Figure C.1 continued: Comparison of the zonally integrated mass transport profiles resulting from the standard model (shaded) and standard model without the bottom water constraints at #A24N and #A36N (solid line), for sections: (g) #A23S, (h) #A27S-W, (i) #A27S-E, (j) #A57S-W, (k) #A57S-E and the meridionally integrated profile for (l) #Drake.

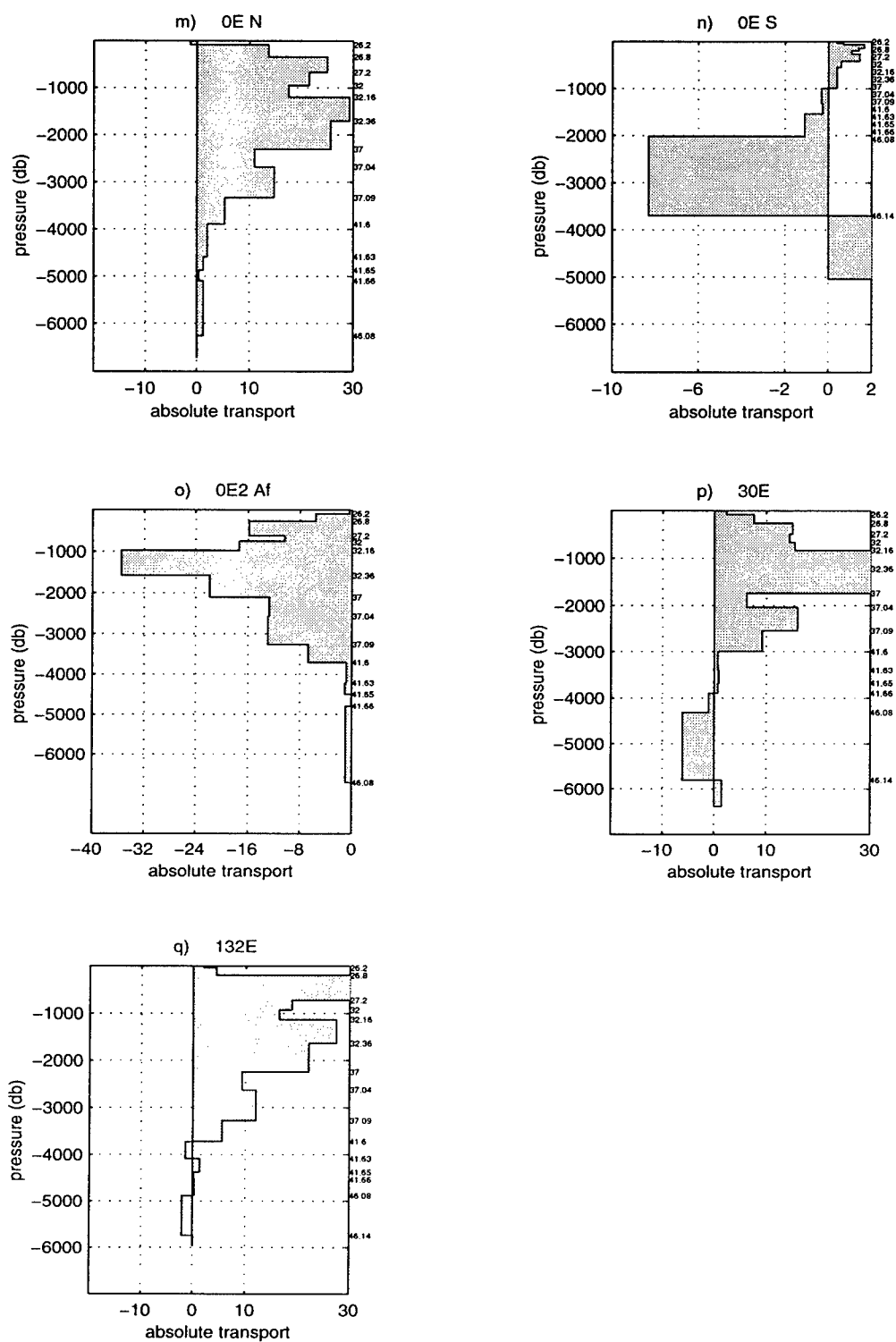


Figure C.1 continued: Comparison of the meridionally integrated mass transport profiles resulting from the standard model (shaded) and standard model without the bottom water constraints at #A24N and #A36N (solid line), for sections: (m) #0E_N, (n) #0E_S, (o) #0E2Afr, (p) #30E and (q) #132E.

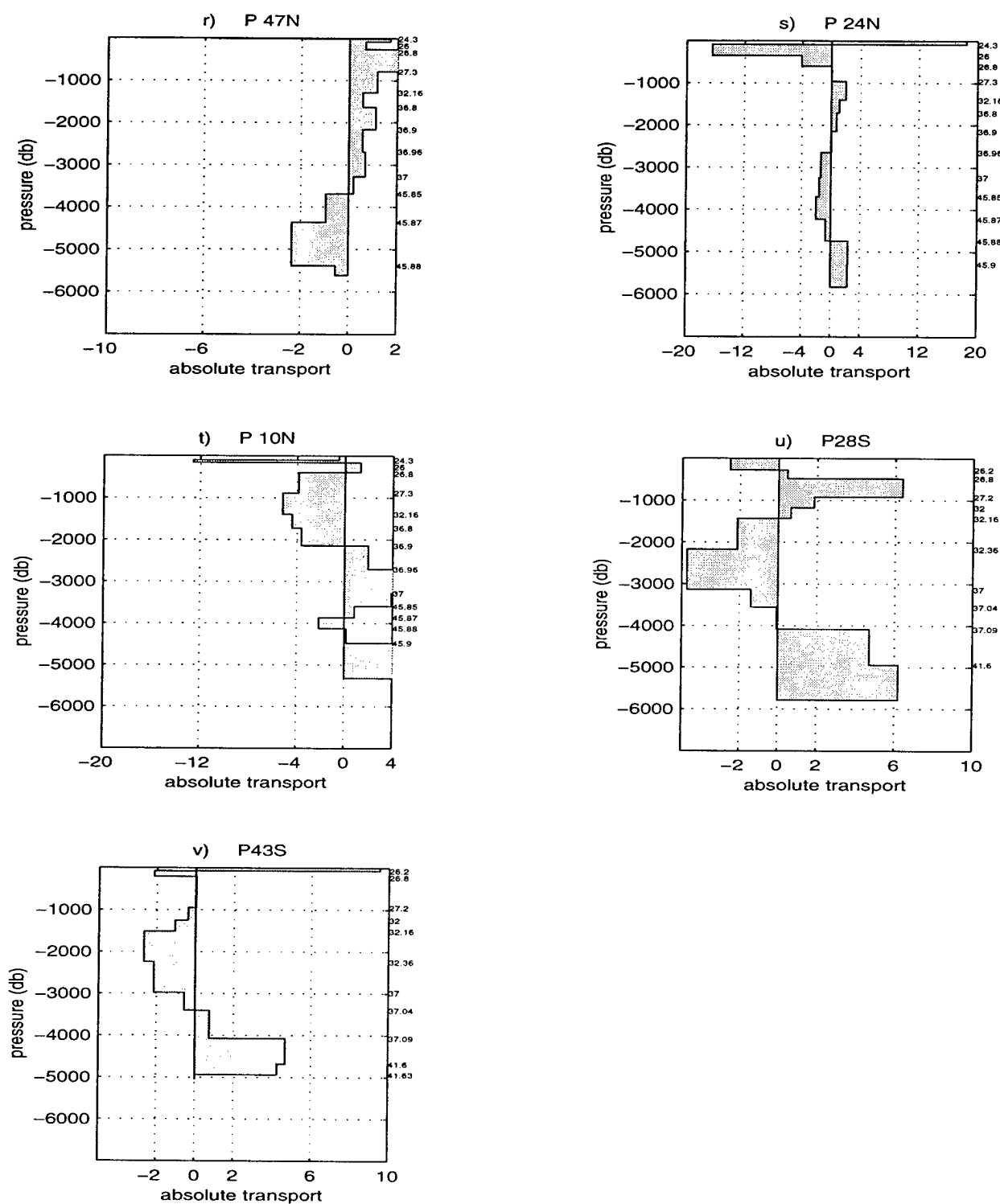


Figure C.1 continued: Comparison of the zonally integrated mass transport profiles resulting from the standard model (shaded) and standard model without the bottom water constraints at #A24N and #A36N (solid line), for sections: (r) #P47N, (s) #P24N, (t) #P10N, (u) #P28S and (v) #P43S.

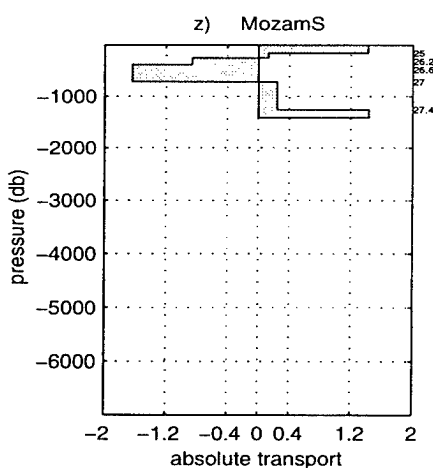
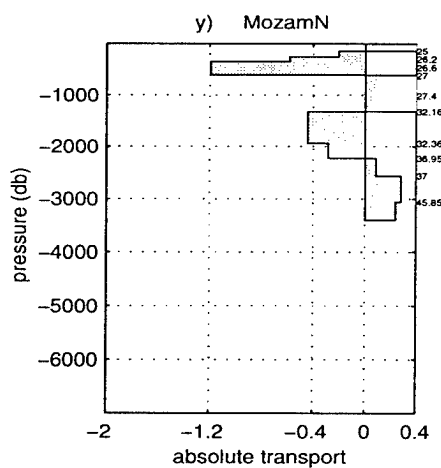
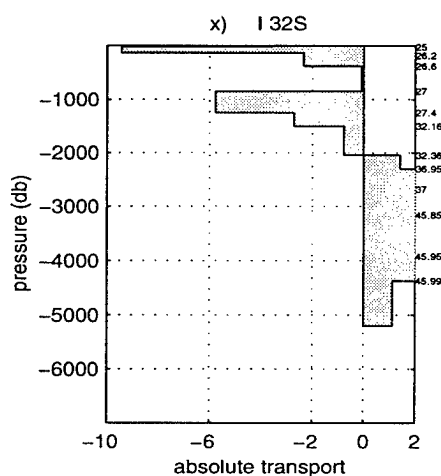
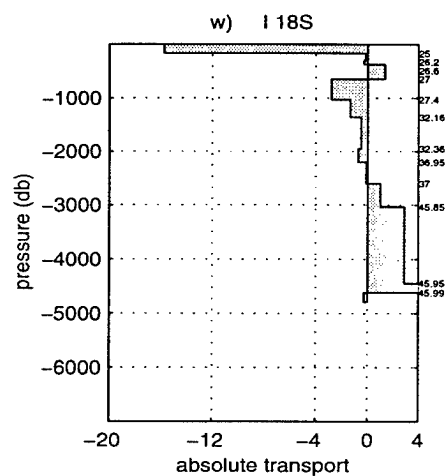


Figure C.1 continued: Comparison of the zonally integrated mass transport profiles resulting from for sections: (w) #I18S, (x) #I32S, (y) #Mz_N, and (z) #Mz_S.

Section	STD FW Transport	NBW FW Transport
#A48N	-1.0	-1.0
#A36N	-1.0	-1.1
#A24N	-0.9	-1.0
#A11N	-1.0	-0.9
#A11S	-1.1	-1.1
#A23S	-0.6	-0.6
#A27S	-0.7	-0.7
#P47N	0.7	0.7
#P24N	0.6	0.6
#P10N	0.8	0.8
#P28S	0.8	0.8
#P43S	0.7	0.7
#I18S	0.2	0.2
#I32S	0.6	0.6
T _{PI}	8.5	8.5

Table C.1: Comparison of freshwater transport estimates from the standard model (STD) and the standard model without bottom water constraints at 24°N and 36°N in the Atlantic (NBW). These estimates are made assuming that the initial Bering Strait throughflow estimate is correct. The uncertainties associated with these values are discussed in section 3.4.6. All values are in 10^9 kg s^{-1} .

Section	STD Ekman Transport	NBW Ekman Transport	Uncertainty
#A48N	-4.2	-4.0	1.3
#A36N	-2.8	-2.8	1.1
#Flst	0.1	0.1	0.5
#A24N	4.2	4.7	1.3
#A11N	8.7	9.4	1.9
#A11S	-12.8	-12.7	1.2
#A23S	-4.1	-4.0	1.1
#A27S_W	-0.8	-0.8	3.0
#A27S_E	-0.2	-0.2	2.8
#A57S_W	1.1	1.1	11.2
#A57S_E	0.9	0.9	11.2
#0E_S	-0.4	0.1	1.0
#P47N	-5.1	-5.1	1.4
#P24N	8.5	8.5	1.3
#P10N	38.3	38.3	1.7
#P28S	-5.3	-5.3	6.9
#P43S	9.2	9.2	7.1
#Mz_N	-0.6	-0.6	1.6
#Mz_S	-0.7	-0.7	1.2
#I18S	-15.3	-15.3	6.5
#I32S	0.4	0.4	6.7
#Drake	0.4	0.4	3.4
#0E_N	1.2	1.2	5.2
#0E2Afr	1.5	1.5	4.6
#30E	2.9	2.9	4.7
#132E	2.2	2.2	7.9

Table C.2: Comparison of Ekman transport estimates from the standard model (STD) and the standard model without bottom water constraints at 24°N and 36°N in the Atlantic (NBW). All estimates have been computed to balance the mass and salinity transports across the sections (see the discussion in section 3.4.6). The Ekman transports across the following sections were not corrected: #Drake, #30E, #0EN, #0E2Afr, #132E and #Mz_N. Uncertainties are taken from the uncertainty in the top to bottom transport across the sections. All values are in 10^9 kg s^{-1} . Positive values are northward and eastward.

Section	Net Mass transport (10^9 kg/s) NBW	Heat/ Θ transport (PW) NBW STD		Uncertainty due to σ_b (PW)	Total Estimated Uncertainty (PW)
#A48N	-1.1 \pm 1.3	0.66	0.65	0.04	0.25
#A36N	-1.1 \pm 1.1	1.01	0.88	0.07	0.26
#Flst+#A24N	-1.0 \pm 1.2	1.07	0.93	0.05	0.26
#A11N+NBC	-1.0 \pm 1.9	1.39	1.34	0.05	0.26
#A11S	-1.1 \pm 1.2	0.89	0.88	0.04	0.25
#A23S	-0.7 \pm 1.1	0.33	0.33	0.04	0.25
#A27S	0.7 \pm 1.2	0.49	0.50	0.05	0.26
#A57S	0.0 \pm 1.9	-0.03	-0.03	0.02	0.25
#P47N	0.6 \pm 1.4	-0.08	-0.08	0.04	0.25
#P24N	0.6 \pm 1.3	0.45	0.45	0.09	0.27
#P10N	0.8 \pm 1.7	0.44	0.44	0.07	0.26
#Mz_N	0.3 \pm 1.6	0.03	0.03	0.05	0.26
#Mz_S	0.2 \pm 1.2	0.01	0.01	0.05	0.26
#0E_S	0.0 \pm 1.0	0.03	0.03	0.01	0.25
<hr/>					
#0E_N	167.4 \pm 5.2	1.86	1.85	0.14	0.29
#0E2Afr	142.7 \pm 4.6	0.90	0.90	0.18	0.31
#Drake	141.1 \pm 3.4	1.40	1.40	0.10	0.27
#30E	143.8 \pm 4.7	1.16	1.16	0.31	0.40
#132E	151.2 \pm 7.9	1.73	1.73	0.35	0.43
#P28S	9.6 \pm 6.9	-0.06	-0.05	0.16	0.30
#P43S	9.6 \pm 7.1	0.25	0.25	0.12	0.28
#I18S	-8.8 \pm 6.5	-1.45	-1.45	0.16	0.30
#I32S	-8.3 \pm 6.7	-1.30	-1.30	0.13	0.28

Table C.3: Comparison of heat and temperature flux estimates for the standard model (STD) as described in Chapters 2 and 3 and the same model without the bottom water constraints at 24°N and 36°N in the Atlantic (NBW). The Ekman transport estimates, corrected to balance the salt equations as described in Section 3.4.6 have been subtracted (see Table C.2).

REFERENCES

- Ajax Expedition, Ajax data report, Physical, chemical and in-situ CTD data from the Ajax Expedition in the South Atlantic Ocean, aboard RV Knorr leg I, 7 October-6 November 1983, Leg II, 11 January-19 February 1984, *SIO Ref 85-24*, Scripps Inst. of Oceanogr., Univ of Calif., San Diego, La Jolla, 1985.
- Aagaard, K., and E. C. Carmack, The role of sea ice and other fresh water in the Arctic circulation, *J. Geophys. Res.*, *94*, 14485-14498, 1989.
- Baumgartner, A., and E. Reichel, *The World Water Balance*, 179 pp., Elsevier Science, New York, 1975.
- Bingham, F. M., and L. D. Talley, Estimates of Kuroshio transport using an inverse technique, *Deep Sea Res.*, *38 Suppl. 1A*, 21-43, 1991.
- Boland F. M., and B. V. Hamon, The East Australian Current 1965-1968. *Deep Sea Res.*, *17*, 777-794, 1970.
- Broecker, W. J., The Biggest Chill, *Natural History Magazine*, *47*, 75-82, 1987.
- Broecker, W. J., The great global conveyor belt, *Oceanography*, *4*, 79-89, 1991.
- Brogan, W. L., Modern Control Theory, 2nd ed., Prentice Hall, Englewood Cliffs, N.J. 509 pp., 1982.
- Bryden H. L., and R. D. Pillsbury, Variability of deep flow in the Drake Passage from year-long current measurements, *J. Phys. Oceanogr.*, *7*, 803-810, 1977.
- Bryden H. L., D. H. Roemmich, and J. A. Church, Ocean Heat Transport Across 24°N in the Pacific, *Deep Sea Res.*, *38*, 297-324, 1991.
- Bunker, A. F., Surface energy fluxes of the South Atlantic Ocean, *Mon. Weather Rev.*, *116*, 809-823, 1988.
- Coachman, L. K., and K. Aagaard, Transports through the Bering Strait: Annual and interannual variability, *J. Geophys. Res.*, *93*, 15535-15539, 1988.
- Cox, M. D., A primitive equation, three-dimensional model of the ocean, *GFDL Ocean Group Tech. Rep. 1*, Geophys. Fluid Dyn. Lab., Princeton, N.J., 1984.
- Dickson, R. W., and J. Brown, The production of North Atlantic Deep Water: Sources, rates and pathways, *J. Geophys. Res.*, *99*, 12319-12341, 1994.

- Edwards, C. A., and J. Pedlosky, The influence of distributed source and upwelling on the baroclinic structure of the abyssal circulation, *J. Phys. Oceanogr.*, **25**, 2259-2284, 1995.
- Evans, D. L., and S. S. Signorini, Vertical structure of the Brazil Current, *Nature*, **315**, 48-50.
- Evans, D. L., S. S. Signorini, and L. B. Miranda, A note on the transport of the Brazil Current, *J. Phys. Oceanogr.*, **13**, 1732-1738, 1983.
- Ffield, A., and A. L. Gordon, Vertical Mixing in the Indonesian Thermocline, *J. Phys. Oceanogr.*, **22**, 184-195, 1992.
- Fieux M., C. Andrie, P. Delecluse, A. G. Ilahude, A. Kartavtseff, F. Mantsi, R. Molcard, and J. C. Swallow, Measurements within the Pacific-Indian oceans throughflow region, *Deep Sea Res.*, **41**, 1091-1130, 1994.
- Fofonoff, N., Physical properties of seawater: a new salinity scale and equation of state for seawater, *J. Geophys. Res.*, **90**, 3332-3342, 1985.
- Fonesca, T., An overview of the poleward undercurrent and upwelling along the Chilean Coast. *Poleward Flows along Eastern Ocean Boundaries*. In: *Coastal and Estuarine Studies*, **34**. S.J. Neshyba, Ch.N.K. Mooers, R.L. Smith and R.T. Barber (Eds.), Springer-Verlag, New York, NY, 203-218, 1989.
- Friedrichs, M. A. M., and M. M. Hall, Deep circulation in the tropical North Atlantic, *J. Mar. Res.*, **51**, 697-736, 1993. Fu, L., The general circulation and meridional heat transport of the subtropical South Atlantic determined by inverse methods, *J. Phys. Oceanogr.*, **11**, 1171-1193, 1981.
- Fu, L., Mass, heat and freshwater fluxes in the South Indian Ocean, *J. Phys. Oceanogr.*, **16**, 1683-1693, 1986.
- Georgi, D. T., and J. M. Toole, The Antarctic Circumpolar Current and the oceanic heat and freshwater budgets, *J. Mar. Res.*, **40**, Suppl., 183-197, 1982.
- Goldenberg, S. B. and J. J. O'Brien, Time and space variability of tropical Pacific wind stress, *Monthly Weather Review*, **109**, 1190-1207, 1981.
- Gordon, A. L., Interocean exchange of thermocline water, *J. Geophys. Res.*, **91**, 5037-5046, 1986.
- Gordon, A. L., Brazil-Malvinas Confluence - 1984, *Deep Sea Res.*, **36**, 359-384, 1989.
- Gordon, A. L., and C. L. Greengrove, Geostrophic circulation of the Brazil-Falkland confluence, *Deep Sea Res.*, **33**, 573-585, 1986.

- Gordon, A. L., R. F. Weiss, W. M. Smethie, Jr., and M. J. Warner, Thermocline and intermediate water communication between the South Atlantic and Indian Oceans, *J. Geophys. Res.*, *97*, 7223-7240, 1992.
- Guiffrida, M. R., Estimates of net Antarctic Circumpolar Current transports and Southern Ocean budgets of mass, heat, freshwater, oxygen and silicate, M.S. thesis, 84 pp., Texas A&M University, College Station, Texas, 1985.
- Halkin, D., and T. Rossby, The structure and transport of the Gulf Stream at 73°W., *J. Phys. Oceanogr.*, *15*, 1439-1452, 1985.
- Hall, M. M., and H. L. Bryden, Direct estimates and mechanisms of ocean heat transport, *Deep Sea Res.*, *29*, 339-359, 1982.
- Hall, M. M., and H. L. Bryden, Profiling the Gulf Stream with a current meter mooring, *Geophysical Research Letters*, *12*, 203-206, 1985.
- Halpern, D., A. Hollingsworth and F. Wentz, ECMWF and SSM/I Global Surface Wind Speeds, *Journal of Atmos. and Oceanic Tech.* *11*, 779-788, 1994.
- Hamon, B. V. and T. J. Golding, Physical Oceanography of the Australian region, *Commonwealth Scientific and Industrial Research Organization, Fisheries and Oceanography Report 1977-1979*, 1-8, 1980.
- Harris, T. F. W., Sources of the Agulhas Current in the spring of 1964, *Deep Sea Res.*, *19*, 633-650, 1972.
- Harrison, D. E., On climatological monthly mean wind stress and wind stress curl fields over the world ocean, *Journal of Climate*, *2*, 57-70, 1989.
- Hastenrath, S., On meridional heat transports in the world ocean, *J. Phys. Oceanogr.*, *12*, 922-927, 1982.
- Hellerman, S. and M. Rosenstein, Normal monthly wind stress over the world ocean with error estimates, *J. Phys. Oceanogr.*, *13*, 1093-1104, 1983.
- Hendry, R. M., Hydrographic Measurements from C.S.S. Hudson Cruise 82-002, *Canadian Technical Report of Hydrography and Ocean Sciences, No 118*, Bedford Institute of Oceanography, Dartmouth, Nova Scotia, 112 pp., 1989.
- Hogg, N. G., A note on the deep circulation of the western North Atlantic: its nature and causes, *Deep Sea Res.*, *30*, 945-961, 1983.
- Hogg, N. G., On the transport of the Gulf Stream between Cape Hatteras and the Grand Banks, *Deep Sea Res.*, *39*, 1231-1246, 1992.

- Hogg, N., P. Biscaye, W. Gardner, and W. J. Schmitz Jr., On the transport and modification of Antarctic Bottom Water in the Vema Channel, *J. Mar. Res.*, 40, Suppl., 231-263, 1982.
- Holfort, J., Grossräumige Zirkulation und meridional Transporte im Südatlantik. Ph.D. thesis, pp. 118., Ber. Inst. Meeresk. Kiel, 290, 1994 (in German, English abstract).
- Hsiung, J., R. E. Newell, and T. Houghtby, The annual cycle of oceanic heat storage and oceanic meridional heat transport, *Q. J. R. Meteorol. Soc.*, 115, 1-28, 1989.
- Jacobs, S. S., and D. T. Georgi, Observations on the Southwest Indian/Antarctic Ocean, *Deep Sea Res.*, Suppl., *A Voyage of Discovery*, edited by M. Angel., pp. 43-84., Pergammon Press, New York, 1977.
- Joyce, T. M., C. Wunsch and S. D. Pierce, Synoptic Gulf Stream velocity profiles through simultaneous inversions of hydrographic and acoustic doppler data, *J. Geophys. Res.*, 91, 7573-7585, 1986.
- Katz, E. J., An interannual study of the Atlantic North Equatorial Countercurrent, *J. Phys. Oceanogr.*, 14, 116-123, 1993.
- Leetmaa, A., and A. Bunker, Updated charts of the mean annual wind stress convergences in the Ekman layers, and Sverdrup transports in the North Atlantic, *J. Mar. Res.*, 36, 311-322, 1978.
- Lewis, R. L., and R. G. Perkin, The practical salinity scale 1978: conversion of existing data, *Deep Sea Res.*, 28A, 307-328, 1981.
- Locarnini, R. A., T. Whitworth, III., and W. D. Nowlin, Jr., The importance of the Scotia Sea on the outflow of Weddell Sea Deep Water, *J. Mar. Res.*, 51, 135-153, 1993.
- Lukas, R., E. Firing, P. Hacker, P. L. Richardson, C. A. Collins, R. Fine, and R. Gammon, Observations of the Mindanao Current during the Western Equatorial Ocean Circulation Study, *J. Geophys. Res.*, 96, 7089-7104, 1991.
- Luyten, J., M. McCartney, H. Stommel, R. Dickson, and E. Gmitrowicz, On the sources of North Atlantic Deep Water, *J. Phys. Oceanogr.*, 23, 1885-1892, 1993.
- Lutjeharms J. R. E., and H. R. Valentine, Southern Ocean thermal fronts south of Africa. *Deep Sea Res.*, 31, 1461-1475, 1984.

- Macdonald, A., Mass, heat, oxygen and nutrient fluxes at 30°S and their implications for the Pacific-Indian through flow and the global heat budget, S.M. thesis, 183 pp., Mass. Inst. of Technol./Woods Hole Oceanogr. Inst. Joint Program, Cambridge, Mass., 1991.
- Macdonald, A., Property fluxes at 30°S and their implications for the Pacific-Indian throughflow and the global heat budget, *J. Geophys. Res.*, 6851-6868, 1993.
- Mantyla, A. W., and J. L. Reid, Abyssal characteristic of the World Ocean waters, *Deep Sea Res.*, 30, 805-830, 1983.
- Martel F., and C. Wunsch, The North Atlantic circulation in the early 1980s-An estimate from inversion of a finite-difference model, *J. Phys. Oceanogr.*, 23, 898-924, 1993.
- McCartney, M. S., and R. A. Curry, Transequatorial flow of Antarctic Bottom Water in the Western Atlantic Ocean: abyssal geostrophy at the equator, *J. Phys. Oceanogr.*, 23, 1264-1276, 1993.
- McDougall, T. J., Neutral surfaces, *J. Phys. Oceanogr.*, 17, 1950-1964, 1987.
- McDougall, T. J., Parameterizing mixing in inverse models, *Dynamics of Oceanic Internal Gravity Waves*, edited by P. Müller and D. Henderson, Proceedings of the sixths 'Aha Huliko' a Hawaiian Winter Workshop, University of Hawaii at Manoa, 355-386, 1991.
- Mestas-Núñez, A. M., D. B. Chelton, M. H. Freilich, and J. G. Richman, An Evaluation of ECMWF-Based Climatological Wind Stress Fields, *J. Phys. Oceanogr.*, 24, 1532-1549, 1994.
- Meyers, G., R. J. Bailey, and A. P. Worby, Geostrophic transport of Indonesian throughflow, *Deep Sea Res.*, (in press) 1995.
- Minster, J.-F., and M. Boulahdid, Redfield ratios along isopycnal surfaces - A complementary study, *Deep Sea Res.*, 34 1981-2003, 1987
- Miranda L. B., and B. M. Castro Filho, Geostrophic flow conditions of the Brazil Current at 19°S. *Ciencia Interamericana*, 22, 44-48, 1982.
- Molinari, R. L., W. D. Wilson, and K. Leaman, Volume and heat transports of the Florida Current: April 1982 through August 1983, *Science*, 227, 295-297, 1985.
- Nierenberg, W, A., R. Radok, and O. M. Phillips, Physical and chemical data from the Southern Ocean between Australia and Antarctica, USNS ELTANIN Cruise 41, 1969-1970, *SIO ref. 10-72-19*, 57 pp., Scripps Inst. of Oceanogr., Univ. of Calif., San Diego, 1970.

- Nowlin, W. D., Jr., and M. Clifford, The kinematic and thermohaline zonation of the Antarctic Circumpolar Current at Drake Passage, *J. Mar. Res.*, 40, Suppl., 481-507, 1982.
- Nowlin, W. D., Jr., and J. M. Klinck, The physics of the Antarctic Circumpolar, *Rev. Geophys.*, 24, 469-491, 1986.
- Oort, A. H., and T. H. Von der Haar, On the observed annual cycle in the ocean-atmosphere heat balance over the northern hemisphere, *J. Phys. Oceanogr.*, 6, 781-800, 1976.
- Peterson, R. G., and L. Stramma, Upper-level circulation in the South Atlantic Ocean, *Prog. Oceanogr.*, 26, 1-73, 1991.
- Peterson, R. G., and T. Whitworth, III, The Subantarctic and Polar Fronts in relation to deep water masses through the Southwestern Atlantic, *J. Geophys. Res.*, 94, 10817-10838, 1989.
- Philander, S. G. H., and R. C. Pacanowski, The mass and heat budget in a model of the tropical Atlantic Ocean, *J. Geophys. Res.*, 91, 14212-14220, 1986.
- Pickard, G. L., and W. J. Emery, *Descriptive Physical Oceanography*, fifth edition, Pergamon Press, New York, 320 pp., 1990.
- Pond S., and G. L. Pickard, *Introductory Dynamical Oceanography*, Pergamon Press, New York, 329 pp., 1983.
- Rago, T. A., and H. T. Rossby, Heat transport into the North Atlantic Ocean north of 32°N latitude, *J. Phys. Oceanogr.*, 17, 854-871, 1987.
- Read, J. F., and R. T. Pollard, Structure and Transport of the Antarctic Circumpolar Current and Agulhas Return Current at 40°E, *J. Geophys. Res.*, 98, 12281-12295, 1993.
- Redfield, A. C., B. H. Ketchum, and F. A. Richards, The influence of organisms on the composition of sea-water, in *The Sea*, vol. 2, edited by M. N. Hill, pp. 26-77, Wiley-Interscience, New York, 1963.
- Reid, J. L., Transpacific hydrographic sections at Lats 43°S and 28°S: The *Scorpio* Expedition -III. - Upper water and a note on southward flow at mid-depth. *Deep Sea Res.*, 20, 39-49, 1973.
- Reid, J. L., On the mid-depth circulation of the World Ocean, In: *Evolution of Physical Oceanography-Scientific Surveys in Honor of Henry Stommel*, edited by B. A. Warren and C. Wunsch, 70-111 pp., MIT Press, Cambridge, MA, 1981.

- Reid, J. L., On the total geostrophic circulation of the South Pacific Ocean, flow patterns, tracers and transports. *Prog. Oceanog.*, 16, 1-61, 1986.
- Reid, J. L., On the total geostrophic circulation of the South Atlantic Ocean: Flow Patterns, tracers and transports, *Prog. Oceanog.*, 23, 149-244, 1989.
- Reid, J. L., On the total geostrophic circulation of the North Atlantic Ocean: Flow Patterns, tracers and transports, *Prog. Oceanog.*, 33, 1-92, 1994.
- Ridgeway, K. R., and J. S. Godfrey, Mass and heat budgets in the East Australian Current: a direct approach, submitted to *J. Geophys. Res.*, 1993.
- Rintoul, S. R., Mass, heat and nutrient fluxes in the Atlantic Ocean determined by inverse methods. Ph.D. thesis, 287 pp., Mass. Inst. of Technol./Woods Hole Oceanogr. Inst. Joint Program, Cambridge, Mass., 1988.
- Rintoul, S. R., South Atlantic interbasin exchange, *J. Geophys. Res.*, 96, 2675-2692, 1991.
- Rintoul, S. R., and C. Wunsch, Mass, heat, oxygen and nutrient fluxes and budgets in the North Atlantic Ocean, *Deep Sea Res.*, 38 Suppl. 1A, 355-377, 1991.
- Roemmich, D., The application of inverse methods to problems in ocean circulation, Ph.D. thesis, 193 pp., Mass. Inst. of Technol./Woods Hole Oceanogr. Inst. Joint Program, Cambridge, Mass., 1980.
- Roemmich, D., The balance of geostrophic and Ekman transports in the tropical Atlantic Ocean, *J. Phys. Oceanogr.*, 13, 1534-1539, 1983.
- Roemmich, D. and T. McCallister, Large scale circulation of the North Pacific Ocean, *Prog. Oceanog.*, 22, 171-204, 1989.
- Roemmich, D., T. McCallister, and J. Swift, A transpacific hydrographic section along 24°N: the distribution of properties in the subtropical gyre, *Deep Sea Res.*, 38 Suppl. 1A, 1-20, 1991.
- Roemmich, D. and B. Cornuelle, Observing the fluctuations of gyre-scale ocean circulation: A study of the subtropical South Pacific, *J. Phys. Oceanogr.*, 20, 1919-1934, 1990.
- Roemmich, D., and C. Wunsch, Two transatlantic sections: meridional circulation and heat flux in the subtropical North Atlantic Ocean, *Deep Sea Res.*, 32, 619-664, 1985.

- Roether, W. M., Sarnthein, T.J. Müller, W. Nellen, and D. Sahrhage, Südatlantik-Zirkumpolarstrum, Reise Nr 11, 3 Oktober 1989–11 März 1990, Universität Hamburg, 90–2, 1990.
- Sarmiento, J. L., On the north and tropical Atlantic heat balance, *J. Geophys. Res.*, **91**, 11677–11689, 1986.
- Sætre, R., and A. J. De Silva, The circulation of the Mozambique Channel, *Deep Sea Res.*, **31**, 485–508, 1984.
- Schmitt, R. W., P. S. Bogden, and C. E. Dorman, Evaporation minus precipitation and density fluxes for the North Atlantic, *J. Phys. Oceanogr.*, **19**, 1208–1221, 1989.
- Schmitz, W. J. Jr., On the interbasin-scale thermohaline circulation, *Rev. Geophys.*, **33**, 151–173, 1995.
- Schmitz, W. J. Jr., and M. S. McCartney, On the North Atlantic circulation, *Rev. Geophys.*, **31**, 29–49, 1993.
- Schmitz, W. J. Jr., and P. L. Richardson, On the sources of the Florida Current, *Deep Sea Res.*, **38 Suppl. 1A**, 379–409, 1991.
- Schott, F., and H. Stommel, Beta spirals and absolute velocities in different oceans, *Deep Sea Res.*, **25**, 961–1010, 1978.
- Scripps Inst. of Oceanogr., South Atlantic Ventilation Experiment (SAVE), Chemical, physical and ctd data report, legs 1, 2 and 3, *SIO ref. 92–9*, Scripps Inst. of Oceanogr., Univ. of Calif., San Diego, 1992a.
- Scripps Inst. of Oceanogr., South Atlantic Ventilation Experiment (SAVE), Chemical, physical and ctd data report, legs 4 and 5, *SIO ref. 92–10*, Scripps Inst. of Oceanogr., Univ. of Calif., San Diego, 1992b.
- Semtner, A. J., and R. M. Chervin, Ocean general circulation from a global eddy-resolving model, *J. Geophys. Res.*, **97**, 5493–5550, 1992.
- Sievers, H. A., and W. D. Nowlin, The stratification and water masses in Drake Passage, *J. Geophys. Res.*, **83**, 10489–10514, 1984.
- Smith, R. L., A. Huyer, J. S. Godfrey, and J. A. Church, The Leeuwin Current off western Australia, 1986–1987, *J. Phys. Oceanogr.*, **21**, 323–345, 1991.
- Speer, K. G., and W. Zenk, The flow of Antarctic bottom water into the Brazil Basin, *J. Phys. Oceanogr.*, **23**, 2667–2682, 1993.

- Stommel, H., Asymmetry of interoceanic fresh-water and heat fluxes, *Proc. Natl. Acad. Sci.*, **77**, 2377-2381, 1980.
- Stommel, H., and A. B. Arons, On the abyssal circulation of the world ocean II. An idealized model of the circulation pattern and amplitude in oceanic basins, *Deep Sea Res.*, **6**, 217-233, 1960.
- Stommel, H., E. D. Stroup, J. L. Reid, and B. A. Warren, Transpacific hydrographic sections at Lats 43°S and 28°S: The *Scorpio* Expedition, I, Preface, *Deep Sea Res.*, **20**, 1-7, 1973.
- Stramma L., and R. G. Peterson, Geostrophic transport in the Benguela Current region, *J. Phys. Oceanogr.*, **19**, 1440-1448, 1989.
- Talley, L., Meridional heat transport in the Pacific Ocean, *J. Phys. Oceanogr.*, **14**, 231-241, 1984.
- Talley, L. D., T. M. Joyce, and R. A. deSzoek, Transpacific sections at 47°N and 152°W: distribution of properties, *Deep Sea Res.*, **38 Suppl. 1A**, 63-82, 1991.
- Talley, L. D., and D. Roemmich editors, Joseph L. Reid a tribute in recognition of 40 years of contributions to oceanography, *Deep Sea Res.*, **38 Suppl. 1A**, pp. 654, 1991.
- Tchernia P., *Descriptive Regional Oceanography*, Pergamon Press, New York, 253 pp., 1980.
- Thompson, R. O. R. Y., Observations of the Leeuwin Current off western Australia. *J. Phys. Oceanogr.*, **14**, 623-628, 1984.
- Toole, J. M., and M. E. Raymer, Heat and fresh water budgets of the Indian Ocean - revisited, *Deep Sea Res.*, **32**, 917-928, 1985.
- Toole, J. M., R. C. Millard, Z. Wang, and S. Pu, Observations of the Pacific North Equatorial Bifurcation at the Philippine Coast, *J. Phys. Oceanogr.*, **20**, 307-318, 1990.
- Toole, J. M., and B. A. Warren, A hydrographic section across the subtropical South Indian Ocean, *Deep Sea Res.*, **40**, 1973-2020, 1993.
- Toole, J. M., E. Zou, and R. C. Millard, On the circulation of the upper waters in the western equatorial Pacific Ocean, *Deep Sea Res.*, **35**, 1451-1482, 1988.
- Trenberth, K. E., J. G. Olson, and W. G. Large, A global ocean wind stress climatology based on ECMWF Analyses, *NCAR Technical Note 338+STR*, 93 pp., National Center for Atmospheric Research, Boulder, Colorado, 1989.

- Trenberth, K. E., W. G. Large, and J. G. Olson, The mean annual cycle in global ocean wind stress, *J. Phys. Oceanogr.* **20**, 1742-1760, 1990.
- Tsuchiya P., Thermostads and circulation in the upper layer of the Atlantic Ocean, *Progress in Oceanography*, **16**, 235-267, 1986.
- Warren, B.A., Transpacific hydrographic sections at Lats 43°S and 28°S: The *Scorpio* Expedition -II. Deep Water, *Deep Sea Res.*, **20**, 9-38, 1973.
- Warren, B. A., Structure of deep western boundary currents, *Deep Sea Res.*, **23**, 129-142, 1976.
- Warren, B. A., Deep Circulation of the World Ocean, *Evolution of Physical Oceanography-Scientific Surveys in Honor of Henry Stommel*, edited by B. A. Warren and C. Wunsch, 6-41 pp., MIT Press, Cambridge, MA, 1981a.
- Warren, B. A., Transindian hydrographic section at Lat. 18°S: Property distributions and circulation in the South Indian Ocean, *Deep Sea Res.*, **28a**, 759-788, 1981b.
- Weaver, A. J., Ocean currents and climate. *Nature*, **34** 432, 1990.
- Whitworth, T., III, Monitoring the transport of the Antarctic Circumpolar Current at Drake Passage, *J. Phys. Oceanogr.*, **13**, 2045-2057, 1983.
- Whitworth, T., III, and W. D. Nowlin Jr., Water Masses and Currents of the Southern Ocean at the Greenwich Meridian, *J. Geophys. Res.*, **92**, 6462-6476, 1987.
- Whitworth, T., III, W. D. Nowlin Jr., and S. J. Worley, The net transport of the Antarctic Circumpolar Current through Drake Passage, *J. Phys. Oceanogr.*, **12**, 960-971, 1982.
- Whitworth, T., III, and R. G. Peterson, The volume transport of the Antarctic Circumpolar Current from bottom pressure measurements, *J. Phys. Oceanogr.*, **15**, 810-816, 1985.
- Wiggins, R. A., The general linear inverse problem: Implication of surface waves and free oscillations for earth structure, *Rev. Geophys. Space Phys.*, **10**, 251-285, 1972.
- Wijffels, S. E., Exchanges between hemispheres and gyres: a direct approach to the mean circulation of the equatorial Pacific, Ph.D. thesis, 267 pp., Mass. Inst. of Technol./Woods Hole Oceanogr. Inst. Joint Program, Woods Hole, Mass., 1993.
- Wijffels, S. E., R. W. Schmitt, H. L. Bryden, and A. Stigebrandt, Transport of freshwater by the oceans, *J. Phys. Oceanogr.*, **22**, 155-162, 1992.

- U.S. WOCE, U.S. Contribution to WOCE Core Project 1 The Program Design for the Indian Ocean, 80 pp., U.S. WOCE Office, College Station, Texas, 1993.
- Wright, W. R., Northward transport of Antarctic Bottom Water in the western Atlantic Ocean, *Deep Sea Res.*, 17, 367-371, 1970.
- Wunsch, C., The general circulation of the North Atlantic west of 50°W determined from inverse methods, *Rev. Geophys. Space Phys.*, 16, 583-620, 1978.
- Wunsch, C., D. Hu, and B. Grant, Mass, heat and nutrient fluxes in the South Pacific Ocean, *J. Phys. Oceanogr.*, 13, 725-753, 1983.
- You, Y., and M. Tomczak, Thermocline circulation and ventilation in the Indian Ocean derived from water mass analysis, *Deep Sea Res.*, 40, 13-56, 1993.
- Zemba, J. C., The structure and transport of the Brazil Current between 27° and 36° South, Ph.D. thesis, 164 pp., WHOI Rep. Num. WHOI-9137, Mass. Inst. of Technol./Woods Hole Oceanogr. Inst. Joint Program, Woods Hole, Mass., 1993.

DOCUMENT LIBRARY

Distribution List for Technical Report Exchange – May 1995

University of California, San Diego
SIO Library 0175C
9500 Gilman Drive
La Jolla, CA 92093-0175

Hancock Library of Biology & Oceanography
Alan Hancock Laboratory
University of Southern California
University Park
Los Angeles, CA 90089-0371

Gifts & Exchanges
Library
Bedford Institute of Oceanography
P.O. Box 1006
Dartmouth, NS, B2Y 4A2, CANADA

Commander
International Ice Patrol
1082 Shennecossett Road
Groton, CT 06340-6095

NOAA/EDIS Miami Library Center
4301 Rickenbacker Causeway
Miami, FL 33149

Research Library
U.S. Army Corps of Engineers
Waterways Experiment Station
3909 Halls Ferry Road
Vicksburg, MS 39180-6199

Institute of Geophysics
University of Hawaii
Library Room 252
2525 Correa Road
Honolulu, HI 96822

Marine Resources Information Center
Building E38-320
MIT
Cambridge, MA 02139

Library
Lamont-Doherty Geological Observatory
Columbia University
Palisades, NY 10964

Library
Serials Department
Oregon State University
Corvallis, OR 97331

Pell Marine Science Library
University of Rhode Island
Narragansett Bay Campus
Narragansett, RI 02882

Working Collection
Texas A&M University
Dept. of Oceanography
College Station, TX 77843

Fisheries-Oceanography Library
151 Oceanography Teaching Bldg.
University of Washington
Seattle, WA 98195

Library
R.S.M.A.S.
University of Miami
4600 Rickenbacker Causeway
Miami, FL 33149

Maury Oceanographic Library
Naval Oceanographic Office
Building 1003 South
1002 Balch Blvd.
Stennis Space Center, MS, 39522-5001

Library
Institute of Ocean Sciences
P.O. Box 6000
Sidney, B.C. V8L 4B2
CANADA

National Oceanographic Library
Southampton Oceanography Centre
European Way
Southampton SO14 3ZH
UK

The Librarian
CSIRO Marine Laboratories
G.P.O. Box 1538
Hobart, Tasmania
AUSTRALIA 7001

Library
Proudman Oceanographic Laboratory
Bidston Observatory
Birkenhead
Merseyside L43 7 RA
UNITED KINGDOM

IFREMER
Centre de Brest
Service Documentation - Publications
BP 70 29280 PLOUZANE
FRANCE

REPORT DOCUMENTATION PAGE	1. REPORT NO. MIT/WHOI 95-25	2.	3. Recipient's Accession No.
4. Title and Subtitle Oceanic Fluxes of Mass, Heat and Freshwater: A Global Estimate and Perspective			5. Report Date September 1995
			6.
7. Author(s) Alison Marguerite Macdonald			8. Performing Organization Rept. No.
9. Performing Organization Name and Address MIT/WHOI Joint Program in Oceanography/Applied Ocean Science & Engineering			10. Project/Task/Work Unit No. MIT/WHOI 95-25
			11. Contract(C) or Grant(G) No. (C) (G)
12. Sponsoring Organization Name and Address Funding was provided by the National Aeronautic and Space Administration through a Graduate Fellowship in Global Change Research and under Contract NAGW-1048 and by a National Science Foundation Grant No. OCE-9205942 through the Massachusetts Institute of Technology.			13. Type of Report & Period Covered Ph.D. Thesis
			14.
15. Supplementary Notes This thesis should be cited as: Alison Marguerite Macdonald, 1995. Oceanic Fluxes of Mass, Heat and Freshwater: A Global Estimate and Perspective. Ph.D. Thesis. MIT/WHOI, 95-25.			
16. Abstract (Limit: 200 words) Data from fifteen globally distributed, modern, high resolution, hydrographic oceanic transects are combined in an inverse calculation using large scale box models. The models provide estimates of the global meridional heat and freshwater budgets and examine the sensitivity of the global circulation, to a variety of external constraints. A solution is found which is consistent with both the model physics and the global data set. The picture of the global circulation which emerges from the models is a complex, turbulent flow. When integrated across ocean basins not one, but two major cells emerge. The first connects an Atlantic overturning cell to the Antarctic Circumpolar Current and thence to the Indian and Pacific Basins. The second cell connects the Pacific and Indian basins to the north and south of Australia. The cells are found to be independent of one another, i.e. the Indonesian Passages do not represent a significant element in a net global circulation. While the models present ample evidence of westward flow around the southern tip of South Africa, the variability of flow in this region makes hydrography a poor estimator of the relative strengths of the controversial "warm" and "cold" water paths.			
17. Document Analysis			
a. Descriptors global circulation heat flux hydrography			
b. Identifiers/Open-Ended Terms			
c. COSATI Field/Group			
18. Availability Statement Approved for publication; distribution unlimited.		19. Security Class (This Report) UNCLASSIFIED	21. No. of Pages 330
		20. Security Class (This Page)	22. Price